The Manipulation of Sound with Acoustic Metamaterials

Gareth Paul Ward
School of Physics
University of Exeter

A thesis submitted for the degree of
Doctor of Philosophy

June 2017

The Manipulation of Sound with Acoustic Metamaterials

Submitted by Gareth Paul Ward to the University of Exeter as a thesis for the
degree of Doctor of Philosophy in Physics
June 2017

This thesis is available for Library use on the understanding that it is copyright material and that no quotation from the thesis may be published without proper acknowledgement.

I certify that all material in this thesis that is not my own work has been identified and that no material has previously been submitted and approved for the award of a degree by this or any other University.

G.P. Ward

Gareth Paul Ward
June 2017

Dedicated to the very many people who have put up with me along the way

Acknowledgements

It is finally done. Take it away from me, so that I may go and play World of Warships, or whatever other no-doubt-shortlived fad grabs ahold of me. I started writing this thesis in my second year, hoping to get some sort of head start, but soon discovered that I am a terrible procrastinator! So here it is, as ready as it is going to be, two months from the end of an adventure-filled four years. It could not have been achieved without many people around me, preventing me from getting too far removed from reality.

A first thank you goes out to those PhD colleagues who have also been great friends. It was both fun and instructive to see you guys go through the thesis stress, and rather odd to see it happen to myself. In my first year, out of our G31 gang, it was Al Murray and Simon Berry who gave me a glimpse of the future, and whom provided a lot of starting advice, something much needed in the first six months where nothing works and everything is hard. Following them in my second year were Joe Dockrey and Laura Parke, whom provided entertainment by being in constant competition with each other. To Joe, thanks for the ideas you generated in the brief period of your acoustics post-doc, and I'm glad someone enjoyed my burning knees after the ground floor tiling failed to save me from friction. To Laura, I maintain it was Ben's fault that you had rancid milk poured over your dress. In my third year, it was Ben's turn to churn out the two-hundred pages, and since my work is basically a copy of his but without polarisation, a great many thanks is appropriate. He also has a collection of embarrassing videos to use as blackmail, should I ever run for parliament. For those who started at the same time as me, good luck with your future careers. Daniel Hewson with your innumerable cakes, Chris Beckerleg with your English rugby banter, Sahaand Zanjani-Pour with your untameable friendliness (and hard tackles on the football pitch) and Rayko Stantchev who both never ceased to produce entertaining presentations, and introduced me to a level of tea customisation that I didn't think possible. There are also those who started their journey after me, whom have also helped immensely. Tom Graham, good luck with that tank of yours, sorry I keep stealing your teabags, and thanks for acting as a human meatshield for the rest of us. Sam Shelley, yes I am now going to read One Piece, so stop nagging and go and run another three-week model (Also, please make more pulled pork). In the year below them, I wish good luck to Joe Beadle, Vicky Kyrimi and Miguel Camacho-Aguilar, whom have really tested my own understanding with difficult questions; should make the viva that much easier! There were many other students outside of our G31 crew who also had a notable impact. Luke Mcdonald, I hope you kept those child-size Newcastle United socks, and Ali Humphrey, sorry you didn't manage to put me off a PhD with your inspirational lab tour back in 2013.

Another big tanks to the various Post-docs who have come and gone. To Tom Constant, the man who put me on to Rstats during my masters project all the way back in 2011, and who provided motivation to us all on our quest to produce ground breaking research with his little nuggets of science info. To Rhiannon Mitchell-Thomas who many times provided a much needed reality check on the limits of what we were doing, and whom could always be counted on to get everyone socialising, something that is underrated in the workplace. Thanks to Ian Hooper, who as well as lending his vast experience where needed, guided me through the second year of my masters project and put up with me when I was an annoying undergraduate. I also owe a big thanks to Ian for recommending to Roy that he offer me a PhD position, based on the brief interactions that we had. Thanks to Helen Rance for all of your help in the early days, especially when I did not know how to deal with supervisor meetings. A thanks to Peter Hale, and his excellent way with words, as well as his gym tenacity and genuine interest in people. Also a thanks to Tim Starkey, whom thought he'd escaped but now finds himself back in the lab, dealing with acoustic problems I've been able to avoid while writing up, and supplying a dry sense of humour not unlike my own. There are many more of course, whom I have interacted with on various time scales - Sam Hornet, good luck with your data science life, Edgar Villads-Johnson, I'm sorry that Wetherspoons will forever toast your buns no matter how much vigorously you instruct them not to.

A thanks to Nick Cole and his merry band of workshop engineers, who's quality of work and ingenious ideas never ceased to amaze me, as well as friendly chat even from the week I began the PhD. No 3D printer could ever replace that!

A special thanks to Ruth Lovelock, whom took on the formidable challenge of the single-slit experiment, and paved the way for me to finish it. Though research was not to be your cup of tea, had you not decided to follow your true passion of teaching, I would not be here writing this right now. I still refer back to your dissertation at times!

Another special thanks to Carl Davies. The man machine himself was an inspiration to me, putting my eight months of pain to shame with his eight-week thesis. I've never known someone capable of pushing themselves that hard, even when it is potentially detrimental. Who runs a half marathon obstacle course with no training whatsoever, furled on a diet of whiskey and KFC? Carl Davies, that's who. "It is only a matter of willpower". But besides the work side of things, you have also been a great friend, and I'll never regret approaching you and demanding you join my Welsh-only tutor group back in 2009. If anyone is going to succeed in the modern high pressure world of academia, it is you, so good luck. Please make sure you spread the gospel of Tom Jones to the Netherlands.

A thanks to all of my non-work related social circle, who have often provided relief from thoughts of boundary layer mechanisms, with their different perspectives on the world, and their willingness to have a good time. There are far too many of you with far too many unique contributions to mention in any great detail, but I'll attempt at least some names! There is the old uni social circle, in order provided by a random number generator, including but not limited to Alun Daley, Neil Horton, Christy Moen, Vikesh Patel, Nathan Coburne, Owen Wood, and Matthew Pocock, all of which I have managed to meet with at least once during the PhD. A thanks to Olivia Atcheson whom provided a much needed new friend back in the loneliest early days, though I'm still annoyed I never won at squash. There are those from Welshsoc whom continued to welcome me with open arms despite me being an old fart, providing the student life aspect of the PhD with the many memorable tours, and some of whom I even lived with. These include Glyn Lewis, Peter Gillibrand, Daniel Griffiths, Lucy Benbow, Jason Elward, Lewis Green, Lewis West, and many, many more. Finally, a huge thanks to the other members of the Three Musketeers and Dogtanian; Ed Folley, with your impressive ability to make other people laugh, even when you don't know them, Geraint Ward, a brother from another mother, to whom a whole separate book would need to be dedicated with the influence on my life to this point, and to Robert Ward, my younger brother whom will likely make this journey himself in future, and who, with a very similar world view to my own, provides a much needed sanity valve.

A thanks of course to my Family. To my parents Wendy and Fred, who despite our very little wealth, have trumped the odds and provided a fantastic environment for me to flourish. Perhaps I'll be able to repay it one day. To my sister Michelle, who regularly sends me small packages of joy in the form of my nieces and nephews Jack, Joy and David's attempts at colouring. Good luck with your new life in Peru, i'll be sure to visit! To Joyce and Gerry, the loving second set of parents that have pushed me for the nearly 26 years I have existed, and who of course provided Geraint to keep me company. To Sherry, who still makes me delicious birthday cakes full of love despite my age, and to all the rest too numerous to name, whom I could count on to help if it were ever required.

A special thanks to Jennifer Lewis, whom since I met in my second year, has provided untold levels of support, having the patience to deal with me in the full range of good and bad. In particular, for the daily cups of tea and lifts, and for the general company, especially needed when at times thesis stress was in danger of making me lose it completely. If I had not met you and you did not provide a stabilising force, I seriously doubt whether I'd have finished the PhD.

Finally, a huge thanks to my three supervisors, Alastair Hibbins, Roy Sambles and John Smith. John, a thanks for your very detailed acoustics insight, and your general pleasantness, including trusting me to present in your place all the way over in Indianapolis, when I had just finished my first year. Apologies for when I have perhaps acted less than professionally, I'll learn eventually. Alastair, thanks for not allowing me to get carried away on pointless side quests, and keeping me on track. Also, thanks for your ever more detailed feedback on written work, and kind words whenever I begin to doubt my research. Last of all thank you to Roy, whom from the day I started my masters project, used his vast experience to find a way to motivate me. Without that challenge, I very much doubt I'd have achieved what I did in my undergraduate degree, never mind the PhD. Your high expectations, combined with a continual faith in my ability to meet them, has driven me to improve myself in immeasurable ways.

Abstract

The original work presented in this thesis pertains to the design and characterisation of resonant-cavity-based acoustic metamaterials, with a focus on airborne sound. There are five separate experimental chapters, each with a unique approach to the design of periodic structures that can support and manipulate air-bound acoustic surface waves via diffractive coupling between resonant-cavities. The first two chapters concern measurement of the acoustic transmission though various kinds of periodic slit-arrays, whilst the latter three chapters utilise a near-field imaging technique to directly record and characterise the dispersion of trapped acoustic surface waves.

The first experimental chapter investigates the effect that thermodynamic boundary layers have on the Fabry-Perot-like cavity resonances that are so often utilised in acoustic metamaterial design. At audio frequencies, these boundary layers have a decay length that is typically more than two orders of magnitude smaller than the width of the resonating slit-cavities, hence it may naïvely be assumed that their effect can be ignored. However, by studying in detail the effect that reducing slit-cavity width has on the frequency of the measured cavity-resonance, for both a single slit cavity and a slit-cavity array, it is found that these boundary layer effects become significant on a far larger scale than their characteristic thickness. This is manifested in the form of a reduction in the resonant frequency as the slit-width is narrowed. Significant attenuation of the resonance and a 5% reduction in the effective speed of sound through the cavity is measured when the boundary layers form only 5% of the total width of each slit. Hence, it is both shown that the prevalent loss free treatment of acoustic slit-cavities is unrealistic, and that one may control the effective speed of sound through the slit-cavities with a simple change in slit-width.

The second chapter explores the effect of ‘compound’ grating structure on trapped acoustic surface waves, a compound grating having a basis comprised of more than one resonating element. The angle dependent acoustic transmission spectra of four types of aluminium slit-array are recorded, and for the compound gratings, it is found that sharp dips appear in the spectra that result from the excitation of a ‘phase-resonance’. This occurs as new degrees-of-freedom available to the acoustic near-field allow the fields of adjacent cavities within a unit-cell to be both out-of-phase and strongly enhanced. By mapping the transmission spectra as a function of in-plane wavevector, the dispersions of the modes supported by each sample are determined. Hence, the origin of the phase-resonant features may be described as acoustic surface waves that have been band-folded back into the radiative regime via diffraction from higher in-plane wavevectors than possible on a simple grating. One of the samples is then optimised via numerical methods that account for thermodynamic boundary layer attenuation, resulting in the excitation of a sharp, deep transmission minimum in a broad maximum that may be useful in the design of an acoustic filter.

The third chapter introduces the near-field imaging technique that can be utilised to directly characterise acoustic surface waves, via spatial fast Fourier transform algorithms of high-resolution pressure field maps. The acoustic response of a square-lattice open-ended hole array is thus characterised. It is found that over a narrow frequency band, the lattice symmetry causes the acoustic surface power flow to be channelled into specific, predictable directions, forming 'beams' with a well defined width.

In chapter four, the existence of the 'acoustic line mode' is demonstrated, a type of acoustic surface wave that may be supported by a simple line of open-ended hole cavities. The near-field imagine technique is again used to extract the mode dispersion. This acoustic line mode may be readily manipulated, demonstrated by arrangement of the line of holes into the shape of a ring. The existence of this type of mode offers a great deal of potential for the control of acoustic energy.

Chapter five explores the effect of 'glide-symmetry' on a pair of acoustic line modes arranged side-by-side. A control sample not possessing glide-symmetry is first characterised, where measurement of the acoustic near-fields show that this sample supports two separate modes at different frequencies, with their phase either symmetric or anti-symmetric about the mirror plane between the lines of holes. One of these lines is then shifted along its periodicity by half of a grating pitch, thus creating glide-symmetry. The resulting sample is found to support a single hybrid mode, capable of reaching a much larger in-plane wavevector than possible on a simple grating with no gaps in its band-structure, and displaying a region of negative dispersion. The third sample demonstrates how one may increase the coupling strength between the two lines of holes via manipulation of the cavity shape, thus enhancing the glide-symmetry effect. The thesis concludes with preliminary investigations into other possible ways of manipulating acoustic surface waves, such as with the use of 'screw-symmetry'.

Contents

List of Figures **v**

1 Introduction **1**

1.1 Aim of Research and Historical Context 1

1.2 Thesis Outline 5

2 Background Theory **9**

2.1 Introduction 9

2.2 Fundamental Acoustics 10

2.2.1 Pressure Oscillations 10

2.2.2 Equation of State for an Ideal Gas 11

2.2.3 Conservation of Mass 12

2.2.4 Conservation of Momentum 13

2.3 The Acoustic Wave Equation 15

2.4 Thermodynamic Loss Effects 17

2.4.1 Equation of State Revisited 18

2.4.2 Navier-Stokes Equation 18

2.4.3 Thermodynamic Boundary Layers 19

2.5 Acoustic Impedance, Reflection and Transmission 22

2.6 Acoustic Interaction with Rigid-Walled Cavities 24

2.7 Acoustic Surface Waves 29

2.7.1 Surface Wave Definition 29

2.7.2 Surface Waves in Acoustics 30

2.7.3 Acoustic Impedance Gratings 31

2.7.4 Dispersion Relations 33

2.7.5 The Effect of Periodicity on Acoustic Surface Waves 36

2.7.6 The Nature of the Radiative Fabry-Perot Evanescent-Wave (FPEV) 42

2.7.7 The Effect of the Marked-Space Ratio on Acoustic Surface Waves 46

2.7.8 A Note on Structures with Periodicity in Two-Dimensions (Bi-Gratings) . . . 47
2.7.9 Surface Acoustic Waves . . . 48
2.8 Conclusion . . . 49

3 Methods 51
3.1 Introduction . . . 51
3.2 The Pulse Measurement Technique . . . 51
3.3 Experimental Equipment . . . 54
3.4 Transmission Measurements . . . 60
3.4.1 No-gap Subtraction . . . 62
3.5 Surface Wave Measurements . . . 63
3.5.1 XZ Translation Stage . . . 63
3.5.2 2D Pressure Field Maps . . . 65
3.5.3 Extracting Dispersion Relations . . . 66
3.5.4 A Note on Colour Scales . . . 67
3.5.5 Measurement Constraints . . . 68
3.6 Sample Fabrication . . . 69
3.7 Numerical Modelling - The Finite Element Method . . . 70
3.7.1 Model Construction . . . 70
3.7.2 Periodic Boundary Conditions . . . 73
3.8 Conclusions . . . 74

4 Thermodynamic boundary layer Effects on Acoustic Transmission Through Narrow Slit Cavities 75
4.1 Introduction . . . 75
4.2 Fabry-Perot-like Cavity Resonances . . . 76
4.3 The Viscous and Thermal Boundary Layers . . . 77
4.4 Boundary Layer Effects on Propagation of Sound Through Tubes . . . 78
4.5 Experimental Configuration . . . 79
4.6 Experimental and Numerical Results . . . 82
4.7 Comparison to Stinson's Generalised Form of Kirchhoff's Equations . . 86
4.8 Boundary Layer Effects on Individual Acoustic Variables . . . 88
4.9 Conclusions . . . 94

5 Acoustic Transmission Through Compound Subwavelength Slit-Arrays 95
5.1 Introduction . . . 95
5.2 Background . . . 96
5.3 Sample Design and Experimental Set-Up . . . 97

5.4 Normal Incidence Transmissivity Spectra . . . 98
5.5 Mapping the Mode Dispersions with Angle-Dependent Transmissivity Spectra . . . 104
5.6 Ordering of Phase-Resonant Field Configurations . . . 110
5.7 Conclusions . . . 113

6 Acoustic Surface Wave Beaming 115
6.1 Introduction . . . 115
6.2 Background . . . 115
6.3 Sample Design and Experimental Configuration . . . 116
6.4 Real and Reciprocal Space Pressure Field Maps . . . 118
6.5 Dispersion of the ASWs Supported by the Square Lattice . . . 123
6.6 Conclusions . . . 125

7 The Acoustic Line Mode 127
7.1 Introduction . . . 127
7.2 Background . . . 127
7.3 Experimental Configuration . . . 128
7.4 One-Dimensional Line of Open-Ended Holes . . . 130
7.5 Two-Dimensional Ring of Open-Ended Holes . . . 134
7.6 Conclusions . . . 138

8 Acoustic Line Modes With Glide Symmetry 139
8.1 Introduction . . . 139
8.2 Background: Glide-Symmetry . . . 140
8.3 Sample Design and Experimental Method . . . 142
8.4 Double-Line-Array Without Glide-Symmetry (Sample A) . . . 145
8.5 Double Line-Array With Glide-Symmetry (Sample B) . . . 150
8.6 Triangular Cavities with Glide-Symmetry (Sample C) . . . 155
8.7 Conclusions . . . 159

9 Future Work 161
9.1 Introduction . . . 161
9.2 Glide-Symmetry in a Hole-Patterned Slit-Cavity . . . 161
9.3 Acoustic Orbital Angular Momentum from Screw-Symmetry in a Cylindrical Patterned Tube . . . 166
    9.3.1 A Note on Future Sample Fabrication . . . 168
9.4 Acoustic Line Modes on Curved Geometry . . . 170
9.5 Other Future Work . . . 172

9.6 Conclusion . . . 174

10 Conclusions 175

11 Publications and Conferences 179

11.1 Publications . . . 179

11.2 Presentations and Conferences . . . 179

11.2.1 Oral Presentations . . . 179

Appendices

A Time-Domain to Frequency-Domain (1D) Fast Fourier Transform 183

A.1 Spectral Leakage . . . 186

A.2 Zero Padding . . . 188

A.3 Window Functions . . . 189

B Real-Space-Domain to Reciprocal-Space-Domain (2D) Fast-Fourier-Transforms 193

References 197

List of Figures

2.1 Qualitative illustration of a longitudinal pressure wave generated by a vibrating plate, with the black points representing molecules of a gas. . 11

2.2 Qualitative illustration of the formation of viscous δ_{v} and thermal δ_{α} boundary layers near a rigid-wall, as a planar wave propagates orthogonally to it. 20

2.3 Qualitative illustration of the amplitude of the pressure field for the first three harmonics supported within both an open-ended and close-ended pipe system. This is a cross-section through the middle of each pipe, and can also represent the modes supported within the equivalent slit system, substituting the radius a for slit-width w[56]. 27

2.4 Qualitative illustration of the acoustic surface wave supported in air above a typical periodic impedance grating. The rigid solid has a series of equally spaced ridges, with dimensions as labelled. The yellow shaded region is the region of air supporting the surface wave, with specific acoustic impedance $\mathbf{z}_{\mathrm{a}1}$, while the purple shaded region represents the region of effective impedance $\mathbf{z}_{\mathrm{a}2}$ induced by the grating. A sketch of the pressure magnitude $|\Delta p|$ of such a surface wave is also included. . . 32

2.5 Qualitative Example of a dispersion plot with important features annotated, for a typical short-pitch ($\lambda_{\mathrm{g}} \ll \lambda_{\mathrm{FP}}$) impedance grating like the one in figure 2.4. Frequency f is plotted against in-plane wavevector k_{x}. The solid red lines represent the behaviour of the eigenmodes of the system, including those associated with the fundamental Fabry-Perot resonance and its first harmonic. Note, the effect of the grating periodicity λ_{g} on the dispersion of each of the modes (other than to allow them to exist) has been neglected for simplicity. 34

2.6 (Rotated) Example of a 'repeated-zone-scheme' dispersion plot for a typical short-pitch ($\lambda_{\mathrm{g}} \ll \lambda_{\mathrm{FP}}$) impedance grating. The ratio of grating period λ_{g} to free space wavelength λ_0 is plotted against reduced in-plane wavevector $\frac{k_{\mathrm{x}}}{k_{\mathrm{g}}}$, where $k_{\mathrm{g}} = \frac{2\pi}{\lambda_{\mathrm{g}}}$ is the grating wavevector. The solid red lines represent the behaviour of the Eigenmodes of the system. Only modes associated with the fundamental cavity resonance are included. The pressure field plots in figure 2.7 were calculated at points highlighted here with blue arrows and labels. 39

2.7 Examples of instantaneous pressure field Δp maps at four unique points on the dispersion curve of an ASW supported by a short-pitch ($\lambda_{\mathrm{g}} \ll \lambda_{\mathrm{FP}}$) impedance grating, in order of ascending frequency from top to bottom. In each case, the pressure field has been normalised to the maximum amplitude present. The top panel shows the infinitely extending fields of the DC mode, which is the ASW at normal incidence with a frequency approaching 0. The second panel shows the fields of the ASW at the first Brillouin zone boundary, $k_{\mathrm{x}} = \frac{k_{\mathrm{g}}}{2}$, where it has formed a standing-wave along x with $\lambda_{\mathrm{x}} = 2\lambda_{\mathrm{g}}$. The third panel shows the fields of the fundamental radiative cavity mode (or FPEV) at normal incidence, $k_{\mathrm{x}} = 0$, also a standing-wave. The final panel shows the fields of the mode that would be the high-frequency standing-wave pair of the ASW in the second panel, also with $\lambda_{\mathrm{x}} = 2\lambda_{\mathrm{g}}$. This requires fields with maxima above the rigid-walls and not inside the cavities, and is thus not a trapped mode but indistinguishable from a grazing-incidence radiative wave that exists at the point where $k_0 = \frac{k_{\mathrm{g}}}{2}$. 40

2.8 'Extended-zone-scheme' dispersion plot for two impedance gratings, identical except for grating pitch λ_{g}. The ratio of grating period λ_{g} to free space wavelength λ_0) is plotted against reduced in-plane wavevector $\frac{k_{\mathrm{x}}}{k_{\mathrm{g}}}$. The top panel is a short-pitch grating, where $\lambda_{\mathrm{g}} \ll \lambda_{\mathrm{FP}}$. The bottom panel is a long pitch grating, where $\lambda_{\mathrm{g}} \approx \lambda_{\mathrm{FP}}$. In each case, The solid red line is the fully non-radiative ASW, the blue lines are the FPEV, and the green lines are the next mode who's character depends on λ_{g}, as explained in the main text. The dotted lines represent other viable locations to draw each mode without the band-folding, included to highlight the break-down of the analogy to the nearly-free electron model (see main text). Points marked A correspond to the pressure field plots in figure 2.9. 44

2.9 Instantaneous pressure field Δp maps of the primary FPEV modes at normal incidence $k_\mathrm{x} = 0$, within and above two separate impedance gratings that are identical except for grating pitch λ_g. (Top) A short pitch grating, $\lambda_\mathrm{FP} \gg \lambda_\mathrm{g}$, thus the FPEV is more FP-like. (Bottom) A long pitch grating, $\lambda_\mathrm{FP} \approx \lambda_\mathrm{g}$, thus the FPEV is more ASW-like. The pressure fields have been normalised to their maximum amplitude. . . . 45

2.10 (Left) Dispersion plot of the modes supported by a typical impedance grating, as the slit-width w is varied (neglecting thermodynamic losses). The ratio of grating period $\lambda_\mathrm{g} = 12$ mm to free space wavelength λ_0 is plotted against reduced in-plane wavevector $\frac{k_\mathrm{x}}{k_\mathrm{g}}$. The solid lines represent the behaviour of the Eigenmodes of the system, with different colours being different slit-widths. The dashed line is the wavelength of the fundamental FP-limit for a 10 mm deep close-ended cavity, as these are. (Right) Numerically calculated Δp field plots for one unit-cell of a $\lambda_\mathrm{g} = 12$ mm pitch grating at normal incidence ($k_\mathrm{x} = 0$), corresponding to the three different slit-widths presented in the left-hand figure. 47

3.1 (A) Time-domain plot of 4 different Gaussian-Sine pulses, with the colours (labelled) representing different centre frequencies, from $4 - 10$ kHz. (B) Frequency response (limited to the human audible range) of the Gaussian pulses in A, after zero padding has been applied. Colours correspond to those in A. 53

3.2 Schematic of acoustic pulse kit used to collect experimental data. 54

3.3 (A) Measured time-domain signals produced by three separate speakers used during data acquisition throughout this thesis, with the Gaussian pulse centred at 6 kHz. Signals are normalised to their own maximum. (B) Frequency-domain data resulting from the FFT functions applied to the signals in A, with only audible frequencies shown. 55

3.4 (A) Measured time-domain signals produced by a single speaker, driven by a Gaussian pulse centered at various frequencies, labelled accordingly. Amplitudes are normalised to the same number to allow cross comparison, which was the maximum value found in the present signals. (B) Frequency-domain data resulting from the FFT functions applied to the signals in A (after zero-padding), with only audible frequencies shown. . 57

3.5 Photographs of the sources and detectors used throughout experimental measurements, labelled accordingly. 58

3.6 Frequency response function of the Brüel and Kjær type 4190 microphone calibrated at standard temperature and pressure, obtained from the supplied documentation. The actuator response is that of the internal mechanism that converts the diaphragm's free field pressure response to an electrical signal. 59

3.7 Frequency response function of the Brüel and Kjær type 4182 probe microphone calibrated at standard temperature and pressure, obtained from the supplied documentation, after the actuator has converted the pressure response of the diaphragm to an electrical signal. 59

3.8 (A) Example of a time-domain pulse signal measured during an experiment, in this case the transmission through a 0.5 mm width slit-cavity, as will be explained in chapter 4. Red, Green and Blue lines represent the raw signal data, the 'no-gap' signal, and the signal resulting from the 'no-gap subtraction' technique. (B) Frequency-domain data resulting from the FFT functions applied to the separate signals in A, with only audible frequencies shown. All signals have been normalised to the speaker response function (see figure 3.3). 61

3.9 Schematic of the XY translation stage, with the probe microphone attached and an open-ended hole sample in place. The end of the source (not shown) is placed inside one of the resonators, according to the sample type. 64

3.10 Examples of the frequency-domain data that can be acquired using the XY stage method outlined in the text. The sample used is the square lattice of open-ended holes from chapter 6, at frequency 11.65 kHz. Three different variables are plotted as a function of position. (A) Instantaneous pressure field amplitude Δp at a temporal phase, (B) Absolute pressure field magnitude $|\Delta p|$. 66

3.11 Example of the use of a 2D Spatial FFT on a real dataset acquired using the XY stage method outlined in the text. The sample used is the square lattice of open-ended holes from chapter 6, at a frequency of 11.65 kHz. (A) Instantaneous pressure field Δp, plotted as a function of real space coordinates x and y. (B) Result of the 2D FFT algorithm applied to the complex data in A, after the FFT-shift function has been applied. Fourier magnitude is plotted as a function of k-space coordinates k_x and k_y. 67

3.12 Dispersion relation for this sample, plotting the Fourier magnitude along unique directions Γ - X, X - M and M - Γ (points of high symmetry in the reciprocal space of the square Bravais lattice[82]) as a function of frequency. Again, important features have been highlighted, with the solid white lines representing the sound-line $k_0 = \frac{2\pi f}{c}$ and the dotted white lines the position of the first Brillouin zone boundaries. The frequency 'slice' of k-space that 3.11B and 3.11C correspond to are highlighted by the position of the dot-dashed white line. 68

3.13 (A) 2D COMSOL model set-up for a non-periodic system, in this case a single slit, with different features labelled accordingly. The bottom grey shaded half is not needed due to the symmetry condition represented by the blue line. (B) Close up of the boundary layer mesh that can be built to improve the mesh in sensitive areas, in this case just at the edge of the single slit, and along its walls. 71

3.14 (A) 3D COMSOL model set-up for a periodic system, in this case the unit cell of a one-dimensional array of open ended holes. The whole face on each side (green) has the Floquet periodic boundary condition applied. Other sections are labelled accordingly. (B) Example of the mesh used to solve for the arrangement shown in A. 73

4.1 (a) Simplified 2D Schematic of the slit-array experimental configuration. The aluminium slats (shaded) were stacked vertically between two mirrors 3 m apart, with a speaker and microphone placed at their focal lengths, 1 m away. The sample stand was covered in acoustic absorber (black fill) and the beam path is indicated by a dashed arrow. (b) Schematic of the slit-array sample itself, with dimensions labelled (not to scale). Here, $L = 19.8 \pm 0.12$ mm, $d = 2.91 \pm 0.03$ mm, and $\lambda_g = d + w$. 80

4.2 Simplified 2D Schematic of the single slit experimental configuration. The shaded blocks represent the aluminium sample, and the black blocks represent an acoustic baffle. The microphone and speaker are $\sim 20°$ off normal in the xz plane, covered in acoustic absorber (black), and separated from the sample faces by 220 and 400 mm, respectively. Here, $L = 35.0 \pm 0.1$ mm. 80

4.3 A representation of the slit-array experimental configuration. The sample was placed on a set of level blocks, normal to the collimated beam produced by the first mirror, where the pair of mirrors were 3 m apart. The speaker and microphone were placed at 1 m from the mirrors, their focal length. The mirrors tilted so that the beam path (labelled dashed white lines) relative to the speaker/microphone was centred on the opposing mirror. The sample height is $d = 400$ mm, and the width $a = 560$ mm. The wooden stage was covered in absorber where possible. (Inset) Real photograph of a close up of the sample face, built with $w = 0.25$ mm, with the other labelled dimensions described in fig 4.1. 81

4.4 A representation of the single slit experimental configuration. The aluminium blocks that form the slit are separated vertically with polyester spacers and held inside the wooden sample holder, which is covered in absorbing foam on both entrance and exit sides. Both the speaker and microphone are wrapped in cotton wool (not rendered) and directed at the sample, $\sim 20^\circ$ off normal in the xz plane, separated from the sample faces by 220 and 400 mm respectively. The width of the sample face $h_\mathrm{a} = 243$ mm, while the height $h_\mathrm{b} = 202$ mm. 81

4.5 Transmission amplitude t (or Transmission magnitude for the single-slit, as this is only a relative measurement) spectrum as a function of frequency, for different slit-widths, from several data sources, labelled accordingly. The line colour corresponds to slit-width w and is labelled in the legend. (Left column) - Spectra for the slit-array sample, (Top row) - Experimental data, (Middle row) - Thermo-viscous Navier-Stokes FEM model data, (Bottom row) - Lossless acoustic wave equation numerical model. (Right column) As the left column, but pertaining to the single slit sample. 83

4.6 (Left Column) The fundamental resonant frequency of each slit-cavity f'_{FP} plotted as a function of the slit-width w. The solid black circles are the mean of the experimentally determined resonant frequencies, with the error bars representing their standard deviation. The dashed blue lines represent a lossless FEM numerical prediction, and the solid red lines a more complete numerical prediction that includes the viscous and thermal properties of each system. The top and bottom panels represent the slit-array and single slit samples, respectively (labelled). (Right column) The fundamental resonant frequency of each slit-cavity f'_{FP}, normalized to that predicted by the Fabry-Perot condition f_{FP} as a function of the ratio of viscous boundary layer thickness δ_{v} to slit-width w. This is the dimensionless form of the plots in the left column. 85

4.7 (Left) Ratio of the calculated effective speed of sound v_{p} to adiabatic speed c_{a} in each slit-cavity, as a function of the slit-width w. Triangular points and accompanying error bars are experimental data converted from figure 4.6, with purple and green representing the slit-array and single slit data, respectively. The dashed lines represent the predictions of Stinson's[57] analytic theory for each sample, coloured accordingly. (Right) Ratio of the calculated effective speed of sound v_{p} to adiabatic speed c_{a} in each slit-cavity, as a function of the ratio of viscous boundary layer thickness δ_{v} to slit-width w. This is the dimensionless form of the left figure. 87

4.8 Weston's predictions for the behaviour of various quantities through a cross-section of a tube, taken from figure 3 of his study[54]. (a) Amplitude of axial particle velocity or temperature fluctuation, (b) amplitude of radial particle velocity, (c) wavefront or equiphase surface. 89

4.9 Various quantities plotted as a function of distance z along the cavity slit-width, measured in mm. Values were extracted from the loss-inclusive FEM model at a distance of $0.25L$ from the slit-cavity centre for both samples. The blue lines correspond to a slit-width w of 1.00 mm, the red lines a slit-width of 0.15 mm. The left and right columns correspond to the slit-array and single slit samples respectively. (Top row) Particle velocity along the slit-length v_{x}. (Second row) Particle velocity across slit-width v_{z}. (Third row) Excess temperature ΔT, measured in degrees Kelvin difference from the ambient temperature T_0. (Bottom row) Instantaneous particle velocity v_{p}, which is the shape of the phase fronts as they propagate through the slit. 90

4.10 Experimental and theoretical results of Yazaki et al.[58] (figure 3 in their work, where a detailed explanation is presented), showing the change in effective speed of sound here labelled v through a long tube as a function of $\omega\tau$, explained in the main text. Also shown (the data with a negative gradient) is the measured change in signal attenuation caused by the boundary layers, represented by scaled propagation constant β. The dashed vertical line represents the point at which propagation within the tube becomes purely isothermal. 92

4.11 (Left column) Data from the FEM model showing the fundamental resonant frequency of each slit-cavity f'_{FP} plotted as a function of the slit-width w, with the effect of separate loss components compared. The solid red line represents the full lossy model with both viscous and thermal loss mechanisms present. The dotted blue line is the result of 'turning off' the thermal boundary layer (by setting α of the air to zero) , leaving just the viscous loss mechanism, with the green dashed line being the opposite (by setting μ to zero). The dashed purple line is the result of disabling both loss mechanisms. The top and bottom panels represent the slit-array and single slit samples, respectively (labelled). (Right column) Generalised form of the left column, where the fundamental resonant frequency of each slit-cavity f'_{FP} is normalized to that predicted by the Fabry-Perot condition f_{FP} as a function of the ratio of viscous boundary layer thickness δ_{v} to slit-width w. 93

5.1 Schematic of a unit cell of each array sample (not to scale). The grey blocks represent the aluminium slats that form the sample, of width $w_{\mathrm{A}} = 2.9$ mm, and length $L = 19.8$ mm. The air gaps that form the cavities are the same size as the slats, except for the $J = 3$b sample, where the central cavity w_{B} has width 5.9 mm, and the outer two have $w_C = 1.5$ mm. Each sample has a period $\lambda_{\mathrm{g}} = 8w_{\mathrm{A}} = 23.2$ mm. 97

5.2 To-scale schematic of the transmission measurement experimental setup, labelled accordingly. The speaker was placed at the focal point of the first mirror, which directed the collimated beam toward the sample. The transmitted signal was then focused on to the microphone by the second mirror. The sample frame was placed onto a computer controlled rotating table, allowing control of the incident angle θ_{i}. Acoustic absorber was placed at appropriate positions to reduce unwanted reflections from the solid surfaces that make up the measuring kit (not shown). 98

5.3 Normal incidence transmissivity T spectra as a function of the ratio of array periodicity λ_g to incident radiation wavelength λ_0 for each of the sample types illustrated in figure 5.1. The solid black line is the experimental data, the short-dashed red and long-dashed blue lines are the lossless and viscous-thermal loss-including numerical model spectra for comparison. The diffraction edge for each experimental sample occurs when $\frac{\lambda_\mathrm{g}}{\lambda_0} = 1$. Fluctuations in the ambient temperature are accounted for in the calculation of λ_0. 99

5.4 FEM simulations of the instantaneous pressure fields Δp corresponding to the three available eigenmodes '$+ + +$', '$+ - +$', and '$+ \ 0 \ -$', of the $J = 3a$ system when there is no net phase shift along x between unit cells, shown at a temporal phase corresponding to maximum field amplitude. The colour scales have been normalised with normalisation constants 2.19, 4.01 and 3.39 respectively. The three eigenmodes have resonant frequencies which correspond to $\frac{\lambda_\mathrm{g}}{\lambda_0}$ values of 0.54, 0.5 and 0.48 respectively. These were calculated using a loss-free FEM model. The grey blocks represent the aluminium slats, in the same orientation as illustrated in figure 5.1. 101

5.5 Lossless (dotted red line) and viscous-thermal (solid blue line) FEM models of the difference in the phase $|\Delta\phi_{\text{Inner, Outer}}|$ of the tangential particle velocity v_x of the central and outer cavities, for the $J = 3$a and $J = 3$b samples, plotted as a function of the ratio of array periodicity to incident wavelength $\frac{\lambda_\mathrm{g}}{\lambda_0}$. The predicted diffraction edge is at $\frac{\lambda_\mathrm{g}}{\lambda_0} = 1$. Phases were evaluated in the centre of each cavity on the transmitting side of the grating. 103

5.6 Transmission data illustrating mode dispersion for each sample illustrated in figure 5.1, labelled accordingly. The ratio of array periodicity to incident wavelength $\frac{\lambda_\mathrm{g}}{\lambda_0}$ is plotted as a function of reduced in-plane wavevector $\frac{k_\mathrm{x}}{k_\mathrm{g}}$, where a value of $\frac{k_\mathrm{x}}{k_\mathrm{g}} = 0.5$ corresponds to the first Brillouin zone boundary. The left column are the recorded experimental data, whereas the right column are the numerical results calculated by the viscous-thermal loss inclusive FEM model. For reference, a solid green line representing grazing incidence k_0 is included on each plot. The onset of first order diffraction is represented by the green dashed line. Fluctuations in ambient room temperature are accounted for in all calculations of λ_0. 105

5.7 Dispersion diagrams showing the extended zone scheme representation of the eigenmodes of the $J = 1$, $J = 2$ and $J = 3\text{a}$ systems (all labelled), plotted as a function of the ratio of array periodicity to incident wavelength $\frac{\lambda_{\mathrm{g}}}{\lambda_0}$ vs reduced in-plane wave vector $\frac{k_{\mathrm{x}}}{k_{\mathrm{g}}}$. Individual eigenfrequencies were calculated using loss-inclusive FEM models. The sound line k_0 is represented by the black solid line. A horizontal black dashed line represents the resonant frequency predicted by the Fabry-Perot condition for a single open-ended slit-cavity. Integer and half integer values of $\frac{k_{\mathrm{x}}}{k_{\mathrm{g}}}$ correspond to different Brillouin zone boundaries, which have been marked with vertical black dotted lines. The solid coloured lines represent the different eigenmodes supported by each grating structure, with colours signifying different field configurations. Red is the naturally radiative FPEV mode, with blue being its fully non-radiative low frequency ASW. Green is the ASW coupled to the low energy phase-resonance field configuration, and purple is the ASW coupled to the high energy phase-resonance field configuration. Eigenmodes associated with the next FP harmonic are not included. 107

5.8 Mode dispersion illustrated by the experimental transmissivity T data for the $J = 3\text{a}$ sample, with its numerically calculated eigenfrequencies associated with the first FP mode overlaid, plotted as a function of the ratio of array periodicity to incident wavelength $\frac{\lambda_{\mathrm{g}}}{\lambda_0}$ vs reduced in-plane wave vector $\frac{k_{\mathrm{x}}}{k_{\mathrm{g}}}$. The value of $\frac{k_{\mathrm{x}}}{k_{\mathrm{g}}} = 0.5$ corresponds to the first Brillouin zone boundary. The solid black line represents the wavevector k_0 of a grazing incidence pressure wave. The onset of first order diffraction is represented by the black dashed line, being $\frac{\lambda_{\mathrm{g}}}{\lambda_0} = 1$ at normal incidence ($\frac{k_{\mathrm{x}}}{k_{\mathrm{g}}} = 0$). The hollow points represent the different eigenmodes supported by the $J = 3\text{a}$ grating structure, with shapes signifying different field configurations. The triangles are the naturally radiative Fabry-Perot like mode, circles are the ASW coupled to the '$+ - +$' phase-resonance and the diamonds are the ASW coupled to the '$+ 0 -$' phase-resonance. The squares are the non-radiative low frequency ASW which cannot be seen in this transmission experiment. 109

5.9 (Top) Dispersion diagrams showing FEM calculated eigenmodes of the two $J = 3$ samples associated with the fundamental cavity resonance, plotted as a function of the ratio of array periodicity to incident wavelength $\frac{\lambda_\mathrm{g}}{\lambda_0}$ vs reduced in-plane wave vector $\frac{k_\mathrm{x}}{k_\mathrm{g}}$. The black dashed lines are the resonant frequency predicted by the FP condition, the black solid lines are the sound lines $k_0 \pm nk_\mathrm{g}$. The coloured solid lines represent the band structure of the ASW, with different colours corresponding to different near-field configurations, as in figure 5.7. The purple and green lines have switched order between samples to highlight the change in energy of the phase-resonant field configurations at normal incidence. (Bottom Left) Instantaneous pressure field configurations across two unit cells of the $J = 3a$ sample showing the two possible phase-resonant modes, at either normal incidence $k_\mathrm{x} = 0$ or at the first Brillouin zone boundary $\frac{k_\mathrm{x}}{k_\mathrm{g}} = 0.5$. The labelled numbers and k_x positions correspond to those marked by labelled black points in the corresponding dispersion plots. (Bottom Right) The same, but for the $J = 3\mathrm{b}$ sample. Note that compared to the $J = 3\mathrm{a}$ sample, the field configurations at normal incidence have reversed their order, while they have the same character at the first Brillouin zone boundary. 111

6.1 Schematic of the open-ended hole-array sample. The acrylic plate is a square of sides $B = 560.00$ mm, having thickness (hole depth) $H = 9.60 \pm 0.23$ mm. There are 60×60 holes of spacing (periodicity) $\lambda_\mathrm{g} = 8$ mm in both x and y directions, and hole radius $R = 3.25 \pm 0.05$ mm. A close up of a single unit-cell of the grating is displayed in the inset. . . . 117

6.2 (Top row) Experimental data showing instantaneous pressure field Δp (colour scale) at a single frequency, measured as a function of x and y coordinates over the array surface. The plot labelled A is the pressure field at 11.65 kHz ($\frac{\lambda_\mathrm{g}}{\lambda_0} = 0.272$), while B is at 13.02 kHz ($\frac{\lambda_\mathrm{g}}{\lambda_0} = 0.304$). The point like source was placed in one of the central holes, positioned at the centre of these plots, x = y = 227.5 mm. (Bottom row) Experimental data showing the absolute pressure field $|p|$ from the same data as used for the top row (where C corresponds to A, and D to B), with a square root function applied to the colour scale to enhance detail. 119

6.3 (A) Two-dimensional reciprocal space (k-space) plots corresponding to the spatial Fourier transforms of the experimentally measured pressure fields at 11.65 kHz ($\frac{\lambda_g}{\lambda_0} = 0.272$) (shown in figures 6.2A and 6.2C), plotted as a function of reduced in-plane wavevectors $\frac{k_x}{k_g}$ and $\frac{k_y}{k_g}$. The colour scale represents the magnitude of the Fourier transform. For reference, several important features are marked. The solid white circle represents the 'sound circle' $k_0 = \sqrt{k_x^2 + k_y^2} = \frac{2\pi}{\lambda_0}$, with the dashed white circles being the diffracted sound-circles from the reciprocal lattice points. The dotted straight lines represent the first and second Brillouin zone boundaries, with the axes truncated at the third. Points of high symmetry for the square-lattice[82] Γ, X and M are labelled accordingly. (B) Identical to A, but for the pressure fields at 13.02 kHz ($\frac{\lambda_g}{\lambda_0} = 0.304$) (shown in figures 6.2B and 6.2D). 121

6.4 Irreducible dispersion diagram for the hole array sample, obtained from the spatial Fourier transforms of the experimentally measured pressure fields on its surface. The magnitude of the Fourier transform (colour scale) is plotted as a function of the ratio of grating periodicity λ_g to incident wavelength λ_0, vs in-plane wavevector $k_{||}$, which is the wavevector along the array surface parallel to directions Γ-X, X-M, and M-Γ. These letters represent the points of high symmetry on the square-lattice sample's reciprocal lattice[82], as marked in figures 6.3A and 6.3B. The two horizontal dotted lines mark the frequencies corresponding to those displayed in prior figures 6.2 and 6.3. The numerically calculated dispersion is represented by the overlaid green circles. 124

7.1 Schematic of the line (subscript L) sample. The acrylic plate has dimensions $l_L = 840.00$ mm (truncated in the figure) and $w_L = 30.00$ mm, with thickness (hole depth) $t_L = 9.80 \pm 0.10$ mm. There are 105 holes of spacing (periodicity) $\lambda_{gL} = 8.00$ mm in the x direction. The holes are of radius $r_L = 3.25 \pm 0.005$ mm. B. Schematic of the ring (subscript R) sample. The acrylic plate has a rectangular cross-section of sides $c_R = 290$ mm with thickness (hole depth) $t_R = 7.51 \pm 0.06$ mm. There are 80 holes that make up the ring, which is of radius $R_R = 10.1 \pm 0.05$ mm. Each of the holes is of radius $r_R = 3.35 \pm 0.005$ mm, separated by arc $\theta_R = \frac{2\pi}{80}$. This gives them a central spacing (periodicity) $\lambda_{gR} \approx 8.00$ mm in the θ direction, around the circumference of the ring R_R. 129

7.2 Experimental data showing (A) Instantaneous pressure amplitude Δp and (B) Absolute pressure magnitude $|\Delta p|$ (with a square root applied to the colour scale for enhanced detail) at frequency 12.31 kHz $\frac{\lambda_{\mathrm{gL}}}{\lambda_0} = 0.287$, measured as a function of x and y coordinates along the surface of the line sample. The point-like source was located at x = 0 mm, y = 25 mm. 131

7.3 Two-dimensional reciprocal space plot corresponding to the spatial Fourier transform of the pressure field at 12.31 kHz shown in figure 7.2A, plotted as a function of reduced in-plane wavevectors $\frac{k_{\mathrm{x}}}{k_{\mathrm{gL}}}$ and $\frac{k_{\mathrm{y}}}{k_{\mathrm{gL}}}$. The colour scale represents the absolute magnitude of the complex Fourier transform. The solid white circle represents the sound circle $k_0 = \frac{2\pi}{\lambda_0} = \sqrt{k_{\mathrm{x}}^2 + k_{\mathrm{y}}^2}$, with the dashed white circles being the diffracted sound lines originating from the reciprocal lattice $\pm k_{\mathrm{gL}}$. The dotted straight lines represent the first Brillouin zone boundaries $\pm\frac{k_{\mathrm{x}}}{k_{\mathrm{gL}}} = 0.5$, with the axis truncated at the second. The x and y axes have been reversed to match the orientation of the pressure field in figure 7.2. 132

7.4 Dispersion for the line sample, obtained from the spatial Fourier transforms of the measured pressure fields on its surface such as in figure 7.3, the cross-section at $k_{\mathrm{y}} = 0$. The magnitude of the Fourier transform is plotted as a function of the normalized frequency (ratio of grating periodicity λ_{gL} to incident wavelength λ_0) vs the normalized in-plane wavevector, $\frac{k_{\mathrm{x}}}{k_{\mathrm{gL}}}$, along the array surface. A numerically-calculated dispersion is represented by the overlaid green circles. The positions of the sound-lines $\pm\, k_0$ are marked by the solid white lines, while diffracted sound lines from $\pm\, (k_0 + k_{\mathrm{gL}})$ (where $k_{\mathrm{gL}} = \frac{2\pi}{\lambda_{\mathrm{gL}}}$) are represented by dashed white lines. The edge of the first Brillouin zone is at $\frac{k_{\mathrm{x}}}{k_{\mathrm{gL}}} = 0.5$, and the value of $\frac{\lambda_{\mathrm{gL}}}{\lambda_0}$ corresponding to the pressure field plot in figure 7.2 is represented by the horizontal dotted line. 133

7.5 (A) Experimental data showing instantaneous pressure field Δp at frequency of 14.63 kHz ($\frac{\lambda_{\mathrm{gR}}}{\lambda_0} = 0.341$), measured as a function of r and θ coordinates along the ring sample's surface. The point-like source was located inside the hole at r∼ 100 mm, θ = 2.3 rad. (B) The same as (A) except for the time averaged absolute pressure magnitude $|p|$ (with a square root applied to the colour scale for enhanced detail). 135

7.6 Experimental dispersion diagram for the ring sample, obtained from the spatial Fourier transforms (in polar coordinates) of the measured pressure fields on its surface around radius $r = R\mathrm{R}$. The magnitude of the Fourier transform is plotted as a function of the ratio of grating periodicity λ_{gR} to incident wavelength λ_0 vs normalized in-plane wavevector k_{θ}, along the array surface in the θ direction, along the holes. λ_{gR} is defined at the radius R_{R}, the centre of each hole. Solid white lines represent the 'sound-lines', the maximum wavevector $k_{0\theta} = \frac{2\pi}{\lambda_{0\theta}}$ that a grazing incidence sound wave can possess, here in the k_θ direction, while the dashed white lines are the diffracted sound lines $\pm\,(k_{0\theta} + k_{\mathrm{gR}})$, where $k_{0\theta}$ and k_{gR} have also been defined at the radius $r = R_{\mathrm{R}}$. A horizontal dot-dashed line marks the frequency to which figure 7.5 corresponds. The numerically calculated dispersion is represented by the overlaid green circles. 136

7.7 Two-dimensional reciprocal space plot corresponding to the spatial Fourier transform of the pressure field at 14.63 kHz shown in figure 7.5A, plotted as a function of reduced in-plane wavevectors $\frac{k_{\mathrm{r}}}{k_{\mathrm{gR}}}$ and $\frac{k_{\theta}}{k_{\mathrm{gR}}}$. The colour scale represents the absolute magnitude of the complex Fourier transform. The solid white circle represents the sound-circles $k_{0\theta} = \frac{2\pi}{\lambda_{0\theta}} = \sqrt{k_{\mathrm{r}}^2 + k_{\theta}^2}$, with the dashed white circles being the diffracted sound lines originating from the reciprocal lattice $\pm k_{\mathrm{gR}}$. The dotted straight lines represent the first Brillouin zone boundaries $\pm\frac{k_{\theta}}{k_{\mathrm{gR}}} = 0.5$. The r dependent values $k_{0\theta}$ and k_{gR} have been defined at the radius $r = R_{\mathrm{R}}$, hence the sound lines are approximate. 137

8.1 2D schematic of the three different unit-cells that make up each of the full length samples A, B, and C depicted in figure 8.2, where grey represents the acrylic, and white-space the air. All three samples have constant periodicity $\lambda_{\mathrm{g}} = 8 \pm 0.01$ mm along x. A is the sample consisting of two adjacent open-ended holes of radius $r_{\mathrm{A}} = 3.20 \pm 0.05$ mm, with hole centres spaced $d_{\mathrm{A}} = 7 \pm 0.01$ mm apart in y, the acrylic plate being $D_{\mathrm{A}} = 36.30 \pm 0.05$ mm wide. Sample B has acrylic plate width $D_{\mathrm{B}} = 35.55 \pm 0.05$ mm, and radius of holes $r_{\mathrm{B}} = r_{\mathrm{A}}$, but compared to sample A, the top line of holes are all shifted by $\lambda_{\mathrm{g}}/2$ in x, and hole centres are separated by $d_{\mathrm{B}} = 6 \pm 0.01$ mm in y (thus with total displacement between centres 7.21 ± 0.01 mm). Sample C consists of approximately equilateral-triangle cavities inverted along the mid plane in y, with triangle-hole centres separated by $d_{\mathrm{C}} = 4 \pm 0.05$ mm in y (total displacement thus 5.65 ± 0.10 mm). Labelled triangle dimensions are $r_{\mathrm{C1}} = 6.8 \pm 0.05$ mm and $r_{\mathrm{C2}} = 5.9 \pm 0.05$ mm, while acrylic width $D_{\mathrm{C}} = 44.40 \pm 0.05$ mm. 143

8.2 Schematic of the three types of acrylic samples, which have had 210 open-ended cavities laser-cut into them. The length of all 3 samples $L = 840$ mm, whilst the thickness $H = 9.7 \pm 0.2$ mm. The position of the source of excitation is marked on each sample by the purple arrow labelled 'S'. 144

8.3 (Sample A) 2D real-space plots of the experimentally measured instantaneous pressure field amplitude Δp (left) and absolute pressure $|\Delta p|$ (right) at two separate frequencies (labelled), that have been normalised to their maximum amplitude for each individual frequency. The point-like source was located in the open-ended hole at $x = 0$ mm, $y = 4$ mm. Here, the spatial resolution is $\Delta x = 0.5$ mm and $\Delta y = 0.5$ mm. The dashed-lines represent the cross-section of the fields referenced in the main text. 146

8.4 (Sample A) 2D k-space plots corresponding to the pressure field plots in figure 8.3 (oriented in the same way). Wavevectors k_{x} and k_{y} are scaled to grating wavevector k_{g}, with the colour scale representing the magnitude of Fourier components. The solid white circle represents the sound-circle $k_0 = \sqrt{k_{\mathrm{x}}^2 + k_{\mathrm{y}}^2} = \frac{2\pi}{c}$, the dashed circles $k_0 \pm nk_{\mathrm{g}}$. Dotted horizontal lines are Brillouin zone boundaries $\pm\frac{nk_{\mathrm{g}}}{2}$. Dot-dashed vertical lines are the cross-sections of k_{y} used to create dispersion plots in figure 8.5. 147

8.5 Dispersion diagrams calculated from the experimental data for sample A, at two different cross-sections of k-space wavevector k_{y} (labelled). The ratio of free-space wavelength to grating wavevector $\frac{\lambda_{\mathrm{g}}}{\lambda_0}$ is plotted as a function of reduced in-plane wavevector $\frac{k_{\mathrm{x}}}{k_{\mathrm{g}}}$. Solid-lines represent sound-line k_0, dashed lines their diffracted counterparts $\pm\, k_0 \ \pm nk_{\mathrm{g}}$. Vertical dotted lines represent the first Brillouin zone boundaries $\pm\frac{nk_{\mathrm{g}}}{2}$, and horizontal dot dashed-lines the frequencies at which figures 8.3 and 8.4 are plotted. In both plots, eigenfrequency predictions of a loss-inclusive numerical model are overlaid as coloured lines. Green represents the even modes, Red the odd modes. A solid line is a mode that has not undergone diffraction from $\pm\, k_{\mathrm{g}}$, a dashed line is one that has. 149

8.6 (Sample B) 2D real-space plots of the experimentally measured pressure field Δp (left) and absolute pressure $|\Delta p|$ (right) at two separate frequencies (labelled, in units of kHz), that have been normalised to their maximum amplitude for each frequency. The point-like source was located in the open-ended hole at $x = 0$ mm, $y = -3$ mm. $\Delta x = \Delta y = 0.5$ mm. Short-dashed and long-dashed lines mark cross-sections of x referenced in the main text. 151

8.7 (Sample B) 2D k-space plots corresponding to the pressure field plots in figure 8.6 (oriented in the same way). Wavevectors k_{x} and k_{y} are scaled to grating wavevector k_{g}, with the colour scale representing the magnitude of Fourier components. The solid white circle represents the sound-circle $k_0 = \sqrt{k_{\mathrm{x}}^2 + k_{\mathrm{y}}^2} = \frac{2\pi}{c}$, the dashed circles $k_0 \ \pm \ nk_{\mathrm{g}}$. Dotted horizontal lines are Brillouin zone boundaries $\pm\frac{nk_{\mathrm{g}}}{2}$. Dot-dashed vertical lines are the cross-sections of k_{y} used to create dispersion plots in figure 8.8. 152

8.8 Dispersion diagrams calculated from the experimental data for sample B, at two different cross-sections of k-space wavevector k_{y} (labelled). The ratio of free-space wavelength to grating wavevector $\frac{\lambda_{\mathrm{g}}}{\lambda_0}$ is plotted as a function of reduced in-plane wavevector $\frac{k_{\mathrm{x}}}{k_{\mathrm{g}}}$. Solid-lines represent sound-line k_0, dashed lines their diffracted counterparts $\pm\, k_0 \ \pm nk_{\mathrm{g}}$. Vertical dotted lines represent the first Brillouin zone boundaries $\pm\frac{nk_{\mathrm{g}}}{2}$, and horizontal dot dashed-lines the frequencies at which figures 8.3 and 8.4 are plotted. Eigenfrequency predictions of a loss-inclusive numerical model are overlaid as coloured lines, with the colour change explained in the main text. Solid lines are modes that are not diffracted, dashed lines are modes diffracted from $\pm\, k_{\mathrm{g}}$. 153

8.9 (Sample C) 2D real-space plots of the experimentally measured pressure field Δp (left) and absolute pressure $|\Delta p|$ (right) at two separate frequencies (labelled), that have been normalised to their maximum amplitude for each frequency. The point-like source was located in the open-ended triangular hole at $x = 0$ mm, $y = 3$ mm, and xy scan resolution was $\Delta x = \Delta y = 0.8$ mm. 156

8.10 (Sample C) 2D k-space plots corresponding to the pressure field plots in figure 8.6 (oriented in the same way). Wavevectors k_x and k_y are scaled to grating wavevector k_g, with the colour scale representing the magnitude of Fourier components. The solid white circle represents the sound-circle $k_0 = \sqrt{k_\mathrm{x}^2 + k_\mathrm{y}^2} = \frac{2\pi}{c}$, the dashed circles $k_0 \pm nk_\mathrm{g}$. Dotted horizontal lines are Brillouin zone boundaries $\pm\frac{nk_\mathrm{g}}{2}$. Dot-dashed vertical lines are the cross-sections of k_y used to create dispersion plots in figure 8.8. 157

8.11 Dispersion diagrams calculated from the experimental data for sample A, at two different cross-sections of k-space wavevector k_y (labelled). The ratio of free-space wavelength to grating wavevector $\frac{\lambda_\mathrm{g}}{\lambda_0}$ is plotted as a function of reduced in-plane wavevector $\frac{k_\mathrm{x}}{k_\mathrm{g}}$. Solid-lines represent sound-line k_0, dashed lines their diffracted counterparts $\pm\ k_0\ \pm nk_\mathrm{g}$. Vertical dotted lines represent the first Brillouin zone boundaries $\pm\frac{nk_\mathrm{g}}{2}$, and horizontal dot dashed-lines the frequencies at which figures 8.3 and 8.4 are plotted. Eigenfrequency predictions of a loss-inclusive numerical model are overlaid as coloured lines, with the colour change explained in the main text. Solid lines are modes that are not diffracted, dashed lines are modes diffracted from $\pm\ k_\mathrm{g}$. 159

9.1 Schematic of the alternative glide-symmetry sample, from two perspectives. Grey represents aluminium. (Left) View through a cross-section across the centre of the hole cavities in the x-z plane. Each hole, of depth $h = 5$ mm and radius $a = 2$ mm, is part of a series of holes of periodicity $\lambda_\mathrm{g} = 10$ mm. The two lines of holes are inverted along their z-axis mirror plane halfway between the two aluminium plates, which are separated by variable width w. One of the aluminium plates is shifted by $\lambda_\mathrm{g}/2$ to create glide-symmetry between the holes. (Right) x-y plane cross-section of the sample. The aluminium plates are of width $d = 12$ mm. 162

9.2 Labelled photo of aluminium sample. An alternative view is shown within the inset. Close-ended holes of depth $h = 5$ mm are drilled into a pair of aluminium plates of length $L = 400$ mm. The lines of holes are arranged in glide-symmetry along the z axis, and source placed on one end. The plate separation w can be varied with the use of acrylic spacers. 163

9.3 Dispersion diagrams calculated from near-field measurements of the sample pictured in figure 9.2, with two different values of plate separation $w = 1.6$ and $w = 1.0$ mm. The ratio of free-space wavelength to grating wavevector $\frac{\lambda_g}{\lambda_0}$ is plotted as a function of reduced in-plane wavevector $\frac{k_x}{k_g}$. Solid-lines represent sound-line k_0, dashed lines their diffracted counterparts $\pm\, k_0\ \pm nk_g$. Vertical dotted lines represent the first Brillouin zone boundaries $\pm\frac{nk_g}{2}$. The pressure fields were recorded along one line along x, hence with no information about wavevectors k_y or k_z measured directly. 164

9.4 Schematics of example of a cylindrical sample, with holes arranged so at to create screw-symmetry. (Left) r-θ plane of the sample, with the periodicity in z not visible. There are three separate lines of holes of depth h_a and radius a, built into a hollow ring of acrylic with inner radius h_b. The holes are periodic in z having periodicity λ_g, and hole centres are equally distributed around the ring by $\theta = \frac{2\pi}{3}$, Each line is shifted by $\lambda_g/3$ relative to the others to create screw symmetry. (Right) Example of z-θ plane, showing the surface of the cylinder as it would appear from a constant radius of $r = h_b$. The periodicy along z of each of the 3 lines of holes is visible, including the $\lambda_g/3$ shift that creates the screw symmetry. 167

9.5 Dispersion diagram with numerically calculated eigenfrequencies of a screw-symmetric cylindrical waveguide with $p = 3$, as in figure9.4. In this reduced zone scheme, the red line represents the mode originating from $k_z = 0$, the blue line the mode band folded from the second Brillouin zone, and the green line that from the third. Black solid and dashed lines represent k_0 and $-k_0 + k_g$ respectively. 167

9.6 Picture of unassembled sample with screw-symmetry, printed by the 3D-prototype machine. 169

9.7 Picture of 3D-prototype printed sample, with schematic overlaid. A set of 46 open-ended cylindrical holes of depth $L = 8$ mm and radius $a = 3$ mm are periodically arranged into the shape of a ring, with periodicity $\lambda_{g\theta} = 2\pi/46$, and cylinder axis pointing along r. 171

9.8 Picture of 3D-prototype printed sample, consisting of a square lattice of open-ended cylinders. Each unit cell contains 4 cylinders, and each cylinder is 'twisted' so that they emerge in a different location on the surface plane of the exit side than on the entrance side. 173

A.1 Example of the properties of a time-to-frequency FFT. (A) One cycle of a 1 Hz sine wave oscillation, measured with number of samples $N = 19$ (red triangular points and red solid line) and $N = 20$ (blue circular points and blue dashed line). (B) Direct result of the FFTs on the two signals in plot A, with colours and points having corresponding meaning. The vertical dashed lines (coloured black and with line-type solid for odd, dashed for even) mark the Nyquist frequency, with higher valued points corresponding to negative frequencies. Zero represents the DC signal. (C) Result of applying the 'FFT-shift' function to B, placing DC in the centre, with positive and negative frequencies either side. Again, colours and line types are inherited from plot A. The extra point at the Nyquist frequency included in the $N = 20$ dataset has been placed on the negative side. 184

A.2 (A) A 1 Hz sine wave signal sampled in the time-domain, measured with number of samples $N = 19$ (red triangular points and red solid line) and $N = 20$ (blue circular points and blue dashed line) (B) Result of the FFT function applied to the signals in A, with the FFT-shift function applied. Colours and line types correspond to those in A. The Nyquist frequency for each signal is represented by the vertical lines, styled accordingly. . 187

A.3 (A) A single cycle of a 1 Hz sine wave signal, without (red triangles and solid line) and with (blue circles and dashed line) zero padding of the dataset. (B) Result of the FFT function applied to the signals in A, with the FFT-shift function applied. Colours and line types correspond to those in A. The Nyquist frequency is represented by the solid vertical line, and does not change between samples. 189

A.4 (A) A zero padded single cycle of a 1 Hz sine wave signal, with the red solid line multiplied by a rectangular window function (dark red solid line) and with the blue dashed line multiplied by a Hanning window function (dark blue dashed line). (B) Result of the FFT functions applied to the signals in A, with the FFT-shift function applied. Colours and line types correspond to those in A. The Nyquist frequency is represented by the solid vertical line, and is unchanging between samples. 190

B.1 Example of two basic spatial (2D) FFTs, with colour scale representing an arbitrary magnitude. (A) 2D signal generated from the Hanning window function, with number of points in each dimension $N_\mathrm{x} = N_\mathrm{y} = 10$ (i.e. an even dataset). (B) Same as A, except with an odd number of points $N_\mathrm{x} = N_\mathrm{y} = 9$. (C-D) Reciprocal space plot showing the absolute value of the direct result of the FFT of the signals in A and B respectively. The white-dashed line represents the 2D Nyquist limit. (E-F) The FFTs from C and D after the FFT-shift function is applied across both dimensions, highlighting the difference between even and odd length signals, with the white-dashed Nyquist limit appearing outside of the odd sample F. 194

Chapter 1

Introduction

1.1 Aim of Research and Historical Context

Sound is one of nature's oldest explored phenomena, affecting all of us in our day to day lives. On a fundamental level, sound can be described as a simple vibration of molecules, which create a pressure wave. Hence, classical acoustic theory is often used to introduce young scientists to basic wave-phenomena, paving the way for perhaps more 'exotic' physics such as quantum mechanics or electromagnetism. Lord Rayleigh, who published his extensive treatise 'The Theory of Sound' in the nineteenth century [1,2], is often considered the father of classical acoustics, though he too built on earlier work by famous physicists including Thomas Young [3] (known for his two slits experiment), Gustav Kirchhoff [4] or even further back, Pierre-Simon Laplace [5] who, by accounting for adiabatic compression, corrected Sir Isaac Newton's value for the speed of sound in air [6]. Since then, most acoustic research has concerned non-linear aerodynamically generated sound such as that produced by jet engines, many problems of which Sir James Lighthill [7] was the first to satisfactorily resolve, later collecting his novel ideas into another great work 'Waves in Fluids' [8]. Other more recent acoustic work is of an engineering nature, such as the study of architectural acoustics [9] that aims to improve sound quality in buildings, or the design and manufacture of commercial audio equipment. In the past decade however, classical acoustics has been thrust back into the limelight, with a dramatic increase in attention associated with the ever-growing field of acoustic metamaterials: the use of subwavelength, periodic structure to control sound.

The use of structure to manipulate electromagnetic energy, in particular the propagation electromagnetic energy confined to a surface, can be traced back to advancements in technology brought on by World War 2 [10]. However, the research largely responsible for the explosion of interest into what are now known as 'metamaterials', (a term coined by John Pendry[11]), was Pendry et al.'s work on wire mesh structures in 1996[12]. They found that if the free-space wavelength of electromagnetic radiation incident on this three dimensional wire mesh was so large that the propagating fields could not resolve the periodic structure (i.e., that the structure was 'subwavelength'), the mesh could treated as though it were not two separate materials, but rather as a single, homogeneous 'effective' medium. The precise mechanism behind what determines these effective parameters depends on the system, and typically involves a resonance within the structure 'seen' by the evanescent near-field components of a wave; this has the perhaps unfortunate side-effect that metamaterials tend to function within only a narrow frequency band. Broadly speaking however, the resulting effective parameters can be analytically derived by utilising well established 'homogenisation' or 'effective medium' theory[13].

For the field of electromagnetism, the material parameters in question are its electric permittivity and magnetic permeability. What makes these metamaterials particularly exciting is that they may have properties that would not be possible with currently available traditional materials. The most obvious example of this is the possibility of a material with simultaneously negative values of both permittivity and permeability, hence possessing a negative refractive index, an idea that was once posed as a mere mathematical curiosity by Veselago[14]. Pendry et al. realised that a carefully-designed metamaterial would be able to make these properties a reality[12], leading to the design of a perfect lens[15], a 'superlens' capable or surpassing the Rayleigh diffraction limit that usually forbids a lens from resolving anything below half a wavelength of the incident radiation. That these periodic structures have been designed, means that they can also be tuned, allowing for devices with highly anisotropic properties, such as science-fiction-like cloaking devices[16]. Hence, there is a burgeoning field dedicated to the research of negative index electromagnetic metamaterials, with extensive reviews having been published[17,18].

The possibility of a negative refractive index is not the only trick a metamaterial can be good for, and also, a whole three dimensional 'bulk' material is not necessarily required to induce the desired behaviour. In light of this, another key piece of research was Ebbesen et al.'s 1998 work[19], who found that by structuring a thin metallic plate with a periodic array of subwavelength holes, 'Extraordinary-Optical-Transmission' could occur: complete transmission of light through the plate at specific, tunable frequencies. This was made possible through the excitation of the 'Surface-Plasmon', a type of electromagnetic surface wave that is confined to the interface between a metal and a dielectric at optical frequencies, and which importantly, evanescently decays into both media. A whole class of such thin metamaterials, sometimes referred to as 'metasurfaces' as they are two-dimensional and relate to waves confined to a surface rather than within a bulk material, now exist, and these too are a fruitful research topic[20]. It is here important to note that the term ‘metamaterial’ has grown not just to describe a material who’s properties may be ‘averaged’, but now encompasses any designed material that produces an unnatural effect based on its subwavelength structure rather than its chemistry[21] (as is the case for the research presented within this thesis).

Naturally, once the metamaterial concept had established itself in the electromagnetic regime, attention was soon turned to other fields, including acoustics. Fundamentally, acoustics is a mechanical process operating on a larger scale than the photonic interactions of electromagnetism. Despite this and other major differences between the two, the effective medium theories used in the electromagnetic regime could be readily translated to acoustics as the underlying field equations bear much similarity, with permittivity and permeability being approximately replaced by the mass density and the bulk modulus (relating to a materials elastic properties)[21,11]. The research that first made use of these similarities and thus paved the way for acoustic analogues of previous electromagnetic work was Liu et al’s study of elastic waves propagating through three dimensional arrays of thin coated spheres[22]. Within a certain frequency band, this structure was shown to behave as though it had effectively negative elastic constants. Later, a double negative acoustic metamaterial capable of achieving a negative index was theorised by Li et al.[23] consisting of rubber spheres submerged in water, and soon after this, Fang et al. experimentally demonstrated a negative index acoustic metamaterial using a chain of water-filled Helmholtz resonators[24]. The untold number of combinations of solids, liquids, gases another other more exotic states of matter, each with unique mechanical properties, means that there are a vast amount of possibilities for the design of such acoustic metamaterials, and an extensive review of what has so far been achieved in this emerging field was published in 2012 by Craster and Guenneau[11].

The acoustic metamaterials so far mentioned relate to ultrasonic waves propagating through solids and liquids. However, when concerned with sound propagating through air, the impedance mismatch between air and most solids is so great that they can all be treated as though they were ‘perfectly rigid’, i.e. the sound does not penetrate them at all. This means that in essence it does not matter what solid is used, the airborne sound’s behaviour will not change (excepting for a small class of extremely fragile and hard to manufacture solids known as ‘Aerogels’[25], through which sound propagates more slowly than air). This, as well as audible wavelengths requiring very large samples, severely limited the options for the creation of air-based acoustic metamaterials, until an important discovery by Pendry et al. changed the way metamaterial design could be approached.

It was thought that the surface-plasmon was an essential component of the creation of many early electromagnetic metasurfaces, as was the case for the previously mentioned work by Ebbeson et al.[19] regarding Extraordinary Optical Transmission. This was until Pendry et al.[26] realised that the surface-plasmon effects could be mimicked even at microwave frequencies, where the metallic plate can be a considered to be a perfectly conductor that expels all electromagnetic fields, and is consequently not able to support a surface-plasmon. This was possible by simply structuring of the metal plate with a periodic arrangement of deep, closely-spaced cavities, whose collective resonant excitation give rise to evanescent fields that resemble a surface-plasmon, thus creating a 'spoof-surface-plasmon'. This result meant that novel structures with scale lengths of order of, or less than, the wavelengths being probed, could allow for the manipulation of electromagnetic surface waves across multiple frequency regimes, not just visible light. Inevitably, it was realised that acoustic energy confined to the air and interacting with perfectly rigid solids could likewise be controlled with the use of 'Acoustic-Surface-Waves', arising from the diffractive-coupling of periodically arranged acoustic cavity-resonators[27,28]. Such structure-induced surface waves were shown to exist as far back as 1959 by Russian scientists Ivanov-Shits and Rozhin[29], but although further work was carried out[30,31,32,33], the potential of air-bound surface-waves for the design of materials with a novel acoustic response remained untapped. Now beginning to be realised, and outlined in recent reviews by both Cummer et al.[34] and Ma et al.[21], air-based acoustic metamaterials have become a thriving and fruitful topic of interest. Innovate research has produced devices that display phenomena including (but not limited to) 'Enhanced Acoustic Transmission'[35,27], collimation and focusing[36,37], subwavelength imaging[38,39], negative refraction[40], or even acoustic cloaking[41,42,43].

The aim of this thesis is to take established metamaterial concepts that have been explored in the electromagnetic regime, in particular the microwave metasurface domain, and apply them to the field of acoustics. The work henceforth presented endeavours to add to our rapidly expanding understanding of how acoustic energy can be manipulated in this way, and in particular, concerns itself with the propagation of sound through air as it interacts with periodically structured rigid-solids. It is hoped that the research advanced throughout this thesis will either directly or indirectly be useful for the design of future air-based acoustic devices. For example, the thermodynamic loss effects studied in the first chapter may be useful for the design of a thin acoustic absorber made from a simple resonant solid, more robust and less bulky than currently available foam-based acoustic absorbers. Similarly, the 'phase-resonant' structures in chapter two may be useful for the design of a passive acoustic filter that is readily tunable. The acoustic-surface-wave supporting structures in the latter three chapters could aid in design of devices that may, for example, channel acoustic energy based on how they affect the propagation of acoustic surface waves, and one day allow the creation of reasonably-sized, portable acoustic devices that work as well for audible sound as some of the electromagnetic metamaterial devices just now beginning to be commercially realised.

1.2 Thesis Outline

The thesis begins with chapter 2, which provides the background theory through which the experimental work that follows may be understood. The basic properties of acoustics are outlined, including a derivation of the acoustic wave equation. The importance of the thermodynamic properties of the medium through which sound propagates, in particular, the presence of thermodynamic boundary layers on the interface between a fluid and a rigid-solid, are discussed. Following this, definitions of acoustic impedance are included, necessary to explain how a rigid-walled air-filled cavity may support an acoustic resonance. These concepts are combined to describe in detail how a trapped evanescent acoustic surface wave may form above a structured solid, a result of the coupling via diffractive effects between resonant cavities arranged in a periodic fashion. Finally, well-known solid-based surface acoustic waves are outlined, whose existence is important, but that do not play a role in this work.

Chapter 3 contains a detailed overview of the methodology behind the various kinds of experiment undertaken through the work. The acoustic pulse method common to all of the experimental measurements is discussed, including its advantages and disadvantages. Two main types of experiment are described, that are the fair-field measurements of acoustic transmission through a sample, and near-field measurements that allow the direct characterisation of acoustic surface waves. A discussion of the numerical finite-element-method used to model each experiment is included at the end.

The first experimental chapter, chapter 4, explores the effect that thermodynamic boundary layers have on the resonant slit-cavities so often utilised to create acoustic metamaterials. These boundary layers are usually more than two orders of magnitude smaller than the width of said cavities, and as such much recent research neglects them, despite there existing research more than a century old suggesting that this is unwise. By investigating in detail the effect of reducing the slit-width on the measured resonant frequency, for both a single-slit-cavity and slit-cavity-array set-up, it is found that these boundary layers have a significant effect even when the form a small fraction of the total cavity width. This is manifested in both a reduction of the measured resonant frequency of each cavity and significant attenuation of that resonance. It is found that effective speed of sound within the cavity is reduced by 5% when the boundary layers occupy only 5% of the total cavity-width, which agrees with existing analytic theory. Hence, the boundary layers cannot simply be ignored, and must be taken into account when designing acoustic metamaterials that rely on cavity resonances to achieve their desired effect.

Chapter 5 is the first chapter directly involving trapped surface acoustic waves and is a study of ‘compound gratings’, gratings with a unit-cell structure comprised of more than one resonant element. This is achieved by the experimental characterisation four aluminium slit-arrays, each having the same periodicity, but with either one, two or three cavities per grating period. Sharp dips are observed in the transmission spectra of the compound gratings. These features result from the excitation of acoustic ‘phase-resonances’, possible as new degrees-of-freedom available to the acoustic near-field allow the fields in adjacent cavities of a single unit-cell to be out-of-phase. By mapping the angle dependent transmission spectrum of each grating, their dispersions are determined. Hence, the origin of the phase-resonant features is described as the band-folding of trapped acoustic surface waves back into the radiative regime, where they may indirectly couple to incident radiation; the phase-change of the fields within a unit-cell, made possible by the extra field configurations, allows the surface modes to exist at larger wavevectors than on a simple grating structure. One of the samples is optimised to include the effect of thermodynamic boundary layers, resulting in the excitation of a broad, deep transmission minimum that may be useful in the design of an acoustic filter.

Chapters 6, 7 and 8 all utilise the high-resolution near-field acoustic measurement technique to directly measure the dispersion of the acoustic surface waves present on three different kinds of acoustic metamaterial. With this technique, spatial Fourier transforms of experimentally recorded pressure field maps provide direct information on the band-structure of the modes present.

In chapter 6, the acoustic response of the square-lattice open-ended hole array that is commonly found in acoustic metamaterial literature is characterised. As a result of the lattice symmetry, it is found that over a predicable frequency band, the acoustic power flow is channelled into specific directions, forming beams with a well defined width.

Chapter 7 introduces the acoustic line mode, a type of acoustic surface wave that may exist on a simple one-dimensional line of resonating cavities. Appearing to have been overlooked in the literature, this type of surface mode is readily customisable, as it follows the shape in which the holes are arranged. This is demonstrated via the reshaping of the line into a circular ring of holes, where an acoustic line mode is found to exist that appears to follow familiar rules of periodicity, except in the theta direction. This change of co-ordinates also has implications for the definition of a surface wave. The existence of such easily manipulated acoustic line modes creates a vast amount of possibility for metamaterial design.

Chapter 8 is the final experimental chapter of the thesis. The effect of 'glide-symmetry' on a pair of acoustic line modes is investigated. This is a kind of symmetry where a unit-cell is inverted along the direction orthogonal to its periodicity, and then one side of this mirror plane translated along the periodic direction by half of its grating pitch, an example being a 'zig-zag'. Three samples are used to provide the comparison, all consisting of two adjacent lines of holes. The first does not have glide-symmetry, and as expected from the results of 5, supports two acoustic line modes with different phase character. The second sample does have glide-symmetry, and it is observed that the previously separate line modes merge to form one of mixed character. This hybrid surface mode does not form a standing wave at the first Brillouin zone boundary but at some point in the second Brillouin zone, and appears to have a region of negative dispersion. The third sample changes the shape of the cavities to increase coupling strength between the two lines, thereby emphasizing the effect that glide-symmetry has. This sort of sample could be useful in the design of acoustic lenses.

Chapter 9 discusses potential extensions to the preceding research, including some existing but unfinished work, and speculation on other ideas that may prove fruitful in future.

Finally, chapter 10 provides a summary of all of the work presented in the thesis. There are two appendices, A and B, that detail some of the well-known signal processing techniques used to analyse the various kinds of experimental data throughout, including the one dimensional and two dimensional fast Fourier transforms.

Chapter 2

Background Theory

2.1 Introduction

Acoustic metamaterials come in many forms, from thin membrane types to those that have active components[21]. To achieve novel desirable properties, many metamaterials rely on coupled resonators: this is the kind that is focused on in the present work. To understand how resonant cavities can be utilised to form trapped surface waves and thus manipulate sound, it is instructive to revise the basic properties of the acoustic wave. Hence, in this chapter, the fundamentals of classical acoustics are outlined. To begin, a derivation of the acoustic wave equation that, with a few key assumptions, describes the propagation of sound through an unbound fluid medium is presented. Next, some of the complexities that come with the full treatment of the viscous forces acting within this fluid medium are examined, in particular for the case when fluid-bound sound interacts with a solid medium, where thermodynamic boundary layers can become important. Subsequently the interaction of sound with rapidly-varying geometry changes is discussed, such as when incident on an open or close-ended tube cavity, which can lead to standing wave resonance conditions. This introduces the end correction that exists at each end of a diffracting open-cavity, which, when placed in a periodic fashion, can induce a finite impedance boundary condition that leads to trapped surface-wave-like features, termed ‘acoustic surface waves’. The concept of the dispersion relation of such a surface wave is outlined, and later used throughout the thesis to interpret physical phenomena. Key behavioural aspects of diffraction-induced surface waves are studied, such as the formation of standing-waves and energy band-gaps when certain conditions are met. Finally, brief outlines of the various kinds of solid-based surface acoustic wave are included, which while not playing a part in any of this research, are important to understand so that they are not confused with the diffraction based phenomena of the airborne wave that *is* the key focus of this thesis.

Much of the classical acoustic theory in this chapter is well known, but is included to support later conclusions regarding metamaterial behaviour. Statements made about the nature of sound and various derivations are all based on the detailed works of Kinsler et al.[44], Raichel[45], Pierce[46] and Rayleigh[1,2].

2.2 Fundamental Acoustics

2.2.1 Pressure Oscillations

At the most basic level, sound can be described as a localised pressure fluctuation that travels with a well defined speed c through some elastic medium, with properties that depend on said medium, and that is typically caused by the vibration of some body contained within it. Sound is a mechanical wave phenomenon carried through molecular collisions, where individual vibrations that combine to form a 'sound' can be expressed as a Fourier series of components each having frequency f and free space wavelength λ_0, related by $c = f\lambda_0$.

To understand how sound is generated, consider one side of a large vibrating plate submerged in some elastic medium (in this case a fluid) that oscillates back and forth along the x-axis, as illustrated in figure 2.1. The fluid molecules immediately adjacent to the plate will be compressed into the next adjacent layer of molecules along x, hence there is a local increase in density $\Delta\rho$ and pressure Δp relative to the undisturbed fluid: a 'compression'. The fluid molecules in this adjacent layer will respond by escaping into a low pressure region further along x, thereby increasing the pressure of that region and causing the whole process to repeat. Hence, the compression can be said to travel. Meanwhile, when the plate recedes to its starting position by moving in the negative x direction, it 'leaves behind' empty space causing the fluid layer immediately adjacent to it to have a localised region of low pressure and density: a 'rarefaction'. The adjacent layer of molecules flood back into the region so again the whole process repeats, leading to a travelling rarefaction. The set of travelling compressions and rarefactions constitute the pressure wave, with wavelength λ_0 measured by the distance between adjacent compressions or adjacent rarefactions, with the amplitude of the oscillation corresponding to the deviation Δp from the background pressure, p_0. For a pure sound wave at a given frequency, this can be represented as a sine-wave oscillation (figure 2.1).

This simplistic picture applies to sound as it propagates through most liquids and gases over short distances (a few wavelengths), where individual molecules are free to move, and complex thermodynamic effects negligible. The situation becomes considerably more complicated when discussing the passage of sound through an elastic solid,

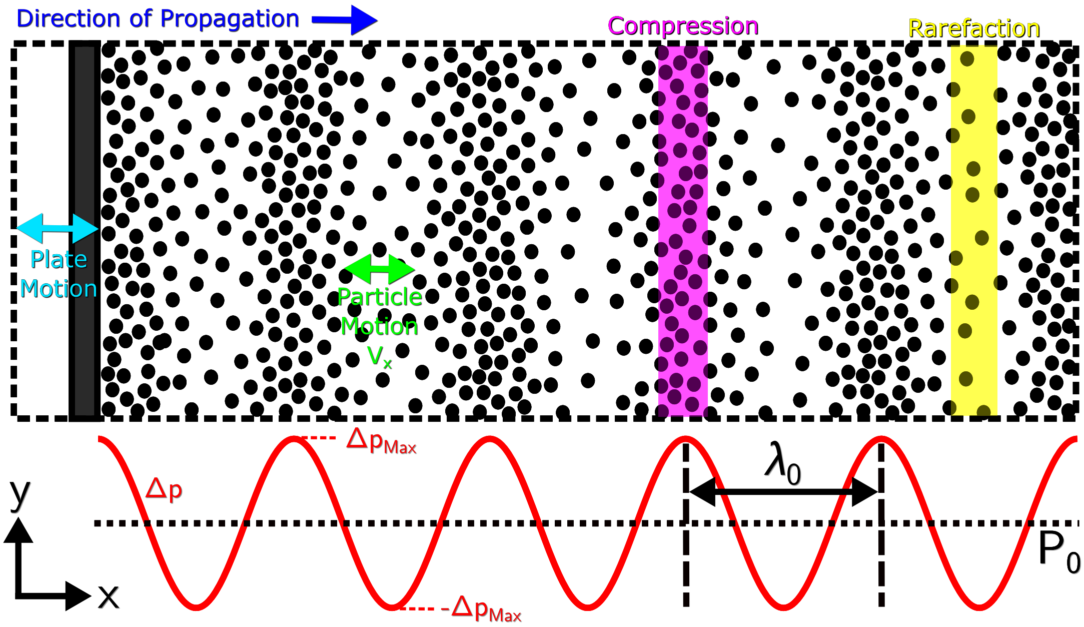

Figure 2.1: Qualitative illustration of a longitudinal pressure wave generated by a vibrating plate, with the black points representing molecules of a gas.

as the pressure fluctuations displace molecules which - being part of a solid - are tightly bound to a lattice. Disruption of this lattice generates extra shear waves (‘s-waves’), which propagate in orthogonal directions to the longitudinal pressure waves (‘p-waves’). Describing the shear and pressure waves within the solid is complex as their behaviour strongly depends on many parameters, from the exact molecular structure of the lattice, to the shape of the solid itself. These solid mechanics are not relevant to this work; all experiments were conducted in air and solids were considered perfectly rigid (to be justified and discussed in section 2.5), henceforth, only the propagation of sound through a gas is considered. Note, a gas may be described as a fluid for the purpose of this chapter.

2.2.2 Equation of State for an Ideal Gas

For the complete mathematical treatment of the acoustic pressure wave, one needs to define a set of relevant variables that can fully describe the physical mechanisms involved as the wave propagates through the host medium. Typically used are the thermodynamic variables of pressure p (Pa), density ρ ($\mathrm{kg} \cdot \mathrm{m}^{-1}$) and absolute temperature T (K), which for any fluid medium are related by an equation of state $p = p(\rho, T)$. The equation of state arises from applying conservation of energy and momentum laws to classic kinetic theory, and, depending on the fluid, can have quite a complicated form, as various intermolecular processes must be accounted for. In the case of an ideal gas (adequate to describe most acoustics[44,45]), the equation of state can be written as:

$$\frac{p}{\rho} = RT \tag{2.1}$$

where R is the 'individual gas constant', which for air takes value 286.9 J K kg^{-1}[47]. Hence, once two independent thermodynamic variables are known, the gas is completely described: any of the other variables can be determined. When discussing the propagation of sound through air, it is typically pressure p and density ρ that are sought.

If the full description of the gas' thermodynamic state is obtained from the pressure p and density ρ, all that remains to fully define the acoustic field is the velocity $\vec{\mathbf{v}}$ of the gas molecules, which has components in Cartesian space of $v_{\mathrm{x}}, v_{\mathrm{y}}$ and v_{z}. This leaves five field variables in total, meaning that five independent equations are required to obtain some solution. These equations can be derived from the the conservation of energy, the conservation of mass and the conservation of momentum along each of the principle directions.

The equation of state for an ideal gas 2.1 arises in part from the conservation of energy, and is sufficient to describe the propagation of sound through an unbound gas in most situations, when the process can be considered adiabatic. Hence, it provides one of the equations that will eventually lead to the acoustic wave equation. However, as will be discussed (section 2.4.1), a more complex form of the equation of state is required when considering thermodynamic boundary layer effects.

2.2.3 Conservation of Mass

Consider a volume element of a fluid $dV = dx\ dy\ dz$ with mass being allowed to flow in or out. Through conservation of matter, net flow into or out of this region must be equivalent to the gain or loss of fluid within it. Through consideration of the net mass flux (flow of the mass of fluid per unit area per unit time t) into this region from any of the principle directions, it can be shown that[44,45]:

$$\frac{\partial \rho}{\partial t} - \vec{\boldsymbol{\nabla}} \cdot (\rho \vec{\mathbf{v}}) = 0 \tag{2.2}$$

which is known as the 'equation of continuity', a statement of the conservation of mass for compressible fluid flow. Here, $\vec{\boldsymbol{\nabla}} = \frac{\partial}{\partial x}\hat{\mathbf{x}} + \frac{\partial}{\partial y}\hat{\mathbf{y}} + \frac{\partial}{\partial z}\hat{\mathbf{z}}$, which is the gradient operator.

2.2.4 Conservation of Momentum

Describing the forces acting on a particle within a fluid will lead to a statement of Newton's second law, but this quickly becomes a convoluted task, as there are a very large number of particles to consider. One of the properties intrinsic to a fluid is its 'viscosity', a measure of how easily the fluid can deform, where a higher viscosity means the fluid is more resistant to change (e.g., honey is far more 'viscous' than water). Viscosity can be quantified in terms of the shear (or 'dynamic') viscosity coefficient η, relating to forces acting on particles between adjacent regions of different net velocity, and bulk viscosity coefficient η_{B}, relating to molecular energy dissipation processes.

In many cases the statement of Newton's second law can be simplified by neglecting viscous forces altogether, since over short sound propagation distances they are typically negligible. One can apply this simplification in the derivation of the loss-free acoustic wave equation, which is sufficient for describing most metamaterial behaviour, as will be discussed in section 2.7. However, as will be the focus of chapter 4, viscous forces can become significant in the presence of a rigid-boundary such as a solid wall, hence it is important to include them in this otherwise brief derivation of the acoustic wave equation.

A particle moving within velocity field $\vec{\mathbf{v}}(x, y, z, t)$ can be shown to have acceleration

$$\vec{\mathbf{a}} = \frac{D\vec{\mathbf{v}}}{Dt} \tag{2.3}$$

where $\frac{D}{Dt}$ is a commonly used operator in fluid mechanics, known as the convective derivative: a time derivative with respect to a moving coordinate system. This operator describes the rate of change of some physical quantity y as it is seen by some material element moving within a macroscopic material, which itself has some velocity field $\vec{\mathbf{v}}$:

$$\frac{Dy}{Dt} = \frac{\partial y}{\partial t} + \vec{\mathbf{v}} \cdot \nabla y. \tag{2.4}$$

The acceleration 2.3 combined with the fluid mass $m = \rho dV$, give one half of Newton's second law. Next, one must sum all of the forces $d\vec{\mathbf{F}}$ acting upon fluid volume element dV. These consist of gravity g, the surface normal force arising from pressure σ_{mm} (the normal stress tensor) and surface tangential force arising from shear $\tau_{mn}, m \neq n$ (the shear stress tensor), where m and n denote axis directions, and both are expressed in terms of force per unit area (both σ_{mm} and τ_{mn} relate to viscosity). Summing all relevant forces, considering only the x direction, and then simplifying yields:

$$dF_{\mathrm{x}} = (\rho g_{\mathrm{x}} + \frac{\partial \sigma_{\mathrm{xx}}}{\partial x} + \frac{\partial \tau_{\mathrm{yx}}}{\partial y} + \frac{\partial \tau_{\mathrm{zx}}}{\partial z}) dx\ dy\ dz. \tag{2.5}$$

Newton's second law states:

$$d\vec{\mathbf{F}} = dm\vec{\mathbf{a}} = \rho dV\frac{D\vec{\mathbf{v}}}{Dt} \tag{2.6}$$

which, writing in full for just the x dimension gives:

$$\rho g_{\mathrm{x}} + \frac{\partial\sigma_{\mathrm{xx}}}{\partial x} + \frac{\partial\tau_{\mathrm{yx}}}{\partial y} + \frac{\partial\tau_{\mathrm{zx}}}{\partial z} = \rho(\frac{\partial v_{\mathrm{x}}}{\partial t} + \frac{dx}{dt}\frac{\partial v_{\mathrm{x}}}{\partial x} + \frac{dy}{dt}\frac{\partial v_{\mathrm{x}}}{\partial y} + \frac{dz}{dt}\frac{\partial v_{\mathrm{x}}}{\partial z}). \tag{2.7}$$

The difficulty in solving this equation lies in the expressions for the σ_{mm} and τ_{mn} forces. If it is assumed the stress due to viscosity is proportional to the rate of angular deformation (i.e. a Newtonian fluid), it is possible to write σ_{mm} and τ_{mn} in terms of velocity gradients and the coefficient of shear viscosity:

$$\sigma_{\mathrm{xx}} = -\Delta p - \frac{2}{3}\eta\vec{\mathbf{\nabla}}\cdot\vec{\mathbf{v}} + 2\eta\frac{\partial v_{\mathrm{x}}}{\partial x} \tag{2.8}$$

$$\tau_{\mathrm{xy}} = \tau_{\mathrm{yx}} = \eta(\frac{\partial v_{\mathrm{y}}}{\partial x} + \frac{\partial v_{\mathrm{x}}}{\partial y}) \tag{2.9}$$

and similar for the other dimensions. Note, these equations arise from complex fluid mechanics not discussed here, but a reference is provided[48]. When substituted into equation 2.7, and after some complex mathematics, the result is the non-linear Navier-Stokes equation (see section 2.4.2), which except under a small set of specific conditions, can currently only be solved via numerical methods. The Navier-Stokes equation contains the information necessary to predict e.g. turbulence, eddie currents and capillary flow. However, when discussing acoustic propagation through an unbound gas, it is safe to treat the fluid as frictionless (inviscid) by setting $\eta = 0$. All of the non-linear effects then become negligible, the shear forces τ_{mn} vanish, and the pressure forces σ_{mm} all reduce to $\sigma_{\mathrm{xx}} = \sigma_{\mathrm{yy}} = \sigma_{\mathrm{zz}} = -\Delta p$. The gravitational force may also be taken as negligible, allowing Newton's second law to be rewritten as:

$$-\vec{\mathbf{\nabla}}(\Delta p) = \Delta\rho\frac{D\vec{\mathbf{v}}}{Dt} \tag{2.10}$$

which is known as the 'linear Euler's equation'[45,49].

However, the frictionless fluid assumption is not always valid. There are acoustic situations where a more full solution is required, such as when the pressure oscillation is of great magnitude, or when the sound is confined to a narrow channel formed of rigid walls. The former is not relevant to the work in this thesis, but the latter will be discussed in section 2.4.

2.3 The Acoustic Wave Equation

For many models of sound propagation, the complex intermolecular forces occurring within a fluid can be ignored, leading to the loss-free acoustic wave equation. To derive this equation from the conservation laws outlined previously, as well as the frictionless fluid condition, three key assumptions are made. First, that the unperturbed fluid has definite-valued and time independent thermodynamic variables pressure p_0, density ρ_0, temperature T_0 and velocity $\vec{\mathbf{v_0}}$. Second, that an acoustic wave will cause the fluid's pressure, density, temperature and velocity to undergo a small perturbation, stated for example as $p_0 + \Delta p$, where $p_0 \gg \Delta p$, $\rho_0 \gg \Delta\rho$ and $T_0 \gg \Delta T$ (ΔT will henceforth be referred to as the 'excess temperature'). As the fluid is assumed to be stationary (i.e. there is no fluid flow), the background velocity $\vec{\mathbf{v_0}}$ is zero. The final assumption is that no heat transfer occurs between regions of high and low pressure/density. While this is not strictly true, at audible frequencies, the temperature gradients are so low that heat transfer is effectively zero (and at still higher frequencies, it cannot occur fast enough). Thus, the propagation of sound can be considered an adiabatic process. Indeed, this is the assumption that Newton missed in his original derivation of the speed of sound, which Laplace later corrected[1].

Considering the above assumptions, that ρ_0 does not vary in space, that $\rho_0 \approx \rho_0 + \Delta\rho$, and treating the x direction only, the continuity equation 2.2 can be shown to reduce to:

$$\frac{\partial \Delta\rho}{\partial t} = -\rho_0 \frac{\partial v_{\mathrm{x}}}{\partial x}. \tag{2.11}$$

Similarly, the momentum equation 2.10 can be expressed as:

$$\frac{\partial \Delta p}{\partial x} = \rho_0 \frac{\partial v_{\mathrm{x}}}{\partial x}. \tag{2.12}$$

For an ideal gas, an adiabatic process has the condition that $p\rho^{-\gamma}$ is constant, where $\gamma = \frac{\mathrm{C_p}}{\mathrm{C_v}}$ is the gas' ratio of specific heat capacities at constant pressure and constant volume (for air, $\gamma = 1.4$[47]). By differentiation of this condition and then by further differentiation with respect to time, it can be shown[45]:

$$\frac{1}{p_0}\frac{\partial \Delta p}{\partial t} = \frac{\gamma}{\rho_0}\frac{\partial \Delta\rho}{\partial t} \tag{2.13}$$

combining this equation with 2.11 and differentiating with respect to time, gives:

$$\frac{\partial^2 \Delta p}{\partial t^2} = \gamma p_0 \frac{\partial^2 v_{\mathrm{x}}}{\partial t \partial x}. \tag{2.14}$$

Equation 2.12 can be differentiated with respect to x, resulting in:

$$\frac{\partial^2 \Delta p}{\partial x^2} = \rho_0 \frac{\partial^2 v_\mathrm{x}}{\partial x \partial t} \tag{2.15}$$

Thus, by equating the cross differential terms in equations 2.14 and 2.15, the acoustic wave equation in terms of pressure for the x direction can be written:

$$\frac{\partial^2 \Delta p}{\partial x^2} = \frac{1}{c_\mathrm{a}^2} \frac{\partial^2 \Delta p}{\partial t^2}. \tag{2.16}$$

Note, unless otherwise stated, c will henceforth refer to the adiabatic propagation speed of the sound wave c_a predicted by Laplace, not the isothermal value c_i predicted by Newton (where $\frac{c_\mathrm{a}}{c_\mathrm{i}} = \sqrt{\gamma}$). For an ideal gas,

$$c = \sqrt{\frac{\gamma p_0}{\rho_0}} = \sqrt{\gamma R T_0}. \tag{2.17}$$

Hence for air at room temperature, $c \approx 343$ ms^{-1} (and $c_\mathrm{i} = 245$ ms^{-1})[50]. Finally, by adding in the other dimensions, one obtains the three-dimensional acoustic wave equation:

$$\vec{\nabla}^2 \Delta p = \frac{1}{c^2} \frac{\partial^2 \Delta p}{\partial t^2}. \tag{2.18}$$

Stating this in terms of angular frequency ω with the Helmholtz equation gives:

$$\vec{\nabla}^2 \Delta p + \frac{\omega^2}{c^2} \Delta p = 0. \tag{2.19}$$

Note, it is a simple matter to change this derivation to obtain the wave equation in terms of particle velocity $\vec{v}$ or density ρ, if necessary.

The general solution of the acoustic wave equation, for a mono-frequency plane wave travelling along the positive x direction, can be written as:

$$\Delta p(x, t) = \mathbf{A} \ e^{i(\omega t - k_\mathrm{x} x)} \tag{2.20}$$

where $\mathbf{A}$ is the complex peak amplitude of the wave, $w = 2\pi f$ is the angular frequency, and $k = \frac{2\pi}{\lambda_0}$ is the wavevector, or wavenumber. Similarly, the particle velocity v_x can be expressed:

$$v_\mathrm{x} = (\frac{\mathbf{A}}{\rho_0 c} e^{i(\omega t - k_\mathrm{x} x)}) \tag{2.21}$$

and likewise for the other directions.

2.4 Thermodynamic Loss Effects

For the majority of the work contained in this thesis regarding trapped surface waves, the lossless acoustic wave equation and its implications (to be discussed) suffice to describe and understand the physical phenomena. It is tempting to completely ignore the complex thermodynamic process that occur on the molecular level, and this is often justified when considering short propagation distances through free space, where these effects are negligible. Even when longer propagation distances or times are considered, such as the ringing of a cavity resonance, it may suffice to use a simplistic model of acoustic attenuation that can account for the gradual dissipation of acoustic energy to heat. This is not always the case however, such as when the propagation medium is in contact with a rigid-boundary, and complex viscous and thermal boundary layer effects come into play that require more thorough analysis.

All acoustic energy will eventually be converted to thermal energy; a sound wave trapped in a small box will not ring indefinitely, contrary to what the ancient Greeks believed[45]. The processes involved in this conversion can be categorised into three groups; internal molecular effects, viscous effects, and thermal effects. The internal molecular losses involve complicated molecular processes, such as the excitation of internal vibrations or rotations, and stored potential energy, all of which depend on the chemical structure of the fluid and discussions of which are beyond the scope of this thesis[44]. Viscous losses can occur within the bulk of medium or at the interface with a rigid boundary, arising from relative motion between adjacent regions of the fluid, which causes shear. Thermal losses can also occur either within the bulk of the medium or near a rigid boundary, as regions of high temperature conduct heat to regions of low temperature, which is then converted to kinetic energy in the form of random molecular motion instead of contributing to the pressure wave.

Ignoring the boundary layer problem, it is possible to account for the loss mechanisms intrinsic to the fluid using the acoustic wave equation alone, with a modification incorporating an acoustic absorption coefficient α_c, which can be measured experimentally, and then used to accurately predict the gradual drop in intensity of a propagating acoustic wave. Alternatively, one could introduce a phase angle between pressure and density to equation 2.18 by adding an imaginary component to the complex wave speed, whose exact nature will depend on the absorption mechanism[45,44]. For waves propagating through free space, this should suffice, but not when the aforementioned boundary layer effects are to be accounted for. To do this, one needs to return to the conservation of momentum equations, and the equation of state for the gas.

2.4.1 Equation of State Revisited

As already covered, the equation of state for a medium allows one to make predictions about its behaviour. When deriving the acoustic wave equation, the process was deemed adiabatic, which simplified the required analysis. However, as was also mentioned, this was not complete; acoustic propagation through air does undergo loss via thermal dissipation of the acoustic energy, even if it is almost negligible. To account for these losses, a more complete equation of state is required, and then the heat transfer that occurs between regions of high and low density as the acoustic wave propagates needs to be considered. This is an involved thermodynamic process, but it can be shown that the energy equation becomes[51]:

$$\Delta\rho \mathrm{C_p}(\frac{\partial T}{\partial t}) = -\vec{\boldsymbol{\nabla}} \cdot (-\kappa \vec{\boldsymbol{\nabla}} T) - \frac{1}{\rho}\frac{\partial \rho}{\partial T}\bigg|_{\mathrm{p}} T\frac{\partial p}{\partial t} \tag{2.22}$$

where κ is the thermal conductivity of the fluid. The first term on the right hand side of this equation is a form of diffusion equation that measures the conduction of heat through the gas, the second term is a measure of the thermal expansion of the gas in regions of high pressure.

2.4.2 Navier-Stokes Equation

In section 2.2.4, the force equation for all of the forces acting on an element of fluid was introduced, with a brief description of and equations for the normal stress tensor σ_{mm} and shear stress tensor τ_{mn}. After elaborate analysis[48], combining the force equation 2.7 with the two tensor equations 2.8 and 2.9 results in the well known Navier-Stokes equation (with no external forces):

$$\Delta\rho\left(\frac{\partial \vec{v}}{\partial t} + (\vec{v}\cdot\vec{\boldsymbol{\nabla}})\vec{v}\right) = -\vec{\boldsymbol{\nabla}}\Delta p + (\frac{4}{3}\eta + \eta_{\mathrm{B}})\vec{\boldsymbol{\nabla}}(\vec{\boldsymbol{\nabla}}\cdot\vec{v}) - \eta\vec{\boldsymbol{\nabla}}\times\vec{\boldsymbol{\nabla}}\times\vec{v} \tag{2.23}$$

where η is the dynamic viscosity, a measure of the momentum lost due to inter molecular collisions between regions of fluid possessing different net velocity (related to kinematic viscosity ν by $\nu = \frac{\eta}{\rho}$) and η_{B} is the bulk viscosity of the fluid, which concerns dissipation of energy via internal molecular processes.

Individual components of equation 2.23 account for different kinds of loss mechanisms. The $(\frac{4}{3}\eta+\eta_{\mathrm{B}})\vec{\boldsymbol{\nabla}}(\vec{\boldsymbol{\nabla}}\cdot\vec{v})$ term is that which accounts for viscous losses that occur within the fluid bulk, which can be approximated via the aforementioned classical absorption coefficient α_{c}. The $\eta\vec{\boldsymbol{\nabla}}\times\vec{\boldsymbol{\nabla}}\times\vec{v}$ 'vorticity' term however deals with viscous losses that occur due to complex non-linear effects such as turbulence, or in particular interest to this thesis (as they can effect cavity-resonance-based metamaterials), those that occur near a rigid boundary.

With the more robust energy equation 2.22 and force equation 2.23, the internal viscous and thermal losses can now be accounted for. Under most typical acoustic situations, the absorption that these mechanisms cause can be treated as wholly separate, and then added together, which is what results in the classical absorption coefficient α_{c} that can be used to modify the acoustic wave equation, with the 'Stoke's assumption' that $\eta_{\mathrm{B}} = 0$, i.e. that internal molecular loss mechanisms are negligible. The Stoke's assumption can fall short in polyatomic gasses such as air, and a full description of these molecular effects, involving things such as molecular vibrational and rotational degrees of freedom, would require a lengthy discussion of thermodynamics[52,53]. Since their magnitude is negligible at audio frequencies in dry or low humidity air, they will not be covered. While this is also true of the internal viscous and thermal loss mechanisms, unlike these two, the molecular loss mechanisms do not play an enhanced role in the presence of a rigid boundary.

2.4.3 Thermodynamic Boundary Layers

When sound propagating through a fluid is incident normally on a solid object, such as a wall, the impedance mismatch (acoustic impedance being a measure of how easily sound can propagate through a medium, discussed in detail in section 2.5) is so huge, that the wall can be treated as though it were perfectly rigid, i.e. the sound does not penetrate the wall and is totally reflected. For sound grazing the wall, the situation becomes more complicated, with the introduction of viscous and thermal boundary layer loss mechanisms that, along with diffraction from periodic structures, are the dominant form of loss in the acoustic experiments conducted throughout this thesis.

Take a lossless plane wave propagating along x, and a wall placed perpendicular to the wave fronts, at $\mathrm{z} = 0$, as depicted in figure 2.2. At the wall boundary, the particle velocity of the wave parallel to the wall v_{x} must fall to zero. This is the well known 'no-slip' boundary condition[8]. As one moves away from the wall, the particle velocity must also evolve back to its free space value. The velocity field within the distance over which this change occurs can be described as a secondary viscous wave, having its own particle velocity v', which can be treated as part of the primary plane wave. Via consideration of the vorticity term in the Navier-Stokes equation 2.23, one can write a diffusion equation for v'[44]:

$$\frac{\partial v'}{\partial t} = \frac{\eta}{\rho_0} \frac{\partial^2 v'}{\partial z^2}. \tag{2.24}$$

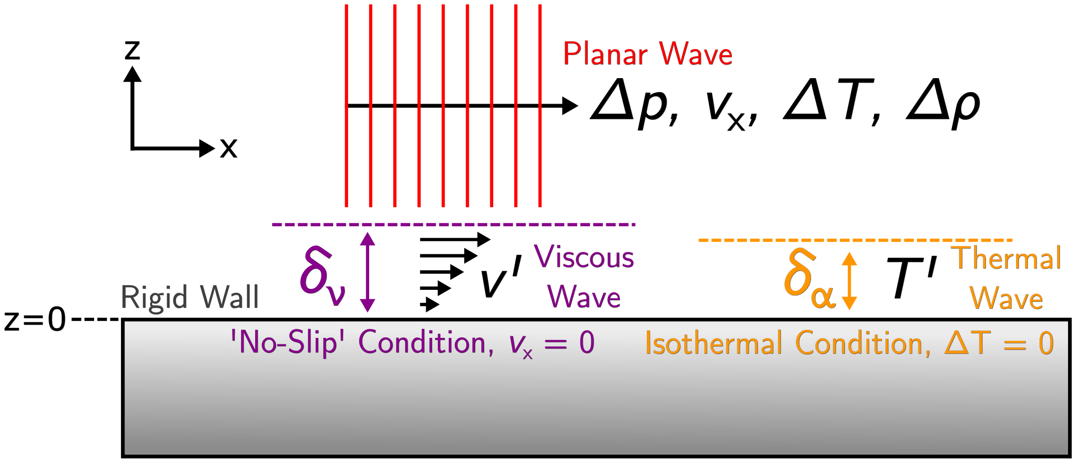

Figure 2.2: Qualitative illustration of the formation of viscous δ_ν and thermal δ_α boundary layers near a rigid-wall, as a planar wave propagates orthogonally to it.

Now, applying the boundary condition that $v' = -v_x$ when $z = 0$, and assuming a frequency dependence of e^{iwt}, the method of separation of variables applied to 2.24 results in the complex solution:

$$\mathbf{v}' = -\mathbf{v}_x e^{-(1+i)\frac{z}{\delta_\nu}} \tag{2.25}$$

where $\mathbf{v}_x$ is the plane wave particle velocity with a complex solution to 2.21 and δ_ν is the frequency-dependent thickness of the viscous boundary layer, a measure of the size of region over which the decay in particle velocity falls to zero. Note, the complex $\mathbf{v}'$ is now the result of a Fourier transform. The viscous boundary layer is typically defined as (although not always, as will be discussed in chapter 4)

$$\delta_\nu = \sqrt{\frac{2\eta}{\rho_0 2\pi f}} = \sqrt{\frac{\nu}{\pi f}}, \tag{2.26}$$

and is quoted in terms of kinematic viscosity ν throughout the remainder of this thesis. For air at 5 kHz, this value is ∼ 20 μm. Forcing the particle velocity to zero in this way causes loss of acoustic energy via shearing between the regions of different net velocity, with this concentrated boundary layer effect being far stronger than the same process occurring in free space. This is not always true however, as the intrinsic viscous loss increases as a function of frequency, whereas the viscous boundary layer size has the opposite dependence - though in air, the balance does not switch below ultrasonic frequencies.

As well as the ‘no-slip’ condition leading to viscous loss effects, the rigid-wall boundary also induces a thermal loss mechanism. The wall acts as an isothermal boundary condition; it can be considered an infinite heat-sink that is at thermal equilibrium T_0

with the environment. Taking the same plane-wave-perpendicular-to-wall scenario as developed for the viscous situation (figure 2.2), the problem can similarly be split into two parts. The excess temperature ΔT generated by the pressure and density fluctuations in the free space propagation of a plane wave of pressure amplitude P can be written[44]

$$\Delta T = T_0 + T_0(\gamma - 1)\left(\frac{P}{\rho_0 c^2}\right)e^{i(\omega t - kx)}. \tag{2.27}$$

Far from the wall, these temperature fluctuations are treated as they were for the lossless case: too slow and insignificant in magnitude to be conducted to surrounding regions of fluid, hence an adiabatic process (this is true in air at audible frequencies). In close proximity to the rigid-boundary however, this excess temperature can be thought of as being immediately conducted into the wall, meaning that the acoustic process switches to isothermal from adiabatic. So, in a similar way to the tangential particle velocity being forced to zero and forming a secondary viscous wave v', a secondary thermal wave T' is formed as the propagation of the acoustic wave evolves from an isothermal process near the wall back to an adiabatic one in free space. Again, the full mathematical description of this process is highly involved[2,54,55,44], but it can be shown to reduce to the thermal diffusion equation previously introduced as part of the equation of state (equation 2.22), applied to the combined thermal field $\Delta T + T'$:

$$\frac{\partial T'}{\partial t} = \alpha \frac{\partial^2 T'}{\partial z^2} \tag{2.28}$$

with $\mathrm{C_p}$ being the heat capacity at constant pressure and $\alpha = \frac{\kappa}{\rho_0 \mathrm{C_p}}$, the thermal diffusivity of the gas. As with equation 2.24, applying boundary conditions and assuming a frequency dependence of e^{iwt}, the combined field of the primary ΔT and secondary T' temperature waves can be written:

$$\Delta T - T_0 = (1 - e^{-(1+i)\frac{z}{\delta_\alpha}})T_0(\gamma - 1)\left(\frac{P}{\rho_0 c^2}\right)e^{i(\omega t - kx)} \tag{2.29}$$

where P is the pressure amplitude of the plane wave, γ the ratio of specific heats, and δ_α the thermal boundary layer thickness given by:

$$\delta_\alpha = \sqrt{\frac{\alpha}{\pi f}}. \tag{2.30}$$

The viscous and thermal boundary layers operate on similar scales, the square of ratio between them depends on the gas and is known as the Prandtl number $\mathrm{P_r}$ where:

$$\mathrm{P_r} = \frac{\delta_\nu^2}{\delta_\alpha^2}. \tag{2.31}$$

Here only the situation of a single rigid-wall adjacent to an unbound medium has been considered. When the geometry is such that the medium is confined to e.g. a rigid-walled cylindrical pipe, these boundary layer effects can become far more pronounced[54], not only causing attenuation of the acoustic wave but also changing its phase speed and effective density. These effects in particular, which have been studied extensively over the past two centuries[4,2,56,54,55,57,58], are the focus of experimental chapter 4, as they are of utmost importance to the design of acoustic metamaterials even when the boundary layer thickness is several orders of magnitude smaller than the wavelengths of interest. As such, they will be revisited in detail.

2.5 Acoustic Impedance, Reflection and Transmission

In this section the different kinds of acoustic impedance are introduced, along with the most basic form of reflection and transmission coefficients and how they are useful for describing how waves travel from one medium to another, which will be necessary when performing the transmission measurements in chapters 4 and 5.

For a wave travelling through an unbound medium, the 'specific acoustic impedance' is a measure of the ratio of acoustic pressure to particle velocity, given by

$$\mathbf{z}_\mathrm{a} = \frac{\mathbf{\Delta p}}{\vec{\mathbf{v}}} = \pm\rho_0 c \tag{2.32}$$

with the right hand side expression applicable when the acoustic wave in question is a plane wave, the sign denoting direction of propagation. The product $\rho_0 c$ is known as the 'characteristic impedance' of the material, measured in 'rayls' ($1\ \mathrm{rayl} = 1\ \mathrm{Pa\,s\,m^{-1}}$). For more complicated situations such as those involving standing waves or diverging waves, or interactions with geometry changes, the specific acoustic impedance takes on the complex form:

$$\mathbf{z}_\mathrm{a} = r_\mathrm{a} + i x_\mathrm{a} \tag{2.33}$$

where r_a is the specific acoustic resistance and x_a is the specific acoustic reactance, that will depend on the specifics of the situation. This expression will be necessary when describing the interaction of sound with pipes, as in section 2.6.

When an acoustic plane wave encounters an impedance mismatch, such as when it travels from a fluid with $z_\mathrm{ai} = \rho_{0\mathrm{i}} c_\mathrm{i}$ to fluid with $z_\mathrm{at} = \rho_{0\mathrm{t}} c_\mathrm{t}$ (neither complex for a plane wave), some of the acoustic pressure will be transmitted and some reflected, depending on the ratio of the impedances and the angle of incidence (note, in this section, subscripts i, t and r donate incident, transmitted and reflected media respectively). The amplitude coefficients of reflection **R** and transmission **T** can be defined in terms of complex pressure amplitudes $\mathbf{P}_\mathrm{i}$ (incident wave), $\mathbf{P}_\mathrm{r}$ (reflected wave), and $\mathbf{P}_\mathrm{t}$ (transmitted wave):

$$\mathbf{R} = \frac{\mathbf{P}_\mathrm{r}}{\mathbf{P}_\mathrm{i}} \tag{2.34}$$

$$\mathbf{T} = \frac{\mathbf{P}_\mathrm{t}}{\mathbf{P}_\mathrm{i}}. \tag{2.35}$$

The intensity of a plane wave is defined as $I = \frac{P^2}{2\rho_0 c}$, hence we can write the reflection and transmission intensity coefficients as:

$$R_\mathrm{I} = \frac{I_\mathrm{r}}{I_\mathrm{i}} = |\mathbf{R}^2| \tag{2.36}$$

$$T_\mathrm{I} = \frac{I_\mathrm{t}}{I_\mathrm{i}} = \frac{\rho_{0\mathrm{i}} c_\mathrm{i}}{\rho_{0\mathrm{t}} c_\mathrm{t}} |\mathbf{T}^2| \tag{2.37}$$

The acoustic power is defined as the intensity multiplied by the cross-sectional area of the incident beam. For a reflected wave, the cross-sectional area does not change, so the power reflection coefficient R_Π is equivalent to R_I ($R_\Pi = R_\mathrm{I}$). The cross-sectional area S may change for the transmitted wave however, so this must be included in writing power transmission coefficient $T_\Pi = \frac{S_\mathrm{t}}{S_\mathrm{i}} T_\mathrm{I}$. The conservation of energy says that the total power of the incident wave must remain in the transmitted and reflected waves, so that $T_\Pi + R_\Pi = 1$ (neglecting absorption through losses). This fact and the previous set of equations hold for when there is a simple planar boundary between two fluids, where for a plane wave at normal incidence, it can be shown that:

$$R = \frac{\rho_{0\mathrm{t}} c_\mathrm{t} - \rho_{0\mathrm{i}} c_\mathrm{i}}{\rho_{0\mathrm{t}} c_\mathrm{t} + \rho_{0\mathrm{i}} c_\mathrm{i}} \tag{2.38}$$

$$T = \frac{2\rho_{0\mathrm{t}} c_\mathrm{t}}{\rho_{0\mathrm{t}} c_\mathrm{t} + \rho_{0\mathrm{i}} c_\mathrm{i}} \tag{2.39}$$

A few observations can be made. The reflection amplitude coefficient is always real, though its sign depends on whether the impedance of the second medium is greater than the first. If the second medium has a greater impedance ($z_\mathrm{at} > z_\mathrm{ai}$), then the reflected wave is positive, and is in-phase with that of the incident wave. Vice versa, if $z_\mathrm{ai} > z_\mathrm{at}$ then the reflective wave is negative and π radians out of phase with the incident one.

Throughout this thesis we are only concerned with air as the propagating medium, which at standard temperature and pressure has $z_\mathrm{aAir} = 428.0$ rayls[47]. The structures of interest consist of either aluminium, with $z_\mathrm{aAl} = 1.7 \times 10^7$ rayls or acrylic $z_\mathrm{aAcr} =$

1.7×10^6 rayls[59]. This means that in all present cases, the impedance mismatch is very significant, i.e. $z_{\mathrm{ai}}/z_{\mathrm{at}} \approx 0$, hence there will be a reflection from the boundary with no reduction in amplitude, and the particle velocity normal to the boundary is zero. This is the 'rigid-wall' boundary condition which has other ramifications as discussed in section 2.4.3. Note, if a wave is incident on the impedance boundary at some arbitrary angle, these expressions will be modified accordingly[45,44].

The above equations break down when the impedance mismatch between two regions results from a geometry change. Alone, the expression for the specific acoustic impedance $\mathbf{z}_{\mathrm{a}}$ cannot predict the reflection that occurs when a wave encounters an impedance mismatch caused by a sudden change in cross-sectional area S (defined by a rigid boundary) of the fluid that is comparable to its free space wavelength. This requires a measure of the conventionally named 'scalar volume velocity' $\mathbf{U} = \oint_S \vec{\mathbf{v}} \cdot \hat{\mathbf{n}}\, dS$ ($\vec{\mathbf{v}} \cdot \hat{\mathbf{n}}$ being frequency-domain particle velocity normal to the sound source, with the surface integral relating to the cross-sectional area of the geometry), leading to 'geometric acoustic impedance' (often, just called the acoustic impedance) $\mathbf{Z}$:

$$\mathbf{Z} = \frac{\boldsymbol{\Delta}\mathbf{p}}{\mathbf{U}} \tag{2.40}$$

where $\boldsymbol{\Delta}\mathbf{p}$ and $\mathbf{U}$ are complex. Geometric and specific acoustic impedances are thus related by $\mathbf{Z} = \mathbf{z}_{\mathrm{a}}/S$. Hence, the sound will not propagate through unhindered when it encounters a change in cross-sectional area of the fluid (of comparable size to the acoustic wavelength λ_0), such as at the entrance or exit of a region of air bounded by a rigid-walled cavity. The propagation wavefunction will change and there will be an impedance mismatch that will cause reflections to occur at the cavity entrance. Note, the situation becomes still more complicated when multiple cavities are introduced. This will be covered in section 2.7.

2.6 Acoustic Interaction with Rigid-Walled Cavities

Locally resonant elements, such as rigid-walled cavities, are required to design geometries that support acoustic surface waves, as near resonance they can couple together via diffraction. Before this is discussed in detail it is necessary to understand how acoustic waves interact with these cavities individually.

When sound is fully confined to some rigid-walled cavity that is of comparable size to its wavelength, such as a low frequency source producing sound in a small room, the full treatment of the acoustic wave equation has the potential to become quite complicated; this is the domain of acoustic waveguides[44], or for even larger environments, architectural acoustics[9]. Ignoring thermodynamic effects, it is much easier to describe the propagation of a wave through a cavity when the dimensions of the cavity are far smaller than the wavelength of interest, i.e. the frequency is less than the waveguide's 'cut-off' frequency, below which, any sound propagating within the cavity can only have planar wavefronts (but, importantly, will still propagate, as it is a longitudinal wave). The waveguide cut-off frequency is determined by the cavity's exact shape and size as well as the properties of the fluid medium within it, and must be calculated on an individual basis[44,45]. All samples henceforth considered have cavities with dimensions where the frequencies of interest lie below each cavity's corresponding cut-off frequency.

Take the case of a small cylindrical cavity which has constant radius a (where $a \ll \lambda_0$) and length L. In acoustic literature, this sort of cavity is known as a pipe or tube, and can either terminate in a rigid boundary ('close-ended') or a return to free space ('open-ended'). Both situations are depicted in figure 2.3. First, consider the close-ended pipe with cross sectional area $S = \pi a^2$, driven by an acoustic source (such as an incident plane wave) at $x = 0$ and terminated by a rigid-wall at x $= L$. Provided $a \ll \lambda_0$ and thus the frequency is below the calculated cut-off frequency of the rigid-walled cavity, the wave in the pipe will have planar form:

$$\mathbf{\Delta p} = \mathbf{A}e^{i[\omega t + k(L-x)]} + \mathbf{B}e^{i[\omega t - k(L-x)]} \tag{2.41}$$

where $\mathbf{A}$ and $\mathbf{B}$ are complex amplitude coefficients determined by the boundary conditions at each pipe end. The fluid in the pipe has its own mechanical impedance $\mathbf{Z}_\mathrm{m}$ (separate from acoustic impedance), where

$$\mathbf{Z}_\mathrm{m} = \frac{\vec{\mathbf{F}}}{\vec{\mathbf{v}}} \tag{2.42}$$

$\vec{\mathbf{F}}$ being the force on the particles and $\vec{\mathbf{v}}$ being their resulting velocity, both having complex value. At the point of the closed-end at x $= L$, this mechanical impedance is

$$\mathbf{Z}_\mathrm{mL} = \rho_0 c S \frac{\mathbf{A} + \mathbf{B}}{\mathbf{A} - \mathbf{B}} \tag{2.43}$$

and the input mechanical impedance $\mathbf{Z}_\mathrm{m0}$ from the source is

$$\mathbf{Z}_\mathrm{m0} = \rho_0 c S \frac{\mathbf{A}e^{ikL} + \mathbf{B}e^{ikL}}{\mathbf{A}e^{ikL} - \mathbf{B}e^{ikL}}. \tag{2.44}$$

The quantity $\rho_0 c S$ is the 'characteristic mechanical impedance', which can be used to normalise the mechanical impedance. Doing this and combining $\mathbf{Z}_\mathrm{mL}$ and $\mathbf{Z}_\mathrm{m0}$ to eliminate **A** and **B**:

$$\frac{\mathbf{Z}_{\mathrm{m0}}}{\rho_0 cS} = \frac{\frac{\mathbf{Z}_{\mathrm{mL}}}{\rho_0 cS} + i\tan kL}{1 + i\frac{\mathbf{Z}_{\mathrm{mL}}}{\rho_0 cS}\tan kL}. \tag{2.45}$$

The substitution $\frac{\mathbf{Z}_{\mathrm{m0}}}{\rho_0 cS} = r_{\mathrm{a}} + ix_{\mathrm{a}}$ (the general form of specific acoustic impedance from equation 2.33) allows one to find the conditions of resonance and anti-resonance within the pipe, which occur when the reactance term ix_{a} falls to zero and the resistance term r_{a} is small (resonance) or large (anti-resonance). In the simplest case, letting $|\mathbf{Z}_{\mathrm{mL}}/\rho_0 cS| \to \infty$ in equation 2.45 provides

$$\frac{\mathbf{Z}_{\mathrm{m0}}}{\rho_0 cS} = -i\cot kL \tag{2.46}$$

whereupon we have the condition of resonance when $\cot kL = 0$ (hence no reactance),

$$k_n L = \frac{(2n-1)\pi}{2} \tag{2.47}$$

rearranging in terms of frequency f

$$f_n = \frac{(2n-1)c}{4L} \tag{2.48}$$

hence all of the resonant frequencies are the odd harmonics of the fundamental, which is determined from the length L of the tube and is when a quarter wavelength fits within it. There is a pressure anti-node at the terminated end of the pipe at $\mathrm{x} = L$, and a pressure node at the entrance $\mathrm{x} = 0$.

The situation changes slightly when the pipe is terminated by an open-end, and the sound can thus be re-radiated into the air. The mechanical impedance $\mathbf{Z}_{\mathrm{mL}}$ at the pipe end does not fall to zero but to $\mathbf{Z}_{\mathrm{r}}$, another type of acoustic impedance known as the radiation impedance, which is the part of mechanical impedance that relates to the coupling of a driving source to an acoustic wave,

$$\mathbf{Z}_{\mathrm{r}} = \int \frac{d\mathbf{f}_{\mathrm{s}}}{\vec{\mathbf{v}}} \tag{2.49}$$

where $d\mathbf{f}_{\mathrm{s}}$ is the normal component of force on element dS of the radiating face. This term will depend on the surroundings immediately outside the vicinity of the open end, as the air outside the cavity loads the column of air within it. This can be come an involved integral depending on the geometry (such as for the impedance gratings in section 2.7.3), but has a few well known approximate solutions. In the case of a 'flanged' pipe at the low frequency limit ($a/\lambda_0 \ll 1$), where the radius of the open pipe

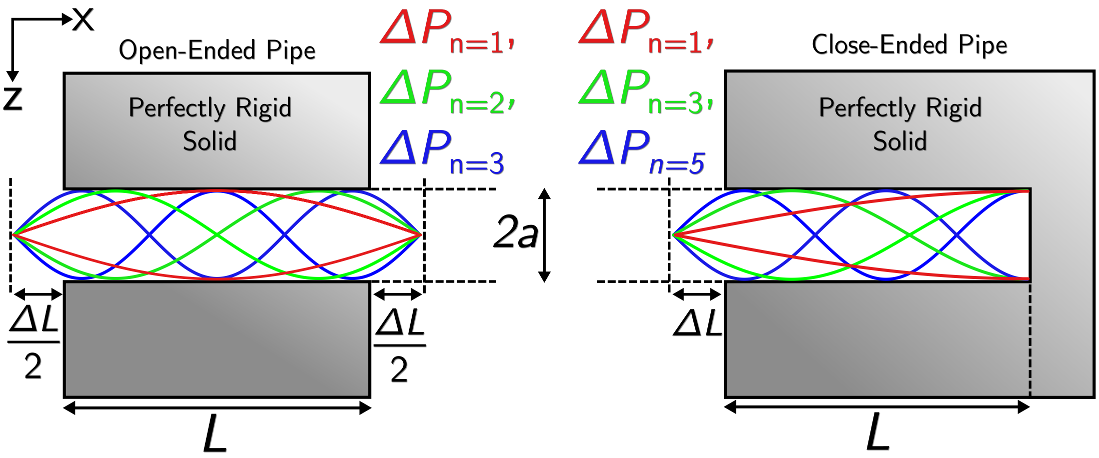

Figure 2.3: Qualitative illustration of the amplitude of the pressure field for the first three harmonics supported within both an open-ended and close-ended pipe system. This is a cross-section through the middle of each pipe, and can also represent the modes supported within the equivalent slit system, substituting the radius a for slit-width w[56].

face a is surrounded by a large rigid flange, $\mathbf{Z}_{\mathrm{r}}$ can be treated as a radiating circular piston. To first order it can thus be written[44]

$$\frac{\mathbf{Z}_{\mathrm{mL}}}{\rho_0 c S} = 0.5(ka)^2 + i(\frac{8}{3\pi}) \tag{2.50}$$

substituting this into 2.45 shows that resonance occurs when $\tan kL = -8ka/3\pi$, yielding resonant frequencies

$$f_n = \frac{nc}{2(L + \Delta L)} \tag{2.51}$$

where $\Delta L = \frac{8a}{3\pi} \approx 0.8a$ is the 'end correction' term, highlighting that for an open-ended pipe the resonant frequencies depend on an effective length $L_{\mathrm{eff}} = L + \Delta L$. This end correction does not currently have an exact analytic solution, and Rayleigh's original approximation of $\sim 0.8a$ used above remains the accepted value[2,44,45].

The form of the standing waves within each of these geometries is illustrated in figure 2.3. Note, there is a key difference between what figure 2.3 shows, and the above derivations for pipe resonances, which also relates to the samples studied throughout this thesis. The derivations above assume a driving source is located directly at $x = 0$, with an input mechanical impedance $\mathbf{Z}_{\mathrm{m0}}$. Hence, for the close-ended pipe (equation 2.48), there appears to be no end-effect term present. Similarly, the open-ended pipe equation (2.51) only has an end-effect term arising from the radiation impedance $\mathbf{Z}_{\mathrm{mL}}$ at point $x = L$. In figure 2.3, the eigenmodes of the pipes are shown as if they were excited by a far field source. This means that as well as the end-effect term at $x = L$

for the open-ended pipe, there is an additional end-effect term for both closed- and open-ended pipe geometries arising from the tube entrance at $x = 0$, which is now free to radiate back into the surrounding medium[28]. This does not change the pattern of the resonances and their harmonics, except for a slight increase in effective length.

Throughout this thesis, this sort of cavity resonance is referred to as 'Fabry-Perot-like', since it can be thought of as a resonance that occurs when reflections from each end of the pipe are in-phase with each other (as they are in the classic Fabry-Perot interferometer[60]), which is the physical interpretation of the conditions which lead to expressions 2.48 and 2.51. The radiation impedance $\mathbf{Z}_{\mathrm{r}}$ is dependent on the tube exit's surroundings, and placing a series of tubes in a periodic fashion can lead to trapped surface wave effects, as is discussed in the next section.

Note, for the case of a finite-length 2D slit-cavity, where instead of having a column of air surrounded by a wall at a fixed radius, the air is only bounded in one dimension via two infinite parallel walls separated by some slit-width w, the analysis yields a similar result for the resonant frequencies in both the closed- and open-ended slit cases. One must only substitute the radius a for slit-width w[56].

When an open-ended cavity such as those discussed above is probed at multiple frequencies with a plane wave, and the transmission coefficient measured (see chapter 3), the standing wave resonances manifest themselves as a series of Lorentzian-shaped peaks in the transmission spectrum (the magnitude of either the transmission amplitude coefficient $\mathbf{T}$ or transmission intensity coefficient T_{I} as a function of frequency). The width of the peaks and the level of the background transmission depend on the end correction term; the larger the tube radius/slit-width, the more damped the resonance, and the higher the background transmission[44]. Conversely, a narrow slit should support a sharp resonance on a low background, but as will be seen in chapter 4, the thermodynamic boundary layer effects present in such a cavity can also cause significant damping, as well as a reduction in the frequency of the resonance. In a similar vein, if the reflection amplitude coefficient $\mathbf{R}$ (or reflection intensity coefficient R_{I}) is measured for a close-ended cavity in a solid plate, the resonance conditions will result in a series of troughs (rather than peaks) in the reflection spectrum, due to absorption within the cavity (width and depth of the troughs again depending on the end-correction term). With no loss, there would no dip in reflection coefficient, as the rigid boundary condition of the solid the cavities are formed from would give a complete reflection.

The analysis within this section is simplified to illustrate how such a close or open-ended cavity can have resonant conditions despite the air medium being unchanged; the full treatment of such a problem will depend on the nature of the excitation, the shape of the cavity, the cavity length, the cavities' immediate surroundings, and also attenuation via boundary layer effects.

2.7 Acoustic Surface Waves

In this section the mechanism by which an acoustic wave contained within the air can be bound to a surface and thus form a 'trapped' Acoustic Surface Wave (ASW) is presented.

2.7.1 Surface Wave Definition

As discussed in section 2.3, a plane wave that propagates through free space in some arbitrary direction **r** has wavevector $k_{\mathbf{r}} = \sqrt{k_{\mathrm{x}}^2 + k_{\mathrm{y}}^2 + k_{\mathrm{z}}^2}$ with a maximum value of $k_0 = \frac{2\pi}{\lambda_0} = \frac{\omega}{c}$. Hence, the most momentum a wave can have in one direction, say x, and still propagate, is $k_{\mathrm{x}} = k_0$ - a plane wave travelling at the speed of sound (within the fluid) along the x direction only.

Consider x being the direction parallel to a boundary between two materials, and z perpendicular to it. It is possible for a wave to have too much momentum to radiate away from this boundary, having a $k_{\mathrm{x}} > k_0$. In a 2D case where $k_{\mathrm{y}} = 0$, this means that to conserve momentum, k_{z} must become complex, with an imaginary component. The physical meaning of a wave which has a pure imaginary is that the wave propagates along x but exponentially decays from the boundary in z into the medium above (or/and below): it is an evanescent 'trapped' wave, known as a 'surface wave'. Typically these waves have longer decay lengths along x than they do in free space, with a $1/x$ rather than a $1/x^2$ amplitude drop off from the source[33].

In particular, a trapped surface wave can exist at the boundary of an impedance mismatch[49]. For all of the discussion on surface waves that follows (including the rest of this section regarding acoustic surface waves), consider only a two dimensional system (x,z) where there is an impedance boundary in z at $z = 0$, and $k_0 = \frac{2\pi f}{c} = \sqrt{k_{\mathrm{x}}^2 + k_{\mathrm{z}}^2}$, as $k_{\mathrm{y}} = 0$. Consider a harmonic pressure field $\Delta p = p(x, z)e^{i\omega t}$ in the plane above this impedance surface, which spans $z \geq 0$. This wave satisfies the Helmholtz equation $\nabla^2 \Delta p + k^2 \Delta p$ (from equation 2.19), with boundary condition

$$\frac{\partial p(x,0)}{\partial z} = -\frac{ik\rho_0 c}{\mathbf{z}_{\mathrm{as}}}\, p(x,0) \tag{2.52}$$

where (from equation 2.33) $\mathbf{z}_{\mathrm{as}} = r_{\mathrm{as}} + ix_{\mathrm{as}}$ is the specific acoustic impedance of the boundary material extending through $z \leq 0$, ρ_0 is fluid density, and c the (adiabatic) speed of sound. Here, r_{as} is the real-valued specific acoustic resistance, and x_{as} is the imaginary specific acoustic reactance. Hence, suitable plane wave solutions are

$$p(x, z) = \mathbf{A}e^{-(i\beta x \pm i\zeta z)}. \tag{2.53}$$

For propagation in positive x, expressions for ζ and β are

$$\zeta = -k_0 \frac{\rho_0 c}{\mathbf{z}_{\mathrm{as}}} \tag{2.54}$$

and

$$\beta = k_0 \sqrt{1 - \left(\frac{\rho_0 c}{\mathbf{z}_{\mathrm{as}}}\right)^2}. \tag{2.55}$$

For an evanescent wave to exist with decreasing exponential amplitude above $z = 0$, k_{z} must be imaginary, thus $\mathrm{Im}(\zeta) > 0$. So, for solutions to satisfy the boundary condition 2.52, it follows that $\mathrm{Im}(\mathbf{z}_{\mathrm{as}}) > 0$, or stated differently

$$x_{\mathrm{as}} > 0, \tag{2.56}$$

(x_{as} being the imaginary part of z_{as}). The physical interpretation of this quality is that the surface's acoustic reactance is a stiffness[61], or that it is 'spring-like'. The decay length into z of the resulting surface wave is of order $z = \mathcal{O}(\lambda_0 |x_{\mathrm{as}}|)$, $\mathcal{O}$ being a general mathematical operator.

Some more important conclusions can be drawn. To observe the surface wave, the pressure amplitude decay into z must be sufficiently rapid, a reasonable criterion being that it falls to $\frac{1}{e}$ of its initial value within one free-space wavelength λ_0, i.e. $\lambda_0 |x_{\mathrm{as}}| > 1$. Also, the decay length along x must not be too short, so $\lambda_0 |x_{\mathrm{as}}| \ll 1$. Combined, this means that a surface wave will be most easily observable on an impedance boundary $\mathbf{z}_{\mathrm{as}}$ provided that the surface's acoustic reactance is greater in magnitude than its acoustic resistance, $x_{\mathrm{as}} > r_{\mathrm{as}}$, and the reactance term lies within the range $2 < \frac{x_{\mathrm{as}}}{\rho_0 c} < 6$[32].

2.7.2 Surface Waves in Acoustics

There are many types of trapped surface wave that exist in acoustics. Within the domain of solid mechanics exist a set of what are commonly known as 'Surface Acoustic Waves', (SAWs), such as the Rayleigh wave that exists at the boundary of an elastic solid and a vacuum[62,63]. These involve shear waves and do not play a role in the measurements taken throughout this thesis, hence they will be ignored - a brief outline of each type and a justification of their being irrelevant is included in section 2.7.9. Another type of trapped wave contained purely within a fluid can exist at the boundary between a fluid of specific acoustic impedance $\mathbf{z}_{\mathrm{a1}}$ and another material of impedance $\mathbf{z}_{\mathrm{a2}}$, provided that the previously discussed impedance conditions are met[30]. There is little consistency in the literature regarding this type of surface wave's name, with variations including 'air coupled Rayleigh-wave' and 'spoof-surface acoustic wave'; they will be referred to as ‘Acoustic Surface Waves’ (ASWs) for the duration of this thesis.

The presence of acoustic surface waves in air was first measured by Ivanov-Shits and Rozhin in 1959[29]. Indeed, the theoretical treatment of the surface wave existing at a finite impedance discontinuity has received much attention[30,31,32]. The difficulty in creating an observable airborne ASW lies in this impedance condition; the impedance mismatch between the air and most solids is so great that the surface wave has an effectively infinite decay length and cannot be considered as bound to the surface in any meaningful sense - the condition $\lambda_0|x_{\text{as}}| > 1$ is not met. To create a finite impedance mismatch with a reactive surface then, one option is to deposit a layer of air-filled porous material above the solid, an idea studied extensively[64,65,66,67] and which has been experimentally observed, such as above soil and grass[68] or even snow[69]. The other option, utilised through the experimental work in this thesis, is to create an ‘impedance grating’[63], a periodic structure formed of rigid material that, near the resonance condition of the cavities formed by the structure, may be treated as a medium with a finite effective impedance. This method has also received a lot of both theoretical[63,70,71] and experimental[72,73,33,61] attention, including Van der Heijden and Martens, who in 1979 dug a series of grooves into the side of a road, thereby creating an ASW and trapping some of the traffic noise[33].

All of this older research came before the explosion of the metamaterial concept - the idea that a material can have unusual effective properties derived from a structure factor rather than its molecular make up - after in 1998 Ebbesen et al. observed surface wave assisted Extraordinary-Optical-Transmission (EOT) through a holey-plate in the electromagnetic regime[19]. It was thought that the ‘Surface-Plasmon’ (a type of dispersive trapped electromagnetic surface wave to which no direct equivalent exists in acoustics) was required to mediate this transmission. However, Pendry et al. later realised that the EOT effect could be induced with an array of subwavelength cavities in the microwave regime[26], where the metal can be considered a perfect conductor and thus not support a surface-plasmon - this was an ‘impedance grating’ not unlike those studied in acoustics, and soon after, a prediction of Enhanced-Acoustic-Transmission by Zhang et al.[74] (alongside other metamaterial-enabled quirks such as negative refraction[24]) began the race to design and develop acoustic metamaterials with the insight gained from the vast amounts of research carried out in the electromagnetic regime.

2.7.3 Acoustic Impedance Gratings

Figure 2.4 is a schematic of a typical periodic structure that forms an impedance grating, allowing the existence of an ASW on its surface (who’s amplitude is also illustrated). There are a series of rigid walls spaced λ_g apart, which is the grating

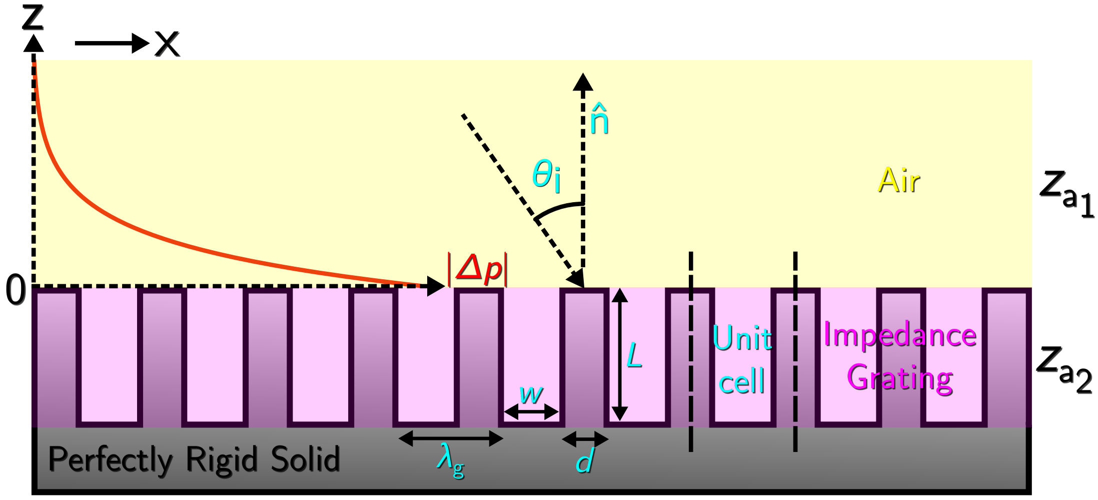

Figure 2.4: Qualitative illustration of the acoustic surface wave supported in air above a typical periodic impedance grating. The rigid solid has a series of equally spaced ridges, with dimensions as labelled. The yellow shaded region is the region of air supporting the surface wave, with specific acoustic impedance $\mathbf{z}_{\mathrm{a}1}$, while the purple shaded region represents the region of effective impedance $\mathbf{z}_{\mathrm{a}2}$ induced by the grating. A sketch of the pressure magnitude $|\Delta p|$ of such a surface wave is also included.

pitch. This is the spacing between the smallest unit of geometry that could be repeated to make the whole structure: the ‘unit-cell’ (sometimes referred to as the ‘meta-atom’ when making analogies between metamaterials and molecular crystal structures). In section 2.6, it was shown how a finite-length rigid-walled cavity of subwavelength cross-section can support Fabry-Perot like resonances with frequencies that depend on the cavity length L and the end correction term ΔL. Arranging a set of these cavities into a periodic structure as in figure 2.4 changes each cavities’ radiation impedance $\mathbf{Z}_{\mathrm{r}}$, as each cavities’ surface integral overlaps, linking them together. This leads to a modified end correction[75,76,28]; each cavity’s radiation impedance has an extra term added to its imaginary reactance x_a that is induced by the build up of diffracted evanescent modes above the surface[71]. In other words, each individual cavity acts as a resonator that is coupled to its adjacent cavities, creating an effective impedance condition, where, as the frequency approaches the cavity resonance frequency, the impedance grating’s effective imaginary reactance approaches infinity[32,28,76]. Hence, over a specific range of frequencies below the now modified Fabry-Perot-like (in reflection) resonant condition, an ASW is created having $k_{\mathrm{x}} > k_0$ and pure imaginary k_{z} above the grating, its phase seen advancing along the surface as the cavities oscillate between negative and positive pressure (see panel two in figure 2.7, described later on).

The ASWs arise from the coupling between the end effects from each individual cavity, finding solutions for which involves surface integrals that can only be solved numerically (having only approximate solutions for even the simplest scenarios such as the ‘baffled piston’ approximation, see section 2.6). Hence, one cannot simply write a general equation predicting the precise behaviour of the ASW, including its dispersion, like is possible with the electromagnetic surface-plasmon dispersion curve on a flat surface[77]. It follows that the ASWs are extremely sensitive to the shape of the resonators that form them, such as their depth, width, their relative spacing, and the lattice shape in which they are arranged (i.e. the Fourier decomposition of their surface).

Some analytic theory that expands on the theory presented in section 2.6 has been developed for the simplest open-ended slit or hole arrays[28,76], including expressions that predict the resonant condition of each coupled slit-cavity, but it is very specific to those geometries and also does not account for significant boundary layer effects (see chapter 4). Detailing it here would thus not prove particularly useful, as it would not necessarily be relevant to the various ASW-supporting geometries to be studied in this thesis. There do exist many approximate numerical methods to predict ASW behaviour, some of the most common methods being the modal-matching method that approximates diffraction effects[27,71,78] and the finite-element method that splits a geometry into small mesh elements and directly solves the necessarily field equations within them[79,80] (used throughout this thesis and covered in section 3). Still however, the models must be constructed from scratch for each specific geometry, and as such the specifics will be detailed in their relevant sections. There are some rules that grating-induced ASWs obey no matter the geometry that allow predictions to be made, to be discussed henceforth.

2.7.4 Dispersion Relations

When describing the behaviour of surface waves, it is useful to plot their ‘dispersion relation’, which is how the frequency f of a surface mode changes as a function of its wavevector along a specific surface direction, the shape of each mode being the ‘band-structure’. This sort of plot is used extensively for the discussion of the three dimensional band structure of photons or phonons interacting with periodic crystal structures[81], much of the language arising from analogies to the nearly-free electron model within ionic solids[82]. These analogies also lend themselves nicely to similar discussions with periodic meta-atoms of acoustic metamaterials[22,83], such as those that form an impedance grating.

A simplified example of a dispersion plot is shown in figure 2.5, a qualitative representation of the dispersion along positive wavevector k_x (parallel to the surface) of the ASW (whose eigenfrequencies occur at frequency denoted by the solid lines) supported on a typical, very short pitch ($\lambda_\mathrm{FP} \ll \lambda_\mathrm{g}$) one-dimensional impedance grating such as the one previously shown in figure 2.4 (for this surface and all those to be studied,

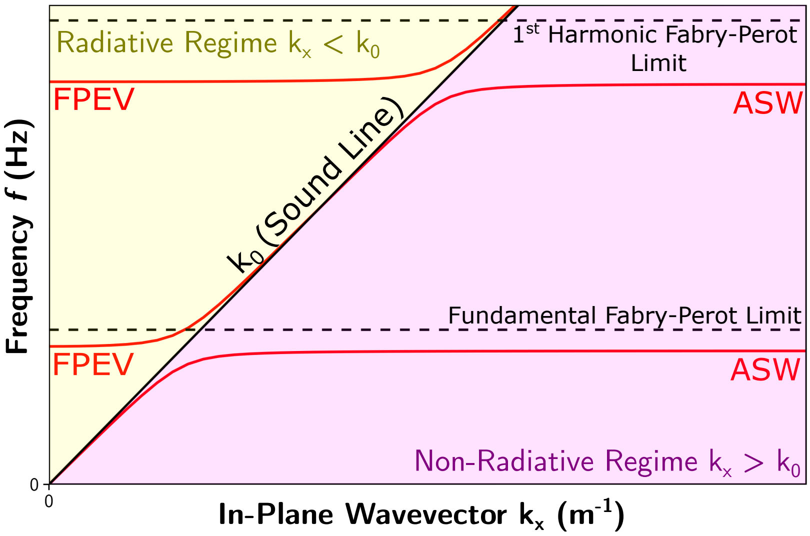
Radiative Regime $k_x < k_0$
FPEV
1st Harmonic Fabry-Perot Limit
ASW
k_0 (Sound Line)
Fundamental Fabry-Perot Limit
FPEV
ASW
Non-Radiative Regime $k_x > k_0$
0
0
Frequency f (Hz)
In-Plane Wavevector k_x (m^{-1})

Figure 2.5: Qualitative Example of a dispersion plot with important features annotated, for a typical short-pitch ($\lambda_g \ll \lambda_{FP}$) impedance grating like the one in figure 2.4. Frequency f is plotted against in-plane wavevector k_x. The solid red lines represent the behaviour of the eigenmodes of the system, including those associated with the fundamental Fabry-Perot resonance and its first harmonic. Note, the effect of the grating periodicity λ_g on the dispersion of each of the modes (other than to allow them to exist) has been neglected for simplicity.

the band-structure in negative k_x and positive k_x is symmetric about $k_x = 0$, so usually only the positive half is displayed). The ASW associated with the fundamental FP resonance and the ASW associated with the first FP harmonic are included. Also shown are the Fabry-Perot-Evanescent-Waves (FPEV), which are the grating-perturbed cavity-resonances that have interesting properties to be discussed forthwith. Note, to simplify figure 2.5 and the following discussion, the effect of the periodic structure on the mode dispersion has been omitted, and will instead be introduced in section 2.7.5.

A vital feature of dispersion relation plots is the position of the sound line $k_0 = \pm \frac{2\pi f}{c}$, the positive k_0 shown as a solid black line in figure 2.5. This is the maximum wavevector a wave that can freely propagate through space can acquire; anything with a magnitude of k_x less than the magnitude of the sound-line ($|k_x| < |k_0|$) is free to propagate, and thus this region of k-space is known as the ‘radiative regime’ (yellow shaded region in figure 2.5). In the radiative regime, if θ_i is the angle of incidence from the surface normal, then $k_x = k_0 \sin\theta_i$, hence at normal incidence $\theta_i = 0°$ and $k_x = 0$, while at ‘grazing’ incidence $\theta_i = 90°$ and $k_x = k_0$. Conversely, any magnitude of k_x greater than magnitude of the sound line ($|k_x| > |k_0|$) has too much momentum at that frequency to propagate at the speed of sound c and must have an imaginary component of k_z, hence this is known as the ‘non-radiative regime’ (purple shaded region in figure 2.5).

A mode can be described as 'dispersive' if its phase velocity $v_\mathrm{p} = \frac{2\pi f}{k}$ changes as a function of frequency, i.e., when the phase velocity is different to the group velocity $v_\mathrm{g} = 2\pi\frac{\partial f}{\partial k}$ (the gradient of any point on a dispersion curve). The ratio between the speed of sound c and the phase velocity v_p is known as the refractive index, $N = c/v_\mathrm{p}$, air being set to have a refractive index of $N = 1$. When the group and phase velocity are equal ($v_\mathrm{p} = v_\mathrm{g}$), the wave is non-dispersive.

While except in a small number of cases where analytic theory has been developed, the precise behaviour of ASWs must be numerically or experimentally determined, there are a few key patterns and features present in the dispersion of a typical ASW, highlighted by figure 2.5. Firstly, the set of Fabry-Perot-like cavity resonances that would exist in each cavity individually, without the presence of the periodic grating structure, would be visible in the radiative regime of figure 2.5 as just non-dispersive flat lines. The frequency f_FP (with corresponding wavelength λ_FP) at which this resonance occurs is predicted by equations 2.48 and 2.51 (or whatever cavity geometry is being used, e.g. a Helmholtz resonator). For a single cavity, the maximum value f_FP can take for a given cavity-length L is when there is no end-effect length-correction term ($\Delta L = 0$), which is designated as the Fabry-Perot-Limit in figure 2.5. Any cavity with a finite width has a finite end-effect, so the actual resonant frequency f_FP will always be lower than this limit. When such cavities are then placed into a periodic array, the end-effect term markedly changes (where as discussed, the impedance condition that determines the end-effect has a term added to its imaginary reactance that is induced by the diffraction effect) acting to further reduce the resonant frequency f_FP of each individual cavity at normal incidence, while forcing the collective resonance to become dispersive with a strong evanescent component. As the FP-like mode approaches the sound line, it interacts with the ASW present in the non-radiative regime (to be discussed), leading to a strong anti-crossing effect. At grazing incidence, the free radiation has a divergent density of states[84], hence after the anti-crossing interaction, the FPEV mode will lie on the sound line k_0. This radiative mode, the Fabry-Perot Evanescent-Wave (labelled FPEV) in the yellow region of figure 2.5, has the character of both a normal cavity resonance and a surface wave, its exact nature depending on the ratio between the wavelength of the cavity mode at the Fabry-Perot limit λ_FP and the grating pitch λ_g (the behaviour of this radiative mode has been a fruitful research topic[27,35,85,28] being involved in 'Enhanced Acoustic Transmission', and will be discussed in detail in section 2.7.6).

The non-radiative trapped ASW (in the purple shaded region of figure 2.5) created by the periodicity that accompanies the cavity resonances (or FPEV) will always occur at a lower energy than them, with the position of the radiative mode at normal-incidence acting as an asymptotic frequency[28]. This can be seen by restating the general equations 2.55 and 2.54. If $\mathbf{z}_{\mathrm{ag}}$ is the effective specific acoustic impedance of the grating, the wavevector along x of the ASW $k_{\mathrm{ASW_x}}$ has the form

$$k_{\mathrm{ASW_x}} = k_0\sqrt{1-\left(\frac{\rho_0 c}{\mathbf{z}_{\mathrm{ag}}}\right)^2} \tag{2.57}$$

and along k_{z}, it has form

$$k_{\mathrm{ASW_z}} = -k_0\frac{\rho_0 c}{\mathbf{z}_{\mathrm{ag}}}. \tag{2.58}$$

So, as the frequency approaches the resonance frequency, the imaginary reactance term x_{ag} in $\mathbf{z}_{\mathrm{ag}}$ approaches infinity[27,28] (neglecting the significant effect of periodicity), hence $ik_{\mathrm{ASW_z}} \to \infty$, causing $k_{\mathrm{ASW_x}} \to \infty$, which can be seen in figure 2.5: the ASW is highly confined to the surface and thus has a huge in-plane wavevector. At low frequencies away from the resonance, the effective impedance of the grating is little different to the impedance of the air (neglecting thermodynamic losses), thus the ASW sits very near the sound line ($k_{\mathrm{ASW_x}} \approx k_0$), being only loosely confined to the surface ($\mathrm{Im}(k_{\mathrm{ASW_z}}) \approx 0$) and resembling a grazing wave. After the frequency of excitation passes the fundamental FP-limit, and provided the grating pitch λ_{g} is sufficiently short (as in figure 2.5), the pattern repeats for the resonant frequency of the first harmonic ($n = 2$ or $n = 3$ depending on whether the resonant cavity is open- or closed-ended), and a second ASW with a higher limit frequency is generated. This pattern will occur for as many FP harmonics that exist below the onset of 1^{st} order diffraction at $\lambda_0 = \lambda_{\mathrm{g}}$, though as discussed next, the periodicity can significantly perturb the shape of the mode dispersion, and put a strict limit on what values $k_{\mathrm{ASW}} = \sqrt{k_{\mathrm{ASW}_\mathrm{x}}^2 + k_{\mathrm{ASW}_\mathrm{z}}^2}$ can reach.

2.7.5 The Effect of Periodicity on Acoustic Surface Waves

In the last section, to avoid introducing too many concepts at once, it was instructive to neglect the effect the grating periodicity λ_{g} has on the mode dispersion. However, this may be misleading, since the periodicity is vital in the creation of the ASW to begin with, and cannot be neglected. In the context of impedance gratings, without the periodicity to induce the diffraction effect and thus the 'springlike' reactance, there would be no measurable ASW.

The analogy of meta-atoms to atoms in crystal structure involves the use of solid-state physics terminology and concepts[82]. The periodic Bravais lattice structures that form the acoustic impedance gratings have a corresponding reciprocal space (referred to as k-space) lattice just as ionic crystal structures supporting nearly-free electrons do, and there are many concepts from e.g. Bloch theory that can be transferred accordingly.

To describe how periodicity changes electron band structure in such crystals, the nearly-free electron model is used, where a weak periodic potential is applied to the free-electron model, and changes observed[86]. The effects of periodicity are strongest at the point whenever the wavevector of the electron k corresponds to the crossing of a Bragg plane, who's positions depend on the reciprocal lattice, and differ depending on the Bravais lattice of the crystal. In one-dimension k_{x}, the first Bragg plane occurs half way between the origin of k-space and the first reciprocal lattice point k_{g} (the grating wave vector, $k_{\mathrm{g}} = \frac{2\pi}{\lambda_{\mathrm{g}}}$), and the region of k-space this covers is known as the first Brillouin zone. Hence, the first Brillouin zone is defined as extending over $-\frac{k_{\mathrm{g}}}{2} \leq k_{\mathrm{x}} \leq \frac{k_{\mathrm{g}}}{2}$. Higher n^{th} Brillouin zones represent regions of space separated by different sets of Bragg planes, so that the n^{th} Brillouin zone corresponds to a region of k-space accessible by crossing $n-1$ Bragg planes from the origin[86].

At the edge of each of the Brillouin zones, there are some key features that the periodicity imposes on the electron energy bands (which are equivalent to ASW bands on dispersion curves, swapping frequency for energy level). Since the Brillouin zone boundary represents the mid point between reciprocal lattice vectors, at this point the electron band that the periodicity has Bragg-scattered with negative group and phase velocity back from the first reciprocal lattice vector $k_{\mathrm{x}} = k_{\mathrm{g}}$ has exactly the same wavevector as the positive group and phase velocity one beginning at the origin $k_{\mathrm{x}} = 0$, and constructive interference between them means that a pair of standing waves π out of phase with each other are set up, each of course having zero group velocity. Hence, the electron band that originated at $k_{\mathrm{x}} = 0$ changes from being a continuous parabola with increasing energy and wavevector (as it would in the free electron model[86]), to having two discrete solutions: an energy band-gap is opened up, the size of which size depends on the Fourier components of the periodic potential. The physical reason for these two solutions having different energies is that their anti-nodes are concentrated in different regions of the ionic lattice that the crystal structures are formed of, thus sit in different potentials[82].

The first Brillouin zone contains all of the information necessary to construct the entirety of the band structure of the modes supported by the grating, as anything existing beyond the first Brillouin zone is diffracted back into it: the periodicity of the grating imparts momentum $\pm\, nk_{\mathrm{g}}$ to the surface modes via Bragg diffraction (with integer n denoting order of diffraction). There are three main ways to represent a band-structure with periodicity imposed. These are: the ‘repeated-zone’ scheme, where every energy (or frequency) band is drawn within every Brillouin zone, the ‘reduced-zone’ scheme, where only the first Brillouin zone is included, but with every mode ‘band-folded' back to $k_{\mathrm{x}} = 0$ via the addition or subtraction of grating wavevector $\pm\ nk_{\mathrm{g}}$, and finally, the 'extended-zone' scheme, where the band structure is extended from the origin to higher k in discrete Brillouin zone regions (i.e., without the band-folding present)[86]. In two or even three dimensional periodic structures, these band-structures have the potential to become quite complicated. All work in this thesis except for chapter 6 deals with one-dimensional periodic structures however, so these are the focus of the forthcoming explanations.

With the analogy flushed out, the discussion of the band-structure of acoustic surface waves can be resumed. An example of a repeated-zone scheme dispersion plot with the Brillouin zones included (marked with vertical dashed lines) is presented in figure 2.6. As well as the sound-lines $k_0 = \pm\ \frac{2\pi f}{c}$, there are also the diffracted sound lines $\pm\ k_0 \pm\ nk_{\mathrm{g}}$.

As the frequency of excitation approaches the resonant frequency, the grating's effective reactance x_{ag} increases, hence the ASW moves further from the sound line in k_{x} and is gradually more confined to the surface, since its imaginary component of k_{z} is rising. All the while, due to approaching the f_{FP} asymptote, the group velocity v_{g} is gradually decreasing with increasing k_{x}, until at the point of the first Brillouin zone boundary ($k_{\mathrm{x}} = \frac{k_{\mathrm{g}}}{2}$) the group velocity falls to zero, the ASW interferes with the ASW associated with diffraction from $-k_0 + k_{\mathrm{g}}$ (or vice-versa) that was propagating in the opposite direction, and a standing wave is formed over the grating surface, as expected from the crystal structure analogy (marked by blue arrows in figure 2.6). At this point, the ASW wavelength along x is exactly twice the grating periodicity λ_{g}, i.e. $\lambda_{\mathrm{ASW_x}} = 2\lambda_{\mathrm{g}}$. There is an apparent problem with the analogy however; there appears to be no higher energy standing wave solution in the non-radiative regime, as might be expected. To understand why, it is helpful to see the pressure field on such a surface at specific values of k_{x}.

Figure 2.7 is a plot of the instantaneous pressure fields Δp of the Eigenmodes at specific points on figure 2.6, with the second panel (labelled ASW) being an example of the standing wave formed at the first BZ boundary. Each cavity is oscillating π out of phase with its nearest-neighbour; at this point on the dispersion diagram the mode has wavevector $k_{\mathrm{ASW_x}} = \frac{k_{\mathrm{g}}}{2}$ and hence must have a spatial wavelength of $\lambda_{\mathrm{ASW_x}} = \lambda_{\mathrm{g}}$ (as $\lambda_{\mathrm{x}} = \frac{2\pi}{k_{\mathrm{x}}}$). This commensurate property will hold true at every Brillouin zone boundary $\pm\ n\frac{k_{\mathrm{g}}}{2}$ with increasing values of n corresponding to shorter spatial wavelengths $\frac{2\lambda_{\mathrm{g}}}{\mathrm{n}}$, where, except under special circumstances (such as periodic glide-symmetry, the topic of chapter 8) a standing wave will always form, provided the near-field has enough degrees of freedom along k_{x} to support the number of nodes and anti-nodes required (to be discussed).

As remarked, there appears to be no higher energy standing wave in the non-

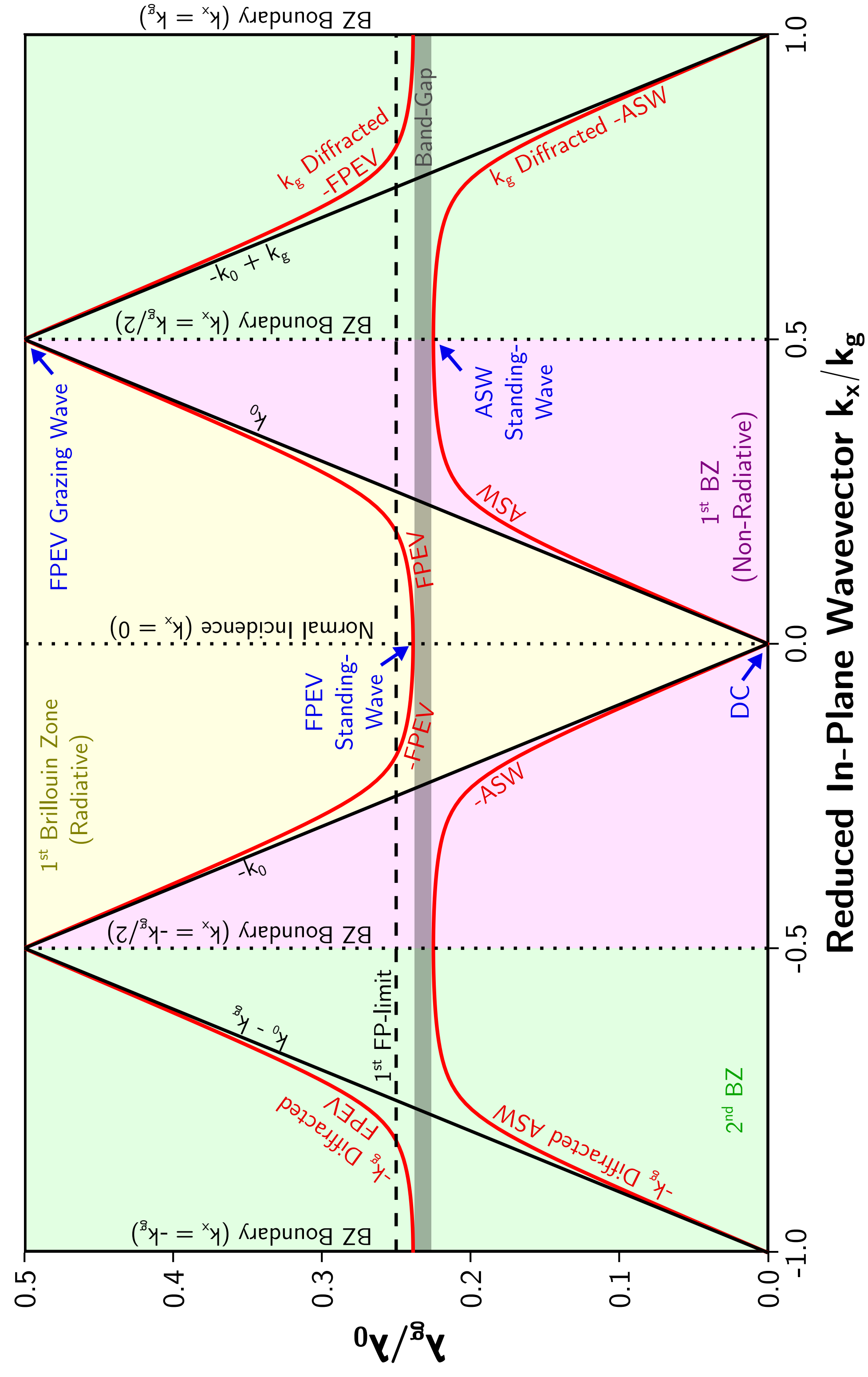

Figure 2.6: (Rotated) Example of a 'repeated-zone-scheme' dispersion plot for a typical short-pitch ($\lambda_g \ll \lambda_{FP}$) impedance grating. The ratio of grating period λ_g to free space wavelength λ_0 is plotted against reduced in-plane wavevector $\frac{k_x}{k_g}$, where $k_g = \frac{2\pi}{\lambda_g}$ is the grating wavevector. The solid red lines represent the behaviour of the Eigenmodes of the system. Only modes associated with the fundamental cavity resonance are included. The pressure field plots in figure 2.7 were calculated at points highlighted here with blue arrows and labels.

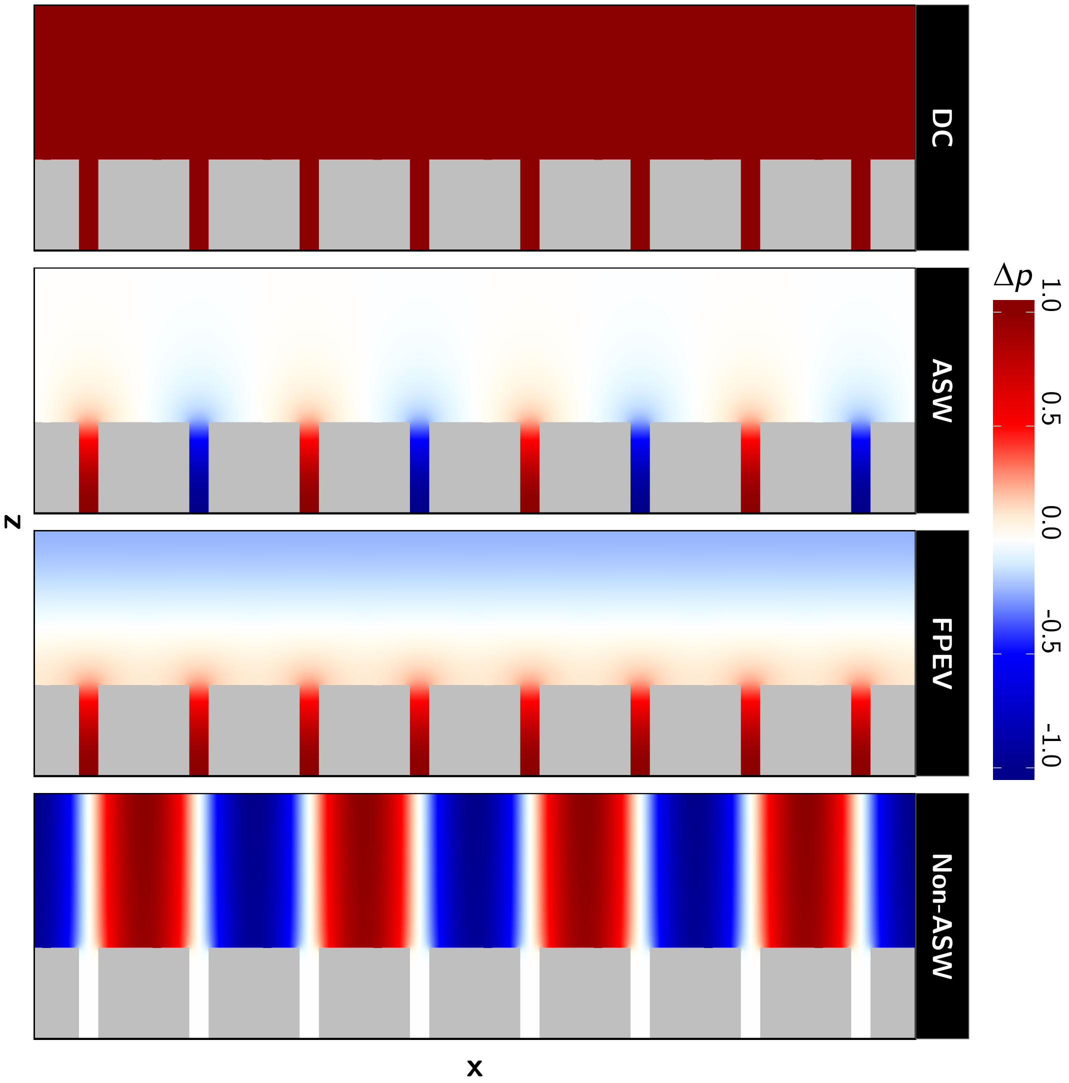

Figure 2.7: Examples of instantaneous pressure field Δp maps at four unique points on the dispersion curve of an ASW supported by a short-pitch ($\lambda_g \ll \lambda_{FP}$) impedance grating, in order of ascending frequency from top to bottom. In each case, the pressure field has been normalised to the maximum amplitude present. The top panel shows the infinitely extending fields of the DC mode, which is the ASW at normal incidence with a frequency approaching 0. The second panel shows the fields of the ASW at the first Brillouin zone boundary, $k_x = \frac{k_g}{2}$, where it has formed a standing-wave along x with $\lambda_x = 2\lambda_g$. The third panel shows the fields of the fundamental radiative cavity mode (or FPEV) at normal incidence, $k_x = 0$, also a standing-wave. The final panel shows the fields of the mode that would be the high-frequency standing-wave pair of the ASW in the second panel, also with $\lambda_x = 2\lambda_g$. This requires fields with maxima above the rigid-walls and not inside the cavities, and is thus not a trapped mode but indistinguishable from a grazing-incidence radiative wave that exists at the point where $k_0 = \frac{k_g}{2}$.

radiative regime of figure 2.6. This is due to the lack of degrees of freedom available to the near-field in such a simple grating structure, having only one cavity per unit cell, which is so narrow ($\lambda_0 \gg w$, excitation frequency is below each cavity's corresponding waveguide cut-off frequency) that on or below its fundamental FP resonance, it can only support either a positive or negative anti-node. The accompanying ASW is present only within the air, existing because of the effective impedance created by the evanescent coupling of the periodic air-filled cavities. Hence, the anti-nodes in the pressure field must be placed primarily inside the resonant cavities, as they are in panel 2 of figure 2.7, since without their excitation, there is no trapped ASW; the impedance mismatch between the solid and the air is so great that the rigid-wall approximation is applicable, which forbids the placing of the pressure fields inside the solid material that forms the cavity surface (Indeed, the rigid wall approximation is necessary for the cavities to become resonant[44]).

This is one consideration then where the electron band structure analogy breaks down. Electrons in solids are existing charges that are perturbed by the imposed ionic periodicity, whereas in acoustic impedance gratings, the periodicity creates the 'charges' (in the form of resonant cavities) to begin with, so the two concepts cannot be separated. Hence when there is only one resonator per unit cell (as in the 1D grating explained thus far), and the grating periodicity is significantly smaller than the cavity resonant frequency ($\lambda_{\text{g}} \ll \lambda_{\text{FP}}$, thus a metamaterial) the rigid boundary condition leads to a strict limit set upon the upper-branch high-energy standing wave that is paired with the low-energy one localised in and above the cavities. To be π radians out of phase with the low energy branch, the high energy branch must have fields of zero within the cavities, with maxima above the metal surface (since the maxima cannot occur within the rigid solid). Hence, the high energy standing wave cannot be a non-radiative mode, as the cavities that create the finite impedance mismatch are not excited. This high energy standing wave solution is thus 'pinned' at the frequency of the boundary between the radiative and non-radiative regimes k_0 where the density of states in the air diverges[84], effectively a grazing sound wave. Stated in terms of the electron band structure analogy, the Fourier components of the periodic potential are such that the high-energy standing wave solution at the first Brillouin zone boundary has a potential approaching infinity. This is the mode in the 4th panel of figure 2.7 labelled 'non-ASW', which is clearly not bound in the z direction. As will be shown in chapter 5, this limit can be overcome with the use of a compound grating structure, where extra 'charges' are available in the form of multiple resonant cavities per grating period, and the ASW is then able to reach higher values of k_{x}. Also note, the separation in frequency between the radiative high-energy standing-wave and the ASW standing wave at the first Brillouin zone band-edge is not a band-gap (as it would be in the nearly-free electron model), because of the FPEV at normal incidence occurring at a slightly higher energy than the low energy ASW standing wave (the separation between these two *is* however a band-gap, marked as the shaded grey region in figure 2.6).

If the grazing-wave at the first Brillouin zone is the high energy standing-wave pair of the ASW, this raises an important point about the nature of the FPEV mode that is excitable at normal incidence in the radiative regime, as this is what the high index branch evolved from at $k_{\mathrm{x}} = 0$. Thus, it is implied that the FPEV is the corresponding upper branch to the ASW that continued to increase in wavevector from the first BZ boundary at $k_{\mathrm{x}} = k_{\mathrm{g}}/2$ to the second BZ boundary at $k_{\mathrm{x}} = k_{\mathrm{g}}$, and has then been band-folded back into the first BZ. Careful inspection of the pressure fields shown in the 3rd panel of figure 2.7 that correspond to the FPEV excited at normal incidence appear to confirm this. A weak phase-shift has occurred between each cavity, satisfying the requirement to have a component of spatial wavelength of exactly $\frac{\lambda_{\mathrm{g}}}{2}$, if this mode was indeed band-folded from $k_{\mathrm{x}} = k_{\mathrm{g}}$; the ASW appears to have hybridised with the originally radiative Fabry-Perot-like mode. However, this mode can not occur in the purely non-radiative regime beyond the first Brillouin zone due to the lack of available degrees of freedom (below the fundamental FP-resonance limit), so, while being surface wave in character, it is not truly bound to the surface, and thus cannot be the upper branch of the non-radiative ASW. This dilemma is the topic of the next section.

Note, at the other extreme, as k_{x} approaches zero, figure 2.6 shows that the ASW curves back toward the sound-line, eventually lying on it and being barely distinguishable from a grazing sound wave - it becomes ‘sound-like’. At $k_{\mathrm{x}} = 0$ the mode must have infinite spatial wavelength and extend out to infinity in z from the grating surface, and this is what is illustrated in figure 2.7 labelled as the ‘DC’ mode in the 1st panel.

2.7.6 The Nature of the Radiative Fabry-Perot Evanescent-Wave (FPEV)

There is one potential cause for confusion in the discussion of ASWs induced by impedance gratings, regarding whether the ‘Enhanced Acoustic Transmission’ (EAT) phenomena, i.e. the excitation of the array cavity-resonances at normal incidence in the radiative regime, can be primarily considered a surface-wave process or a Fabry-Perot-like resonance process. This debate is highlighted in particular by the work of Hou et al.[35] and Christensen et al.[27], after the experimental observation of the phenomenon required more explanation[87].

Another way to frame the discussion is to ask whether the mode excitable at normal incidence (labelled FPEV in figure 2.6) which appears to disperse, can be considered the band-folded-from-k_{g} (thus diffracted) upper branch of the non-radiative ASW, or a resonant cavity mode that exists at normal incidence without the diffraction grating, as indeed it would. To resolve this, it is necessary to conclude that the mode is both of these mechanisms simultaneously; the cavity-resonances hybridise with the diffraction-grating-induced evanescent waves, causing the cavity resonances to become dispersive but also causing the evanescent modes to become excitable in the radiative regime (i.e., the radiation impedance term $\mathbf{Z}_{\mathrm{r}}$ that determines each cavity's resonance condition has been fundamentally altered by the periodicity[76]). If the pitch of the grating λ_{g} is short compared to the cavity depth L and thus resonant wavelength $\lambda_{\mathrm{FP}} \approx 2L$ (i.e. $\lambda_{\mathrm{g}} \ll \lambda_{\mathrm{FP}}$), then the mode is more cavity-resonance like, and if the pitch of the grating is of the order of the cavity resonance wavelength (i.e. $\lambda_{\mathrm{g}} \approx \lambda_{\mathrm{FP}}$), then the mode is more surface-wave like. Hence, the labelling of the modes as Fabry-Perot-Evanescent-Wave[35] or as 'leaky guided surface modes'[27]. Note, if $\lambda_{\mathrm{g}} \gg \lambda_{\mathrm{FP}}$, then the surface is no longer a metamaterial and is thus not relevant.

A better understanding of the nature of the FPEV can be achieved with a plot of the extended-zone scheme[86], a useful tool in the discussions of surface modes and their origin. The extended zone scheme illustrates the band-structure of the modes, but without their band-folding back into the first Brillouin zone, thereby removing the 2π degeneracy that allows modes from high k_{x} to be excited at normal incidence. Attempting to plot this for the ASW and the FPEV highlights the simultaneous nature of the FPEV as both a radiative FP-mode and a diffractively coupled ASW. This has been done in figure 2.8, which is the extended zone scheme representation of two simple acoustic impedance gratings, a short pitch grating (top, $\lambda_{\mathrm{g}} < \lambda_{\mathrm{FP}}$) and long pitch (bottom, large $\lambda_{\mathrm{g}} > \lambda_{\mathrm{FP}}$) grating.

The mode starting at $k_{\mathrm{x}} = 0$ and $\frac{\lambda_{\mathrm{g}}}{\lambda_0} = 0$ is the non-radiative ASW (red solid lines), and has the same behaviour in both long- and short-pitch gratings, though in the long pitch grating, at the first Brillouin zone boundary the ASW is much less confined to the surface than that in the short pitch one at the same point. Now, in the short-pitch grating (top panel of figure 2.8) the FPEV mode (solid blue line) is drawn originating at normal incidence in the first Brillouin zone. In this short-pitch grating the FPEV is flat-banded at small k_{x}, then strong anti-crossing with the sound-line at high k_{x} gives it a positive curvature, losing its character as a fundamental FP-resonance as it crosses the FP-limit and becomes indistinguishable from a grazing wave. The next mode beyond this would be the ASW associated with the 1st order harmonic of the cavity (green solid line). The top panel of figure 2.9, a plot of the pressure field Δp of this mode at normal incidence, appears to confirm the decision to place this FPEV mode as originating at $k_{\mathrm{x}} = 0$. The cavities are so close together in this short pitch grating that the fields above the cavity do not appear to go through the significant phase-change along x between unit-cells that a mode originating at the point $k_{\mathrm{x}} = k_{\mathrm{g}}$ would require. In other words, the evanescent component is relatively weak, and it

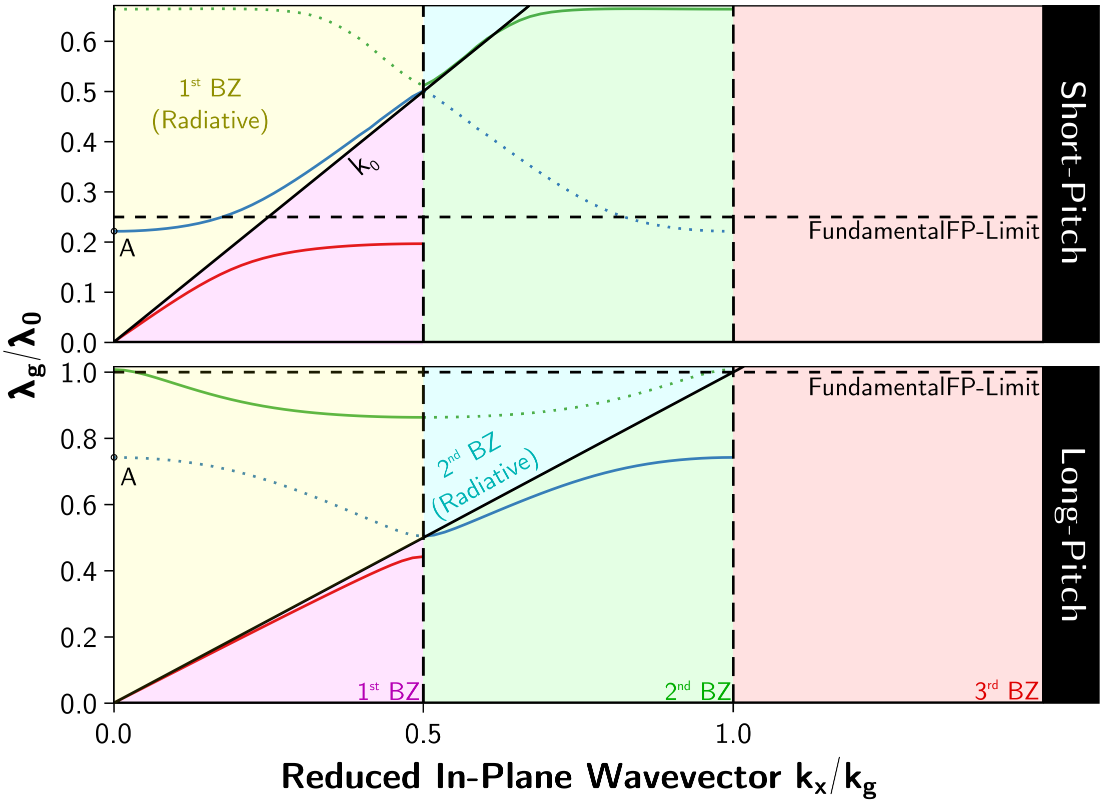

Figure 2.8: 'Extended-zone-scheme' dispersion plot for two impedance gratings, identical except for grating pitch λ_g. The ratio of grating period λ_g to free space wavelength λ_0) is plotted against reduced in-plane wavevector $\frac{k_x}{k_g}$. The top panel is a short-pitch grating, where $\lambda_g \ll \lambda_{FP}$. The bottom panel is a long pitch grating, where $\lambda_g \approx \lambda_{FP}$. In each case, The solid red line is the fully non-radiative ASW, the blue lines are the FPEV, and the green lines are the next mode who's character depends on λ_g, as explained in the main text. The dotted lines represent other viable locations to draw each mode without the band-folding, included to highlight the break-down of the analogy to the nearly-free electron model (see main text). Points marked A correspond to the pressure field plots in figure 2.9.

behaves more like an unperturbed FP-resonance.

By contrast, in the long-pitch grating, the FPEV mode appears markedly different in its character. It has a strong negative curvature that would appear to be negative dispersion if the mode did indeed originate at normal incidence (dotted blue line), where it is excitable. Inspection of its pressure field Δp at normal incidence (bottom panel of figure 2.9) reveals that there is a clear phase shift between each cavity above the solid, thus it has the character of a surface wave of wavelength $\frac{\lambda_g}{2}$ band-folded from $\pm\, k_g$ with a relatively strong evanescent component. Hence, it would make sense to draw this mode as belonging in the second Brillouin zone, which is done in figure 2.8 (solid blue line), and then in a reduced-zone scheme, band-folded back into the radiative regime via diffraction (blue dotted line): it is surface-wave-like. An extra mode below

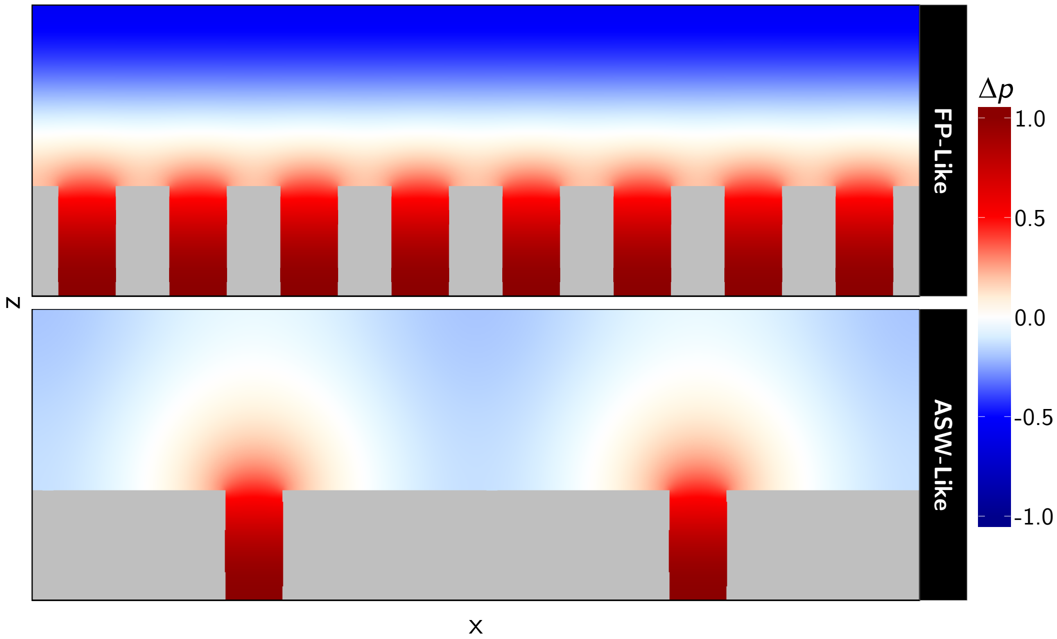

Figure 2.9: Instantaneous pressure field Δp maps of the primary FPEV modes at normal incidence $k_{\mathrm{x}} = 0$, within and above two separate impedance gratings that are identical except for grating pitch λ_{g}. (Top) A short pitch grating, $\lambda_{\mathrm{FP}} \gg \lambda_{\mathrm{g}}$, thus the FPEV is more FP-like. (Bottom) A long pitch grating, $\lambda_{\mathrm{FP}} \approx \lambda_{\mathrm{g}}$, thus the FPEV is more ASW-like. The pressure fields have been normalised to their maximum amplitude.

the fundamental FP-limit has also been drawn in the long-pitch grating that was not in the short pitch grating. This is the mode on the diffracted sound-line which the FPEV mode has anti-crossed with, now sitting on the FP-limit. As this mode approaches k_0, it begins to look like a mode associated with the 1^{st} order harmonic, just as this mode looked on the short pitch grating if numbered the same way, which has been included figure 2.8 (solid and dotted green lines). This changing character adds another element of confusion, since the different FP harmonics begin to blend into each other under heavy perturbation by a periodic grating, whereas on a short pitch grating they appear to be well defined and separate. The argument about the nature of the FPEV mode at the 1^{st} harmonic then repeats, hence the inclusion of the two possible locations of this mode (dotted and solid green lines).

Another important behaviour highlighted by the extended zone scheme representation is how beyond the first Brillouin zone (the non-radiative part of which is the only truly non-radiative regime, as nothing in this region can be diffracted back into the radiative regime), a true non-radiative mode is not supported with only one cavity per unit cell. This can only occur if there is a second resonator present (i.e. a compound grating structure, explored in chapter 5), or if the pitch of the grating is sufficiently long that the cavities can be excited near their resonant frequency and a full wavelength in x can still fit between each cavity, though this would mean that the grating was not a subwavelength one ($\lambda_{\mathrm{g}} \gg \lambda_{\mathrm{FP}}$), hence the impedance grating model would begin to fail. The fields in figure 2.9 of the long pitch grating approach this condition, which is why the FPEV is more surface-wave like, but it is still not truly a non-radiative mode. Beyond the second Brillouin zone for this one-degree-of-freedom grating, there is no feature present that appears to have a wavelength along x of a something that originated in the third or higher Brillouin zones (i.e. having $\lambda_{\mathrm{ASW_x}} < \lambda_{\mathrm{g}}/2$), while also being below the fundamental FP limit (and thus in the frequency regime in which the impedance grating could be considered subwavelength). Hence, in figure 2.9, there is simply nothing drawn in this region and beyond.

So, the conclusion to be drawn from the nature of the FPEV mode is that analogies to solid state physics used to explain acoustic metamaterials need to be viewed with caution. The existence of the ASW relies on the periodicity being in place to begin with, so to speak of a mode being perturbed by the addition of a periodicity is misleading, and care must be taken to explain the nature of each mode when a band-folding picture is used. It may even be argued that to use the extended-zone scheme representation as done above is invalid, since one can never have the ASW without the periodicity-induced band-folding present. Similar conclusions were reached by Christensen et al.[27] who remark on a fundamental difference between the oft-compared surface-plasmon-assisted phenomenon 'Extraordinary Optical Transmission' and the acoustic version (EAT through arrays of open-ended cavities): 'In the acoustic case, these modes [the FPEV modes] are not truly surface modes as the two surfaces of the plate are always connected via a propagating wave. This fact provokes that acoustic guided modes [ASWs] always hybridize strongly with the Fabry-Perot resonances associated with the hole or slit cavities'.

2.7.7 The Effect of the Marked-Space Ratio on Acoustic Surface Waves

The size of the frequency band over which the ASW evolves from the sound-line to the standing-wave condition depends on how strongly the cavities are coupled together, determined non-trivially by the geometry that creates the diffracted evanescent fields. A general rule is that periodic structure factors with a lower mark-to-space ratio will increase the coupling strength between cavities and support ASWs that curve away from the sound line in k_{x} over a broader frequency range. This behaviour is illustrated in figure 2.10, where the width of the slit-cavity w is increased in a grating of constant pitch λ_g and depth L, and the resulting change in mode shape highlighted.

For the narrowest slit (highest marked-space ratio) the cavities are only weakly

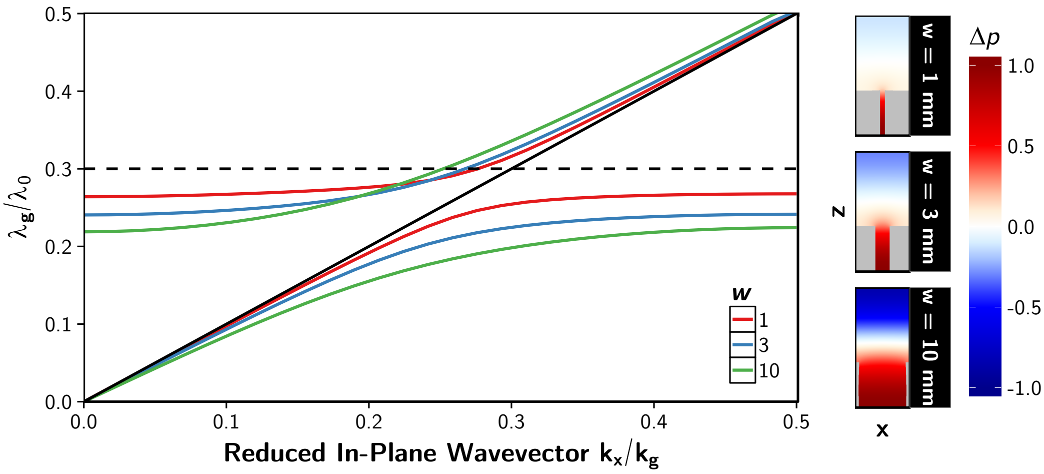

Figure 2.10: (Left) Dispersion plot of the modes supported by a typical impedance grating, as the slit-width w is varied (neglecting thermodynamic losses). The ratio of grating period $\lambda_g = 12$ mm to free space wavelength λ_0 is plotted against reduced in-plane wavevector $\frac{k_x}{k_g}$. The solid lines represent the behaviour of the Eigenmodes of the system, with different colours being different slit-widths. The dashed line is the wavelength of the fundamental FP-limit for a 10 mm deep close-ended cavity, as these are. (Right) Numerically calculated Δp field plots for one unit-cell of a $\lambda_g = 12$ mm pitch grating at normal incidence ($k_x = 0$), corresponding to the three different slit-widths presented in the left-hand figure.

coupled, and both the FPEV and ASW are mostly flat banded, the FPEV being very close to its FP-limit. For the widest slit, (lowest marked-space ratio) the FPEV and ASW are far more dispersive, the curvature of the modes being apparent over a larger frequency range. The frequency at which the FPEV occurs at normal incidence has also decreased, due to the larger end-correction ΔL arising from the increased slit-width (see section 2.6). Not shown here, is that a smaller mark-to-space ratio will also increase the level of background transmission as more of the grating is just free-space. Also, the width of each one of these frequency bands will be affected by the mark-to-space ratio in a non-trivial way, with both thermodynamic losses and diffraction losses playing a role.

2.7.8 A Note on Structures with Periodicity in Two-Dimensions (Bi-Gratings)

The shape of the first Brillouin zone and consequently all of the rest for a in two-dimensional reciprocal space (e.g. a plot of k_x vs k_y) will depend on the Bravais lattice of the metamaterial being studied[82]. For example, the Brillouin zones of resonant elements arranged in a square-lattice will have a different shape and different set of principal directions than a hexagonal or rhombic lattice. For a one-dimensional grating periodic in x, the position of the BZ boundaries is simply at every integer multiple of $k_\mathrm{x} = \frac{k_\mathrm{g}}{2}$, having no dependence on the other directions. Throughout this thesis, all but one of the periodic structures studied are one-dimensional in their periodic nature; the square-lattice structure studied in section 6 will contain more information about the Brillouin zones for a two-dimensional square-lattice. Also, in two-dimensional k-space, the sound-line takes on the form of a circle, with radius $k_0 = \sqrt{k_\mathrm{x}^2 + k_\mathrm{y}^2}$.

2.7.9 Surface Acoustic Waves

A brief note on the Surface Acoustic Wave (SAW) is necessary, to avoid confusion over the similarity of terminology, and clarify that they play no part in the Acoustic Surface Wave (ASW) mechanisms introduced.

When sound propagates through a solid, the acoustic wave equation changes dramatically[62], since as well as the longitudinal pressure waves that exist within a fluid (P-waves), there are also shear waves (S-waves) that result from the strong restoring force acting on molecules tightly bound to the solid lattice, which can be polarised. There is another special subset of trapped surface waves in solids, known as 'surface acoustic waves'. There are many types of surface acoustic wave[63], and they have long been a subject of interest, being the main cause of damage when an earthquake occurs, or being useful in Piezoelectric devices. There also have been many studies on the creation of phononic crystals, a class of metamaterials devoted to solid-based acoustics[88,83,22,89,90].

The simplest of the SAWs is the Rayleigh wave, a type of SAW that exists at the interface between an (infinite) solid and a vacuum, decaying away exponentially from the boundary into the solid, and with elliptical particle oscillations (as opposed to purely longitudinal). In this case, the vacuum actually constitutes any gas, since the interaction between the Rayleigh wave and a gas is vanishingly small; the SAW is completely confined to the solid medium. The penetration depth of a Rayleigh wave into the solid is approximately one wavelength and it travels at around 95% of the speed of the shear waves within the solid. At first glance, this sort of wave may appear similar to the surface-plasmon in electromagnetism (a form of electromagnetic surface-wave that is often compared to ASWs), but unlike the surface-plasmon, the Rayleigh wave present on the flat boundary of a solid does not have a frequency dependence or limit frequency (in an infinite system); it is non-dispersive. Also, it only decays into one medium, not both.

Another type of SAW is the Sholte wave. This wave exists between a solid-fluid interface, such as at the bottom of the ocean between sand and water. The Sholte wave decays into both media, and does have a slight frequency dependence, but only if the fluid layer has some finite depth D, and then acts as a waveguide. In the limit of an infinitely thick fluid (such as the ocean can be treated) this dependence vanishes. If the fluid layer shrinks to zero thickness, this is actually the situation described by the Rayleigh wave, hence is also non-dispersive. The Sholte wave is most similar to the surface-plasmon as it exists in both bounding media.

Thirdly, at the interface between two solids, there exists a Stoneley wave. This is the most complicated type of SAW, and decays into both solid media.

The final type of SAW is the Love wave, a type of shear wave whose particle's oscillate parallel to an interface rather than transverse to it like all of the others. It can propagate within solid layers, but also be guided by the existence of a solid-fluid interface, leading to its SAW classification.

Another key point; all of these SAWs exist when the solid is perfectly flat and of infinite depth. When finite sized solids are studied, such as separate metal slats that may make a slit-array, or large metal plates that could be drilled to make a hole array, the speed of sound in metals is so high that the infinite plane assumption usually made in the discussion of SAWs is no longer valid, and in treatment of the acoustics in the solid one must consider the many types of highly shape-dependent plate modes that the SAWs become, such as the set of Lamb waves or the flexural plate mode[91]. There are many types of these plate modes that do indeed disperse, and which may be of interest to future work regarding ASWs[92], but in none of the samples studied throughout this thesis do these modes play a role. This has been checked for each individual sample via numerical modelling.

This brief outline of the various kinds of SAW hopefully satisfy the reader that they are not relevant to the physics of the ASW studied throughout this thesis. All solids are treated as perfectly rigid, meaning that by definition the SAW cannot exist, but since this is an approximation, one might assume that the SAW does play a part, but with the severe impedance mismatch between air and the solids studied, these SAWs will not be excited with any significant amplitude. Of course if one replaces the air with water where the impedance mismatch is far less severe, several of the modes which may exist in the solid could become important.

2.8 Conclusion

In this chapter, the basic properties of an acoustic wave were introduced, including a description of the loss free acoustic wave equation that can be used to describe the majority of sound behaviour, and a detailed discussion of the treatment of thermodynamic acoustic loss mechanisms which are involved in much of the experimental work contained in this thesis. The details of how sound interacts with subwavelength rigid cavities were discussed, leading to the resonant conditions that depend on cavity geometry. Finally, trapped acoustic surface waves were introduced, and how a set of resonant cavities can be utilised to support them in a gas medium. Dispersion diagrams were explained, and the basics of the interaction of the surface waves with periodic structures summarised. A brief description of the many kinds of solid based surface acoustic wave was included. In the next chapter, the experimental methods used to measure the behaviour of these coupled acoustic resonances are covered in detail.

Chapter 3

Methods

3.1 Introduction

In this chapter, the methodology common to the acquisition of the experimental data is presented. First, the basic principles behind the acoustic-signal processing method are discussed, followed by a description of the equipment used to collect it, and the techniques used to perform each sort of measurement. Two different types of experiment are explained, one for far-field radiation measurements that can characterise transmission spectra, and one for near-field radiation measurements used to characterise the dispersion of non-radiative surface modes. Other details on e.g. sample fabrication are present, and a summary of the numerical finite element method is also included.

3.2 The Pulse Measurement Technique

To understand how the experimental samples interact with sound, their acoustic response functions must be determined. This is achieved by probing them with a range of frequencies, and comparing the resulting spectrum to a measurement made without the sample in place. One way of doing this could be to have a speaker emit a pure sine wave at a given frequency, perform the measurement with and without the sample. Then, repeat the measurement while sweeping the frequency through some defined range, thus collecting the amplitude response for a range of frequencies (Alternatively, 'white noise' or 'pink noise' measurements could be used, which radiate all audible frequencies at once, the latter containing a equal amount of energy in each). This 'continuous-wave' (CW) method would provide a measurement in the frequency-domain directly. However, this technique is not always preferable for acoustics.

For acoustic waves travelling through a gas or liquid, any solid crossing its path has such a large impedance mismatch that it will act as a mirror and almost completely reflect the acoustic wave (see section 2.5). This is a serious problem, since anything solid near the sample one wishes to characterise will generate reflections that are likely to interfere with the desired signal. At lower audible frequencies, most everyday objects will even have the sound diffract around them, which is not something that is easy to control. Even the person doing the measurement could interfere with the result. A second issue with acoustic CW measurements is that of background noise, with the typical laboratory environment bristling with life and other loud machines. Low frequency sound can penetrate walls easily, while other frequencies leak through gaps present in doors or air-vents

There are some possible solutions to both of these problems. For example, air-porous shaped foam panels are commercially available, capable of scattering the reflection of an incident sound wave into multiple directions, and absorbing some of the energy through losses within the many small air pockets that form them[93]. However, acting alone and over small surface areas, they offer only a partial improvement over the plain solid surface. A sound isolated chamber with acoustic absorber padding positioned appropriately can be much more effective, as the sound will scatter off multiple absorbing panels, losing some energy each time. However, building such an 'anechoic chamber' requires a great deal of space and may be expensive. Another potential solution is to use a device known as an impedance tube, where the sample is placed inside a tube who's acoustic response is well defined under a strict set of conditions, allowing the user to isolate the response of the sample. This piece of equipment however can be rather expensive, is limited in size and frequency range, and difficult to calibrate[94].

A much more cost effective solution is to do experiments in the time-domain, by probing the sample with an acoustic pulse. The well-known Fast-Fourier-Transform algorithm can then be utilised to extract frequency-domain information from the time-domain signal. A detailed breakdown on what this commonly used signal processing technique involves, including information on various post-processing methods, is provided in appendix A.

A short length in time corresponds to a broad range in frequency. Hence, if a signal is excited with an acoustic pulse, a broad range of frequencies are probed simultaneously. This method avoids the pitfalls of the CW method as the speed of sound in air ($\sim$ 343 ms^{-1} at Standard Temperature and Pressure[44]) is reasonably manageable; provided objects are a certain distance apart, the frequency response of a sample can be probed with a pulse, and the desired time signal recorded before any reflected signals can arrive at the detector. As mentioned in appendix A, this 'time-gating' limits our frequency resolution, but the distances required to delay the time signal reflections a sufficient amount are not so large to be insurmountable. A sample with characteristic lengths of order say 1 mm can be characterised before objects acting as mirrors greater than say 1

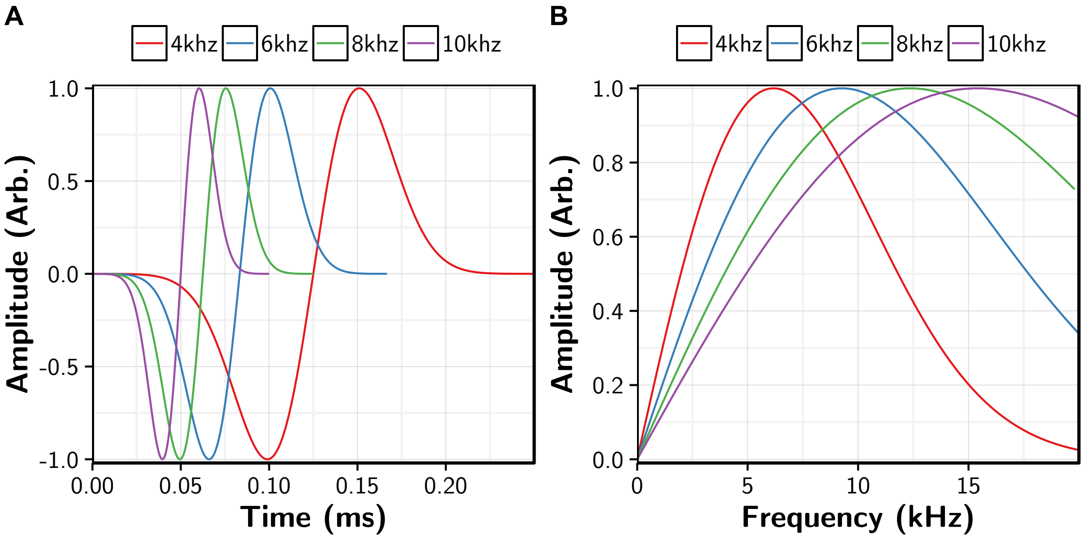

Figure 3.1: (A) Time-domain plot of 4 different Gaussian-Sine pulses, with the colours (labelled) representing different centre frequencies, from 4 − 10 kHz. (B) Frequency response (limited to the human audible range) of the Gaussian pulses in A, after zero padding has been applied. Colours correspond to those in A.

meter away can cause any problems. Another CW pitfall avoided is background noise - the pulse happens in a fraction of a second when using frequencies of order of 5 kHz, so fast that background noises are unlikely to be recorded coherently within the allotted time-window (the period of time over which a signal is recorded). Also, any random background noise that *does* cause a problem can have its effect reduced by taking the mean of multiple repetitions of the pulse. If there is a systematic background noise, such as the sound of an air conditioning unit, this unchanging signal can be accounted for either via reference signals, or by redesigning the experiment to place important features in a different frequency range. A further advantage of the acoustic pulse technique is that the speed of sound is extremely slow relative to modern electronic signal processing kits, hence relatively cheap measurement equipment provides adequate service (since the speed of light is so high, similar time-domain measurements in, for example, the electromagnetic optical spectrum, can present a formidable challenge).

An acoustic pulse can be tailored in many ways, but for the forthcoming experiments, a simple Gaussian-shaped pulse sufficed, illustrated in figure 3.1. This is the electronic pulse that is sent for the speaker to reproduce as sound, and as figure 3.1B shows, it has a broadband response with no sharp features. The 'centre frequency' of the pulse can be altered by having it occur over a shorter time span, as the different colour lines in figure 3.1A represent, allowing the experimenter some control over the amplitude distribution of the frequency spectrum. Also note that the frequency response in figure 3.1B has been limited to between 20 Hz and 20 kHz, which is the typically quoted frequency range of the human ear, a.k.a. audio[49].

3.3 Experimental Equipment

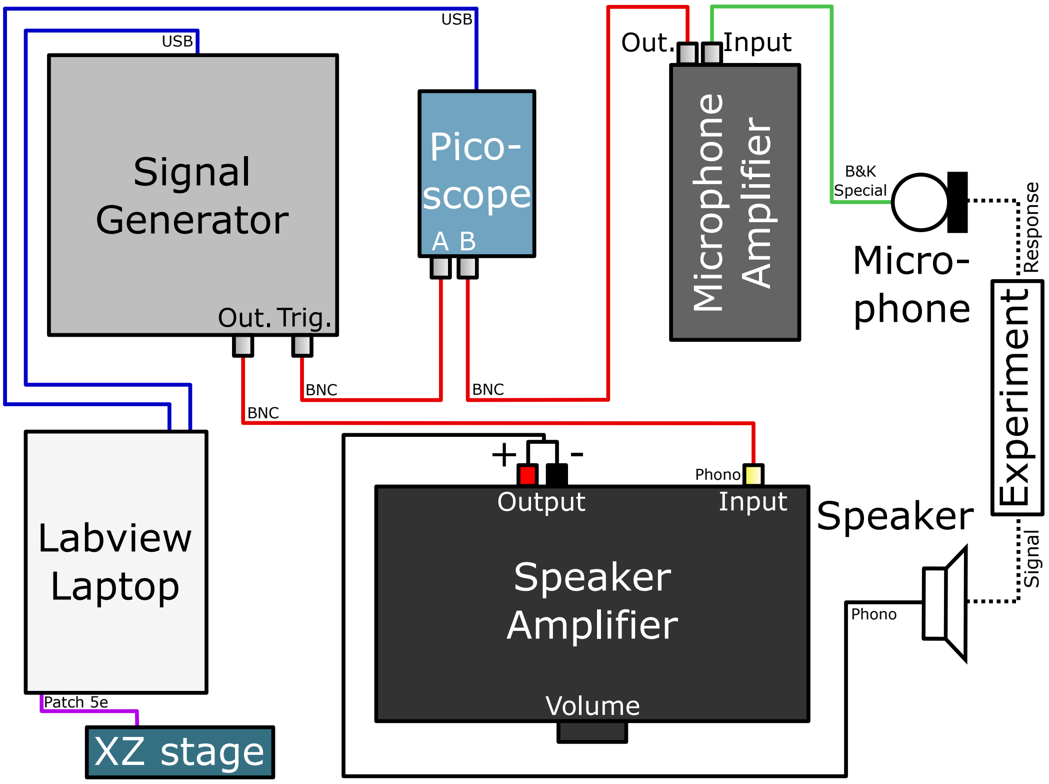
USB
USB
Signal Generator
Out.
Trig.
Pico-scope
A B
BNC
BNC
BNC
Out.
Input
Microphone Amplifier
B&K Special
Micro-phone
Response
Experiment
Signal
Labview Laptop
Patch 5e
XZ stage
+
-
Output
Phono
Input
Speaker Amplifier
Volume
Speaker
Phono

Figure 3.2: Schematic of acoustic pulse kit used to collect experimental data.

Figure 3.2 is a schematic of the equipment used to perform the pulse technique measurements throughout this thesis, with all utilised cable types and ports labelled accordingly. A laptop programmed with LabView is connected to an Agilent 3200 series signal generator, and a digital oscilloscope that is either a PicoScope 2206a series, or a PicoScope 4262 series. The signal generator is capable of generating arbitrary waveforms with frequencies in the MHz range, far beyond the kHz signals needed for audible frequency range measurements. The two PicoScopes are digital oscilloscopes that differ in their signal recording capabilities. The PicoScope 2206a has an 8 bit amplitude resolution (one part in 256), with memory allowing recording of up to 12,000 samples. The PicoScope 4262 can operate at a 16 bit resolution (one part in 65,536), and a memory that can record many millions of samples, which was necessary for the high resolution field scans of later experiments. Both PicoScopes are capable of sample frequencies that far exceed those necessary for the experiments.

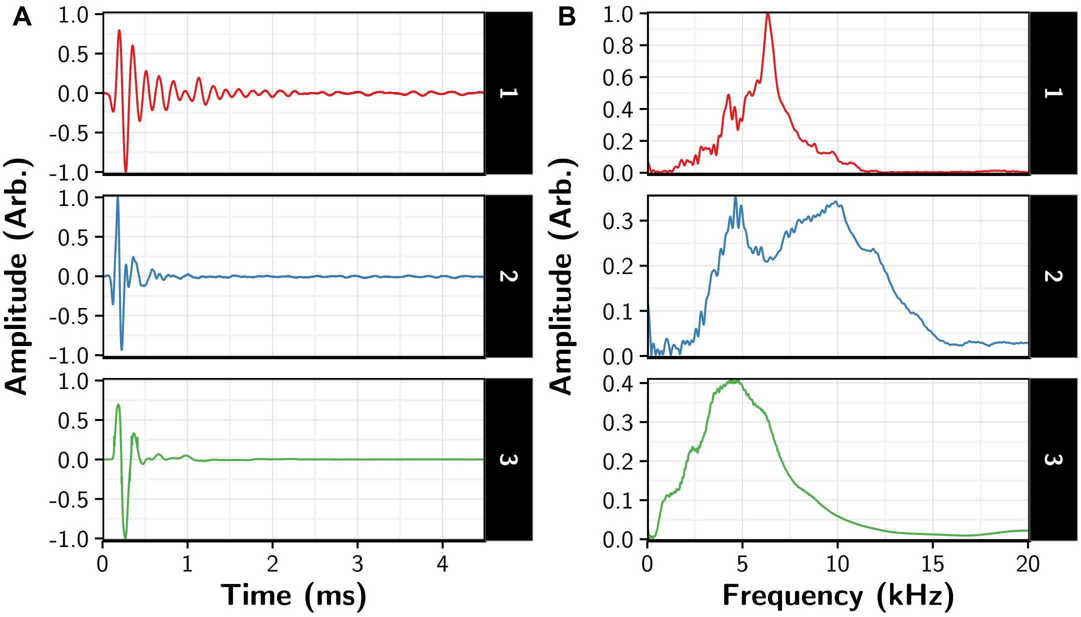

Figure 3.3: (A) Measured time-domain signals produced by three separate speakers used during data acquisition throughout this thesis, with the Gaussian pulse centred at 6 kHz. Signals are normalised to their own maximum. (B) Frequency-domain data resulting from the FFT functions applied to the signals in A, with only audible frequencies shown.

The signal generator is connected to a Cambridge Audio Topaz AM5 amplifier, which then powers one of a variety of standard speakers. As audio equipment for the reproduction of e.g. music is widely commercially available, almost any speaker will suffice, as they are designed to have a broad response with no missing audible frequencies. As such, three standard speakers available from the electronics store Maplin were utilised, chosen based on their frequency response and type of experiment performed, where ‘tweeters’ were used for the higher frequencies, and either mid-range speakers or ‘woofers’ for the lower frequency measurements. Where the approximation of a point source was very important (such as in field scan measurements, section 3.5), a tapered metal cone was attached to a ScanSpeak D3004 tweeter, which limited the sound produced through a 1 mm radius aperture without changing the response function of the speaker significantly enough to change the result of any relevant measurements (as was confirmed). Examples of some of a typical speaker’s response functions are in figure 3.3, measured via direct transmission of a Gaussian pulse signal from speaker to microphone. It is clear from the time signals that some of the speakers ring longer than others after the initial pulse is sent (the difference in time signals from the speakers labelled 1 and 2 in figure 3.3 is very significant), and this causes them to have a narrowed frequency response. Most importantly in all cases however, is that the signal strength does not wildly oscillate between very low and high amplitudes across the frequency ranges of interest, hence any local minima can be easy normalised out. The effect of changing the centre frequency of the Gaussian pulse (as in figure 3.1) on a given speaker's response function is shown in figure 3.4. A lower quality speaker is shown here to illustrate that changing the centre frequency does not simply shift the frequency response; the shape changes because the speaker may have internal resonances that will ring more loudly when being driven by some frequencies than by others. This is most clear with the 2 kHz signal in figure 3.4, where some sort of harmonic appears in the frequency response at $\sim$ 7 kHz that does not appear when driven at 3 or 4 kHz centre frequencies. Generally, the better a speaker's quality the less this is a problem, and in any case, a normalisation technique involving reference signals made the non-flat response a non-issue (to be discussed forthwith). Note, the amplifier also has a response function, but this is linear, stays constant between measurements and is thus also accounted for with a reference signal normalisation, so long as the voltage is not so high that it causes the speaker to deform and produce non-linear behaviour. This is tested by increasing the voltage output until the produced time pulse starts to change shape rather than just scale in amplitude (it is also strikingly obvious to the human ear when this change occurs).

The speaker's emitted signal is recorded via one of either two microphones. For all transmission measurements (section 3.4), the Brüel and Kjær type 4190 microphone was used, whereas for all field scan measurements (section 3.5), the Brüel and Kjær type 4182 probe microphone was used (see figure 3.5). Both microphones were necessary as they have different specifications. The type 4190 microphone specialises in sensitivity, allowing the accurate recording of very small amplitude signals that transmit through some of the samples. However, this microphone has a relatively large, 1 cm diameter aperture, which can significantly perturb near-field scans (see section 3.5), as the hard surface of the microphone acts as a mirror to sound. It also provides poor spatial resolution. The type 4182 probe microphone has a very small aperture protruding from a long metal tube (which can be interchanged with others of varying length), keeping the body of the microphone far away from the near field and recording near field signals without disrupting them significantly, solving this problem at the expense of sensitivity, which is sufficient for near-field signals but making it undesirable for use in far-field measurements (see section 3.4). The response function of both high quality microphones is flat up to around 5 kHz, but then rapidly diminishes as the frequency is increased, as can be seen in the supplied documentation, scans of which are provided in figures 3.6 and 3.7 for reference. In practise, it was found that useful data could be recorded up to around 30 kHz. Both of these microphones are connected to a Brüel and Kjær type 2690-A Nexus amplifier, allowing the user to adjust the sensitivity of the microphones accordingly with a negligible effect on their response function.

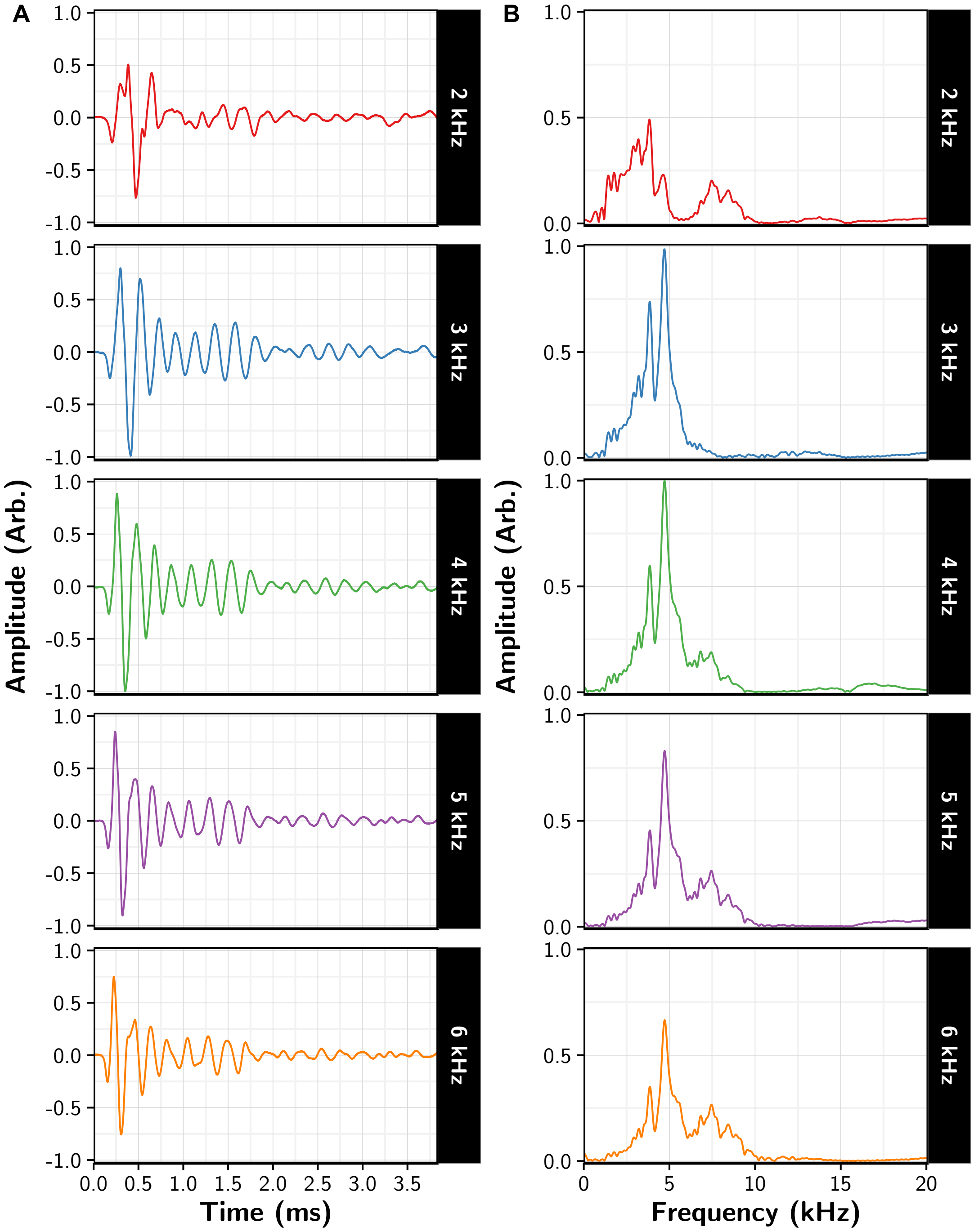

Figure 3.4: (A) Measured time-domain signals produced by a single speaker, driven by a Gaussian pulse centered at various frequencies, labelled accordingly. Amplitudes are normalised to the same number to allow cross comparison, which was the maximum value found in the present signals. (B) Frequency-domain data resulting from the FFT functions applied to the signals in A (after zero-padding), with only audible frequencies shown.

Helix
OXFORD
Shatter Resistant
1 cm

(a) Speaker drivers of different sizes, placed near a ruler for scale

(b) Makeshift point source, consisting of a metallic cone attached to a tweeter and covered in blutac to reduce signal leakage

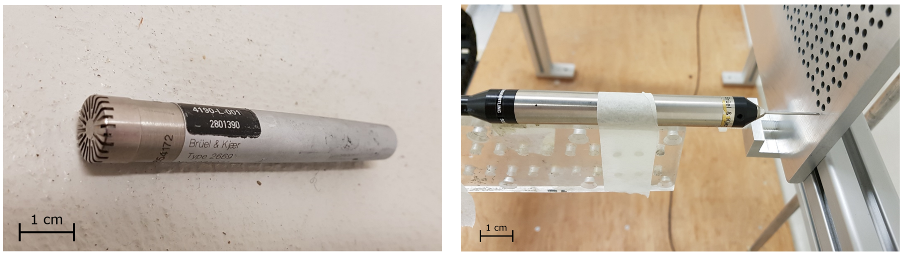

(c) Brüel and Kjær type 4190 microphone, used in transmission measurements

(d) Brüel and Kjær type 4190 microphone, used in transmission measurements

Figure 3.5: Photographs of the sources and detectors used throughout experimental measurements, labelled accordingly.

The microphone amplifier amplifies the microphone's detected pressure fluctuations (converted to an electrical signal via an internal actuator, whose response for the type 4190 microphone is also shown in figure 3.6, but was not shown separately in the equivalent documentation for the type 4182 probe microphone) and sends it to the connected digital oscilloscope (either a PicoScope 4262 or PicoScope 2206a) that can then sample that signal for use in an FFT algorithm. To make sure that the oscilloscope's recording of time is synchronised to the pulse emission, it is connected to the signal generator, which produces a rectangular 'trigger' pulse that signals to the oscilloscope that the Gaussian pulse is about to be emitted. The time accuracy with which the oscilloscope can detect that trigger pulse is determined by the sample frequency. For consistency across measurements, it may be necessary to increase this to its maximum value to ensure that all recorded pulses start measuring from as consistent a point in time as possible, then discard surplus points after measurement. This is not an issue for far-field measurements, which only record a time signal arriving at a single position in

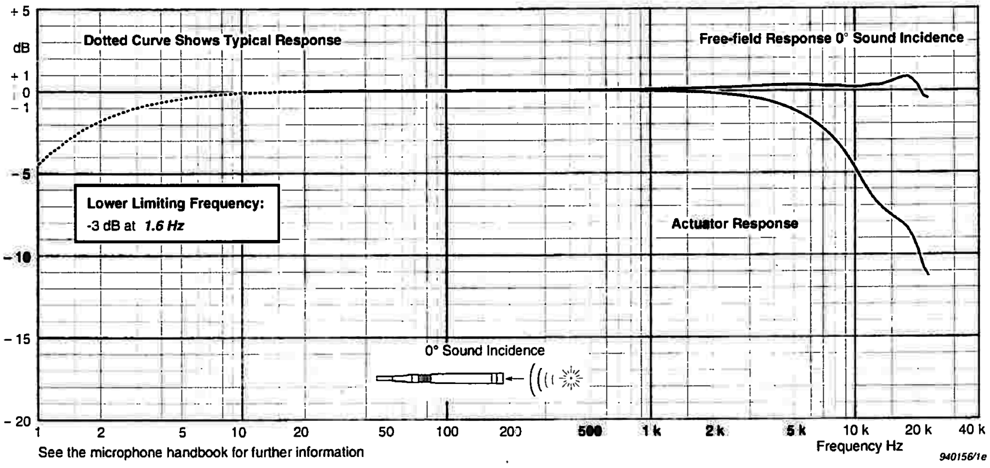

Figure 3.6: Frequency response function of the Brüel and Kjær type 4190 microphone calibrated at standard temperature and pressure, obtained from the supplied documentation. The actuator response is that of the internal mechanism that converts the diaphragm's free field pressure response to an electrical signal.

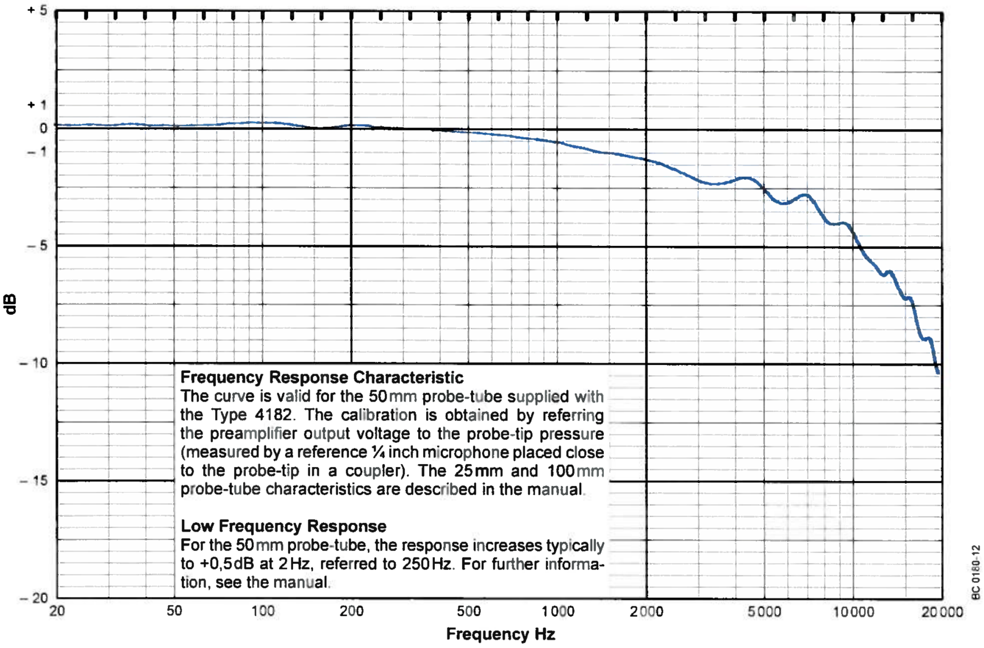

Frequency Response Characteristic
The curve is valid for the 50mm probe-tube supplied with the Type 4182. The calibration is obtained by referring the preamplifier output voltage to the probe-tip pressure (measured by a reference ¼ inch microphone placed close to the probe-tip in a coupler). The 25mm and 100mm probe-tube characteristics are described in the manual.

Low Frequency Response
For the 50mm probe-tube, the response increases typically to +0,5dB at 2Hz, referred to 250Hz. For further information, see the manual.

Figure 3.7: Frequency response function of the Brüel and Kjær type 4182 probe microphone calibrated at standard temperature and pressure, obtained from the supplied documentation, after the actuator has converted the pressure response of the diaphragm to an electrical signal.

space (with no phase information, only amplitude), but it is necessary for the near-field measurements, since the time signals must be synchronised to each other as the microphone is scanned across a coordinate grid from which phase information can be determined. This sample rate setting and many others, such as voltage, bit-rate and number of samples recorded are all controlled via the Labview program. In particular, the sample frequency is set based on what is labelled by the digital oscilloscope's brand PicoScope as the 'timebase', an integer value with a minimum value of zero (highest sample frequency). The equation that converts this number to a sample frequency and allows the user to determine their time axis (hence frequency axis) depends on both the model of the PicoScope, the bit-rate used, and the value of the timebase itself. Tables for this information can be found in the programmers documentation[95]. The LabView code also controls the signal generator, with parameters such as centre frequency, pulse rate, pulse shape and pulse amplitude being set within the code.

3.4 Transmission Measurements

As has been alluded to already, there are two main types of experiment performed throughout this thesis. The first one involves measurements where sound is projected onto some sample, transmitted through it, then recorded on the other side. By comparison to a signal recorded with no sample in place, the transmission spectra of the sample in question can be obtained. These transmission measurements concern the far-field radiation component, i.e. the 'radiative-regime' (see section 2.7), where sound interacting with the sample can couple to modes of the structure, and then re-radiate into free-space.

Specifically, a sample will be set up such that a speaker and microphone are directly or indirectly transmitting to each other, and the sample placed in the beam path, so that to a good approximation, only signals that travelled through the sample are recorded by the microphone. The specifics of how this sample is mounted and what kind of wave (e.g. planar) was used to probe it change significantly depending on the experiment and so will be detailed in the relevant chapters (these are chapters 4 and 5). However, with the sample in place, the underlying method is identical for both.

A Gaussian pulse such as those in section 3.2 is sent to the speaker, which will then produce a pressure wave containing a broad range of frequencies, designed to have most amplitude in the frequency spectrum of interest. This signal interacts with the sample, is transmitted through it, and the resulting pressure signal recorded by the microphone at a point in space. To improve the signal to noise ratio, this pulse measurement is recorded at least 60 times (although this could increase to ~ 1000 for some of the more sensitive measurements), with the mean amplitude for each time

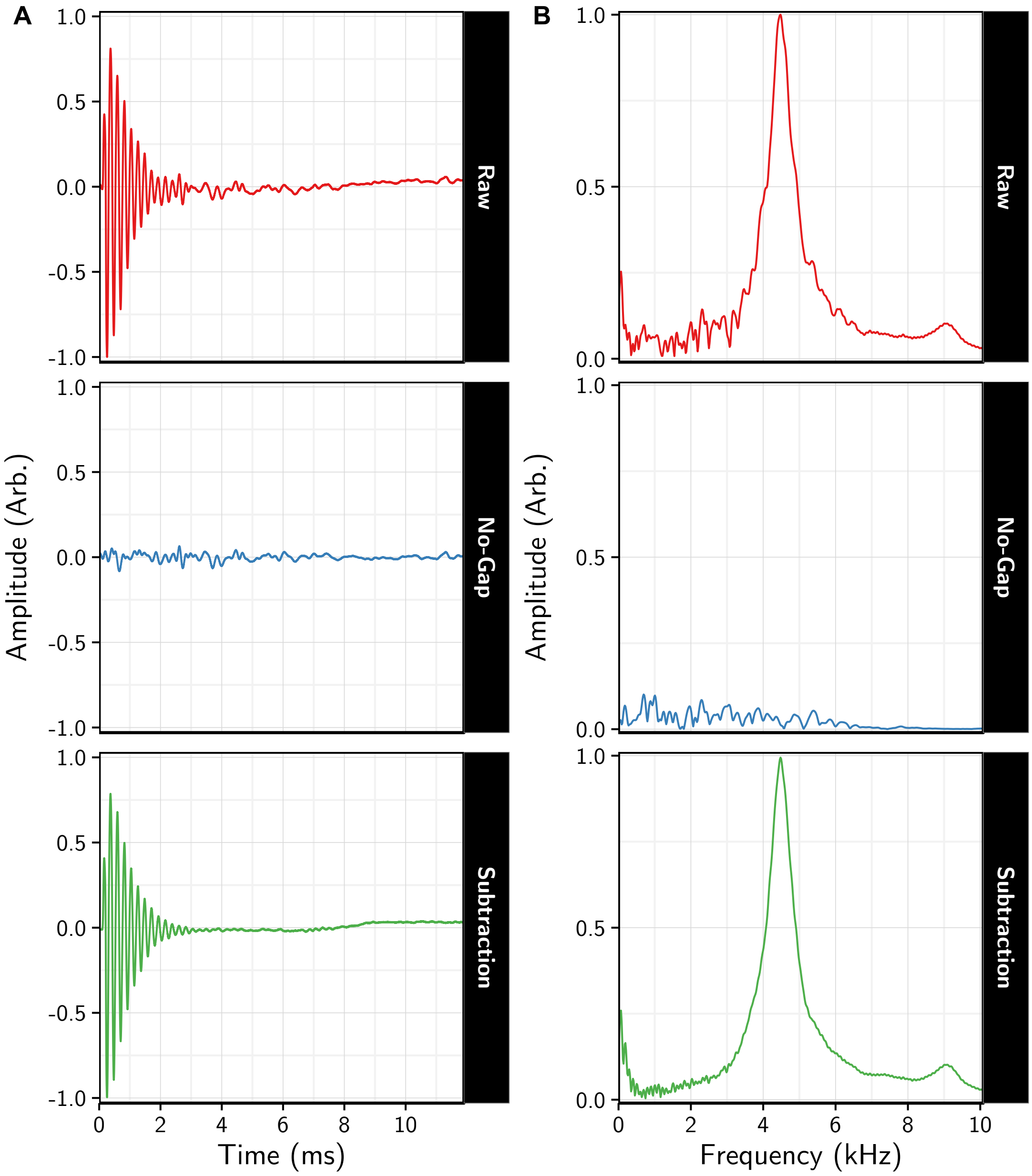

Figure 3.8: (A) Example of a time-domain pulse signal measured during an experiment, in this case the transmission through a 0.5 mm width slit-cavity, as will be explained in chapter 4. Red, Green and Blue lines represent the raw signal data, the 'no-gap' signal, and the signal resulting from the 'no-gap subtraction' technique. (B) Frequency-domain data resulting from the FFT functions applied to the separate signals in A, with only audible frequencies shown. All signals have been normalised to the speaker response function (see figure 3.3).

coordinate taken as the final time-domain signal. This signal is passed to the FFT algorithm, and a frequency spectrum obtained. Then, the sample is removed, and the experiment is repeated, to provide reference spectra such as those in figure 3.3. The two signals are normalised to the same measurement voltage and then the sample signal is divided by the reference signal, accounting for the (linear) response of the experimental circuit. Note, the sensitivity of the oscilloscope may need to change to maximise amplitude resolution if the sample only transmits a small amount compared to the reference, a particularly common issue with the 8-bit amplitude resolution of the PicoScope 2206a, but this is trivial to account for when performing the normalisation. This reference normalisation technique nearly isolates the transmission spectrum, but is not perfect, as not all sound transmitted through the sample may come from where it was intended. To correct for this problem, a ‘No-gap’ subtraction technique is used.

3.4.1 No-gap Subtraction

When the sample is in place, it is assumed the signal transmitted through it dominates the signal reaching the microphone. However, sound can travel through any gap with sound hard walls (section 2.6), and diffract around or reflect off of any solid object, so there will be extra signal transmitted from imperfections present in the set up that may interfere with the measurement. This is particularly true when the transmission spectra is expected to be weak, such as when measuring transmission through narrow slit-cavities in chapter 4, or at high angles of incidence when recording angle dependent spectra in chapter 5. A simple technique can be employed to correct for most of this.

With the ‘no-gap’ subtraction, the experimenter can isolate the transmission through the intended part of the sample from the unwanted transmission. To achieve this, the intended transmitting area of the sample face is covered in a sound hard material that fits its shape perfectly, and that sound hard material is covered in specialised sound absorbing foam to minimise reflection. This is done on both incident and transmitting sides. Then, the pulse measurement is repeated, and any signal that is being transmitted to the microphone must come from somewhere other than through the sample. While it is desirable to find and reduce the sources of this signal, it is not always possible to completely eliminate them. Instead, the extra signal can be isolated and subtracted (in the time-domain) from the transmitted signal intended for analysis, and thus leaving behind only what was transmitted through the area that was covered up. This method works very well, particularly when the transmitted signal is weak, as shown in figure 3.8, an example of each of the component signals and their frequency spectra. In this case, transmission through a 0.5 mm wide single slit-cavity was being measured (see chapter 4), and it is clear that the isolated no-gap signal is having a significant effect on the recorded frequency spectra, since when it is subtracted, the signal becomes a smooth peak with a significant reduction in noise.

3.5 Surface Wave Measurements

The latter half of this thesis, chapters 6, 7 and 8, concerns the characterisation of acoustic-surface-waves (ASWs), outlined in section 2.7. Briefly, these are sound waves that possess too much momentum to propagate away from the sample's surface (i.e. are in the non-radiative regime), and are thus 'trapped', evanescently decaying away from the surface normal. They arise from near-field diffractive coupling between acoustic resonators, such as periodically arranged open-ended hard-walled cavities. The far-field measurement techniques are thus of no use, since with this method only modes which can couple to free-space waves (i.e. the radiative regime) will be detected. Instead, a near-field measurement technique must be used, which will allow the recording of information present in the non-radiative regime. To achieve this, both a speaker source and a probe microphone must be placed very close to the sample surface, to both evanescently excite and detect the ASWs with as good a signal-to-noise ratio as possible. Directly measured ASWs will be characterised via their dispersion in k-space rather than their effect on the transmission coefficient, and to do this it is important to measure accurately how the near-field varies across the sample surface, thereby providing a 2D pressure field 'map'. In this section, each part of this process is explained in detail. Unlike the far-field measurements, all of the near-field measurements in this thesis use the same set-up, and will be fully described here.

3.5.1 XZ Translation Stage

To create the required 2D pressure field maps, the Brüel and Kjær type 4182 microphone probes the pressure field at a range of points in some grid. A specially designed XY translation stage has been built to this end, and is illustrated in 3.9 (a real photo of the probe microphone aligned to a sample is provided in figure 3.5d). There are two precision stepper motors, one that drives the track of the two horizontal arms and thus the x position of the probe microphone, and one that controls the track of the vertical y arm, which has the probe microphone attached. Each of these motors are capable of driving ~ 5 μm steps, over a maximum area of 640×640 mm. The probe microphone has an aperture of ~ 1 mm diameter, and the sample is aligned so that this aperture is within 1 mm of the sample surface. The stepper motors can be programmed to move in a grid of specified coordinates, such as a standard Cartesian grid, or a grid based on the polar coordinates r and θ. The narrowest end of the source (not shown in

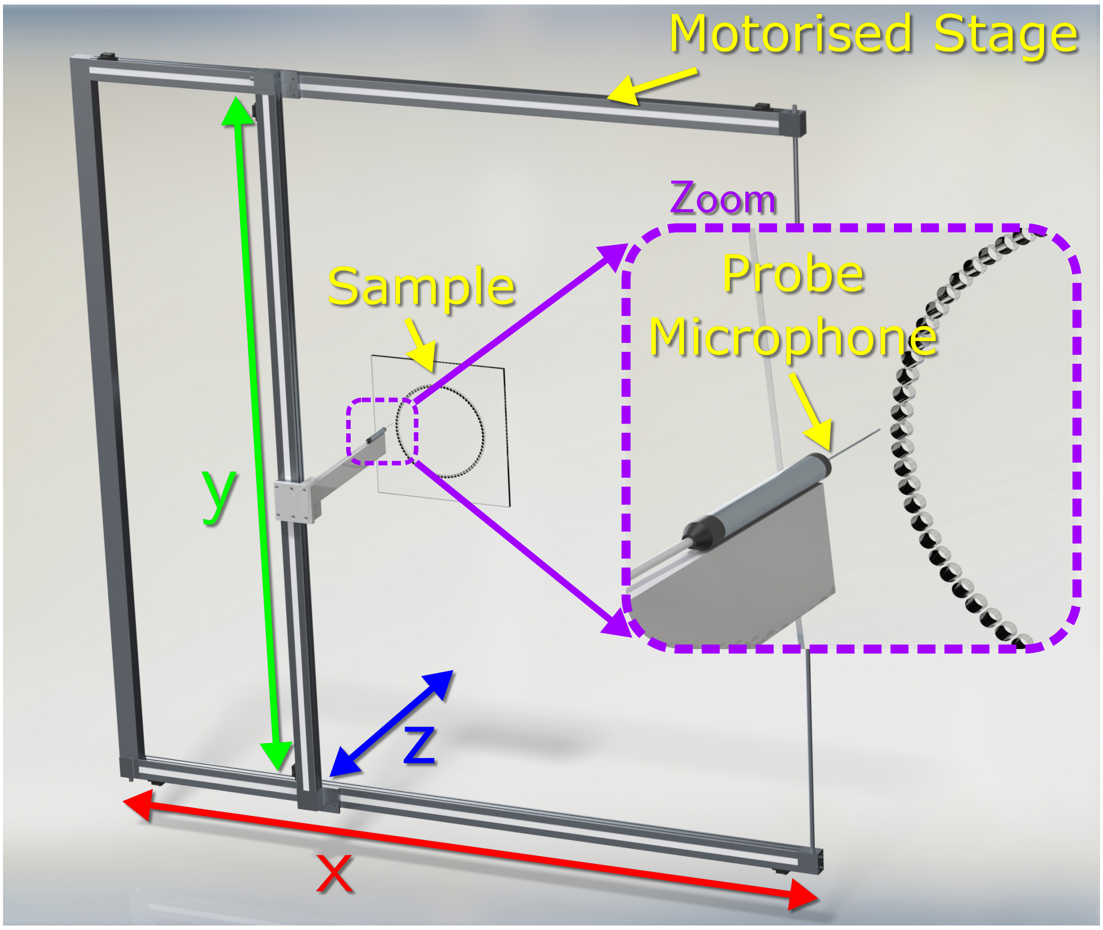

Figure 3.9: Schematic of the XY translation stage, with the probe microphone attached and an open-ended hole sample in place. The end of the source (not shown) is placed inside one of the resonators, according to the sample type.

figure 3.9, but a real photo is provided in figure 3.5b) is placed behind the sample on the opposite side of the scanning face inside one of the sample's cavities. This way it minimises free-space radiation direct through the air to the detector, it strongly excites the first cavity resonance, and also it does not impede the probe microphone's scanning path. In samples with close-ended holes this is not possible, so the source was instead placed at one of the sample ends with the normal of the speaker's aperture parallel to the sample's surface (i.e. pointing along the same direction as the excited ASW's in-plane wavevector, usually k_{x}). The sample itself is held in place with either a series of simple clamp stands, or a specially designed frame. In each case, it is important that the sample's xy plane is aligned to the grid that will be scanned by the translation stage, and also that the distance in z from the probe microphone to the sample is kept constant and less than 1 mm (this will be affected by variations in sample thickness and by it not being perfectly flat, but in negligible amounts).

With the sample, source and microphone in place and the scanning size and resolution chosen, the sample can be probed in a method similar to that used for the far-field measurements. The source emits a Gaussian pulse containing a broad range of frequencies (as before), which will excite the ASW to be characterised. The microphone is then moved to the next point on the grid, and the pulse measurement repeated. This process continues until the time-domain pulse has been recorded at every position in the specified grid. To reduce background noise, the mean of multiple pulses can be combined at each position, although the strength of the acoustic near-field is so great near the source that this is a small problem. It is a bigger problem at larger distances from the source, but this signal has proportionally less effect on the calculated dispersion of the ASW.

3.5.2 2D Pressure Field Maps

With the time-domain data collected, it is then be combined into one file and plotted as a function of position. This allows the creation of an animation in time that shows how the pressure field propagated over the sample. Sadly, interactive paper does not exist as I write this in 2017, so these often revealing animations can only be shown as part of online supplementary material. What is possible however, is show the evolution of the pulse with a select few time snapshots, or perhaps more usefully, perform a time-to-frequency FFT (see appendix A) for the signal at each point, hence producing a picture of the pressure field at a given frequency. An example of this sort of plot for the sample used in chapter 6 is shown in figure 3.10, where features such as cavity resonators are clearly visible in the oscillation of pressure amplitude. It is also possible to animate a full phase cycle at each frequency - it is not known if the waves are travelling forward or backward at each individually recorded point since the absolute phase information was not included in the time signal, but how the signal changed relative to the adjacent points is known, providing relative phase information in the chosen coordinate grid.

While inspection of the near-field pressure plots can prove useful for understanding how an ASW behaves, it is not very good for actually quantifying the behaviour, since there are so many waves with different wave momenta (or wave number/vector $k = \frac{2\pi}{\lambda}$) superimposed on each other. To do this, the dispersion of the ASW is explored, which is a measure of how the wave vector of a mode in a specified direction changes with frequency (dispersion relations are explained in detail in section 2.7.4). To obtain this information one transfers from the real-space domain of meters and unit cells, to the reciprocal-space (or k-space) domain of m^{-1} and Brillouin zones. This is achieved via the spatial fast Fourier transform, or 2D FFT. As with the 1D time-to-frequency FFT, the signal processing techniques involved are well known, though some details on the

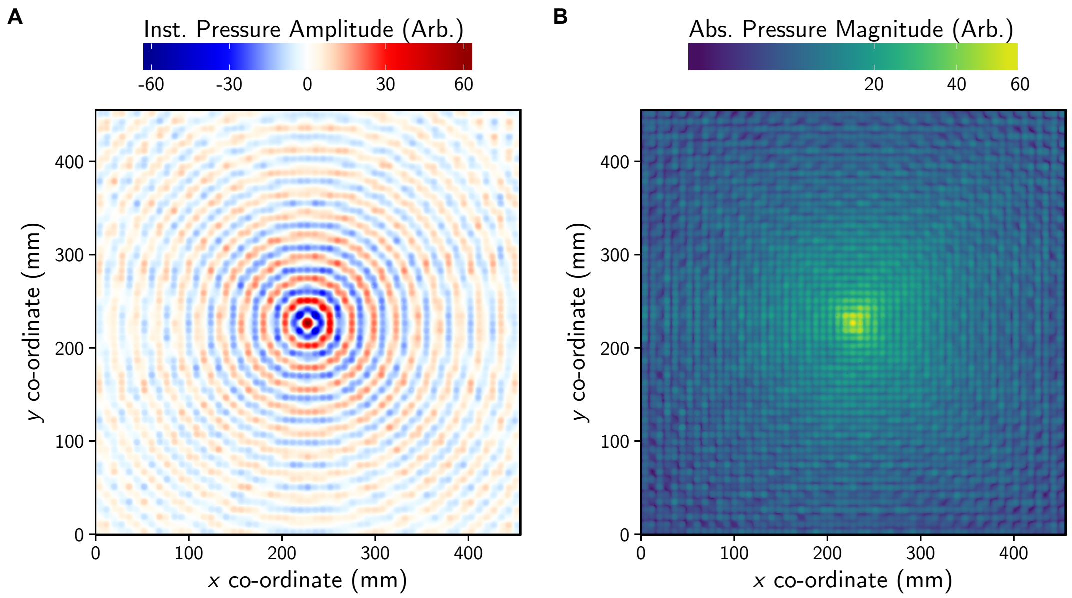

Figure 3.10: Examples of the frequency-domain data that can be acquired using the XY stage method outlined in the text. The sample used is the square lattice of open-ended holes from chapter 6, at frequency 11.65 kHz. Three different variables are plotted as a function of position. (A) Instantaneous pressure field amplitude Δp at a temporal phase, (B) Absolute pressure field magnitude $|\Delta p|$.

2D spatial FFT process are included in appendix B. An example of the result of such a technique is shown in figure 3.11.

3.5.3 Extracting Dispersion Relations

While examining the reciprocal-space images for individual frequencies is revealing, it is often more useful to plot the dispersion relation which, as described in section 2.7.4, looks at a cross-section in frequency of the Fourier magnitude of a specific plane in reciprocal-space. Once all of the reciprocal-space FFTs have been calculated, this is a simple task, as no new number crunching is required. A range of k coordinates are chosen, such as along k_x when $k_\mathrm{y} = 0$, and then the Fourier magnitude at each k is plotted as a function of frequency. An example of the result of this process is shown in figure 3.12. These plots are useful in that they allow one to visualise the band structure of an ASW, which has the many benefits described in section 2.7.4.

The aformentioned method of spatial field characterization has been undertaken in the electromagnetic case[96,97] and also recently in the solid-acoustics case by Otsuka et al.[98] who used an ultra-fast imaging technique to measure acoustic pulses propagating through two dimensional phononic crystals, hence directly visualising the present surface acoustic waves (section 2.7.9).

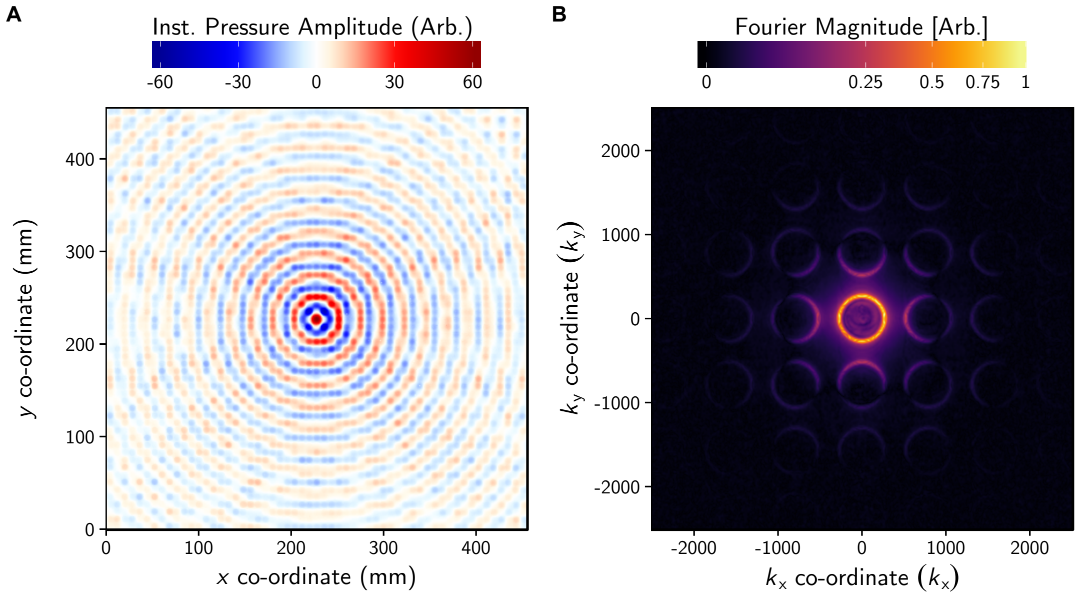

Figure 3.11: Example of the use of a 2D Spatial FFT on a real dataset acquired using the XY stage method outlined in the text. The sample used is the square lattice of open-ended holes from chapter 6, at a frequency of 11.65 kHz. (A) Instantaneous pressure field Δp, plotted as a function of real space coordinates x and y. (B) Result of the 2D FFT algorithm applied to the complex data in A, after the FFT-shift function has been applied. Fourier magnitude is plotted as a function of k-space coordinates k_{x} and k_{y}.

3.5.4 A Note on Colour Scales

Throughout this thesis, there are many data sets with three variables of interest that are plotted as a colour map imposed on a two-dimensional grid. There are two types of colour scale employed. For colour scales that oscillate about zero, such as any pressure field amplitude plot (e.g. figure 3.10A), a smooth transition from blue to red is used, with zero represented by white. This allows the reader to quickly determine the shape of the wavefronts and the position of nodes, reducing the potential for illusions created by sharp changes in colour, which is a common problem with the commonly used 'jet' colour scheme that does not account for the frequency response of the human eye, and has some arbitrary colour at the mid-point. The second type of colour scale involves any variable that starts at zero, such as the pressure magnitude (e.g. 3.10C) or Fourier magnitude (e.g. 3.12). These plots make use of the R viridis package[99], which contain colour scales designed to be perceptually uniform to the average human eye, both in colour and brightness. Combined with the use of a square root function applied to the scaling designation to prevent the brightest features 'washing out' the weakest features (except where absolute magnitude is important, such as in the transmissivity plots of chapter 5), maximum detail is presented to the reader.

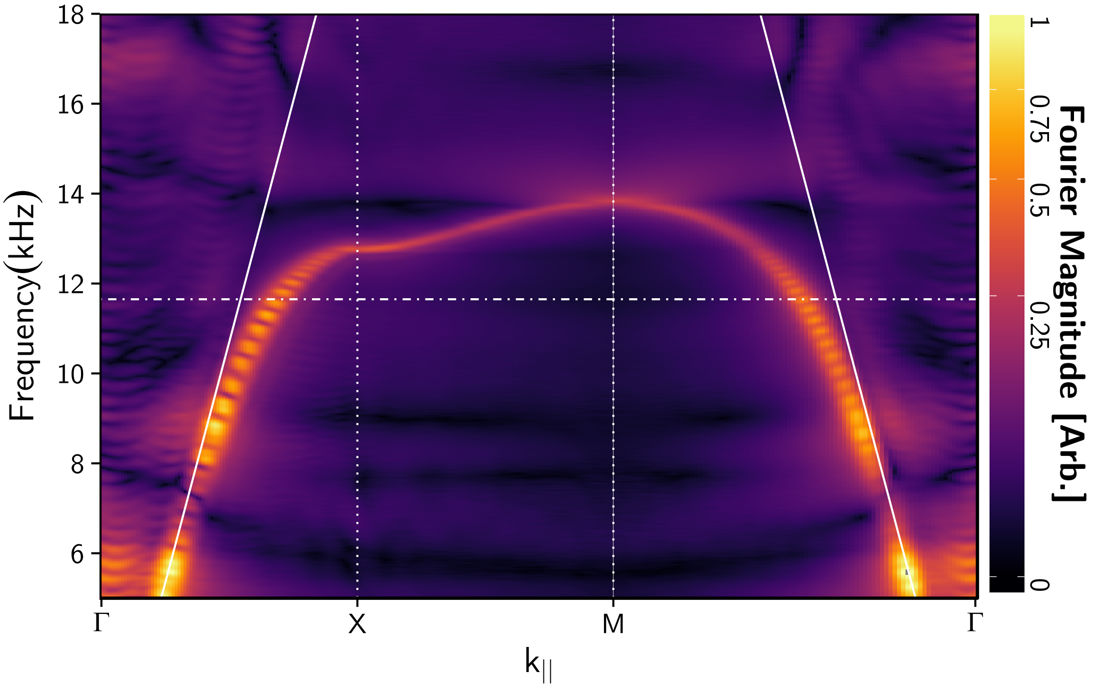

Figure 3.12: Dispersion relation for this sample, plotting the Fourier magnitude along unique directions Γ - X, X - M and M - Γ (points of high symmetry in the reciprocal space of the square Bravais lattice[82]) as a function of frequency. Again, important features have been highlighted, with the solid white lines representing the sound-line $k_0 = \frac{2\pi f}{c}$ and the dotted white lines the position of the first Brillouin zone boundaries. The frequency 'slice' of k-space that 3.11B and 3.11C correspond to are highlighted by the position of the dot-dashed white line.

3.5.5 Measurement Constraints

Ideally, when setting up near-field measurements, one would choose a coordinate grid that spanned the greatest distance possible (for maximum k-space resolution), in the smallest steps possible (to reach maximum k values), recording a sample for as long as possible (for maximum frequency resolution) and with many repeats at each point (to improve signal-to-noise ratio). However, in practise there are severe constraints imposed by time of measurement, computer memory, and computer processing power.

A typical sample could be 80 unit cells long, with a periodicity of 8.2 mm, requiring a spatial resolution less than 4.1 mm to avoid aliasing, ideally a distance incommensurate with the periodicity such as 1 mm. To scan a typical whole sample (or at least the maximum area the XY stage allows) then requires a grid of around ~ 600 mm^2, in steps of ~ 1 mm in each direction. At each one of these points, a time signal with around $10,000$ samples is recorded, which could take anywhere from half a second to 3 seconds depending on the number of averages used, with the information recorded including pressure amplitude and axis position in both space and time. So, combining all this information, a quality scan will need to have $40,000$ high precision numbers for $360,000$ different coordinates, giving a total amount of numbers of $14,400,000,000$. Performing calculations on this amount of data in a reasonable time requires extremely powerful computers, so realistically one must impose limits on what is recorded. As for measurement time, with $360,000$ points at an average of 1 second each, not including hard drive write speed and calculations to be done, the scan is already at an acquisition time of 100 hours, or more than 4 days. Considering atmospheric conditions constantly fluctuate, the conditions at the end of the scan could be very different to those at the start, and that is assuming nothing goes wrong in those 4 days. One could tackle these number problems with an increasingly expensive laboratory, but in practise this is not needed. On the computing side, one can work out the minimum resolution needed in each parameter to show the behaviour of interest thus limiting the data size. Also, modern programming algorithms such as the data.table package in the open-source Rstats software are continuously updated, providing incremental improvements in calculation efficiency From the time perspective, the measurements can be performed at less busy times of day, such as overnight, where less averages are needed to reduce signal-to-noise, allowing the measurement to finish before the environment changes significantly. The most ambitious scan performed for this thesis was that of the two-dimensional array in chapter 6, which took just over two days, and produced 92 gigabytes of raw data, which is 11.5 times more than the RAM available in a typical laptop (as of 2016). Hence, a specialised workstation had to be used for subsequent analysis.

3.6 Sample Fabrication

Presently the complex properties of sound when travelling through solid objects are not of concern. Hence, when designing the acoustic metamaterials used in this thesis, only the structuring of the material was of importance and not what it was made of, provided that it was acoustically rigid (section 2.5). In practise, almost any solid can be treated as perfectly-rigid when compared to air, as the impedance mismatch is so huge. Indeed, even cellotape was found to satisfy the acoustically hard-boundary approximation. Sample fabrication then becomes a matter of whatever is cheapest to produce while maintaining its structure. For the first two experimental chapters, Aluminium was cut to shape with standard metal-work techniques to create the various slit-cavity structures. For the latter 3 experimental chapters, Acrylic was sent to a local company to be precision cut with a high powered laser, which proved cheaper and faster than drilling Aluminium, yet precise enough for these experiments. 3D printed samples were also tested and shown to be viable, but studies of these are not included in this thesis.

3.7 Numerical Modelling - The Finite Element Method

Throughout this thesis, experimental results are compared to numerical simulations. These simulations will arise from a set of fundamental equations that have no simple solution (such as you might find with an analytical model), but by application of a set of boundary conditions, numerical solutions can be calculated with brute force computer power. This achieves several things. First, if the models predict the same behaviour as the experiment shows, then it is confirmed that important physical variables have not been omitted. Secondly, once it is ascertained that the model is predicting the correct behaviour, it can be used to extract detailed information about the experiment that cannot be easily measured with the equipment, for example, the shape of the fields contained within a small resonant cavity, or how the particle velocity field $\vec{v}$ varies. Expanding on this, purely numerical experiments can be performed to test what happens if some fundamental variable is altered, such as the temperature of the air, or what would happen if the air was replaced with some other medium. In this way new experiments can be conceived of that would have been too expensive to test on a whim.

There are many possible ways to numerically model a system, one such being the modal-matching technique mentioned in section 2.7. In this work, the 'Finite-Element-Method' (FEM)[100] is exclusively made use of, a computationally expensive technique that has become gradually more feasible as computing power has improved. A geometry is divided into a large amount of small mesh elements (usually tetrahedra in a three-dimensional model and triangles in a two-dimensional one), boundary conditions applied and material properties set, and a system of equations solved in each individual element that all combine to produce a final result. The commercially available software COMSOL Multiphysics[101] has been used for this purpose.

3.7.1 Model Construction

The first step of the finite element method involves building a model of the experimental environment one wishes to test. This starts with creating a basic geometry, and then assigning parts of that geometry material properties, e.g. a solid cavity surrounded by air. Exactly which parts of the geometry to include will depend on the experiment, it is preferable to make the system as simple as possible. For example, a real three-dimensional slit-cavity sample does not vary significantly along the breadth of the slit, and can adequately be treated as a two-dimensional system with only two spatial variables. An example of such a single slit-cavity model is shown in figure 3.13. In this model and all others, the solid is treated as perfectly rigid, so the solid itself does not need to be meshed for inclusion in the calculations (though this assumption was checked

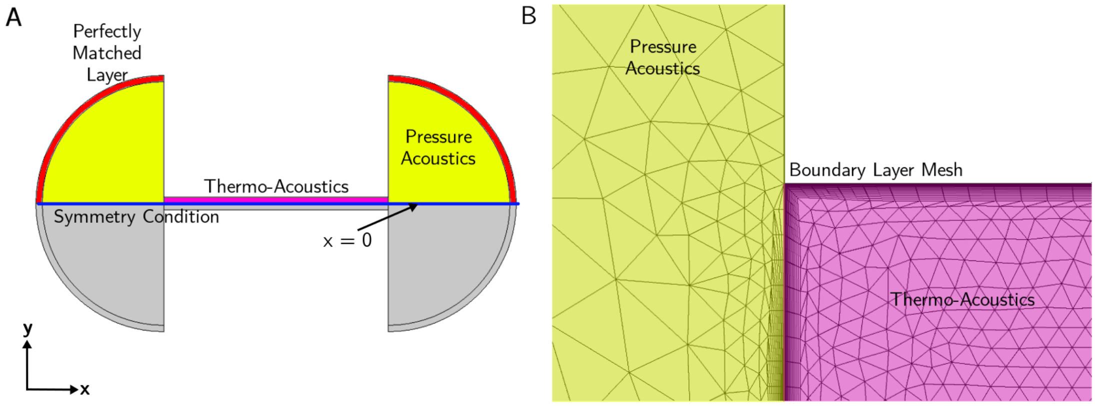

Figure 3.13: (A) 2D COMSOL model set-up for a non-periodic system, in this case a single slit, with different features labelled accordingly. The bottom grey shaded half is not needed due to the symmetry condition represented by the blue line. (B) Close up of the boundary layer mesh that can be built to improve the mesh in sensitive areas, in this case just at the edge of the single slit, and along its walls.

with the use of the solid mechanics module[102] for each individual experiment). It is only necessary to model the gas medium, hence the model includes only a narrow strip of air (coloured purple) surrounded by two larger semicircles of air (coloured yellow).

The next step is to choose what conditions will apply at the geometry's many boundaries. A quick way to simplify the model is to look for any symmetries that could reduce the necessary computation time. In this particular model there is one symmetry plane along the middle at $y = 0$, highlighted by the blue line in figure 3.13A. Next, the other boundary conditions are chosen. Bounding the slit-cavity, are walls that have the rigid wall condition applied. The surrounding air is not bound by anything, but it is not possible to extend the model to infinity, nor feasible even to the size of the laboratory. Instead, a 'Perfectly-Matched-Layer' (PML) condition is used 3.7, which is a region of space designed to simulate infinity by applying a complex coordinate scaling that can absorb any incident radiation before it can hit the edge of the PML and reflect, which would interfere with calculation of the fields in the model. This works very well at most angles of incidence, but breaks down when a wave is incident nearly tangentially to the PML. This means that the shape of the PML is important and must be chosen carefully based on the geometry. In this case a semi-circle works most effectively.

With the boundary conditions determined, the set of equations to be solved are chosen. For acoustics, two systems are used. Where thermodynamic effects are not significant (yellow regions), the COMSOL 'Pressure-Acoustics' (PA) model[102] is used, which solves the basic loss free acoustic wave equation, (in the form of the Helmholtz equation 2.19), described in section 2.3. This module is computationally cheap, since it is used for regions of linear acoustics described only by a scalar pressure variable. It allows for some basic modelling of loss, for example by adding an imaginary component to the wave speed (see section 2.4), but for application to acoustic metamaterials, this tends to be too simplistic, as will be examined in chapter 4. So, where necessary, such as in the small acoustic cavities (purple) the 'Thermoviscous-Acoustics' (TA) module[102] must be employed, which solves the linearised Navier-Stokes equation for fluid flow (equation 2.23), as well as a detailed form of the equation of state (equation 2.22) hence computing the intermolecular effects on acoustic variations of pressure, velocity, and temperature that are outlined in section 2.4. This system of equations has many more degrees of freedom than the simpler PA module, dramatically increasing computation time. It also requires a finer mesh than the pressure acoustics module since there are so many small scale mechanisms at play, particularly in confined spaces such as solid walled cavities, where the complex interaction of sound with the viscous and thermal boundary layers (section 2.4.3) must be accounted for correctly.

The next stage is to define the mesh that will determine where to solve the relevant equations. The more dense the mesh the better, but this comes at the cost of computation time and memory. There is a great deal of literature regarding the optimisation of this process[103,104] but this goes beyond the scope of this thesis, and is mostly handled by COMSOL's internal programming. All the user needs to do is choose a basic maximum size of element. A good rule of thumb is setting this to be 5 times smaller than the shortest wavelength of interest, though this figure might rise to 10 or even 20 in the regions where there is spatially fast variation. To test whether the mesh is adequate, COMSOL runs the model with a slightly finer mesh, and compares the result to the one obtained with previous mesh density, by subtracting the fields at each point. There will always be some variation, but the magnitude of the result of the subtraction is below the tolerance level, such as 1×10^{-6}, then the model has 'converged', and the mesh is assumed to be adequate. An example of a typical mesh is shown in figure 3.13B, which is a close up of the transition between the slit-cavity section and free-space. The mesh in the yellow region is much less dense than the mesh in the purple section, since the equations are simpler, and the unbound fields do not vary as significantly. Also shown is how it is possible to apply special refinements to the mesh, such as defining a boundary layer mesh. At the rigid cavity walls, the thermo-viscous boundary layers exist (see section 2.4.3) and strongly affect the sound propagation even though they are tiny (see chapter 4). The boundary layer mesh allows the user to increase the resolution of the mesh in these regions, without slowing down the rest of the model.

Finally, the system of equations can now be solved to find specific answers. One way of doing this is to use the Eigenvalue solver. This type of solver explores the shape of the geometry supplied, and finds the frequencies of the unique fundamental

Eigenmodes that will fit inside, by finding solutions for the relevant equations when the field is initially zero everywhere (i.e. there is no source). This is very useful when trying to find the shape of the modes that are being excited in the experiment, and also for finding precise resonant frequencies. As will be explained, this type of model can also be used to map the dispersion of a mode. However, it does not tell us about coupling strength to the mode, only that it exists. To acquire that information, an acoustic source can be placed in the model. This sort of driven 'frequency sweep' model will find full solutions to the relevant equations at a set of desired frequencies as though they were emitted by the source, coupling to multiple eigenmodes simultaneously. In this way one can more closely simulate an experiment thus and determine transmission or reflection spectra. Both types of model are made use of throughout this thesis.

3.7.2 Periodic Boundary Conditions

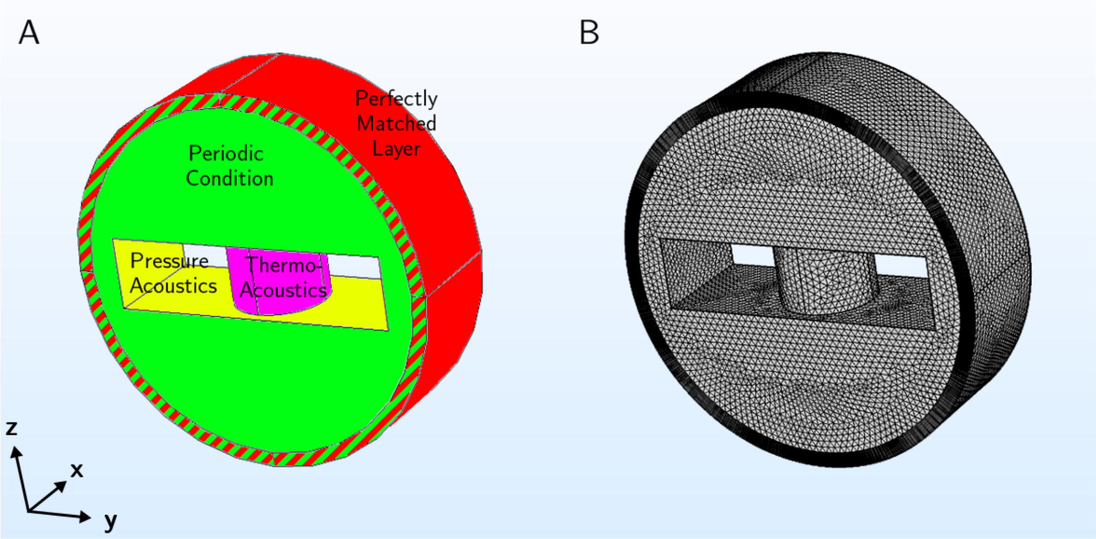

Figure 3.14: (A) 3D COMSOL model set-up for a periodic system, in this case the unit cell of a one-dimensional array of open ended holes. The whole face on each side (green) has the Floquet periodic boundary condition applied. Other sections are labelled accordingly. (B) Example of the mesh used to solve for the arrangement shown in A.

Another important feature to explain is the periodic boundary condition. Most of the samples studied in this thesis can be broken down to one periodic unit-cell, repeated in a given direction. An example of this would be the 'line-mode' sample in chapter 7, or the phase-resonant compound grating configurations in chapter 5. It would be far too computationally expensive to model the whole sample, so instead the model is split it into its unit-cells and the Floquet periodic boundary conditions are applied to each unit-cell boundary. An example of this is shown in figure 3.14A, which is a single unit-cell of the line-mode sample from chapter 7. This 3D model is periodic in one direction only, so only has one pair of periodic conditions, on the front face (green) the back face (not visible). The periodic condition will set up the fields such that they must be identical on either side of the unit-cell (normal incidence) or they must have a specified difference in wavevector (oblique incidence). When using the Eigenfrequency solver, this difference is not limited to the radiative regime, and modes that exist with k beyond the sound-line (i.e. $|k| > |k_0|$) can be found, allowing one to map out dispersion relations for periodic structures. It is important that the mesh elements have an identical layout on each periodic face, so that the fields are solved for correctly.

3.8 Conclusions

In this section the important experimental techniques that underpin the results of this thesis were outlined, and also looked at post processing methods that allow us to extract information about our results. First, the Gaussian pulse measurement technique was explained, and a breakdown of all the equipment used to make such measurements presented. The radiative-regime transmission measurement technique used in chapters 4 and 5 is explained next, followed by an explanation of the field measurement techniques that allow the characterisation of acoustic-surface-waves, as done in chapters 6, 7 and 8. This includes a discussion of how two-dimensional pressure field maps can be analysed with two-dimensional spatial fast-Fourier-transforms to measure the dispersion of a mode. A brief discussion of sample fabrication methods is included. Finally, the finite-element-method that is used to produce numerical simulations of all of the experiments contained in this thesis is explained.

Chapter 4

Thermodynamic boundary layer Effects on Acoustic Transmission Through Narrow Slit Cavities

4.1 Introduction

Fundamentally, sound is a result of the vibration of adjacent particles in some medium. This means that there are complex molecular effects at play, beyond the simple oscillation of a particle. Typically, when describing the propagation of sound though a gas-medium over a short distance, it is safe to ignore these effects, thereby significantly simplifying analytic or numerical calculations. However, this is not always the case. One such manifestation of these molecular dynamics are the thermodynamic boundary layers that exist on a rigid-wall, discussed in section 2.4.3.

Resonant cavities, such as narrow slits or holes, formed of hard materials, are often utilised in the design of acoustic metamaterials[24,87,79,39]. When considering the propagation of sound through air, it is common to consider any solid as being perfectly rigid, as the mismatch between acoustic impedances can be phenomenally large (typically of order 10^5, see section 2.5). Thus, thermodynamic boundary layers must exist on any given cavity wall where the airborne sound is confined. This scenario was first tackled by Kirchhoff[4] nearly 150 years ago, who presented a detailed analysis of the thermodynamic effects in an infinitely long narrow-tube, with many subsequent studies exploring its implications[54,55,57], including a specific treatment of the narrow slit-cavity by Lord Rayleigh[56]. However, despite this full treatment, most of the recent acoustic metamaterial studies do not incorporate thermodynamic effects; in the interest of simplicity they are naively assumed to be negligible, which may seem justified given that the boundary layers are typically more than two orders of magnitude smaller than the slit-width or tube radius of the cavities being used[54,44].

In this chapter, the resonant transmission of airborne sound through slit-cavities of subwavelength widths is studied, for both a periodic array structure and a single element. It is found that viscous and thermal boundary layer effects become important for slit-widths far greater than, as one might expect, the boundary layer thickness. This is manifested through both a reduction in the effective speed of sound through the apertures, and significant attenuation of the transmitted signal. Lord Rayleigh's prediction is compared to experimental results and fully verified, in the form of a generalised analytic theory that Stinson[57] derived from Lord Rayleigh's work. Finally, exactly how the different boundary layers manifest themselves is explored in some detail, with results compared to the detailed analysis of Weston[54] and Tijdeman[55]. This study shows how the prevalent loss-free treatment of resonant cavities in the wider acoustic metamaterial community is unrealistic.

4.2 Fabry-Perot-like Cavity Resonances

Consider a single, open-ended cavity of length L, enclosing air bounded by two infinitely wide, perfectly rigid parallel walls spaced w apart. Since, in a gas, sound is a longitudinal wave, there will be no cut-off frequency or slit-width below which the sound will not propagate through it. Instead, if the slit-width is much less than the free space wavelength ($w \ll \lambda_0$) sound will propagate through as a plane wave only[44]. Hence sound of any wavelength incident upon the cavity will be guided through it, with the impedance mismatch at each end causing partial reflections (see section 2.6). At specific frequencies, determined mostly by the cavity length L, the reflections will form a standing wave within the cavity. This will result in resonant enhanced transmission via a Fabry-Perot (FP)-like resonance at frequencies given by:

$$f_{\mathrm{FP}} = \frac{n c_{\mathrm{a}}}{2(L + \Delta L)} \tag{4.1}$$

here n is a positive integer, c_{a} is the adiabatic speed of sound, and ΔL is a correction to the cavity length that arises from diffractive end-effects, which to first order is approximately $8w/3\pi$[75,44,2]. Hence, when studying the transmission spectra of a slit-cavity, it is expected that there will be a background transmission associated with the mark-space-ratio, and a series of broad peaks that are predicted by the FP resonance condition as described in section 2.6. Note that, in the case of the slit-array, the end correction takes on a more complex form, as each periodically arranged slit-cavity can couple to its neighbours via evanescent field. It is the collective excitation of periodic subwavelength cavities that leads to the acoustic-surface-wave (ASW) effects that have been studied extensively in recent years[74,87,27,28,105,35,79,106,107], and which the later chapters of this thesis are concerned with. However, numerical models typically employed to describe them, such as the modal-matching model developed by Christensen et al.[27], or the analytic model developed by Wang[28], do not take into account boundary layer perturbation of these guided modes.

In the forthcoming experiment the effect of reducing slit-width w while keeping slit-length L constant is explored. For both the slit-array and single-slit, the characteristic resonant frequency f'_{FP} strongly diverges from the prediction of the simple FP analysis. For narrow slits there is a significant reduction in the resonant frequency away from equation 4.1 which is attributed to the thermodynamic boundary layer effects within the air, present on each rigid wall.

4.3 The Viscous and Thermal Boundary Layers

For any acoustically rigid solid material bounding a fluid cavity, the particle velocity tangential to the wall is forced to zero, i.e. the well known ‘No-slip’ condition[44,8]. As illustrated in figure 2.2 of section 2.4.3, the tangential particle velocity gradually evolves back to its original free space value with increasing distance away from the wall, causing layers of different velocities to shear. This gives rise to a lossy viscous boundary layer, having a characteristic thickness[58]:

$$\delta_\nu \approx \sqrt{\frac{\nu}{2\pi f}} \tag{4.2}$$

where ν is the kinematic viscosity. A second boundary layer arises due to the heat exchange between the gas and the wall, which acts as an infinite heat-sink. In free space, any heat generated by the rapid oscillation of the air particles cannot be conducted to its surrounding regions due to the rapidity of said oscillation, the increase in kinetic energy of the particle instead contributing to the speed of sound (see section 2.4.1). This is known as the adiabatic speed of sound c_{a}, first calculated by Laplace. Near the wall however, the heat generated is absorbed by the wall, reducing the speed of sound to its isothermal value c_{i}, which is the value first calculated by Newton, who neglected to include the effect of heat[56]. The two are linked by the specific heat capacity of the fluid γ, where $\frac{c_{\mathrm{a}}}{c_{\mathrm{i}}} = \sqrt{\gamma}$ (at standard temperature and pressure, c_{a} and c_{i} are 343 ms^{-1} and 240 ms^{-1} respectively[44]). As with the viscous boundary layer, the switching from adiabatic to isothermal speed causes a lossy thermal boundary layer, having characteristic thickness[58]:

$$\delta_\alpha \approx \sqrt{\frac{\alpha}{2\pi f}} \tag{4.3}$$

where α is the thermal diffusivity of the gas (note, expressions 4.2 and 4.3 are $\sqrt{2}$ smaller than the commonly used definitions (section 2.4.3), to be consistent with Weston[54], Tijdeman[55], and Yazaki et al.[58]). The ratio between the two thicknesses squared is known as the Prandtl number, $\sigma = \delta_\nu^2/\delta_\alpha^2$, and for air it is ~ 0.7[44]. The origin of the thermodynamic boundary layers is discussed in greater detail in section 2.4.3.

4.4 Boundary Layer Effects on Propagation of Sound Through Tubes

A mathematical treatment of the propagation of sound through gas confined to narrow channels was first sought by Kirchhoff[4], who constructed a full solution which describes waves propagating through infinitely long, circularly cross-sectioned 'tube' geometries. This full treatment is complicated, being in the form of a complex transcendental equation, but depending on the tube-radius-to-frequency-ratio, different assumptions can be applied to define a set of regimes. Kirchhoff himself studied the 'wide-tube' regime, with Lord Rayleigh[2] later including narrower tube geometries, and Weston[54] many more such as the 'wide-to-narrow' transition regime.

One might naively expect that boundary layer effects would only become important when the radius of the tube through which the sound propagates is of the order of either δ_ν or δ_α, which have a thickness of $\delta_\nu \sim 20$ µm at frequency 5 kHz (at atmospheric pressure). However, a detailed analysis of Kirchhoff's theory undertaken by Weston[54], showed that both the wave attenuation and the particle velocity across the entire tube are affected by the boundary layers, even when they form only a tiny fraction of the tube radius r.

Weston's study[54] detailed the various regimes where different mechanisms govern the exact nature of the wave perturbation, depending on the precise ratio of the tube radius to the frequency of sound. As mentioned, these regimes are called, for example, 'very-wide-tube', 'narrow-tube' or 'wide-to-narrow transition', and differ by what assumptions can be used to simplify Kirchhoff's full equations. Generally, for the narrowest cases the viscous layer dominates, since the entire tube becomes isothermal (i.e., the thermal boundary layers vanish), but for larger tubes, both viscous and thermal mechanisms play a role. In 1975, Tijdeman[55] was able to unify all of these regimes into a general model, which more recently Yazaki et al.[58] experimentally verified. They found experimental agreement in the predicated attenuation and phase velocity of a wave propagating through an ‘infinitely’ long tube, over 4 orders of magnitude of tube radii. A 10% reduction in the phase velocity of the pressure wave $v_{\mathrm{p}} = f\lambda_0$ (λ_0 = free space wavelength) relative to the adiabatic speed of sound c_{a} is exhibited when the tube radius is roughly 10 times larger than the thickness of the thermodynamic boundary layers.

Lord Rayleigh extended Kirchhoff’s solutions to the ‘parallel wall’ geometry (i.e., the slit)[2,56], remarking that Kirchhoff’s treatment of tubes is still valid for slits with a substitution of the slit-width w for tube radius r, a statement that (until now) had not been verified by experiment. Stinson[57] simplified Kirchhoff’s equations for tube cross sections of arbitrary shape, including an infinitely long slit-cavity, finding agreement with Lord Rayleigh, and providing a simplified method for predicting the phase velocity of a confined sound wave.

While much attention has been paid to what effects thermodynamic boundary layers have on confined sound, not much attention has been paid to their effect on diffraction from periodic structures. There has been some recent work, with Homentcovschi and Miles[108,109] studying a non-resonant system of periodic, very thin screens ($L \ll \lambda_0$) with slit-widths of the order of the boundary layer thickness, also investigating the acoustic attenuation. However, no research has explored the effect of boundary layer perturbation on a resonant slit system, which is the focus of the current study.

4.5 Experimental Configuration

Figures 4.1 through 4.4 show the experimental set ups for the measurement of each sample. To make the slit-array sample depicted in figures 4.1 and 4.3, thin aluminium slats ($d \ll \lambda_0$) of size $600 \times 2.9 \times 19.8$ mm were stacked vertically in a wooden sample holder, separated by sets of polyester spacers of sizes 0.05 ± 0.01 mm, 0.1 ± 0.01 mm, and 0.5 ± 0.03 mm, resulting in a sample area of width $b = 560$ mm by height $a = 400$ mm. In order to have incidence sound approximate an infinite planar wave, the sample was placed between two parabolic mirrors of radius 220 mm and focal length 1 m. One mirror collimated a sound signal from a Scan-Speak D3004 speaker positioned at its focal point; the other focused the sound to a Brüel and Kjær 4190 microphone. The sample was positioned such that the collimated beam was incident normal to the front face of the array of slit cavities. The transmission measurement technique outlined in section 3.4 of the methods chapter was applied, including the no-gap subtraction, to obtain transmission spectra for each slit-width. The experiment was repeated four times for each slit-width, and the mean resonant frequencies were extracted from the transmission spectra by the fitting of a Lorentzian function to each peak. Error bars

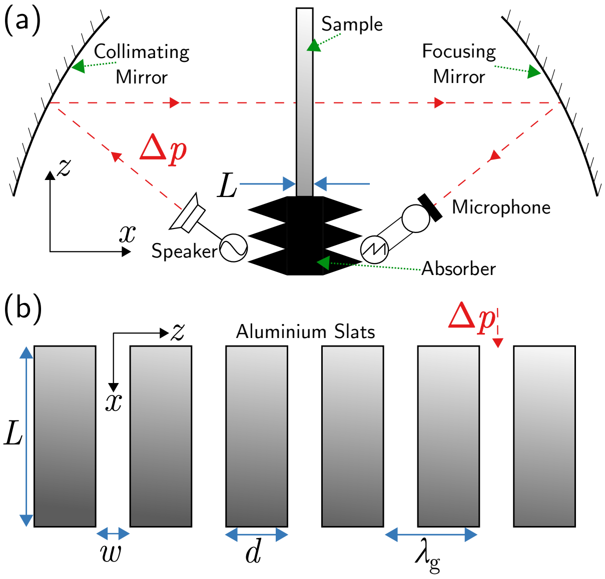
(a)
Collimating Mirror
Sample
Focusing Mirror
Δp
z
L
x
Speaker
Microphone
Absorber
(b)
z
Aluminium Slats
Δp
x
L
w
d
λ_g

Figure 4.1: (a) Simplified 2D Schematic of the slit-array experimental configuration. The aluminium slats (shaded) were stacked vertically between two mirrors 3 m apart, with a speaker and microphone placed at their focal lengths, 1 m away. The sample stand was covered in acoustic absorber (black fill) and the beam path is indicated by a dashed arrow. (b) Schematic of the slit-array sample itself, with dimensions labelled (not to scale). Here, $L = 19.8 \pm 0.12$ mm, $d = 2.91 \pm 0.03$ mm, and $\lambda_g = d + w$.

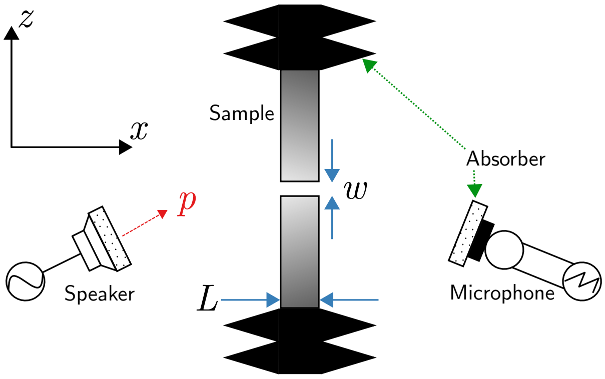
z
x
Sample
Absorber
w
p
Speaker
L
Microphone

Figure 4.2: Simplified 2D Schematic of the single slit experimental configuration. The shaded blocks represent the aluminium sample, and the black blocks represent an acoustic baffle. The microphone and speaker are ~ 20° off normal in the xz plane, covered in acoustic absorber (black), and separated from the sample faces by 220 and 400 mm, respectively. Here, $L = 35.0 \pm 0.1$ mm.

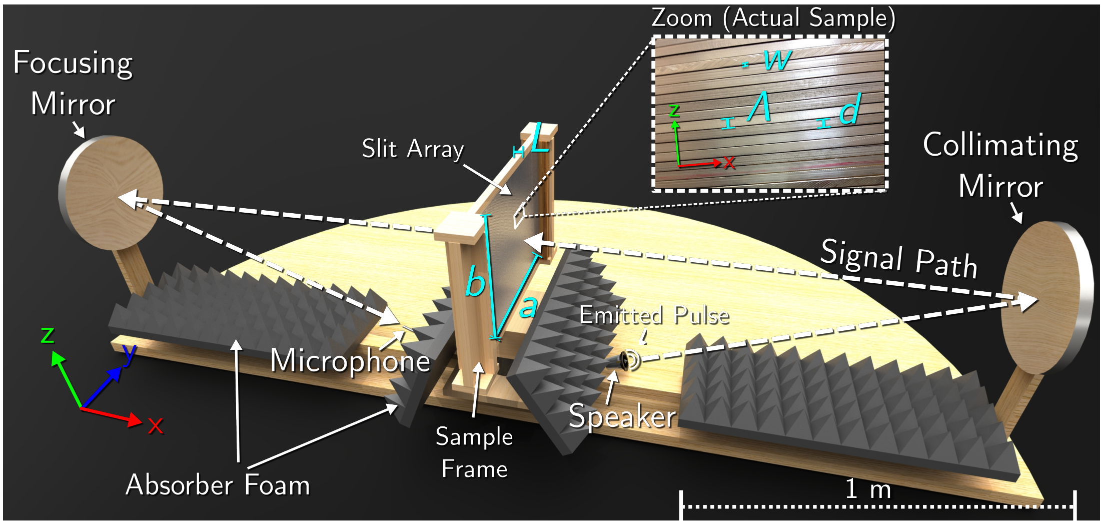
Zoom (Actual Sample)
Focusing Mirror
Slit Array
L
w
A
d
z
x
Collimating Mirror
Signal Path
b
a
Emitted Pulse
z
y
x
Microphone
Speaker
Sample Frame
Absorber Foam
1 m

Figure 4.3: A representation of the slit-array experimental configuration. The sample was placed on a set of level blocks, normal to the collimated beam produced by the first mirror, where the pair of mirrors were 3 m apart. The speaker and microphone were placed at 1 m from the mirrors, their focal length. The mirrors tilted so that the beam path (labelled dashed white lines) relative to the speaker/microphone was centred on the opposing mirror. The sample height is $d = 400$ mm, and the width $a = 560$ mm. The wooden stage was covered in absorber where possible. (Inset) Real photograph of a close up of the sample face, built with $w = 0.25$ mm, with the other labelled dimensions described in fig 4.1.

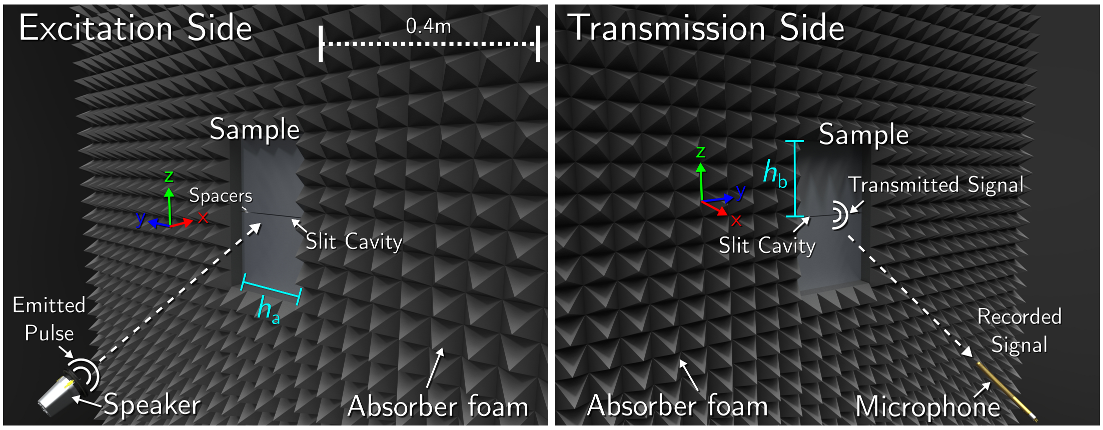
Excitation Side
0.4m
Sample
Spacers
z
y
x
Slit Cavity
h_a
Emitted Pulse
Speaker
Absorber foam
Transmission Side
Sample
z
y
x
h_b
Transmitted Signal
Slit Cavity
Recorded Signal
Absorber foam
Microphone

Figure 4.4: A representation of the single slit experimental configuration. The aluminium blocks that form the slit are separated vertically with polyester spacers and held inside the wooden sample holder, which is covered in absorbing foam on both entrance and exit sides. Both the speaker and microphone are wrapped in cotton wool (not rendered) and directed at the sample, $\sim 20^\circ$ off normal in the xz plane, separated from the sample faces by 220 and 400 mm respectively. The width of the sample face $h_\mathrm{a} = 243$ mm, while the height $h_\mathrm{b} = 202$ mm.

represent the standard deviation from these means. This process was repeated for the single slit case (Figures 4.2 and 4.4), with two blocks of aluminium of dimensions width $h_{\mathrm{b}} = 243$ mm, height $h_{\mathrm{a}} = 202$ mm and depth $L_{\mathrm{ss}} = 35$ mm. The only difference in the method was the lack of collimating mirrors. With only one slit in the sample, a collimated beam was not required to approximate a planar wave since the phase difference across the narrow gap is insignificant ($w \ll \lambda_0$, i.e. the slit is below the waveguide cut-off frequency discussed in section 2.6), and recording direct transmission between the receiver and detector produced significantly stronger signals, offsetting the problem of low total transmission caused by having only one slit-cavity for a signal to pass through. Both the microphone and speaker were tilted $\sim 20°$ off the x axis and covered in absorber to weaken standing waves set up between them and the sample faces. Typical transmission spectra for both the slit-array and single slit samples are shown in figure 4.5.

The samples were chosen to ensure that the slit-widths and array periodicities remained subwavelength to incident sound ($100w < \lambda_0 < 300w$, and $8\lambda_{\mathrm{g}} < \lambda_0 < 14\lambda_{\mathrm{g}}$), avoiding any strong acoustic-surface-wave phenomena (i.e. the Fabry-Perot-evanescent-wave supported by the slit-array was more Fabry-Perot-like than acoustic-surface-wave like, see section 2.7.6). The measurements were taken under different temperatures, pressures, and humidities, the latter two having negligible effect[50]. However, a change in temperature alters the adiabatic speed of sound and thus the frequency of each resonance. To determine the size of this shift, an FEM loss-inclusive model (section 3.7) was solved with different ambient temperatures, for a number of slit-widths, in the case of both the slit-array and the single slit. A polynomial fit to the resulting resonant frequency as a function of temperature then provided a value for the frequency shift of $1.64 \times 10^{-3} f$ K Hz^{-1}, hence all data points were normalized to 293.15 K.

In the slit-array, owing to random bowing of the slats and machining imperfections in the aluminium, the slit-width was not constant across the area of the sample. Air gaps that are slightly larger in size allow more signal through and may contribute more to the overall response, particularly for the narrow slits, where the deviation in gap size could be as high as 40% of that which was intended. To account for this systematic error, all of the experimental slit-widths were increased by 40 µm from the measured polyester spacer slit-widths, resulting in excellent agreement with the loss-inclusive FEM model.

4.6 Experimental and Numerical Results

Figure 4.5 shows the transmission amplitude spectra for both the slit-array (left column) and single slit (right column) samples, for a variety of slit-widths. These spectra

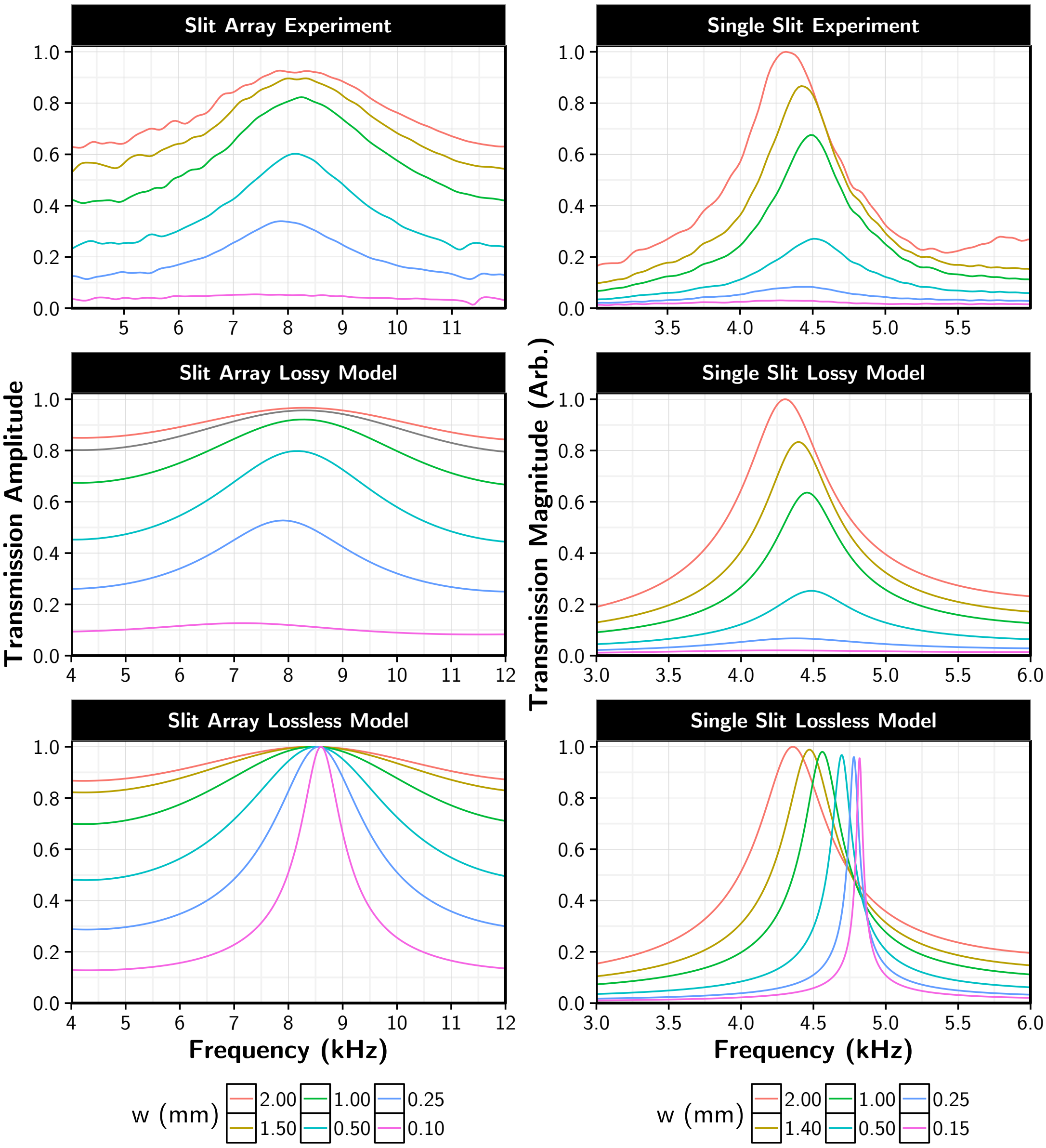

Figure 4.5: Transmission amplitude t (or Transmission magnitude for the single-slit, as this is only a relative measurement) spectrum as a function of frequency, for different slit-widths, from several data sources, labelled accordingly. The line colour corresponds to slit-width w and is labelled in the legend. (Left column) - Spectra for the slit-array sample, (Top row) - Experimental data, (Middle row) - Thermo-viscous Navier-Stokes FEM model data, (Bottom row) - Lossless acoustic wave equation numerical model. (Right column) As the left column, but pertaining to the single slit sample.

were acquired from both the experimentally recorded data (top row) and the frequency domain solver of the finite element method (FEM) software COMSOL multiphysics (detailed in section 3.7) with and without thermo-viscous effects accounted for (middle and bottom rows, respectively). The results of the multiple experimental spectra recorded for each slit-width were then used to create figure 4.6, which shows the mean measured fundamental $n = 1$ resonant frequency f'_{FP} of the slit-cavity vs the slit-width w for both the slit-array (top) and single slit (bottom) samples. A dimensionless form of this data is also shown, where the ratio of f'_{FP} to that predicted by the Fabry-Perot condition (4.1) f_{FP} is plotted as a function of the fraction of slit-width w occupied by viscous boundary layer δ_{v}. Both experimental data sets are compared with numerical data obtained from the eigenfrequency solver of the FEM model, again with and without thermal and viscous contributions. Note, the eigenfrequency solver was employed instead of fitting a Lorentzian to find the peak of the modelled frequency spectra depicted in figure 4.5, as this method was both computationally faster and more accurate.

Resonant frequency uncertainties at the smallest gaps are increased due to broadening of the modes, as well as a reduction in the signal-to-noise ratio. For the array, the largest gap resonances were also significantly broader, due to a reduction in the quality factor caused by decreasing the rigid body filling-fraction $\frac{w}{d}$. These effects are visible in both the experimental and loss-inclusive numerically-calculated frequency spectra shown in figure 4.5.

For gaps where $(\frac{\delta_{\text{v}}}{w}) < 0.03$ (i.e. $w > 0.5$ mm), the trend of the data agrees with the predictions of the lossless FEM models (dashed blue lines in figure 4.6), which solve the acoustic wave equation (2.18). The diffractive end correction ΔL is the dominant physical mechanism shifting the resonance down in frequency in these regimes, increasing with w. It has been confirmed that Christensen's lossless model-matching model[27] agrees very well with these lossless FEM models in both single element and array cases (not shown here because it is too difficult to separate from the loss-free model), serving to illustrate a typical model used in modern acoustic metamaterial research.

The important result for both samples is the marked deviation between the lossless models and the experiment for $(\frac{\delta_{\text{v}}}{w}) > 0.03$ (i.e. $w \leq\sim 0.5$ mm). To explain this, the thermal and viscous properties of the air need to be incorporated into the FEM model. This is done by utilising the linearised Navier-Stokes equation for a viscous fluid (2.23) and setting tangential particle velocity to zero at the walls by applying the no-slip boundary condition. Also, heat transfer between the fluid and solid walls is allowed via use of the isothermal boundary condition and the equation of state (2.22). Figure 4.6 demonstrates good agreement between these more complete models (solid red line) and the experimental data for all slit-widths. Hence, on a scale more than an order

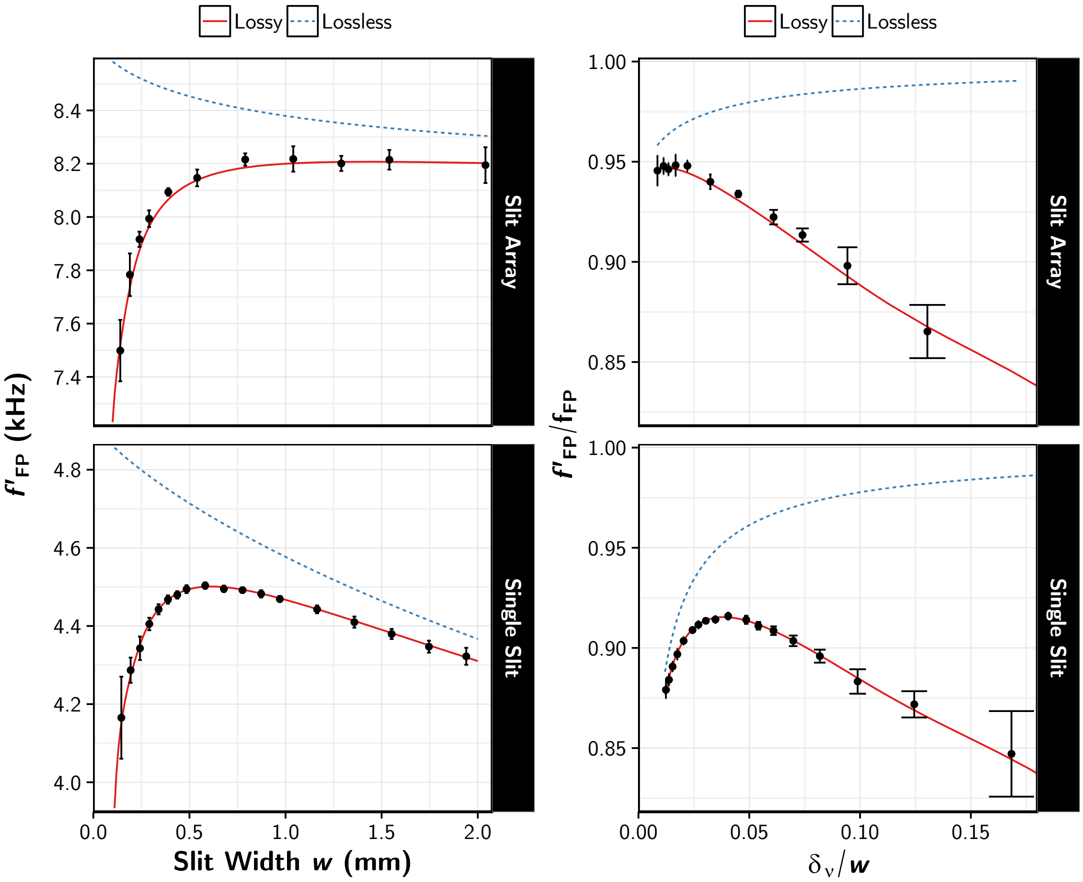

Figure 4.6: (Left Column) The fundamental resonant frequency of each slit-cavity f'_{FP} plotted as a function of the slit-width w. The solid black circles are the mean of the experimentally determined resonant frequencies, with the error bars representing their standard deviation. The dashed blue lines represent a lossless FEM numerical prediction, and the solid red lines a more complete numerical prediction that includes the viscous and thermal properties of each system. The top and bottom panels represent the slit-array and single slit samples, respectively (labelled). (Right column) The fundamental resonant frequency of each slit-cavity f'_{FP}, normalized to that predicted by the Fabry-Perot condition f_{FP} as a function of the ratio of viscous boundary layer thickness δ_v to slit-width w. This is the dimensionless form of the plots in the left column.

of magnitude larger than the boundary layer thickness, these thermodynamic effects are significant. Upon closer inspection, the results of the loss-free and loss-inclusive models have not converged even for the largest measured slit-widths ($(\frac{\delta_v}{w}) < 0.03$ or $w > 0.5$ mm). Note: it is not just the position of the resonant frequency f'_{FP} that the lossless equation fails to predict; inspection of the spectra obtained by said models in figure 4.5 reveals the prediction of the resonance quality factor to increase with a reduction in slit-width, in stark contrast to the drastic decrease that the experimental and loss-inclusive model spectra demonstrate.

As the slits are narrowed, the influence of the boundary layers becomes more substantial, and there is a strong reduction in the resonant frequency attributed to a decrease in the phase velocity v_{p} (i.e. the effective speed of sound)[54]. This is because the wavelength is fixed by the FP condition (4.1) that is tied to unchanging cavity length L. It is important to note that the simplistic treatment of loss possible by incorporating the classical absorption coefficient α_{c} in the wave equation, or by adding a phase delay to the sound velocity in air (for both, see section 2.4), does not predict this frequency reduction in the FEM model. Such treatment yields only part of the increased signal attenuation for the narrowest slits, lacking both the complex shear velocity information that the vorticity term in the Navier-Stokes equation accounts for, and the thermal diffusion term from the improved equation of state. In addition, it was checked that the ratios of slit-width to array periodicity $\frac{w}{\lambda_{\mathrm{g}}}$, slit-width to slat-width $\frac{w}{d}$, or array periodicity to incident wavelength $\frac{\lambda_{\mathrm{g}}}{\lambda_0}$ do not significantly impact on the phenomena of interest, provided that $\lambda \gg \lambda_{\mathrm{g}}$. The effects that the thermodynamic boundary layers can have on some diffraction phenomena, i.e. when λ is of the order of λ_{g}, are discussed in later chapters.

4.7 Comparison to Stinson's Generalised Form of Kirchhoff's Equations

To confirm Lord Rayleigh's statement that Kirchhoff's equations for a tube are applicable to the slit-cavity, with a simple substitution of tube radius in place of slit-width[56], it is useful to compare the present results to such an analytic model. Calculating an answer directly from Kirchhoff's transcendental equations would be a formidable challenge, it is instead fruitful to use a model based on those equations but simplified to the single slit-cavity case. Stinson has derived such a model[57], providing solutions for the wave vector $k = \frac{2\pi}{\lambda_0}$ of a wave travelling through an infinitely long slit of a given width at a given frequency, from which one can extract the phase velocity v_{p}. Application of Stinson's model to the present resonant slit geometry requires the determination of the

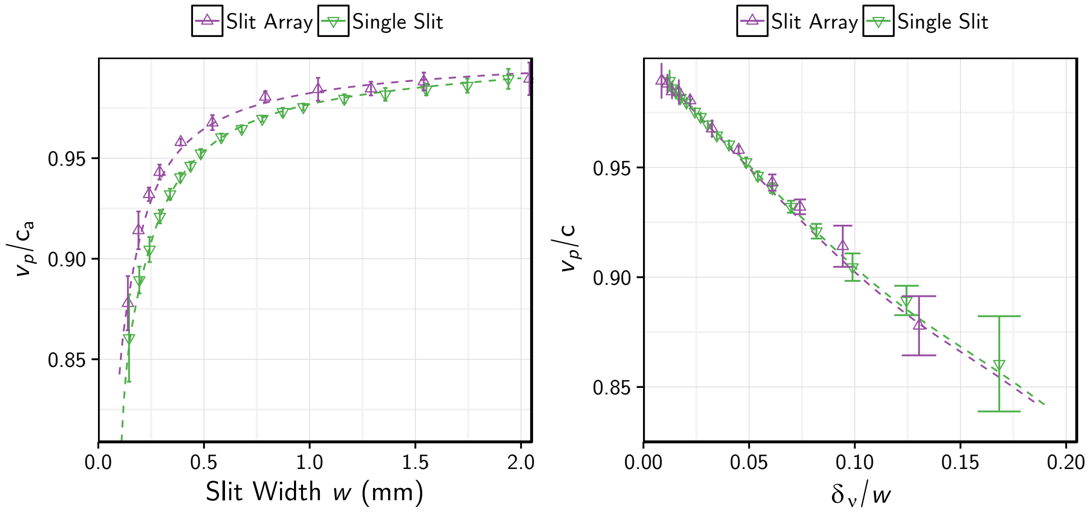

Figure 4.7: (Left) Ratio of the calculated effective speed of sound v_p to adiabatic speed c_a in each slit-cavity, as a function of the slit-width w. Triangular points and accompanying error bars are experimental data converted from figure 4.6, with purple and green representing the slit-array and single slit data, respectively. The dashed lines represent the predictions of Stinson's[57] analytic theory for each sample, coloured accordingly. (Right) Ratio of the calculated effective speed of sound v_p to adiabatic speed c_a in each slit-cavity, as a function of the ratio of viscous boundary layer thickness δ_v to slit-width w. This is the dimensionless form of the left figure.

characteristic frequency f'_FP in order to calculate the boundary layer thickness for each slit-width. This was estimated from the loss-inclusive FEM model. Further, to directly compare the experimental results with Stinson's prediction for v_p, the wavelength of the fundamental resonance of the finite-length slit cavities corresponding to $2(L+\Delta L)$ must be determined. This allows a calculation of v_p by solving the Fabry-Perot equation 4.1. An estimate of ΔL that includes the effects of the viscous and thermal boundary layers can be extracted from the FEM loss-inclusive model (and then applied to the experimental data), using the relation

$$\Delta L = L_{n=2} - 2L_{n=1} \tag{4.4}$$

where $L_{n=2}$ is the length of slit for which the $n = 2$ mode matches the resonant frequency of the fundamental $n = 1$ mode for $L_{n=1}$. Applying (4.4) and then fitting a polynomial to the calculated ΔL as a function of w allows one to determine an approximate ΔL for any given slit-width. This was performed separately for the slit-array and the single slit. Note, for a single slit, to first order $\Delta L = \frac{8w}{3\pi}$[75], so $\Delta L \to 0$ when $w \to 0$. For a slit-array this diffraction-induced end correction has a different form[75], but it contains a similar dependence, and also tends to zero (the boundary layers do not significantly alter ΔL in this case[108], confirmed by comparison between the loss-inclusive and loss-free FEM models). Thus, for the smallest and thus most-important slit-widths, any error in this estimation of ΔL is negligible, allowing the calculation of the phase velocity v_{p} for the experimental data using 4.1, plotted in figure 4.7.

Figure 4.7 shows the dependence on slit-width w of the effective speed of sound v_{p}, as a fraction of the adiabatic speed of sound c_{a} (at standard temperature and pressure). The experimental results (triangular points) are compared with those derived analytically by Stinson[57] (dashed lines). Both samples are plotted simultaneously, with purple and green colours representing the slit-array and single-slit samples respectively. The separate data sets follow the same trend, but lie on different curves. This is because of the different lengths L used for each sample (hence different fixed wavelengths), where the array sample was $L_{\mathrm{as}} = 19.80$ mm, and single slit $L_{\mathrm{ss}} = 35.05$ mm. This can be accounted for by scaling the slit-width as a ratio of boundary layer thickness $\frac{\delta_{\mathrm{v}}}{w}$, as done in figures 4.5 and 4.6. This dimensionless form is shown on the right hand column of fig 4.7. There is very good agreement between Stinson's prediction for v_{p} and the experimental data across the whole range of measured slit-widths for both samples. The change from infinite to finite-length tubes does have an effect on Kirchoff's formulae, however, as Weston[54] remarks, this correction is negligible for all but the shortest tubes, supported by the agreement between the present results and Stinson's model.

The reduction in effective sound speed follows the same linear trend for both the slit-array and single slit, confirming that it is the ratio of slit-width to thermodynamic boundary layer size that is the important parameter. There is a negligible systematic shift resulting from slight inaccuracies in the modelled prediction for ΔL. For the smallest gap in the single slit case, where $\frac{\delta_{\mathrm{v}}}{w} \approx 0.18$, v_{p} falls by nearly 15%, consistent with the results of Yazaki[58] (substituting slit-width w for tube radius r) and thus verifying Lord Rayleigh's theory. Even when the size of a viscous boundary layer is only 5% that of the whole slit, there is a significant $\sim 5\%$ drop in v_{p}, indicating that it is unwise to use an idealistic loss-free model in the design of an airborne-acoustic metamaterial.

4.8 Boundary Layer Effects on Individual Acoustic Variables

It is useful to use the FEM model to inspect in detail the loss mechanisms at work in the present study, and compare the results with the analytic theory previously developed. As already mentioned, different solutions to Kirchhoff's[4] general tube equations

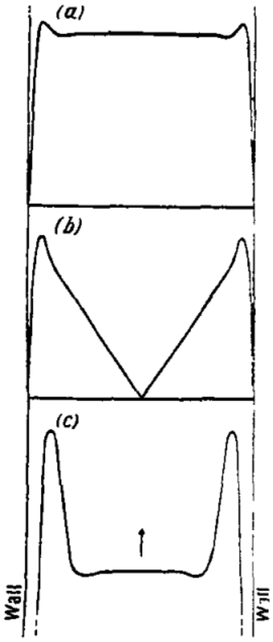

Figure 4.8: Weston's predictions for the behaviour of various quantities through a cross-section of a tube, taken from figure 3 of his study[54]. (a) Amplitude of axial particle velocity or temperature fluctuation, (b) amplitude of radial particle velocity, (c) wavefront or equiphase surface.

result in the definition of separate regimes, the 'narrow-tube', the 'wide-tube' and the 'very-wide-tube'[2], depending on the ratio of tube radius to excitation frequency. Weston's detailed analysis of Kirchhoff's solutions included a boundary layer model that was able to predict the dependence of particle velocity v across the tube, in both the axial and radial directions, as well as the shape of the instantaneous phase fronts as the sound propagates along the tube, all of which he plotted for the 'wide-tube' geometry, presented here in figure 4.8. In Stinson's[57] further analysis of this problem, he adds a plot of the excess temperature ΔT (which he labels T'), the 'trapped' temperature generated by the motion of particles that is not conducted away in an adiabatic pressure wave (see section 2.4). Stinson also compares the variation of these quantities between the wide-tube and narrow-tube geometry. For the slit-cavity scenario then, the behaviour of the different variables should be identical, but for the substitution of slit-width for radius.

Figure 4.9 shows the values of the tangential particle velocity amplitude $|v_{\mathrm{x}}|$ in the direction of the slit-length (equivalent to tube axial particle velocity), the normal particle velocity amplitude along the direction of the slit-width $|v_{\mathrm{z}}|$ (equivalent to tube radial particle velocity), the excess temperature ΔT, and the shape of the phase fronts represented by plotting $|v_{\mathrm{p}}|$, all plotted as a function of distance z along the cavity

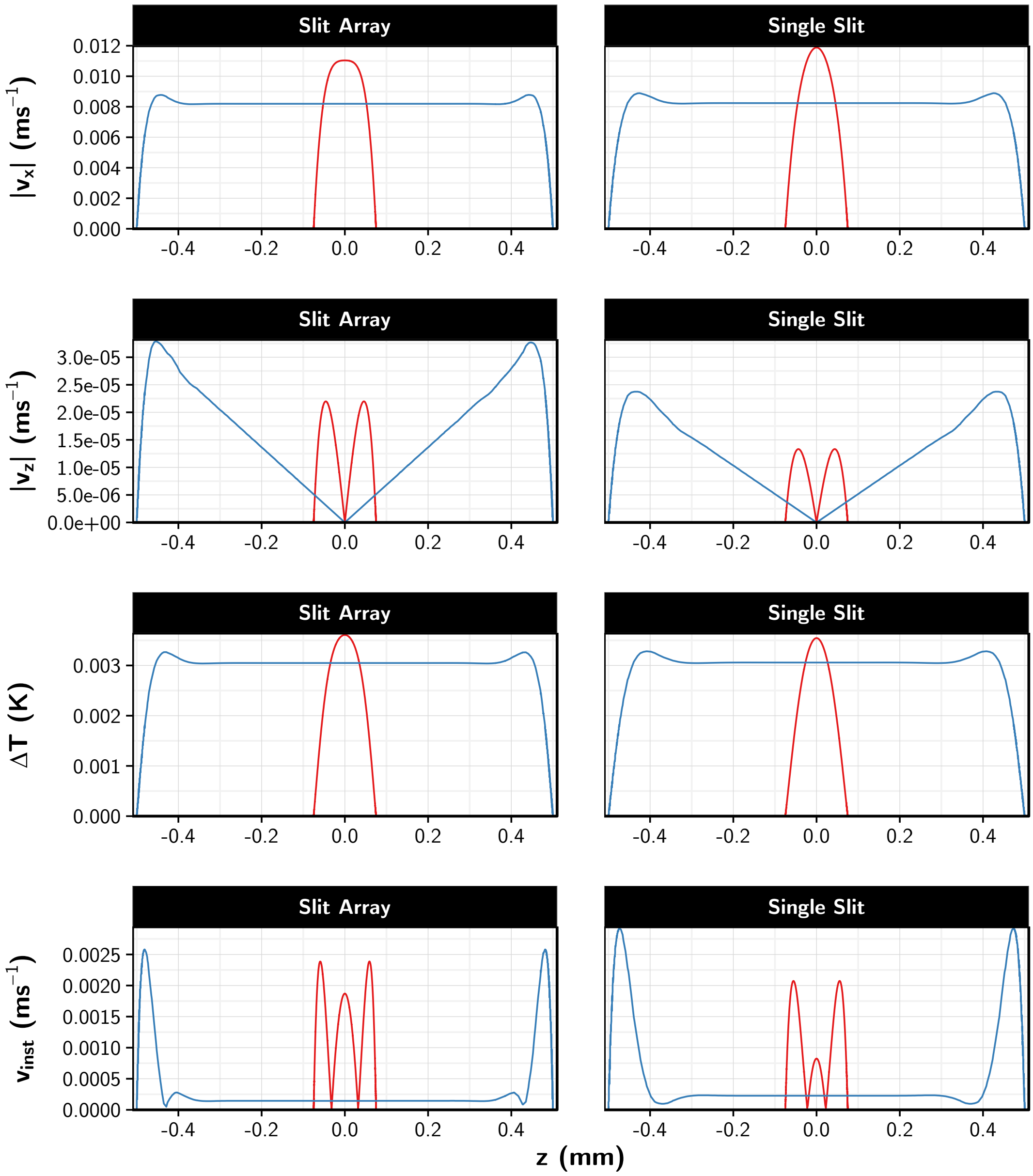

Figure 4.9: Various quantities plotted as a function of distance z along the cavity slit-width, measured in mm. Values were extracted from the loss-inclusive FEM model at a distance of $0.25L$ from the slit-cavity centre for both samples. The blue lines correspond to a slit-width w of 1.00 mm, the red lines a slit-width of 0.15 mm. The left and right columns correspond to the slit-array and single slit samples respectively. (Top row) Particle velocity along the slit-length v_{x}. (Second row) Particle velocity across slit-width v_{z}. (Third row) Excess temperature ΔT, measured in degrees Kelvin difference from the ambient temperature T_0. (Bottom row) Instantaneous particle velocity v_{p}, which is the shape of the phase fronts as they propagate through the slit.

slit-width. Both the slit-array and single-slit are presented, with the blue and red lines corresponding to slit-widths w of 1.00 and 0.15 mm respectively. All values were extracted from the loss-inclusive FEM model, a slit cross-section taken at $0.75L$ (the middle distance between nodes in the pressure and velocity fields, which, being π out-of-phase with each other, are in opposite locations). By inspection of Weston's[54] table and figure that define separate regimes, and also by using Yazaki's[58] definition of $\omega\tau \gg 2$ (angular frequency and thermal relaxation time, which Tijdeman[55] used to unite all of the different tube regimes under one mathematical framework, without having to apply different assumptions to Kirchoff's original equations), it can be seen that for both samples, the slit-widths measured range from the 'wide-tube' regime, to the 'wide-to-narrow-tube' transition regime, each of which have been chosen for representation in figure 4.9. Yazaki's experimental and theoretical work have been included for reference in figure 4.10.

Comparison between our results and Weston's/Stinson's show that the behaviour of particle velocity, excess temperature and phase fronts for the $w = 1.00$ mm slit matches those of Weston's and Stinson's wide-tube predictions. In this regime, the motion is mostly adiabatic; the thermal boundary layers do not overlap. Hence both thermal and viscous loss mechanisms play an important role in the behaviour of the resonator. The generation of a thermal wave occurs in the thermal boundary layer as excess heat is conducted to the isothermal region, while the shear forces between particles generate a lossy viscous wave inside the viscous boundary layer (section 2.4). These effects are directly illustrated by the particle velocities $|v_\mathrm{x}|$, $|v_\mathrm{z}|$ and excess temperature ΔT falling to zero at the slit-walls. Note, the small peak in each of these values near the walls are a result of the Bessel functions in Kirchhoff's formulae. Toward the centre of the cavity, $|v_\mathrm{x}|$ and ΔT stabilise to their adiabatic values, while $|v_\mathrm{z}|$ falls to zero - the normal particle velocity switches sign across the cavity and integrates to zero, its effect being to distribute the extra forces generated by the boundary layers at the walls across the cavity cross section[54].

The 'narrow-tube' regime differs from the 'wide-tube' one in that since the thermal boundary layers have overlapped in the latter, the whole tube takes on Newton's isothermal speed of sound. Thus no loss can occur from conduction between adiabatic and isothermal regions, the remaining losses are of pure viscous form (ignoring intrinsic losses). The behaviour of the plotted quantities in figure 4.9 for the $w = 0.15$ mm slit is closer to the behaviour of the 'narrow-tube' prediction shown by Stinson, although strictly not falling into that category, as the thermal boundary layers have not quite overlapped - it is clearly different to the wide-tube regime however, which is why a transition regime definition was deemed necessary by Weston.

A different way to measure the contribution of separate boundary layer mechanisms

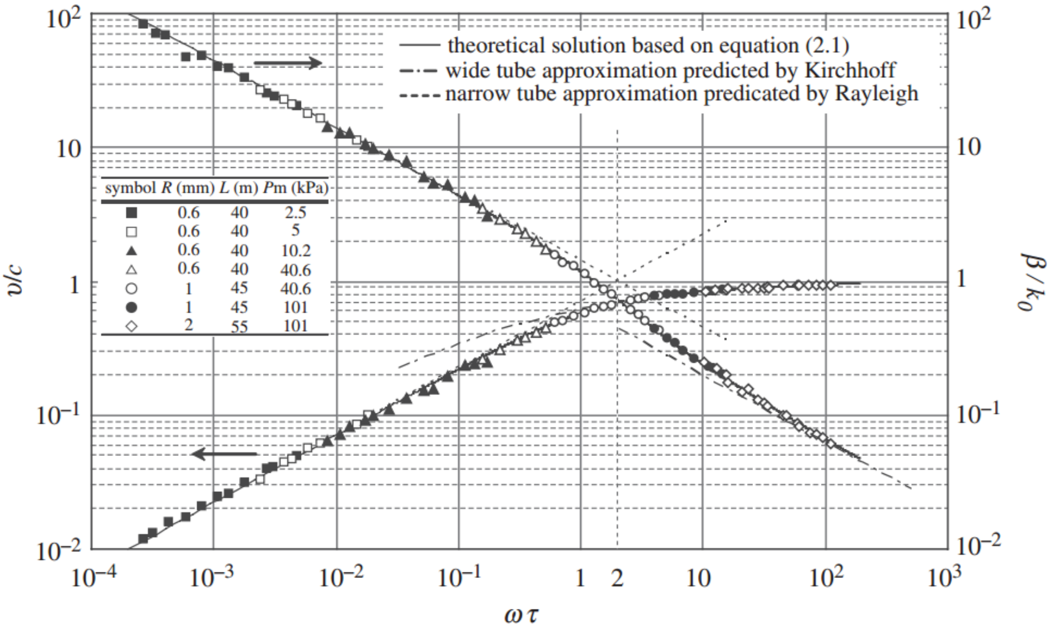

Figure 4.10: Experimental and theoretical results of Yazaki et al.[58] (figure 3 in their work, where a detailed explanation is presented), showing the change in effective speed of sound here labelled v through a long tube as a function of $\omega\tau$, explained in the main text. Also shown (the data with a negative gradient) is the measured change in signal attenuation caused by the boundary layers, represented by scaled propagation constant β. The dashed vertical line represents the point at which propagation within the tube becomes purely isothermal.

is shown by the FEM modelling in figure 4.11, which plots the contribution of the thermal and viscous boundary layers to the resonant frequency f'_{FP} reduction separately. This is achieved in the loss-inclusive FEM model by either reducing the kinematic viscosity ν of the air to zero (thus removing the viscous boundary layer), or by reducing the thermal diffusivity of the air α to zero (thus removing the thermal boundary layer). The frequency ‘turn down’ is present when each type of boundary layer is isolated in this way, once more confirming that, as realised by Tijdeman[55], both the thermal diffusivity and the viscosity contribute to the turn down and can be subsumed within a single constant, the exact nature of amalgamation dependent on the slit-width. This is perhaps a better way of interpreting Kirchhoff’s equations, Tijdeman[55], showed that $S = \frac{r}{\delta_\nu}$ (r is the tube radius) is the universal parameter describing the propagation of sound through narrow-tubes, allowing all regimes to be unified and showing that the terms ‘wide-tube’ and ‘narrow-tube’ are arbitrarily defined (their results are presented in figur 4.10). Using Tijdeman’s definition of when the sound propagation within the tube becomes isothermal ($\omega\tau < 2$), it is predicted that slit-widths of ~ 0.06 mm and ~ 0.09 mm are required for the slit-array and single-slit samples to support purely

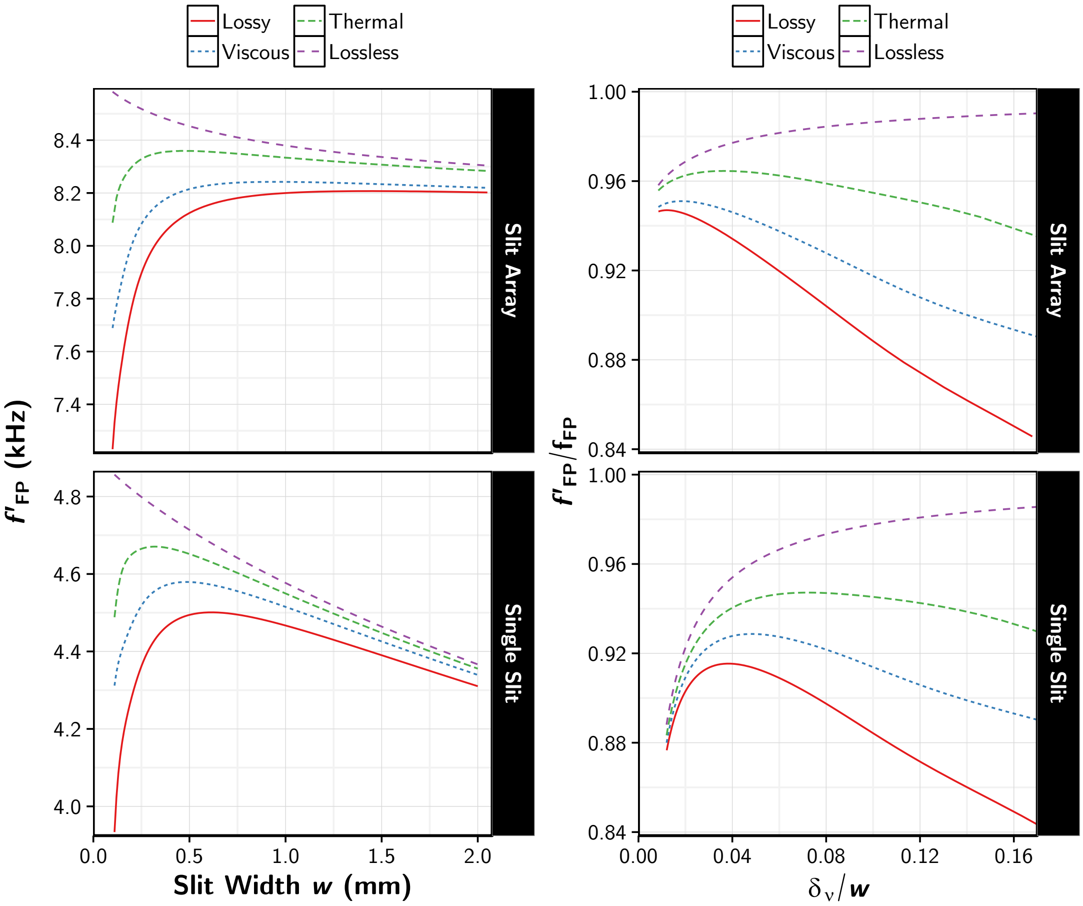

Figure 4.11: (Left column) Data from the FEM model showing the fundamental resonant frequency of each slit-cavity f'_{FP} plotted as a function of the slit-width w, with the effect of separate loss components compared. The solid red line represents the full lossy model with both viscous and thermal loss mechanisms present. The dotted blue line is the result of 'turning off' the thermal boundary layer (by setting α of the air to zero) , leaving just the viscous loss mechanism, with the green dashed line being the opposite (by setting μ to zero). The dashed purple line is the result of disabling both loss mechanisms. The top and bottom panels represent the slit-array and single slit samples, respectively (labelled). (Right column) Generalised form of the left column, where the fundamental resonant frequency of each slit-cavity f'_{FP} is normalized to that predicted by the Fabry-Perot condition f_{FP} as a function of the ratio of viscous boundary layer thickness δ_v to slit-width w.

isothermal propagation. Also note, with no kinematic viscosity ν, the sharp reduction in f'_{FP} does occur at a smaller w, as the viscous loss that has been eliminated has a larger characteristic thickness than its thermal counterpart in air (the Prandtl Number $P_r = 0.7$).

4.9 Conclusions

In this chapter, the resonant transmission of sound in narrow air slits ($100w < \lambda_0 < 300w$) through both a subwavelength periodic slit-array ($8\lambda_{\mathrm{g}} < \lambda_0 < 14\lambda_{\mathrm{g}}$) and a single slit-cavity has been measured for a range of slit-widths. It was found that slit-widths an order of magnitude larger than viscous and thermal boundary layer thickness showed a significant reduction in resonant frequency and substantial damping of the resonance compared to the simple end-corrected Fabry-Perot condition and to lossless modal matching models[27]. A detailed discussion of the thermodynamic effects that cause this frequency reduction is included, with comparisons to work previously done by Weston[54], Tijdeman[55] and Stinson[57], where it is concluded that the boundary layers cause a significant reduction in the effective speed of sound through each cavity. Not only does this study show that boundary layer effects play a significant role in slit-cavities where they only form a tiny fraction of the whole width (e.g. in a 1 mm air-filled slit at 5 kHz), but it also opens up new possibilities for metamaterial design. Irrespective of the solid material used, a simple rigid-walled cavity filled with air can act as a broadband absorber, and the effective speed of sound inside it can be controlled via the slit-width.

Chapter 5

Acoustic Transmission Through Compound Subwavelength Slit-Arrays

5.1 Introduction

In the present chapter, the angular dependence of the transmission of sound in air through four types of two-dimensional slit-arrays, each formed of aluminium slats, is explored. Both experimental and numerical methods are utilised. For a simple, subwavelength periodic slit-array, it is well known that Fabry-Perot-like wave-guide resonances, supported by the slit-cavities and coupled to diffracted evanescent waves, result in 'Enhanced Acoustic Transmission' at frequencies determined by the length, width and separation of each slit-cavity (section 2.7). It is demonstrated that altering the spacing or width of some of the slits to form a compound array (i.e. an array having a basis comprised of more than one slit) results in sharp dips in the transmission spectra, that may have a strong angular dependence. These features correspond to 'phase-resonances', which have been studied extensively in the electromagnetic case[110,111,112,113,114,115]. This geometry allows for additional near-field configurations compared to the simple array, whereby the field in adjacent cavities can be out-of-phase. This allows the excitation and diffraction of trapped acoustic surface waves that posses a greater in-plane wave-momentum than those supported by a simple grating structure. Several types of compound slit-array are investigated; one such structure is optimised to minimise the effect of boundary-layer loss mechanisms present in each slit-cavity, thereby achieving a deep, sharp transmission minimum in a broad maximum.

5.2 Background

The experimental discovery of Extraordinary Optical Transmission (EOT) through subwavelength hole arrays[19] opened a whole new area of research into how structured resonant layers can affect the propagation of light. This research has been extended to the acoustic case, where similar behaviour is observed, sometimes termed Enhanced Acoustic Transmission (EAT)[74,116,35,87,27,28] (not extraordinary, since below the acoustic waveguide cut-off frequency, longitudinal sound waves can still propagate as plane waves through gaps/holes in rigid sound-hard bodies, as explained in section 2.6). The observed phenomena for both electromagnetic and acoustic cases in such structures are due to complex interplay between surface-wave (or surface-wave-like) modes and waveguide (Fabry-Perot-like) modes, the exact nature being dependent on many structural parameters[117,35,27,28].

Other types of transmission anomaly have been discovered in the electromagnetic case that stem from EOT. One such anomaly is the ‘phase-resonance’, which appears as a sharp dip in the transmission of transverse-magnetic polarised light through ‘compound grating’ structures[110,111,112,113,114,115]. In the case of a two-dimensional metal slit-array this can be achieved by having unequally-sized slits, or multiple slits in each period (i.e. unequally-sized metal slats). In a singularly periodic grating structure, symmetry requires that the fields in all slit-cavities are identical when excited by a normally incident planar wave. Compound gratings introduce new degrees of freedom to the near-field configurations, and at specific frequencies fields in adjacent cavities may be both out-of-phase with one another and strongly enhanced[111] leading to ‘phase-resonant’ features in their electromagnetic response. Being simply a lattice/symmetry phenomenon, there is an expectation that these phase-resonances will also exist in the acoustic case[118,106,119].

Here, the existence of the airborne acoustic phase-resonance is experimentally demonstrated with a compound slit-array grating, where good agreement with numerical model predictions is found. One of the grating structures is then optimised via modelling to achieve stronger coupling to its phase-resonance excitable at normal incidence, accounting for viscous and thermal boundary layer effects that have a significant importance in the phase-resonant coupling mechanism. Finally, the existence of the phase-resonance is explained in terms of the band-folding of an acoustic surface wave, with extra degrees-of-freedom available to the near-field allowing the ASW to exist at, and hence be diffracted from, larger wavevectors. Being coupled to ASWs, different phase-resonant configurations can occupy different energies depending on their structure factor, the finer details of which are also discussed.

5.3 Sample Design and Experimental Set-Up

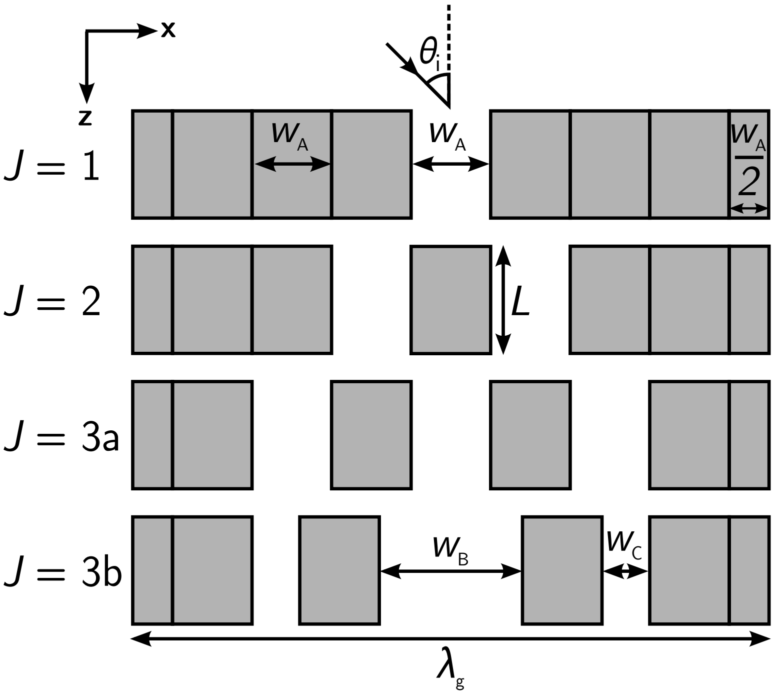

Figure 5.1: Schematic of a unit cell of each array sample (not to scale). The grey blocks represent the aluminium slats that form the sample, of width $w_{\rm A} = 2.9$ mm, and length $L = 19.8$ mm. The air gaps that form the cavities are the same size as the slats, except for the $J = 3$b sample, where the central cavity $w_{\rm B}$ has width 5.9 mm, and the outer two have $w_C = 1.5$ mm. Each sample has a period $\lambda_{\rm g} = 8w_{\rm A} = 23.2$ mm.

The periodic unit-cells that form the experimental samples are illustrated in figure 5.1, and the measurement set-up in figure 5.2. J denotes the number of slits per grating period, with $J = 3$a and $J = 3$b having the same number of slits but with different slit-width ratios. Such gratings are formed of aluminium slats of size 600 mm × 2.9 mm × 19.8 mm, stacked in a wooden sample holder, with small polyester spacers used to create the appropriately-sized air gaps. The total sample area is 560 mm × 400 mm, and it is placed with the slats vertical, on a rotating table, symmetrically situated between two spherical mirrors 3 m apart, of radius 220 mm and focal length 1 m. One mirror collimates the sound of a speaker placed at its focal point, directed so that the beam is normal to the face of the slit-cavities when the rotating table is set to $\theta_{\rm i} = 0°$(normal incidence) producing a beam-width smaller than the sample face to approximate an infinite sample size. The other mirror focuses the beam transmitted through the sample on to a Brüel and Kjær 4190 microphone. The speaker is driven by a signal generator producing a Gaussian pulse centred on 8 kHz, containing a broad

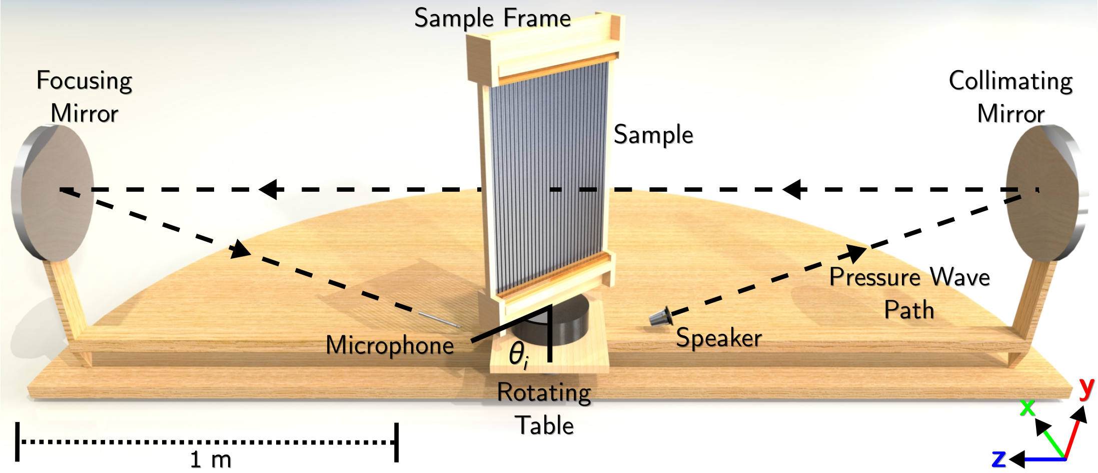

Figure 5.2: To-scale schematic of the transmission measurement experimental set-up, labelled accordingly. The speaker was placed at the focal point of the first mirror, which directed the collimated beam toward the sample. The transmitted signal was then focused on to the microphone by the second mirror. The sample frame was placed onto a computer controlled rotating table, allowing control of the incident angle θ_i. Acoustic absorber was placed at appropriate positions to reduce unwanted reflections from the solid surfaces that make up the measuring kit (not shown).

range of audible frequencies. The sample is rotated over the range $-2.5^\circ \leq \theta_\mathrm{i} \leq 65^\circ$ (limited by the sample size and frame), and the averaged time-domain signal from multiple pulses of the speaker for each angle is recorded by a PC-based oscilloscope. To account for small leakage of the signal around the sample, a large sound-opaque slab with anti-reflection absorber foam attached is placed on the incident side of the source. Transmission measurements are then repeated for all angles, and the resulting data subtracted from the original sample data in the time-domain spectra, leaving only the signal transmitted through the sample holder. This is then Fourier analysed to obtain the angular dependent frequency response of the sample. A reference spectrum for each angle is obtained by repeating the experiment with only the wooden sample frame in place, and used to normalise the transmitted signal in the frequency domain. Further detail on this experimental method is presented in section 3.4.

5.4 Normal Incidence Transmissivity Spectra

Figure 5.3 shows the transmissivity spectra for each sample when probed at normal incidence, as a function of the ratio of array periodicity λ_g to incident wavelength of radiation λ_0. Also included are the predicted spectra calculated using the Finite-Element-Method (FEM) detailed in section 3.7. The red dashed line is the result obtained from the model solving the lossless acoustic wave equation (equation 2.18), while the blue

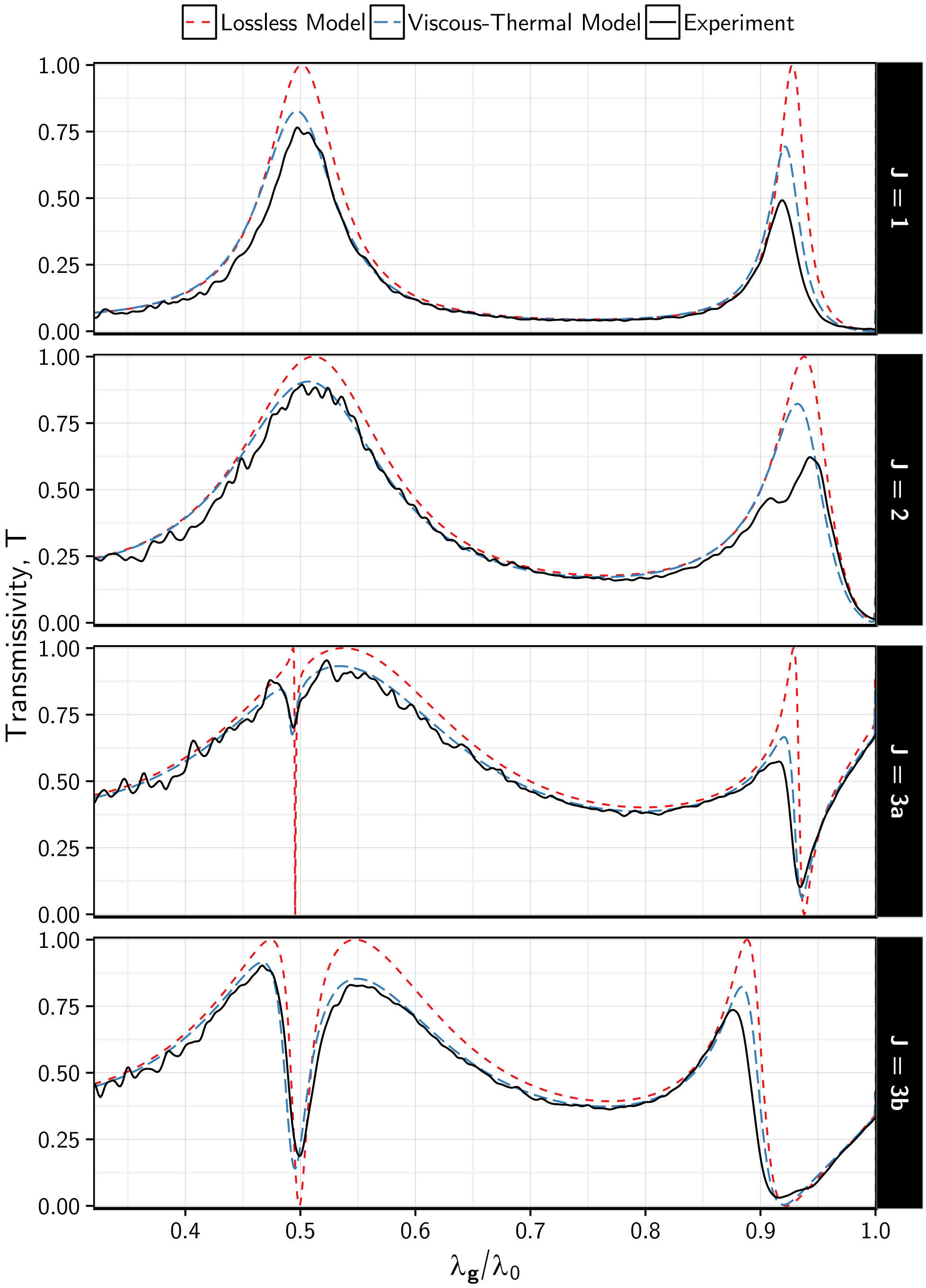

Figure 5.3: Normal incidence transmissivity T spectra as a function of the ratio of array periodicity λ_g to incident radiation wavelength λ_0 for each of the sample types illustrated in figure 5.1. The solid black line is the experimental data, the short-dashed red and long-dashed blue lines are the lossless and viscous-thermal loss-including numerical model spectra for comparison. The diffraction edge for each experimental sample occurs when $\frac{\lambda_g}{\lambda_0} = 1$. Fluctuations in the ambient temperature are accounted for in the calculation of λ_0.

long-dashed line comes from a model that solves the linearised Navier-Stokes equation (equation 2.23) and allows heat conduction within the air (equation 2.22), thus accounting for viscous and thermal boundary layer effects at each rigid, sound-hard wall, the importance of which, in the context of resonant-cavity-based metamaterials, is discussed at length in chapter 4. The position of the onset of diffraction corresponds to $\frac{\lambda_\mathrm{g}}{\lambda_0} = 1$. The calculated incident wavelength for each sample takes into account changes in ambient temperature T_0 between measurements which varied between 18 K and 21 K, acting to vary the adiabatic speed of sound in air c. Atmospheric pressure and humidity changes have negligible effect on these measurements[50,44].

It is well known that sound incident on an air cavity bounded by two parallel, infinitely wide, rigid-solid walls of length L will have a broad transmission peak at a frequency naïvely predicted by the Fabry-Perot (FP) condition, $f_\mathrm{FP} = \frac{nc}{2(L+\Delta L)}$, where n is an integer (section 2.6), hence for the fundamental resonance, $\lambda_\mathrm{FP} = 2(L + \Delta L)$. There is a correction ΔL that takes into account end effects at the exit/entrance of each cavity. For each flanged open-end of the cavity this correction is to first order approximated by $\Delta L = \frac{8w}{3\pi}$, w being the width of the slit[75,28]. When such cavities are placed in an equally spaced array of period λ_g, such as in sample $J = 1$, the radiation impedance term $\mathbf{Z}_\mathrm{r}$ (see section 2.7)that determines the end effect changes significantly[28,76], resulting in the build-up of diffractive evanescent waves[71]. As explained in section 2.7, the coherent effect of these evanescent waves is to form a collective resonance, effectively creating a finite impedance mismatch. This gives rise to an air-bound Acoustic Surface Wave (ASW) that is guided along the surface of the grating but decays exponentially away from it. The enhanced fields associated with the ASW on each face of the array couple together via the FP-like modes within the slit-cavities, forming Fabry-Perot-Evanescent-Waves (FPEVs) (see section 2.7 for more detail). This is the mechanism by which EAT can occur at specific frequencies, where on resonance the effective impedance of the grating can match that of the air (excepting losses) and result in large peaks in its transmission spectrum[76]. Indeed, figure 5.3 shows two broad peaks in the $J = 1$ spectrum, at $\frac{\lambda_\mathrm{g}}{\lambda_0} = 0.5$ and 0.92. These correspond to the first and second order FPEV modes, with the frequency of the $n = 2$ mode perturbed by the strong evanescent diffracted fields near the onset of diffraction (i.e., the waveguide modes within the cavities are so strongly perturbed by the diffracted fields that the FPEV is more ASW-like than FP-like). This mechanism has been studied extensively in the past decade[87,35,27,28,76].

The transmission spectrum of the $J = 2$ sample is little different, except for a slight broadening of the FPEV modes and a small upward frequency shift due to a reduction in the strength of the Fourier amplitude component of the grating profile that causes first order scattering (and, as will be explained later, the ASW that hybridises with

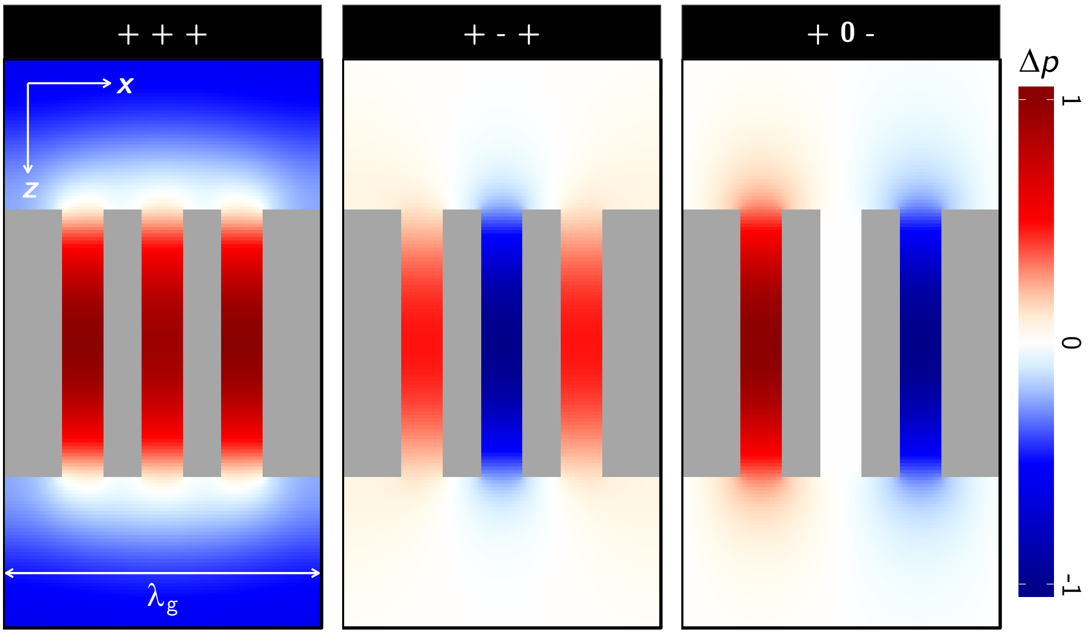

Figure 5.4: FEM simulations of the instantaneous pressure fields Δp corresponding to the three available eigenmodes '$++ +$', '$+-+$', and '$+ \ 0 \ -$', of the $J = 3a$ system when there is no net phase shift along x between unit cells, shown at a temporal phase corresponding to maximum field amplitude. The colour scales have been normalised with normalisation constants 2.19, 4.01 and 3.39 respectively. The three eigenmodes have resonant frequencies which correspond to $\frac{\lambda_g}{\lambda_0}$ values of 0.54, 0.5 and 0.48 respectively. These were calculated using a loss-free FEM model. The grey blocks represent the aluminium slats, in the same orientation as illustrated in figure 5.1.

the FP resonance to create the FPEV now sits at a higher frequency). For the $J = 3$ samples, as well as further broadening and upward-frequency-shifting of the FPEV modes, a new feature, the 'phase-resonance', appears in the low frequency wing of each primary resonance. As described in the electromagnetic case by both Skigin et al.[111] and Hibbins et al.[113], this is because there is a new degree of freedom available to the system. In the $J = 1$ and $J = 2$ cases, the fields in each adjacent cavity must have identical phase at normal incidence, hence an incident planar wave cannot excite a phase-resonance. However, with three cavities per period, the outer two slits have different surroundings to the central one. Hence, by symmetry, two field configurations can now be excited at normal incidence; all of the fields in-phase (labelled the '$+++$' mode), and the central and outer cavity fields out-of-phase (the '$+-+$' mode, where '$-$' corresponds to a phase shift of π radians relative to '$+$'). This is illustrated in (both) figures 5.4 and 5.5.

Figure 5.4 shows the instantaneous pressure field of the eigenmodes of the $J = 3$a system with no net phase change across the unit cell in the x direction (which simulates excitation by a plane wave at normal incidence), calculated with the lossless FEM model, and normalised to their maximum amplitude of Δp, different for each mode. The mode labelled '$+++$' corresponds to the primary resonance at $\frac{\lambda_g}{\lambda_0} = 0.53$, where all of the fields within the cavities are resonating in-phase, with similar amplitude. This is the FPEV mode that is highly radiative and results in the broad transmission peak, with the maximum absolute pressure amplitude within the slits being 3.1 times greater than in the incident wave. The second panel, with the mode labelled '$+-+$', illustrates the phase-resonance eigenmode that is excitable at normal incidence. The outer two cavities are oscillating exactly π radians out of phase with the central one, which, as the colour scale shows, has a greater field amplitude. Note, the maximum absolute pressure field amplitude within the cavities has now become 55.7 times greater than in the incident wave, a significant increase compared to the '$+++$' mode, indicating a stronger degree of localisation. Another interesting feature is the apparent standing wave that has formed in the x-direction, seen from looking at just the top or bottom of the slits; the cavity resonances appear to be coupled with each other within a single unit-cell. There is a third field configuration available in the form of the anti-symmetric '$+\ 0\ -$' mode, where the outer two cavities are π radians out-of-phase with each other, and $\pi/2$ radians out-of-phase with the central cavity, in which there is no mode amplitude. The $J = 2$ configuration supports a similar '$+-$' mode, but in neither configuration are these modes excitable by an incoming plane wave at normal incidence, as they each have an opposite-phase degenerate pair and thus a phase-change along the surface in the x direction is required to excite one of them (incidentally, a weak feature has appeared in the experimental data for the $J = 2$ sample as the collimating mirror does not produce a perfect planar wave, and allows weak coupling to one of these modes). Direct coupling to any of the phase-resonant configurations is impossible as the pressure field within the slit-cavities is out of phase with the incident field. Hence, they can only be excited via coupling between slits, and appear as sharp dips in transmission within the primary '$+++$' FPEV resonance peak.

Another way of illustrating the phase-resonance is shown in figure 5.5, which is a plot of the numerically calculated phase difference $|\Delta\phi_{\text{Inner, Outer}}|$ of the velocity field v_x between the central and outer slits, evaluated at the mid-width of the transmitting side of each slit-cavity. The structure was excited by a normally incident planar wave, with varying frequency. For both $J = 3\text{a}$ and $J = 3\text{b}$ samples, at frequencies corresponding to the position of the transmission dips in figure 5.3, the lossless acoustic wave equation model (red dashed line) predicts a π radian phase difference between the slits, while away from these resonances and below the onset of diffraction, $|\Delta\phi_{\text{Inner, Outer}}|$ is close to zero.

To obtain the strongest possible reduction in transmission at the phase-resonance

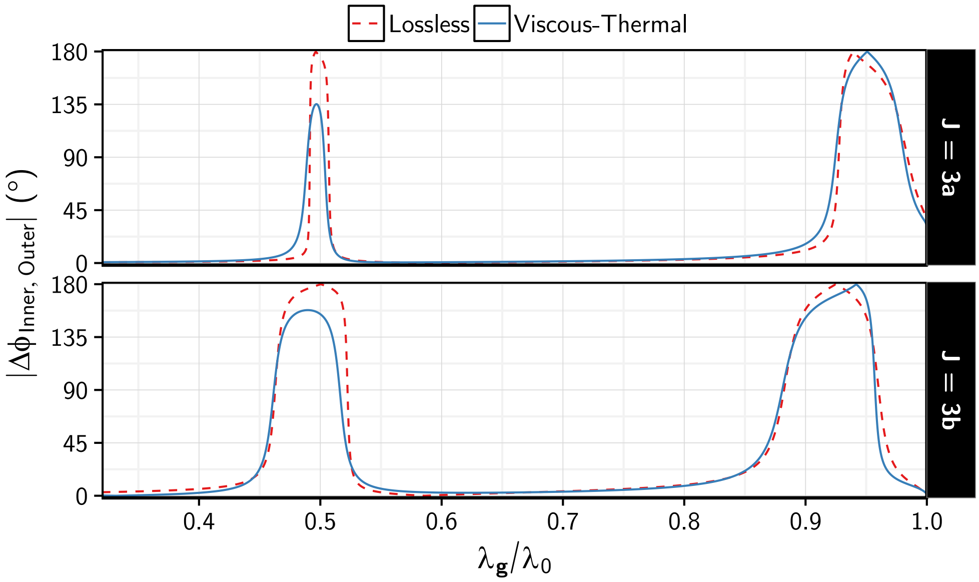

Figure 5.5: Lossless (dotted red line) and viscous-thermal (solid blue line) FEM models of the difference in the phase $|\Delta\phi_{\text{Inner, Outer}}|$ of the tangential particle velocity v_{x} of the central and outer cavities, for the $J = 3\text{a}$ and $J = 3\text{b}$ samples, plotted as a function of the ratio of array periodicity to incident wavelength $\frac{\lambda_g}{\lambda_0}$. The predicted diffraction edge is at $\frac{\lambda_g}{\lambda_0} = 1$. Phases were evaluated in the centre of each cavity on the transmitting side of the grating.

frequency, there must be perfect balance between the radiative and non-radiative losses in the system. This is the well known 'critical coupling condition'. Non-radiative thermodynamic loss effects form a part of this balance and thus must be accounted for. With sample $J = 3\text{a}$, the '$+ - +$' resonance is a weak feature in the experiment, only reducing transmission by 15% at $\frac{\lambda_g}{\lambda_0} = 0.49$, being much stronger in the second order mode ($\frac{\lambda_g}{\lambda_0} = 0.94$), reaching a reduction of $\sim 50\%$. The lossless FEM model, solving the acoustic wave equation, predicts a very sharp, 100% deep resonance at $\frac{\lambda_g}{\lambda_0} = 0.49$ in the transmission spectrum. However, when viscous-thermal contributions are included (via solving of the linearised Navier-Stokes equation 2.23 and allowing heat conduction within the gas), which results in a much better agreement with the experimental data, this resonance is significantly more damped. The effect stems from the viscous-thermal boundary layers at the rigid, sound-hard walls, that cause significant attenuation of the fields within the slit-cavities, as was measured in chapter 4. Note, it has been verified that a simpler model including only a bulk-loss term added to the free-space acoustic wave equation (section 2.4.3) does not predict the increased damping effect; once again, it is the boundary-layer loss rather than the loss intrinsic to the air that is having such a large effect on the resonances, despite forming a tiny fraction of each slit-cavity (in this case < 1 %, an *even smaller* fraction than the largest slits studied in chapter 4).

Sample $J = 3\text{b}$ is optimised geometrically to balance the radiative and non-radiative loss effects as close to critical coupling as possible while keeping periodicity and slat-size constant. This grating is a simple modification of the $J = 3\text{a}$ sample, with an inner-cavity-to-outer-cavity-width ratio of around four-to-one. As figure 5.3 shows, the experimental data exhibits a much deeper, broader phase-resonance in both the fundamental and second order modes. Figure 5.5 gives extra insight into this phenomenon, showing that the loss-inclusive model for the $J = 3\text{a}$ sample predicts a maximum $|\Delta\phi_{\text{Inner, Outer}}|$ of $\sim 0.75\pi$ radians at the occurrence of the phase-resonance, while it reaches $\sim 0.9\pi$ radians for the optimised $J = 3\text{b}$ sample, thus displaying stronger coupling to the '$+ - +$' eigenmode.

5.5 Mapping the Mode Dispersions with Angle-Dependent Transmissivity Spectra

By recording angle (θ_{i}) dependent transmissivity data, the mode dispersion is mapped and a greater understanding of their origin is attained. Figure 5.6 shows the transmissivity of each grating as a function of the ratio of array periodicity to incident wavelength, and reduced in-plane wave vector $\frac{k_{\text{x}}}{k_{\text{g}}}$, where $k_{\text{x}} = k_0 \sin\theta_{\text{i}}$ and $k_{\text{g}} = \frac{2\pi}{\lambda_{\text{g}}}$.

The simplest $J = 1$ grating exhibits a fundamental mode that is largely flat-banded, being strongly localized in the slit-cavity with FP-like fields, where the cavity's length L and width w_{A} are the dominant variables in determining the resonance position, the surface wave hybridisation being of less importance. This mode starts from just below the FP frequency at $k_{\text{x}} = 0$, and only becomes perturbed as the diffracted sound line from $k_{\text{x}} = k_{\text{g}}$ is approached. There is similar perturbation of the second order FPEV mode ($\frac{\lambda_{\text{g}}}{\lambda_0} = 0.9$), although as this mode is far closer to the diffraction edge at $\frac{\lambda_{\text{g}}}{\lambda_0} = 1$, the periodicity and thus coupling between adjacent cavities dominate the position of this resonance: the second order mode is more ASW-like than FP-like[35,28].

Additional transmission dips become apparent in the response of the $J = 2, 3\text{a}$ and 3b samples at $\frac{\lambda_{\text{g}}}{\lambda_0} = 0.5$ and $0.1 \leq \frac{k_{\text{x}}}{k_{\text{g}}} \leq 0.4$. These are the anti-symmetric phase-resonances that can now be excited with the addition of a phase difference along the grating surface[111,113], associated with $\theta_{\text{i}} \neq 0$. For $J = 2$, at high k_{x} it is now possible to excite the '$+ -$' mode, were the two cavities are π radians out-of-phase. The $J = 3\text{a}$ and $J = 3\text{b}$ samples also exhibit the additional feature, which has appeared on the low frequency wing of the FPEV resonance at $\frac{\lambda_{\text{g}}}{\lambda_0} = 0.5$. This corresponds to the anti-symmetric '$+\ 0\ -$' phase-resonance shown in figure 5.4. In all cases, one can see that at least one of the phase-resonances has a strong k_{x} dependence, indicating that they are surface-wave-like in character. It is possible to deploy a surface-wave band-folding

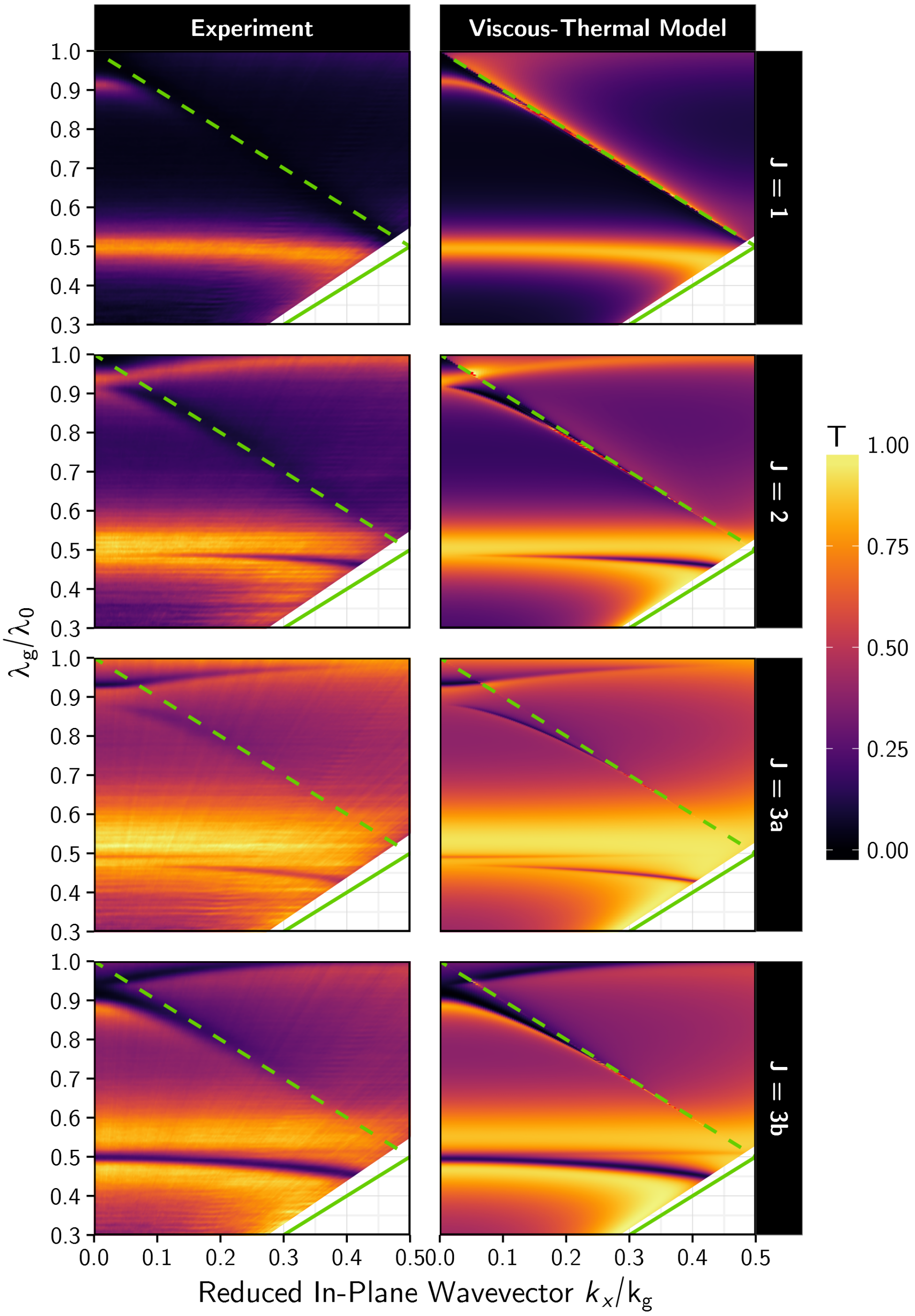

Figure 5.6: Transmission data illustrating mode dispersion for each sample illustrated in figure 5.1, labelled accordingly. The ratio of array periodicity to incident wavelength $\frac{\lambda_g}{\lambda_0}$ is plotted as a function of reduced in-plane wavevector $\frac{k_x}{k_g}$, where a value of $\frac{k_x}{k_g} = 0.5$ corresponds to the first Brillouin zone boundary. The left column are the recorded experimental data, whereas the right column are the numerical results calculated by the viscous-thermal loss inclusive FEM model. For reference, a solid green line representing grazing incidence k_0 is included on each plot. The onset of first order diffraction is represented by the green dashed line. Fluctuations in ambient room temperature are accounted for in all calculations of λ_0.

picture to explain the dispersion relations in figure 5.6, like those introduced in section 2.7.4. To understand this it is helpful to plot the band-structure of each sample using the extended zone scheme representation, i.e., by drawing the band-structure without band-folding present. This is illustrated in figure 5.7.

Adding cavities to the structure of each periodic unit-cell opens up new degrees of freedom to the system, and allows coupling of the phase-resonant near-field configurations to diffracted fields (ASWs) that originate from the diffractive end effects. Figure 5.7 is a plot of the underlying band structure of the eigenmodes of the $J = 1$, $J = 2$ and $J = 3\mathrm{a}$ samples, in the form of a dispersion diagram with the same axes as those in figure 5.6. The eigenfrequencies were calculated using the loss-inclusive FEM model. Note that the thermodynamic losses strongly affect only the coupling strength to each mode in this instance, the band structure changing with only a slight reduction in the frequency of each band.

With one cavity per unit-cell, the $J = 1$ configuration has only two modes available (considering only first order cavity-resonance harmonics); the naturally radiative primary FPEV resonance (denoted by the solid red line) and the low frequency ASW (denoted by the solid blue line). The latter is only accessible in the non radiative regime as it has in-plane-wavevector $k_\mathrm{x} > k_0$. Here, k_0 is represented by the black dashed line, i.e. the ‘sound line’, this is the wavevector that a grazing incidence pressure wave would possess. Since this structure has only one cavity per unit cell, and the sample walls can be treated as perfectly rigid, the only degree of freedom available to the near-field is the cavity being either a positive or negative anti-node, which is the fundamental FP-like cavity resonance. This means that any mode that has a shorter surface wavelength λ_x than the spacing of the cavities λ_g **cannot** exist in the non-radiative regime, as they require a pressure field maximum within the walls, and zero within the cavities. This is not possible, since the walls are effectively perfectly rigid (as discussed in section 2.7, there may be a pressure maximum above the rigid walls in the non-radiative regime only if $\lambda_\mathrm{g} > \lambda_\mathrm{FP}$, which would not be a subwavelength grating structure, hence not of interest to this work). Thus, beyond the first Brillouin zone at $k_\mathrm{x} = \frac{k_\mathrm{g}}{2}$, the ASW ceases to exist in the non-radiative regime - this mode instead hybridises with the otherwise non-dispersive and naturally radiative FP cavity mode[27,35]. So, at normal incidence, with band-folding (where the grating periodicity k_g can be added or subtracted to any mode, thereby scattering non-radiative modes into the radiative regime), only the primary FP-like mode which has surface wave character (an FPEV) is excitable. Note that because of the ASW hybridisation, the FPEV mode is fixed at the crossing point of the sound-line k_0 at the first Brillouin zone, becoming just a grazing wave (see section 2.7). The ratio of grating pitch λ_g to cavity length L (hence λ_FP) will determine exactly how the FPEV evolves with k_x.

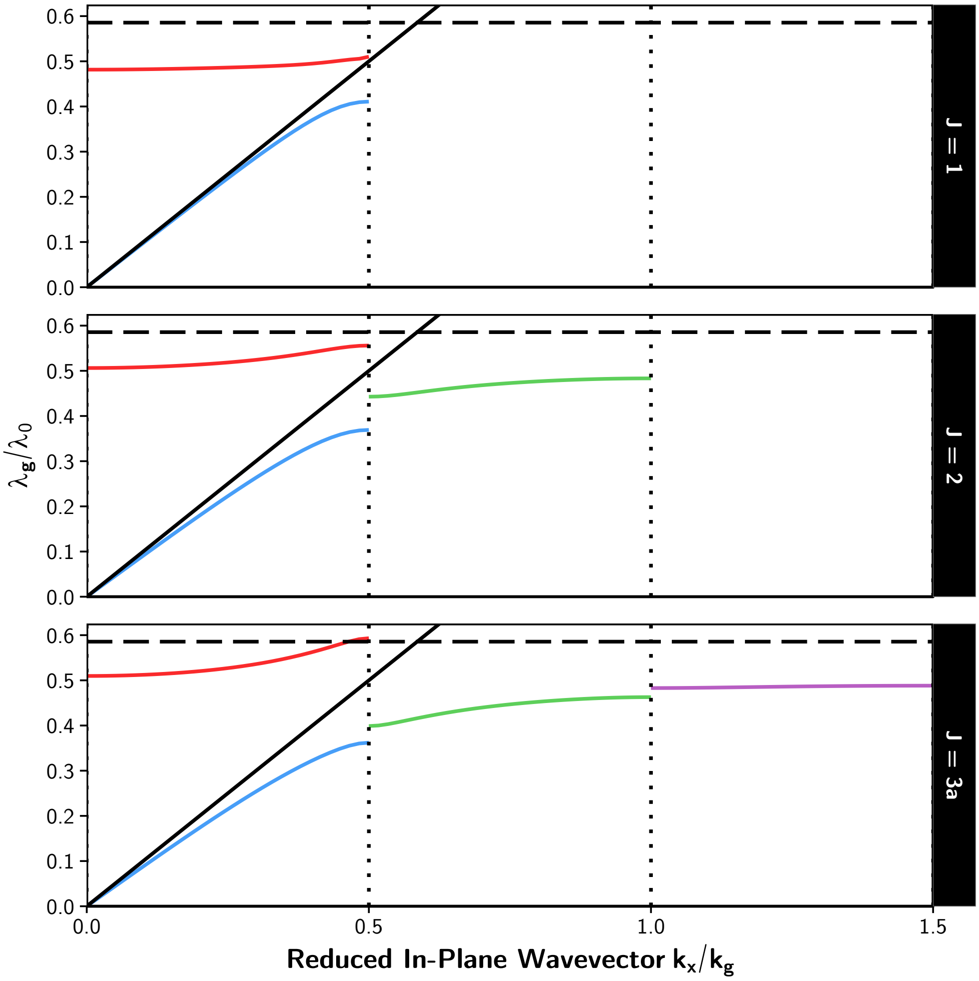

Figure 5.7: Dispersion diagrams showing the extended zone scheme representation of the eigenmodes of the $J = 1$, $J = 2$ and $J = 3\text{a}$ systems (all labelled), plotted as a function of the ratio of array periodicity to incident wavelength $\frac{\lambda_\text{g}}{\lambda_0}$ vs reduced in-plane wave vector $\frac{k_\text{x}}{k_\text{g}}$. Individual eigenfrequencies were calculated using loss-inclusive FEM models. The sound line k_0 is represented by the black solid line. A horizontal black dashed line represents the resonant frequency predicted by the Fabry-Perot condition for a single open-ended slit-cavity. Integer and half integer values of $\frac{k_\text{x}}{k_\text{g}}$ correspond to different Brillouin zone boundaries, which have been marked with vertical black dotted lines. The solid coloured lines represent the different eigenmodes supported by each grating structure, with colours signifying different field configurations. Red is the naturally radiative FPEV mode, with blue being its fully non-radiative low frequency ASW. Green is the ASW coupled to the low energy phase-resonance field configuration, and purple is the ASW coupled to the high energy phase-resonance field configuration. Eigenmodes associated with the next FP harmonic are not included.

When there are two cavities per unit cell (sample $J = 2$), there is another possible field configuration apart from the FPEV '+ +' mode. The adjacent cavities can now oscillate π radians out of phase with each other, creating the anti-symmetric '+ −' (or '− +') phase-resonance. Now, it is possible for a ASW with a shorter wavelength in x than λ_{g} to exist, since the extra anti-node per unit cell it requires can be satisfied. Thus, the low frequency ASW which previously vanished from the non-radiative regime above $k_{\mathrm{x}} = \frac{k_{\mathrm{g}}}{2}$ now band-splits at this first Brillouin zone, and continues up to the next at $k_{\mathrm{x}} = k_{\mathrm{g}}$. This mode is represented by the green line in figure 5.7, and in the experiment, is band-folded back into the radiative regime by first order scattering from k_{g}, forming the deep, sharp resonance in the experimental data for the $J = 2$ sample at high k_{x}. Above $k_{\mathrm{x}} = k_{\mathrm{g}}$, the ASW again ceases to exist as a trapped mode; as before, it requires another anti-node per unit cell, and this is forbidden by the lack of a possible near-field configuration. Further, the creation of this extra non-radiative band by the extra degree-of-freedom allows the radiative FPEV mode to increase in frequency from k_0 at the first Brillouin zone boundary (where it was previously fixed) since it is no longer paired with the low frequency ASW; this mode now hybridises with an ASW band-folded from a larger wavevector and thus at a higher energy than for the simple grating. Hence, the FPEV mode rises in frequency (to its FP-limit), anti-crossing with the diffracted sound line at a lower wavevector than before, eventually interacting with set of ASWs that arise from the second FP harmonic (not shown in figure 5.7), as with rising frequency the grating ceases to be subwavelength.

Finally, by increasing the number of cavities per unit cell to three (sample $J = 3\mathrm{a}$), yet another degree of freedom is available in terms of near-field distribution. There is now the primary '+ + +' configuration, the '+ − +' mode, and the '+ 0 −' anti-symmetric mode. Thus, the three-anti-nodes-per-unit-cell condition required for wavevectors larger than $k_{\mathrm{x}} = k_{\mathrm{g}}$ is satisfied, the ASW band-splits at $k_{\mathrm{x}} = k_{\mathrm{g}}$ and extends to the next Brillouin zone at $k_{\mathrm{x}} = \frac{3k_{\mathrm{g}}}{2}$, where the same pattern repeats, and beyond this point the mode once again ceases to exist. The second order scattering at $k_{\mathrm{x}} = 2k_{\mathrm{g}}$ band-folds this ASW back into the radiative regime, resulting in the two sharp dips seen in the experimental dispersion data for the $J = 3\mathrm{a}$ sample (the band structure for the $J = 3\mathrm{b}$ sample is identical in shape since it has the same number of cavities per unit cell, only the coupling strengths and frequencies have changed). This is illustrated in figure 5.8, where the band-folded eigenmodes calculated using the loss-inclusive FEM model are overlaid onto the $J = 3\mathrm{a}$ experimental transmission data. One can see that the dips in transmissivity correspond to the diffracted ASWs. Once again the radiative FPEV mode is able to rise slightly higher in frequency, as it has hybridised with a higher frequency band-folded ASW than was previously possible. Using this band-folding picture it is easy to see that every time one adds an air cavity to the unit-cell,

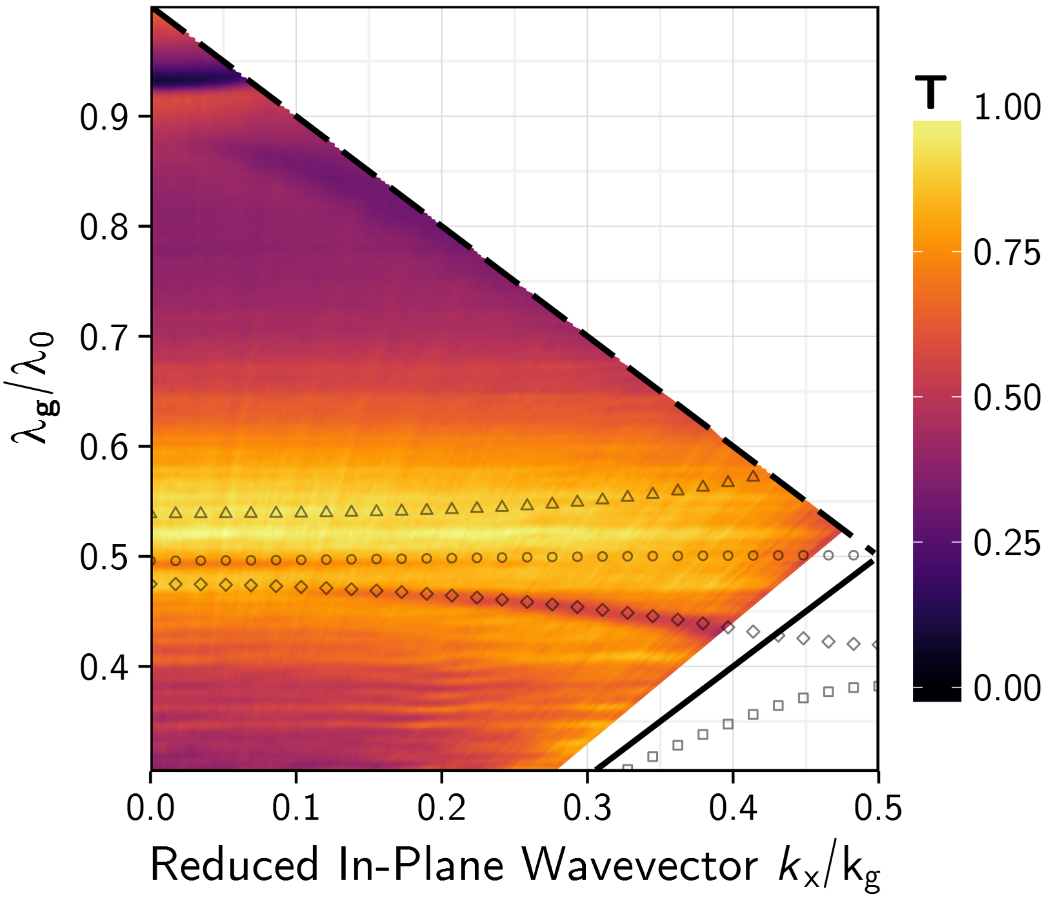

Figure 5.8: Mode dispersion illustrated by the experimental transmissivity T data for the $J = 3$a sample, with its numerically calculated eigenfrequencies associated with the first FP mode overlaid, plotted as a function of the ratio of array periodicity to incident wavelength $\frac{\lambda_g}{\lambda_0}$ vs reduced in-plane wave vector $\frac{k_x}{k_g}$. The value of $\frac{k_x}{k_g} = 0.5$ corresponds to the first Brillouin zone boundary. The solid black line represents the wavevector k_0 of a grazing incidence pressure wave. The onset of first order diffraction is represented by the black dashed line, being $\frac{\lambda_g}{\lambda_0} = 1$ at normal incidence ($\frac{k_x}{k_g} = 0$). The hollow points represent the different eigenmodes supported by the $J = 3$a grating structure, with shapes signifying different field configurations. The triangles are the naturally radiative Fabry-Perot like mode, circles are the ASW coupled to the '$+ - +$' phase-resonance and the diamonds are the ASW coupled to the '$+\ 0\ -$' phase-resonance. The squares are the non-radiative low frequency ASW which cannot be seen in this transmission experiment.

a new degree of freedom is available to the near-field, hence a shorter wavelength ASW is able to be band-folded back into the radiative regime, resulting in the appearance of a sharp dip in the transmission spectrum.

5.6 Ordering of Phase-Resonant Field Configurations

The frequency ordering of the phase-resonant field configurations at normal incidence is dependent on sample geometry. This is demonstrated by comparing the behaviour of samples $J = 3\text{a}$ and $J = 3\text{b}$ (figure 5.6). For the identical-width-cavity $J = 3\text{a}$ case, one can see that the '$+\ 0\ -$' configuration (not excitable at normal incidence) is occupied by the low energy band with high curvature, while the '$+ - +$' configuration is the high energy flat-banded mode scattered by $2k_{\text{g}}$. When the central slit is widened to create the $J = 3\text{b}$ sample, this behaviour is reversed, and now the low energy band is excitable at normal incidence. This is because widening the central cavity has redistributed the energies of the ASWs coupling to the '$+ - +$' configuration and the '$+\ 0\ -$' configuration, where the '$+\ 0\ -$' ASW now has the greater energy of the two (possessing a sharper field gradient along x), and is at a higher frequency. The FEM modelled phase-resonant field configurations at normal incidence for two adjacent unit-cells, shown in figure 5.9 (with corresponding FEM modelled dispersion diagrams) illustrate this mode switching behaviour. While it is clear the shape of the band structure does not change significantly between the samples, the model does predict the switching in frequency order of the field configurations, labelled modes 2 and 3 in the figure according to the order in which they occur with rising frequency.

This 'mode-switching' highlights another important point regarding the discussion of ASWs. At arbitrary values of k_{x}, it is meaningless to assign '$+\ 0\ -$' and '$+ - +$' labels to each of the modes, as there is no standing wave formed across the grating surface. This is only true when k_{x} is some integer or half integer value of k_{g}, hence the surface mode phase change is commensurate with the grating periodicity λ_{g} (the wavelength along x is the ASW wavelength, $\lambda_{\text{x}} = \lambda_{\text{ASW}} = \frac{2\pi}{k_{\text{x}}}$). In addition, such a labelling system still breaks down at the first Brillouin zone $k_{\text{x}} = \frac{k_{\text{g}}}{2}$; the π phase shift across each unit cell in the x direction requires that two grating wavelengths be labelled before the pattern repeats ($\lambda_{\text{ASW}} = 2\lambda_{\text{g}}$). This is shown in the field configurations at the first Brillouin zone boundary in figure 5.9. The phase shift of the ASW at this wavevector results in, for example, the '$+ - + - + -$' or '$+\ 0\ - -\ 0\ +$' configurations.

Incidentally, the order of the field configurations at normal incidence bears no relation to how they appear at this first Brillouin zone. At normal incidence, depending on from which Brillouin zone the mode was band-folded, λ_{ASW} is either λ_{g} or $\frac{3}{2}\lambda_{\text{g}}$ (or higher if there are more degrees of freedom available to the near field). If the mode

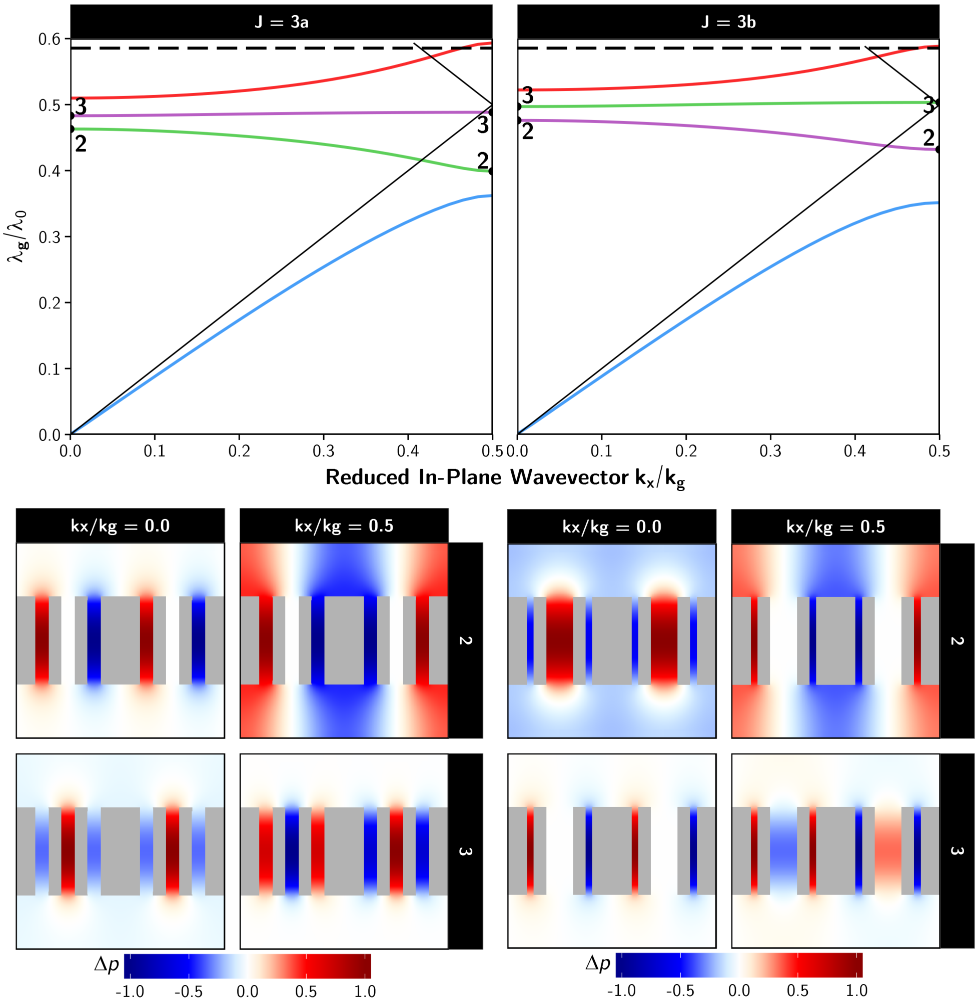

Figure 5.9: (Top) Dispersion diagrams showing FEM calculated eigenmodes of the two $J = 3$ samples associated with the fundamental cavity resonance, plotted as a function of the ratio of array periodicity to incident wavelength $\frac{\lambda_g}{\lambda_0}$ vs reduced in-plane wave vector $\frac{k_x}{k_g}$. The black dashed lines are the resonant frequency predicted by the FP condition, the black solid lines are the sound lines $k_0 \pm nk_g$. The coloured solid lines represent the band structure of the ASW, with different colours corresponding to different near-field configurations, as in figure 5.7. The purple and green lines have switched order between samples to highlight the change in energy of the phase-resonant field configurations at normal incidence. (Bottom Left) Instantaneous pressure field configurations across two unit cells of the $J = 3a$ sample showing the two possible phase-resonant modes, at either normal incidence $k_x = 0$ or at the first Brillouin zone boundary $\frac{k_x}{k_g} = 0.5$. The labelled numbers and k_x positions correspond to those marked by labelled black points in the corresponding dispersion plots. (Bottom Right) The same, but for the $J = 3$b sample. Note that compared to the $J = 3$a sample, the field configurations at normal incidence have reversed their order, while they have the same character at the first Brillouin zone boundary.

labelled '$+\ 0\ -$' is at the higher energy and thus band-folded from $2k_{\mathrm{g}}$, it will still evolve to look like the '$+-+-+-$' mode at the first Brillouin zone. The '$+-+-+-$' configuration's pressure field is forced through a π phase shift between every cavity as at $k_{\mathrm{x}} = 2k_{\mathrm{g}}$, $\lambda_{\mathrm{ASW}} = \lambda_{\mathrm{g}}/2$, so this field configuration always possesses a greater energy than the '$+\ 0\ -\ -\ 0\ +$' configuration no matter what the sizes or separations of the cavities are, as the latter has a wavelength of $\lambda_{\mathrm{ASW}} = 2\lambda_{\mathrm{g}}$ hence must occur at the first Brillouin zone boundary.

A further change in behaviour is visible when the central cavity is widened. In the $J = 3$b sample, the '$+\ 0\ -$' mode is significantly weaker than it was for the $J = 3$a configuration. Narrowing the cavities to 1.5 mm has both increased the quality factor of the mode and increased the relative size of the viscous and thermal boundary layers, leading to significant attenuation (see chapter 4).

It is also possible to reduce the frequency of the primary '$+++$' FPEV mode down below the '$+-+$' and '$+\ 0\ -$' phase-resonances, if the ratio of grating pitch λ_{g} to cavity length L is such that $\frac{\lambda_{\mathrm{g}}}{\lambda_{\mathrm{FP}}} \longrightarrow 1$. Perturbing the grating in this way can cause the FPEV to cross the threshold whereby it can be considered more ASW-like than FPEV like, splitting into two separate high frequency and low frequency modes due to anti-crossing with the mode present on the diffracted sound-line at a low angle of incidence (as discussed at length in section 2.7.6). Hence the low frequency FPEV can then be considered part of the ASW band structure, whereby it may occur at a lower frequency than the phase resonances. Indeed, careful inspection of the modes associated with the second order FPEV (which has a resonant cavity wavelength λ_{FP} of the order of λ_{g}) for both the $J = 3$ samples in figure 5.6 show that this has occurred.

While not included here, numerical models have shown it is also possible for the phase-resonances to occur at a higher frequency than the primary FPEV mode without changing the grating pitch λ_{g}. This is made possible by heavily perturbing the grating structure, so that the two inner rigid slats are very thin and thus the three cavities are very closely spaced (with periodicity constant). This increases the coupling strength between cavities, so that they begin to behave as a single wide cavity, thereby increasing the strength of the first order scattering Fourier component. This increases length correction ΔL, hence reducing the resonant frequency of the primary FPEV mode. The phase-resonances simultaneously rise to a higher frequency; the phase shift between cavities has to occur over a shorter distance in x, increasing their energy as before. For the grating periodicity of the samples studied in this chapter, where $\lambda_{\mathrm{FP}} \approx \frac{\lambda_{\mathrm{g}}}{2}$, the anti-crossing and thus splitting of the FPEV mode occurs near grazing incidence.

5.7 Conclusions

The existence of the acoustic phase-resonance phenomenon has been experimentally and numerically demonstrated, by studying the transmission of sound through a two-dimensional array of airborne metal slits arranged in four separate configurations. It is found that increasing the number of slit-cavities per array period, while keeping that period constant, opens up new degrees of freedom to the near-field. As well as the standard coupling of the Fabry-Perot modes with diffracted evanescent waves that result in broad transmission peaks, dips in the normal incidence transmission spectra appear when there are three cavities per grating period, these being the 'phase-resonant' modes. The transmission of these structures is also mapped as a function of incident angle θ_{i}, where it is found that extra field configurations can be excited with the addition of a phase change across the grating surface, for any sample that has more than one slit per period. With this information the origin of each feature is described with a surface-wave band-folding picture; each mode is a diffractively coupled acoustic-surface-wave band-folded from increasingly higher orders of diffraction (larger in-plane wavevectors), which can be excited via the new field configurations. In addition, the importance of including thermodynamic loss effects when modelling this sort of structure is once again demonstrated. One of the samples is optimised with attenuation by viscous and thermal boundary layer effects accounted for, resulting in measured broad and deep phase-resonances that could be useful for the design of acoustic filters.

Chapter 6

Acoustic Surface Wave Beaming

6.1 Introduction

In this chapter, the acoustic surface wave supported by a set of open-ended hole-cavities arranged as a square-lattice is characterised. This bi-grating structure is found to support an acoustic surface wave exhibiting strong 'acoustic beaming' over a narrow frequency band, whereby the acoustic energy is channelled into specific directions forming 'beams' with a well defined width. This is visualised using the high resolution near-field imaging technique detailed in section 3.5, which, from high quality pressure field maps, allows direct characterisation of the reciprocal-space band structure and the full dispersion of this surface wave. As well as providing new experimental insight into the open-holed square-lattice configuration typically used to support for example enhanced acoustic transmission[35] or subwavelength imaging[39], this chapter serves as a demonstration of what can be achieved with the acoustic near-field imaging technique, offering a contrast to the acoustic-line-mode-type samples studied in the forthcoming chapters 7 and 8.

6.2 Background

Metamaterials typically consist of an array of 'meta-atoms', which are sufficiently small that an impinging wave cannot resolve them fully. Possibly the simplest 'meta-atom' is a void in an otherwise rigid structure. At wavelengths much greater than their periodicity, a regular array of such voids forms a two-dimensional metamaterial solid, supporting the Acoustic Surface Waves (ASWs) introduced in section 2.7. Briefly, an ASW bound to the material surface can exist when a periodic array of subwavelength cavities, each supporting its own resonance, couple together over the array surface (in the x-y plane, parallel to it) via diffractive effects and create an effective impedance condition[71,27,76]. One simple form of acoustic metamaterial consists of an array of open-ended holes cut into a rigid body (which most solid bodies approximate to for airborne sound: see section 2.5). However, as mentioned in section 2.7, both the exact periodic arrangement and the shape of the resonant cavities have a significant effect on the supported acoustic surface wave, not only in terms of the position of the asymptotic resonant frequency (dictated most significantly by the depth and thus Fabry-Perot-like resonant wavelength λ_{FP} of the cavities), but also in how the ASW band structure evolves as a function of in-plane momentum components k_{x} and k_{y}.

One of the more common configurations is the square-lattice of either open[87,35,79,27,28,39] or close-ended[38,37] holes, the former typically involved in (but not limited to[39]) the EAT phenomenon, the latter in subwavelength imaging or acoustic lensing. In this study, a high resolution near-field acoustic imaging technique is utilised to characterise in detail and visualise directly the trapped acoustic surface waves present on the open-ended-hole version of the square-lattice configuration, where spatial fast Fourier transforms can extract the mode dispersion in the non-radiative regime. It is found that in a range of predictable frequencies, the array channels the ASW into specific directions, forming 'beams' with well-defined widths, creating the potential for the control of acoustic energy.

6.3 Sample Design and Experimental Configuration

The sample, depicted in figure 6.1, is a two-dimensional hole array, consisting of circular, open-ended holes of radius $R = 3.25 \pm 0.05$ mm, arranged in a 60×60 element square lattice. It was formed via laser cutting of an acrylic plate of sides 560×560 mm (B), with thickness $H = 9.60 \pm 0.23$ mm. The separation between hole centres in both the x and y directions is $\lambda_{\mathrm{g}} = 8.00$ mm. This structure supports a trapped ASW on its surface in the x-y plane, which decays away exponentially in the z direction. Exciting and then measuring the ASW is made possible by using the near-field measurement technique outlined in section 3.5. Briefly, it is achieved by placing the source inside one of the sample holes and scanning a detector probe over a grid of coordinates in the x-y plane, the probe being within 0.8 ± 0.05 mm of the sample surface in the z-plane. This distance is much less than the wavelength of the fundamental cavity resonances $\lambda_{\mathrm{FP}} \approx 2H \approx 19.60$ mm (chosen to make the sample of manageable size and allowing the use of audible frequencies), and thus detects the evanescently decaying fields associated with the surface waves. Variation in sample thickness and slight bowing of the acrylic made it impossible to maintain the same separation distance across the whole sample face, but the maximum change of ~ 0.3 mm has only a negligible effect on the measurements. The chosen set of discrete points was a grid of 455×455 mm in steps of $\Delta \mathrm{x} = \Delta \mathrm{y} = 1.25$

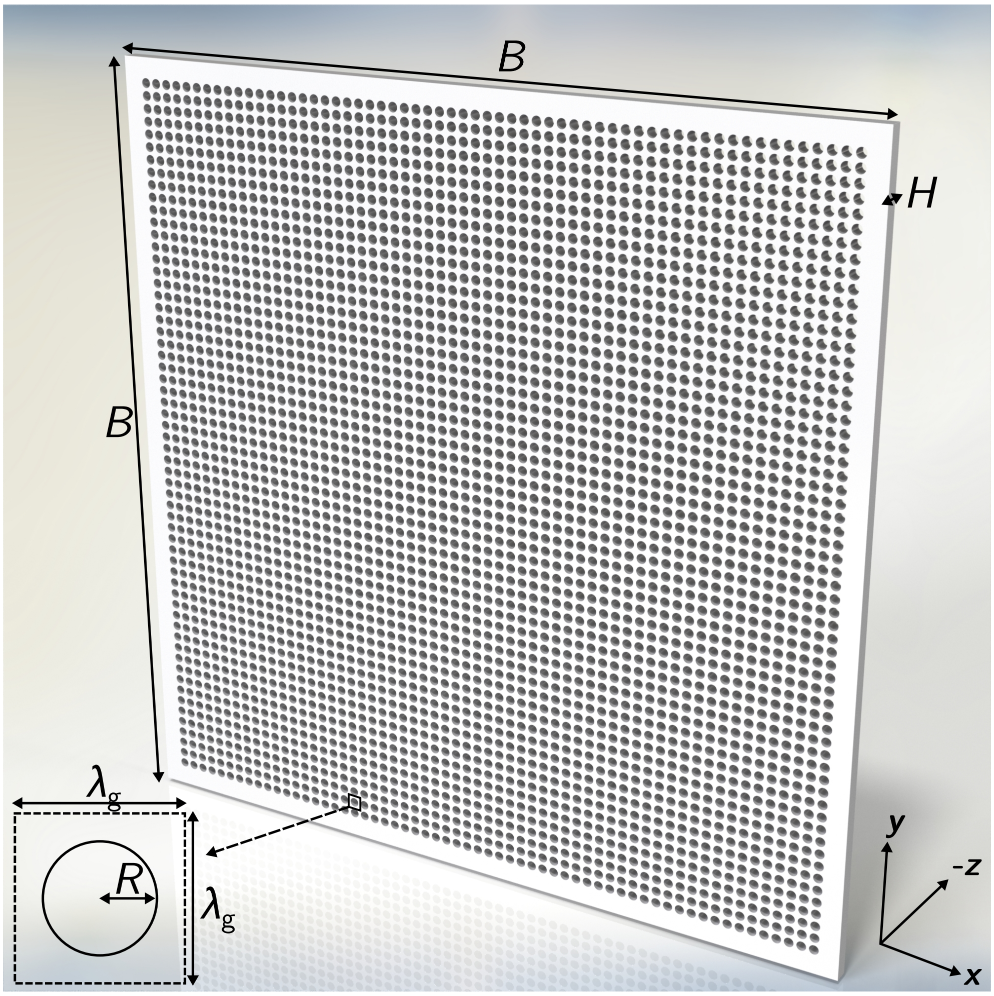

Figure 6.1: Schematic of the open-ended hole-array sample. The acrylic plate is a square of sides $B = 560.00$ mm, having thickness (hole depth) $H = 9.60 \pm 0.23$ mm. There are 60×60 holes of spacing (periodicity) $\lambda_g = 8$ mm in both x and y directions, and hole radius $R = 3.25 \pm 0.05$ mm. A close up of a single unit-cell of the grating is displayed in the inset.

mm, satisfying ($\Delta \mathrm{x} = \Delta \mathrm{y}) \ll \lambda_{\mathrm{g}}$, thus preventing aliasing at wavevectors of interest in the measured near-field. The choice of resolution was limited by measurement time and data usage constraints. The mean ambient temperature during the measurement was 292.15 K, with fluctuations in this temperature, atmospheric pressure and humidity being small enough to have negligible effect.

Once all of the time domain data had been collected, it was Fourier analysed, providing a corresponding frequency spectrum for the signal at each coordinate. From this the pressure field could be displayed at any measurement frequency as a function of x-y coordinate, creating a map of the field's phase and amplitude pattern at any given instant (the process undertaken to produce figure 6.2). Finally, a spatial Fourier transform algorithm was applied to each of these field maps (see appendix B), allowing visualisation of the wavevector amplitude in reciprocal space (or k-space) at any given frequency (figure 6.3), and thus providing the dispersion of the excited surface modes (figure 6.4). The spatial pressure field maps were zero-padded to improve resolution, and a standard Hanning window function was applied to remove Fourier transform artefacts which result from the measurement area having finite width. More information on these processes can be found in chapter 3.

6.4 Real and Reciprocal Space Pressure Field Maps

The plots in the top row of figure 6.2 (labelled A and B) show the experimentally recorded instantaneous pressure field Δp on the surface of the square-lattice sample at an arbitrary temporal phase for two specific frequencies, 11.65 kHz ($\frac{\lambda_{\mathrm{g}}}{\lambda_0} \approx 0.27$) and 13.02 kHz ($\frac{\lambda_{\mathrm{g}}}{\lambda_0} \approx 0.3$) respectively. The bottom row of figure 6.2 (labelled C and D) shows the corresponding absolute pressure field $|\Delta p|$, with a square root applied to enhance the detail of weaker features.

These two frequencies have been carefully chosen to show the two kinds of ASW that this sample supports. The low frequency images (figures 6.2A and 6.2C) are in the deep subwavelength regime, where the periodicity of the grating is much less than the wavelength of the sound $\lambda_{\mathrm{g}} \ll \lambda_0$, and here the ASW supported by the structure propagates almost isotropically, hence, the pressure field looks the same in almost every direction. Note that even though the radius of the cavity holes R is 3.25 mm, which is only $\sim 9\%$ of the free space wavelength at this frequency ($\lambda_0 = 29.42$ mm), they are still clearly visible in the pressure field map; the microphone is detecting near-field radiation.

The higher frequency images (figures 6.2B and 6.2D) are at a frequency where the grating pitch is still subwavelength ($\lambda_0 = 26.34$ mm), but here the pressure fields in figure 6.2B appear to be confined to the diagonal directions only, giving a distinct,

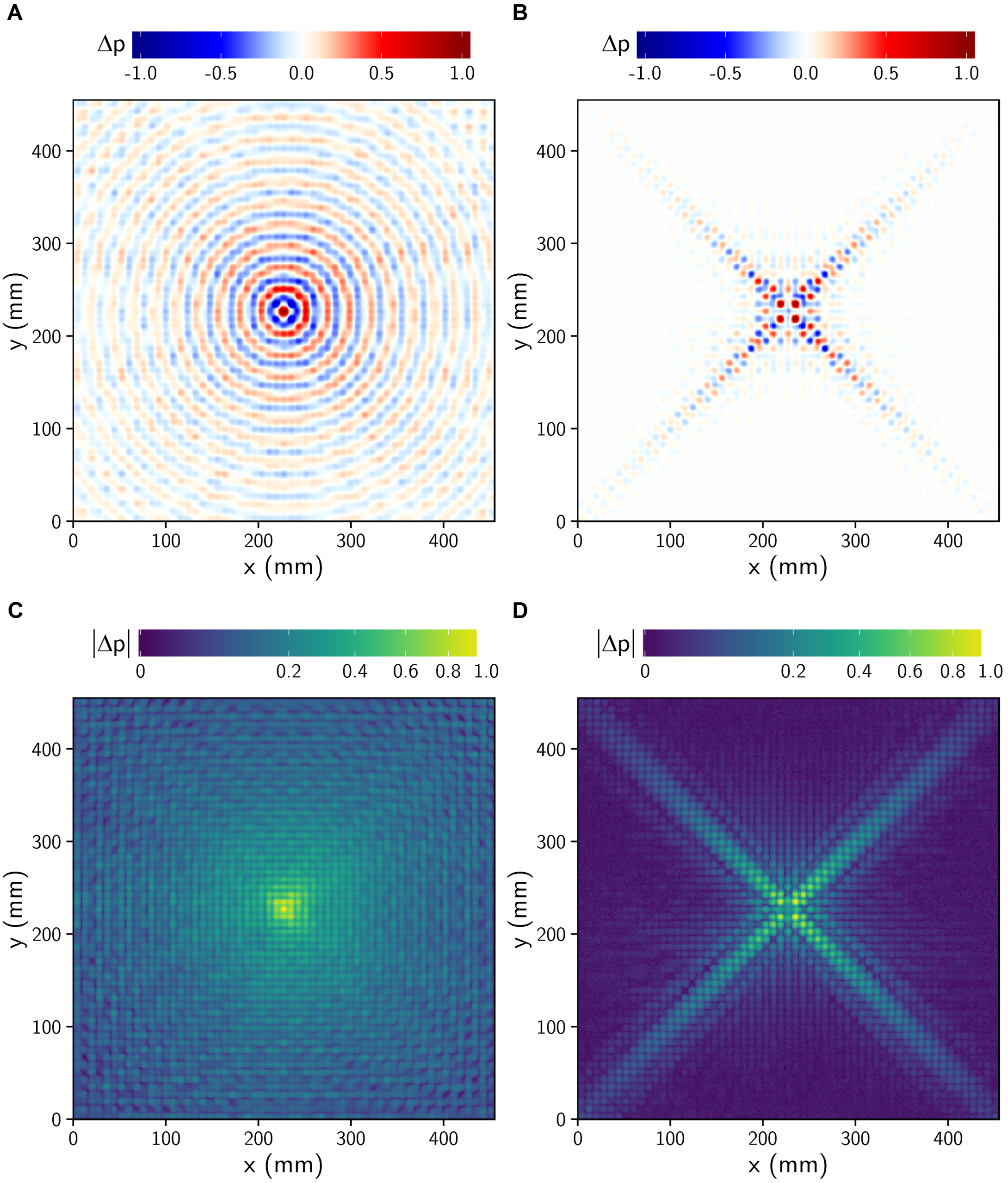

Figure 6.2: (Top row) Experimental data showing instantaneous pressure field Δp (colour scale) at a single frequency, measured as a function of x and y coordinates over the array surface. The plot labelled A is the pressure field at 11.65 kHz ($\frac{\lambda_g}{\lambda_0} = 0.272$), while B is at 13.02 kHz ($\frac{\lambda_g}{\lambda_0} = 0.304$). The point like source was placed in one of the central holes, positioned at the centre of these plots, x = y = 227.5 mm. (Bottom row) Experimental data showing the absolute pressure field $|p|$ from the same data as used for the top row (where C corresponds to A, and D to B), with a square root function applied to the colour scale to enhance detail.

narrow 'beaming' effect. This is clearer in the absolute pressure field plot figure 6.2D, where the amplitude decay length from the centre hole along either the vertical or horizontal directions is much shorter than for the diagonal. This behaviour arises in part because while the spacing of the nearest holes in the diagonal directions is $\sqrt{2}$ bigger than it is along the horizontal and vertical directions, the lines of holes are closer by $\frac{\sqrt{2}}{2}$ (i.e. the mode has both k_{x} and k_{y} and can 'zig-zag' between holes along the diagonal axis). This means that the frequency at which the ASW forms a standing wave, and thus at which the group velocity vanishes, is higher than for the other directions. Hence there must be a range of frequencies where the mode is propagating in the diagonal direction but not the horizontal or vertical. Figures 6.2B and 6.2D are at a frequency in this range. It is clear from these figures that the beaming is quite strong and the beam-width narrow relative to the periodicity. This arises not just because of the frequency gap discussed above, but also because the mode's equi-energy contour has very straight regions. This can be seen directly by inspection of the reciprocal space corresponding to each individual frequency's pressure field map.

Figures 6.3A and 6.3B are the reciprocal space plots that are the spatial Fourier transforms of the pressure field plots in figure 6.2, with A and B being the low and high frequencies respectively. The magnitude of the Fourier transform is plotted as a function of k_{x} and k_{y}, centred on zero. The 'grazing' sound wave $k_0 = \frac{2\pi}{\lambda_0}$, which is the maximum wave vector a propagating wave can possess along the surface plane, is represented by the solid white circle $k_0 = \sqrt{k_{\mathrm{x}}^2 + k_{\mathrm{y}}^2}$. Anything within the radius of this circle is in the radiative regime (k_{z} is real-valued). Conversely, anything outside of the circle, the non-radiative regime, has momentum greater than k_0; the wave cannot propagate from the surface into free space and is thus a 'trapped' wave, in this case having an imaginary k_{z} component. The dashed white circles represent sound circles $k_0 \pm nk_{\mathrm{gx}} \pm mk_{\mathrm{gy}}$ (n and m are integers representing orders of diffraction) diffracted by the periodic lattice $k_0 = \frac{2\pi}{\lambda_{\mathrm{g}}}$ in which the holes are arranged. In this case, the periodic structure is a square Bravais lattice[82], hence having three principal directions: Γ-X, X-M, and M-Γ, with the points of high symmetry Γ, X and M that define these directions marked on figure 6.3. The boundaries of the first and second Brillouin zones for this type of lattice are represented by the short-dashed and dotted white lines respectively, while the plot axes terminate at the third.

Several important features are visible in these k-space maps. In the low frequency spatial Fourier transform (figure 6.3A) there is a strong (bright), almost circular feature centred on the origin, with a radius just larger than that of the sound circle. This is the trapped ASW that the array supports, arising from the coupling together of sound in each neighbouring hole. Acoustic power flow is given by the energy gradient in k-space, being orthogonal to the equi-energy contours[82]. At the low frequency the

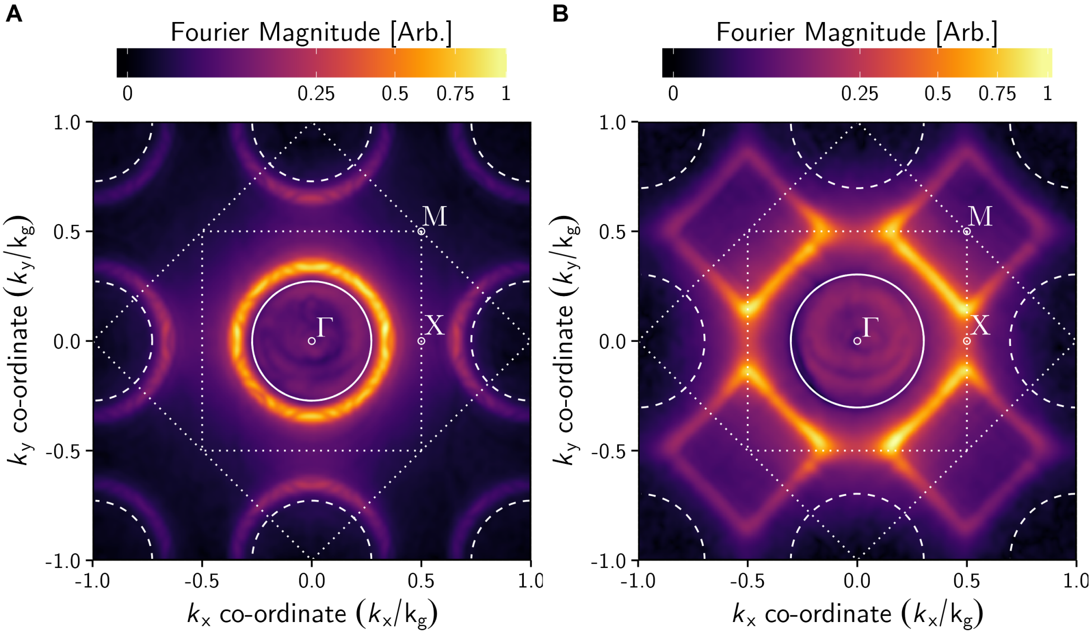

Figure 6.3: (A) Two-dimensional reciprocal space (k-space) plots corresponding to the spatial Fourier transforms of the experimentally measured pressure fields at 11.65 kHz ($\frac{\lambda_g}{\lambda_0} = 0.272$) (shown in figures 6.2A and 6.2C), plotted as a function of reduced in-plane wavevectors $\frac{k_x}{k_g}$ and $\frac{k_y}{k_g}$. The colour scale represents the magnitude of the Fourier transform. For reference, several important features are marked. The solid white circle represents the 'sound circle' $k_0 = \sqrt{k_x^2 + k_y^2} = \frac{2\pi}{\lambda_0}$, with the dashed white circles being the diffracted sound-circles from the reciprocal lattice points. The dotted straight lines represent the first and second Brillouin zone boundaries, with the axes truncated at the third. Points of high symmetry for the square-lattice[82] Γ, X and M are labelled accordingly. (B) Identical to A, but for the pressure fields at 13.02 kHz ($\frac{\lambda_g}{\lambda_0} = 0.304$) (shown in figures 6.2B and 6.2D).

almost circular nature of the equi-energy contour gives nearly isotropic power flow, with no significant differences between the principal propagation directions Γ-X, and Γ-M. However, the slight difference that *is* present is the cause of the faint interference patterns visible in figures 6.2A and 6.2C. Also visible as circular features are the diffracted ASWs which mirror the original, but are centred on different reciprocal lattice points $k_0 \pm nk_{\mathrm{gx}} \pm mk_{\mathrm{gy}}$. At this frequency, none of these features overlap, as the periodicity of the grating is much less than the freespace wavelength ($\lambda_{\mathrm{g}} \ll \lambda_0$). Note, the data within the sound circle k_0 can be disregarded as the experiment was not optimised to accurately characterise the radiative regime.

The spatial Fourier transform of the higher frequency data is shown in figure 6.3B. At this frequency, the ASW features that previously formed a circle now intersect the Brillouin zone boundary and are distorted by the formation of standing wave band-gaps. This results in the 'beaming' effect visible in figures 6.2B and 6.2D. The previously almost circular equi-energy contours have become almost square, with the 'square' tilted 45° to the x-y directions. As mentioned, these straight portions mean that power flow is channelled into the Γ-M directions, giving the strong beaming present in the pressure field maps (fig 6.2B and 6.2D). As the frequency is further increased, the side length of this 45° square is gradually reduced, consequentially increasing the width of the beams in real space. Eventually, the squares reduce to points located on each of the high symmetry M positions. Beyond this frequency, the surface wave ceases to exist, as there is only one degree of freedom per unit cell and the standing wave with its maximum amplitude between the holes and zero within them is not supported (see chapter 5).

Similar 'beaming' behaviour has been documented in the electromagnetic infra-red regime by Ulrich and Tacke[120], though at the time their set up did not enable direct visualisation of the surface waves. More recently, Dockrey et al.[97] used an analogous field scanning technique to that employed here in the microwave case, reporting both strong beaming as well as a region of true negative dispersion present for a 'Sievenpiper mushroom' array. In acoustics, this 'beaming' behaviour was utilised on a close-ended hole version of the square-lattice array to achieve subwavelength imaging[38], though, being optimised to detect a small area of pressure field, the sample was too small and experimental set-up too limited to directly extract the ASW dispersion.

6.5 Dispersion of the ASWs Supported by the Square Lattice

The dispersion curve for the ASWs supported by the square-lattice hole-array structure is presented using the irreducible Brillouin zone representation in figure 6.4. This shows the dispersion relation of the supported ASWs along each of the unique symmetry planes Γ-X, X-M, and M-Γ normalised to the ratio of periodicity λ_{g} to wavelength λ_0. The solid white lines again represent the sound line k_0. Above this line is the radiative regime, and below it is the non-radiative regime. In the frequency range studied, all of the X-M segment is beyond k_0 and is thus non-radiative. The dashed vertical lines at the X and M points indicate the edge of the first Brillouin zone. At the M point, this dashed line also represents the edge of the second Brillouin zone. The low and high frequencies to which the plots in figures 6.2 and 6.3 correspond are represented by the constant frequency (horizontal) dotted white lines.

In the Γ-X direction, a bright feature is clearly visible in the non-radiative regime ($k_{||} > k_0$), which is the localised ASW propagating in the x direction. As $k_{||}$ is increased, the group velocity of the ASW drops and at $\frac{\lambda_{\text{g}}}{\lambda_0} = 0.29$, the ASW reaches the first Brillouin zone at $k_{||} = \frac{k_{\text{g}}}{2}$, where the group velocity falls to zero and the mode forms a standing wave along either the horizontal or vertical axis (i.e. along either k_{x} or k_{y}). Changing direction and increasing $k_{||}$ beyond this point from X-M (the ASW now has y momentum with fixed x momentum, so $k_{||}$ has both a $k_{\text{x}} = \frac{k_{\text{g}}}{2}$ component and a varying k_{y} component) this standing wave becomes a 'zig-zag' state, remaining a standing wave in x but simultaneously propagating along y. At the M point, $\frac{\lambda_{\text{g}}}{\lambda_0} = 0.32$, a standing wave is now formed in the diagonal Γ-M directions, where lines of holes are spaced closer than in the Γ-X direction by $\frac{\sqrt{2}}{2}$, thus shortening the effective lattice periodicity λ_{g}. Following $k_{||}$ from M-Γ shows the ASW having very similar behaviour to the Γ-X segment, except over a broader frequency range. As highlighted, the two frequencies chosen for display in figures 6.2 and 6.3 have an important difference. At the lower frequency, a slice through $k_{||}$ intersects a surface wave feature in x, y and the (x,y) directions, but at the higher frequency there is no ASW propagating in the x or y direction alone. 'Beaming' will occur at frequencies between the two asymptotes, $0.29 \leq \frac{\lambda_{\text{g}}}{\lambda_0} \leq 0.32$, the beam-width tending to be narrowest at the lower frequencies where the mode is most 'flat' and wide in k-space. Also plotted are Eigenfrequency solutions calculated using the numerical finite element method, accounting for the thermodynamic losses discussed in chapter 4. These show excellent agreement with the data (green circles), and it is noted that thermodynamic losses act only to shift and dampen the resonance slightly in this grating set-up.

Another detail to remark upon is the presence of dark bands in the bright ASW

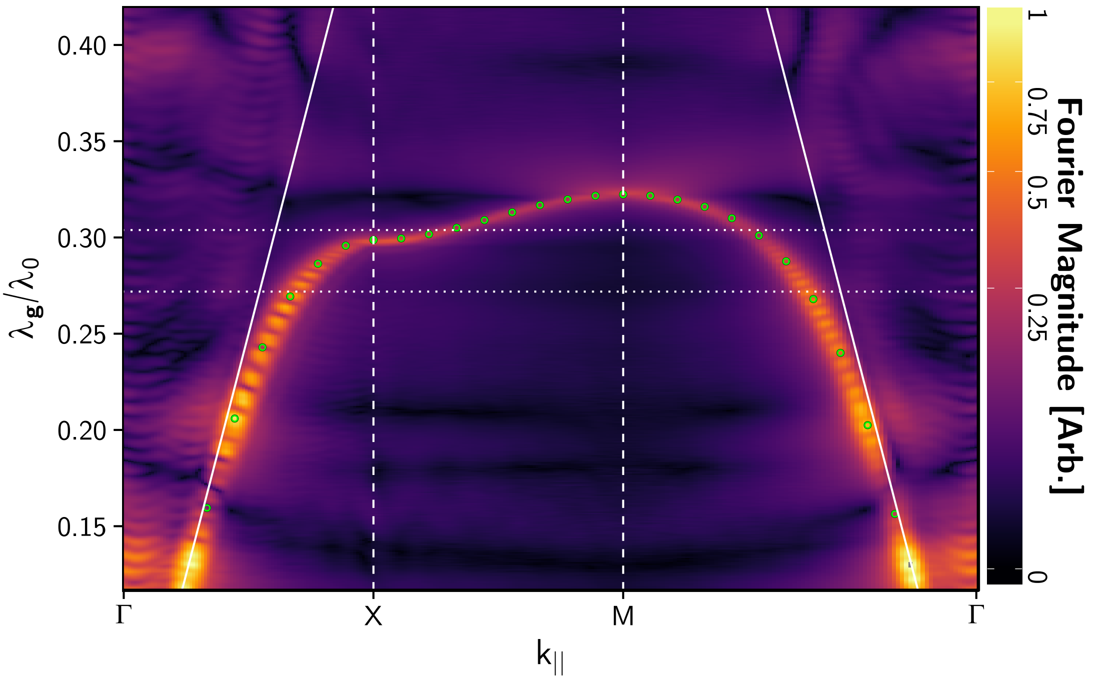

Figure 6.4: Irreducible dispersion diagram for the hole array sample, obtained from the spatial Fourier transforms of the experimentally measured pressure fields on its surface. The magnitude of the Fourier transform (colour scale) is plotted as a function of the ratio of grating periodicity λ_g to incident wavelength λ_0, vs in-plane wavevector $k_{||}$, which is the wavevector along the array surface parallel to directions Γ-X, X-M, and M-Γ. These letters represent the points of high symmetry on the square-lattice sample's reciprocal lattice[82], as marked in figures 6.3A and 6.3B. The two horizontal dotted lines mark the frequencies corresponding to those displayed in prior figures 6.2 and 6.3. The numerically calculated dispersion is represented by the overlaid green circles.

feature. The separation in $k_{||}$ of these bands corresponds to the quantisation caused by the finite-sized sample[121]; the sample edges act as mirrors, due to the abrupt change in surface impedance. The dark banding is weaker and more closely spaced in the diagonal Γ-M directions, as the quantisation corresponds now to the (x,y) direction, where the square sample is both larger and has a less well defined edge. A final important detail, or lack thereof, is the non-existence of an upper branch to this mode, due to there being only one degree of freedom per unit cell. The addition of a second cavity per unit cell to form a compound array would of course allow this mode to exist, as it did in the phase-resonant compound slit-array configurations (see chapter 5), though exactly how this occurred would require further study.

As the beaming is determined by the coupling between adjacent holes in the lattice, some degree of control over its nature is possible with manipulation of the shape of the resonant cavities (keeping periodicity λ_g and plate thickness H constant). For example, one could make the hole filling fraction much greater with the use of square cavities rather than circular ones, each be separated by thin walls. This would enable the fields in the cavities to couple over the surface more easily[35,76], thereby increasing the contribution of the end-effect terms that determine the cavity resonances and ASW behaviour and perturbing the dispersion in such a way as to increase the range over which the beaming would occur. However, doing so would simultaneously cause the equi-energy contours to be less flat, as the power flow between the now-more-strongly-coupled cavities is less restricted, hence the beaming would not be as narrow. Increasing the hole filling fraction by having small radius holes would have the opposite effect, reducing the frequency range over which the beaming would occur whilst narrowing the beam-width. The ratio of periodicity λ_{g} to hole depth D would also play an important role in the nature of the beaming, appropriately changing the coupling strength between adjacent-unit cells.

6.6 Conclusions

A high-resolution spatial-imaging technique has been employed to measure the evolution in time of acoustic pulses over the surface of an acoustic metamaterial formed from a square array of open-ended circular holes cut into a plate of acrylic. By recording, in time, acoustic pulses propagating over the sample surface, and then performing spatial Fourier transforms on the resulting two-dimensional field maps, it has been possible to directly measure the fields and the dispersions of the trapped acoustic surface waves supported by the structure. It is found that this kind of metamaterial supports a highly anisotropic surface wave over a narrow frequency band, which leads to the ‘acoustic beaming’ phenomenon, where acoustic power flow is confined to specific and predictable directions. Design of future metamaterials could incorporate this phenomenon to control the flow of sound trapped on a surface.

Chapter 7

The Acoustic Line Mode

7.1 Introduction

This chapter studies how a line of identical, equally-spaced holes cut into in a flat rigid material can support a trapped acoustic surface mode: an Acoustic Line Mode. Its dispersion is fully characterised for both a straight line of holes, and more interestingly for a circle of holes. The existence of the mode for a curved line, the circle, illustrates the potential for manipulating sound propagation by the simple use of lines of patterned holes on a rigid surface.

7.2 Background

So far throughout this thesis, the samples of interest have all been varieties of two types of resonant-cavity-based acoustic metamaterial; the two-dimensional square-lattice hole-array (chapter 6) and each of the slit-arrays in chapters 4 and 5, which can be represented with only two dimensions but are treated as though extending infinitely into the third. Indeed, in recent years, studies using different variations on these two dimensional arrangements of either holes or slits have reported phenomena such as Enhanced Acoustic Transmission (EAT)[35,27], acoustic filtering[122,123], collimation and focusing[37], and subwavelength imaging[38,39], with more complicated hole arrangements like the 'honeycomb lattice' enabling phenomena such as negative refraction[40], or acoustic analogues to graphene[124]. These structures all utilise the trapped 'Acoustic Surface Wave' (ASW) phenomenon and thus share some aspects of their behaviour. The surface normal (z) dimension contains the hole depth or plate thickness that dictates each individual cavities resonant condition, the coherent coupling between these cavities enabling the existence of the trapped ASW (see section 2.7). The remaining two dimensions in the plane of the surface (x and y) dictate the band structure of the surface mode as a function of in-plane momentum k_x and k_y, changing band structure as well as coupling strength. (Although, a study on how the band structure of the ASW in the slit-array varies with k_y has not been included in this thesis and to the authors knowledge, has not been characterised in detail for acoustics). However, notwithstanding this extensive development, the simplest patterned structure which supports a surface-localized acoustic wave appears to have been overlooked. This structure, where the third dimension is of little significance lending itself easily to the manipulation and control of sound, is simply a line of identical holes cut into a rigid solid.

Here, using a near-field measurement technique that allows direct imaging and hence characterisation of acoustic fields, the dispersion of the acoustic surface mode formed on a single straight line of equi-spaced, rigid-walled, and open-ended hole resonators, termed 'The Acoustic Line Mode' (ALM), is presented. Further, this line of holes is arranged to form a closed ring, thereby demonstrating how the ALM follows readily around a curved path: the ALM may be readily directed by design, opening up the potential for novel manipulation of acoustic energy.

7.3 Experimental Configuration

The two experimental samples studied are depicted in figures 7.1A and 7.1B. The first, figure 7.1A, is a simple line of 105 equally separated open-ended holes, laser cut into a plate of acrylic. Figure 7.1B illustrates the second sample, which is an R_R radius ring of 80 holes (giving them a periodicity in θ along their centre equivalent to the periodicity in x of the line sample), mechanically drilled into a square plate of acrylic. All relevant dimensions are included in the figure caption, with dimensions chosen such that the resonances of interest would occur around 14 kHz, i.e. $\lambda_0 \sim 20$ mm, meaning that the samples are of a manageable size and that widely available audio equipment could be used for the measurements.

These structures both support acoustic line modes, which, being a form of trapped acoustic surface wave, decay away exponentially from the surface normal in z. The ALM on the line sample is non-radiative, and is excited using a near-field source, then detected using a near-field probe. The mode supported by the ring sample will radiate slightly due to the curvature of the arrangement of holes[125] but similarly cannot be easily excited by a far-field plane wave due to its bound nature. Hence, the near-field measurement technique explained in detail in section 3.5 was utilised to characterise both ALMs. Briefly, a source was placed inside one of the holes at the positions indicated in figure 7.1, which emitted a Gaussian-shaped pulse containing a broad range of frequencies ($\sim 4 - 18$ kHz), thus exciting the cavity resonances. A probe microphone, mounted on a motorized translation stage and with its 0.5 mm radius tip

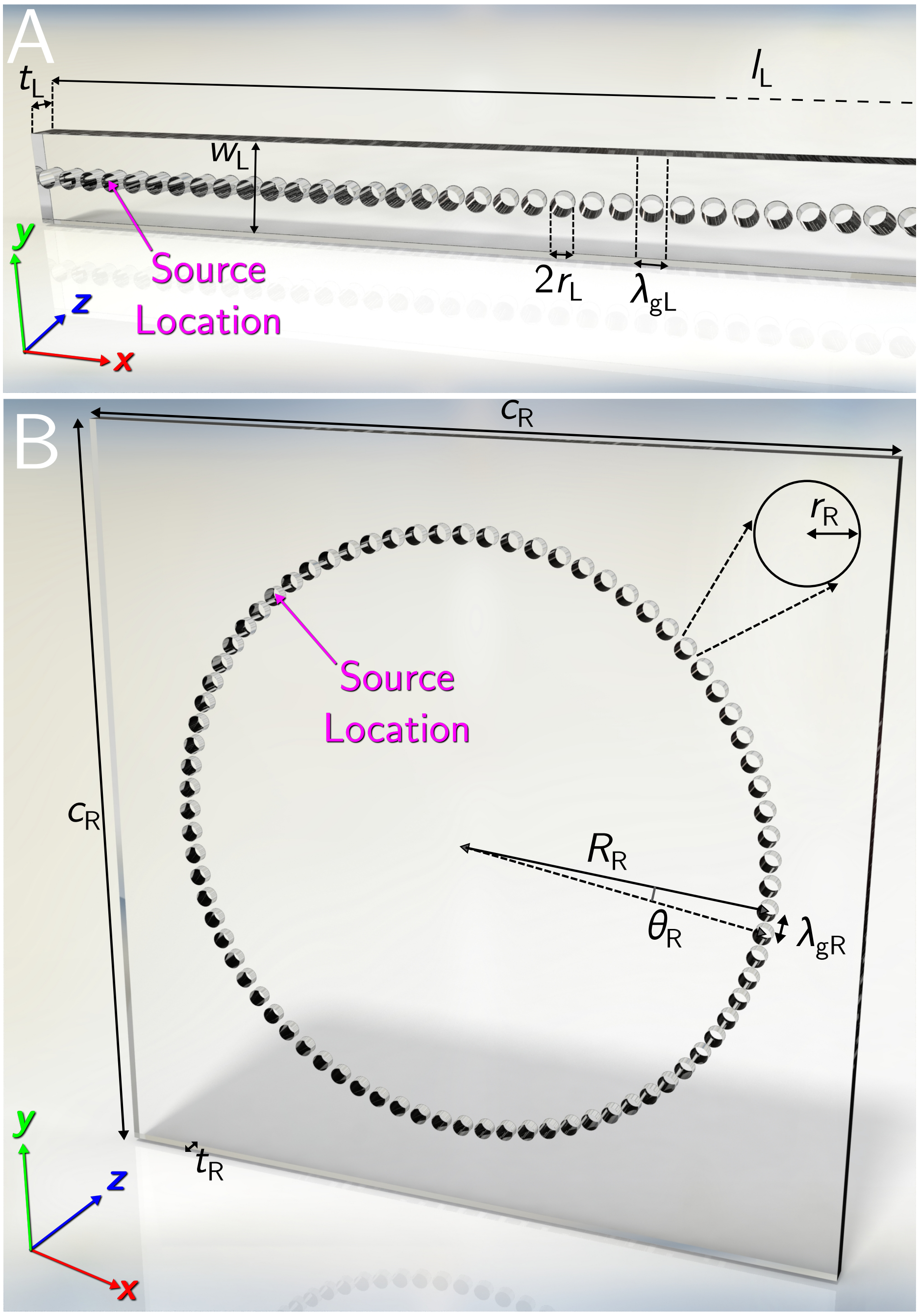
A
t_L
l_L
w_L
Source Location
$2r_L$
λ_{gL}
y
z
x
B
c_R
c_R
r_R
Source Location
R_R
θ_R
λ_{gR}
t_R
y
z
x

Figure 7.1: Schematic of the line (subscript L) sample. The acrylic plate has dimensions $l_{\mathrm{L}} = 840.00$ mm (truncated in the figure) and $w_{\mathrm{L}} = 30.00$ mm, with thickness (hole depth) $t_{\mathrm{L}} = 9.80 \pm 0.10$ mm. There are 105 holes of spacing (periodicity) $\lambda_{\mathrm{gL}} = 8.00$ mm in the x direction. The holes are of radius $r_{\mathrm{L}} = 3.25 \pm 0.005$ mm. B. Schematic of the ring (subscript R) sample. The acrylic plate has a rectangular cross-section of sides $c_{\mathrm{R}} = 290$ mm with thickness (hole depth) $t_{\mathrm{R}} = 7.51 \pm 0.06$ mm. There are 80 holes that make up the ring, which is of radius $R_{\mathrm{R}} = 10.1 \pm 0.05$ mm. Each of the holes is of radius $r_{\mathrm{R}} = 3.35 \pm 0.005$ mm, separated by arc $\theta_{\mathrm{R}} = \frac{2\pi}{80}$. This gives them a central spacing (periodicity) $\lambda_{\mathrm{gR}} \approx 8.00$ mm in the θ direction, around the circumference of the ring R_{R}.

placed less than 1 mm in front of the sample (which lies in the x-y plane), recorded the pulse in the time domain, with the measurement repeated for an array of points in the x-y plane (or the θ-r plane for the ring sample). The microphone was scanned across an area of 640×50 mm in $\Delta \mathrm{x} = \Delta \mathrm{y} = 0.5$ mm steps for the line sample using a computer-controlled translation stage. Data for the ring sample was measured in polar coordinates to allow analysis of the θ dependence, across an area of 70 mm $\times$ 2π radians in steps of $\Delta \mathrm{r} = \frac{70}{175} \approx 0.4$ mm and $\Delta\theta = \frac{2\pi}{500}$ radians. For both samples, the resolution in each coordinate was fine enough to satisfy $(\Delta \mathrm{x}, \Delta \mathrm{y}, \Delta\theta, \Delta \mathrm{r}) \ll (\lambda_{\mathrm{gL}}, \lambda_{\mathrm{gR}})$, and microphone close-enough to detect the acoustic near-field. The choice of resolution was limited by measurement time and data constraints. The mean ambient temperatures were 292.35 K and 292.15 K during the line array and ring array measurements respectively, with fluctuations in the temperature, atmospheric pressure and humidity during the sample measurements being small enough to have negligible effect[50].

7.4 One-Dimensional Line of Open-Ended Holes

The experimental pressure-field map (at 12.31 kHz) illustrating excitation and propagation of the ALM on a single line of holes is presented in figures 7.2A (instantaneous pressure field amplitude Δp) and 7.2B (absolute pressure field magnitude $|\Delta p|$). The geometry of the open-ended holes is clearly evident in the pressure fields of both figures, despite the radius r_{L} being $\sim$ 10% of the excitation wavelength of the radiation λ_0, demonstrating subwavelength resolution in the measurements of the near-field. Even though only the first cavity resonance was directly excited, at this frequency, chosen just below the FP-like cavity resonance limit of the open-ended holes (equation 2.51), all of the other holes are clearly also 'ringing'. Hence they are coupled together, with a gradual decay in amplitude along the x direction but no propagation along y or z: a form of air-bound surface wave is present, termed the 'Acoustic Line mode'. This frequency was chosen such that the ALM has not yet formed a standing wave at the first Brillouin zone boundary (see section 2.7.8), but has $k_{\mathrm{x}} > k_0$, thus is distinct from a simple grazing-incidence pressure wave. In contrast to the samples studied in chapters 4, 5 and 6 as well as the ASW being bound in the surface normal z direction, here there is also an evanescent decay along the y dimension, since the evanescent fields generated by each resonator have no grating periodicity along y to couple to. What is also visible as a sudden change in field amplitude at $y = \pm 15$ mm (significantly more so in 7.2B) is the edge of the sample in this y dimension, which acts as a weak mirror due to the sudden geometric acoustic impedance change. Hence, the shape and size of the sample in y dimension has an effect on the propagation length along x, despite there being no periodicity.

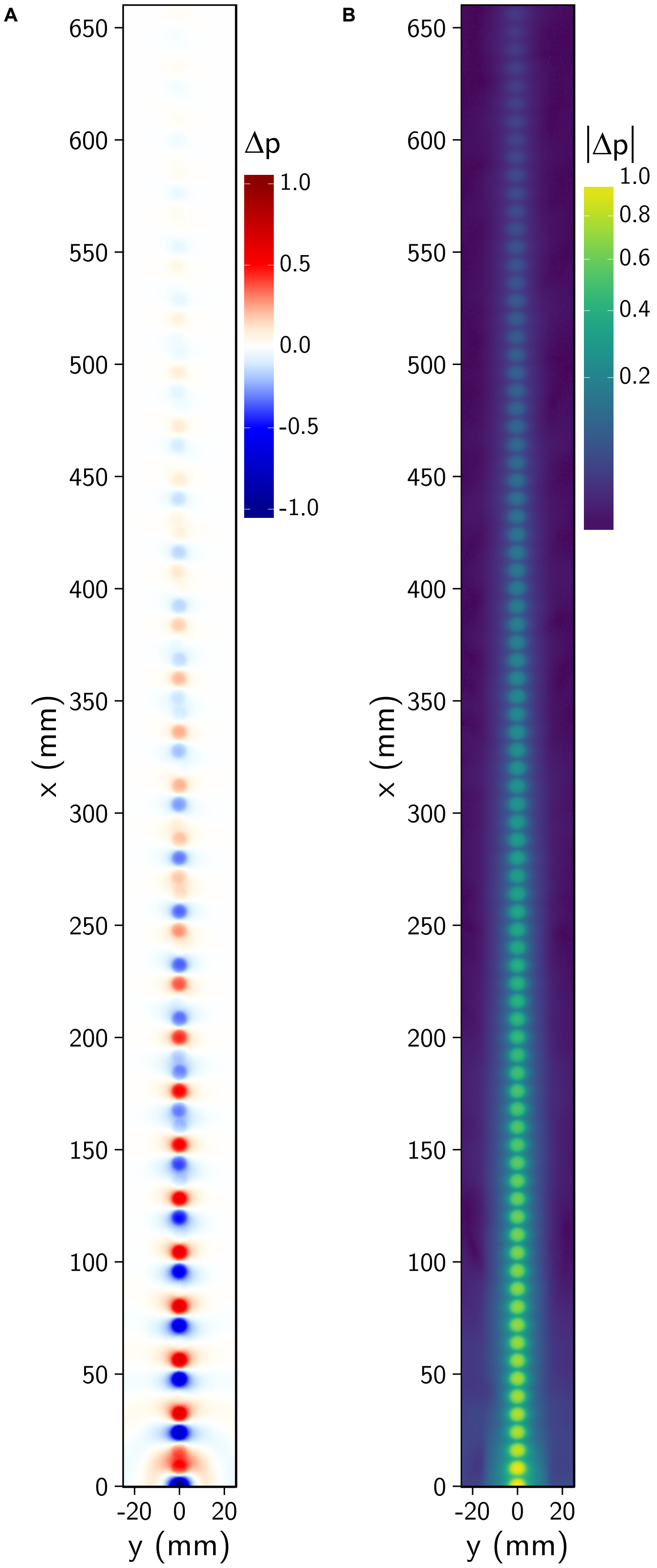

Figure 7.2: Experimental data showing (A) Instantaneous pressure amplitude Δp and (B) Absolute pressure magnitude $|\Delta p|$ (with a square root applied to the colour scale for enhanced detail) at frequency 12.31 kHz $\frac{\lambda_{\mathrm{gL}}}{\lambda_0} = 0.287$, measured as a function of x and y coordinates along the surface of the line sample. The point-like source was located at x = 0 mm, y = 25 mm.

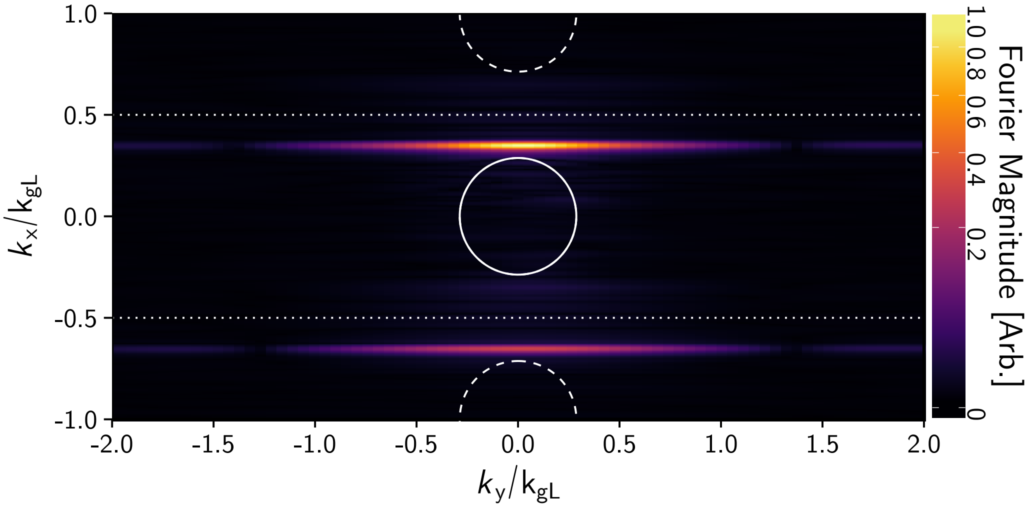

Figure 7.3: Two-dimensional reciprocal space plot corresponding to the spatial Fourier transform of the pressure field at 12.31 kHz shown in figure 7.2A, plotted as a function of reduced in-plane wavevectors $\frac{k_x}{k_{gL}}$ and $\frac{k_y}{k_{gL}}$. The colour scale represents the absolute magnitude of the complex Fourier transform. The solid white circle represents the sound circle $k_0 = \frac{2\pi}{\lambda_0} = \sqrt{k_x^2 + k_y^2}$, with the dashed white circles being the diffracted sound lines originating from the reciprocal lattice $\pm k_{gL}$. The dotted straight lines represent the first Brillouin zone boundaries $\pm\frac{k_x}{k_{gL}} = 0.5$, with the axis truncated at the second. The x and y axes have been reversed to match the orientation of the pressure field in figure 7.2.

By taking the 2D spatial Fourier transform of the pressure field at each frequency component of the excitation pulse, the amplitude of each wave-vector-component (k_x and k_y) is calculated, allowing visualization of the dispersion of the eigenmodes of the surface. The result of this is presented in figure 7.3, the reciprocal space image of the measured pressure field at 12.31 kHz (as in figures 7.2A and 7.2B, with the inclusion of the imaginary component of Δp in the calculation). To improve this data, the matrix of pressure data was convolved with a Hanning window function, and then padded with zeros, to artificially increase spatial resolution and remove Fourier transform artefacts. Several key features have been marked on this plot such as the sound-circle k_0 and positions of the Brillouin zones, detailed in the figure caption. Since this sample is only periodic in one direction, x, the Brillouin zones are one-dimensional, and are represented by a straight line extending to infinity in k_y, spaced $\frac{k_{gL}}{2}$ apart along k_x. The existence of the ALM in this data is clear as a bright yellow feature in the Fourier spectrum, sitting outside of the sound circle at $\frac{k_x}{k_{gL}} \approx 0.37$ (and also its diffracted counterpart at $\frac{k_x}{k_{gL}} \approx -0.63$, and thus in the non-radiative regime. Again, because of the sample only having periodicity in the x direction, the shape of the mode has no significant k_y dependence, and it appears as a flat line with a well-defined width (as opposed to a one-dimensionally periodic slit-array, or the previously studied two-dimensional

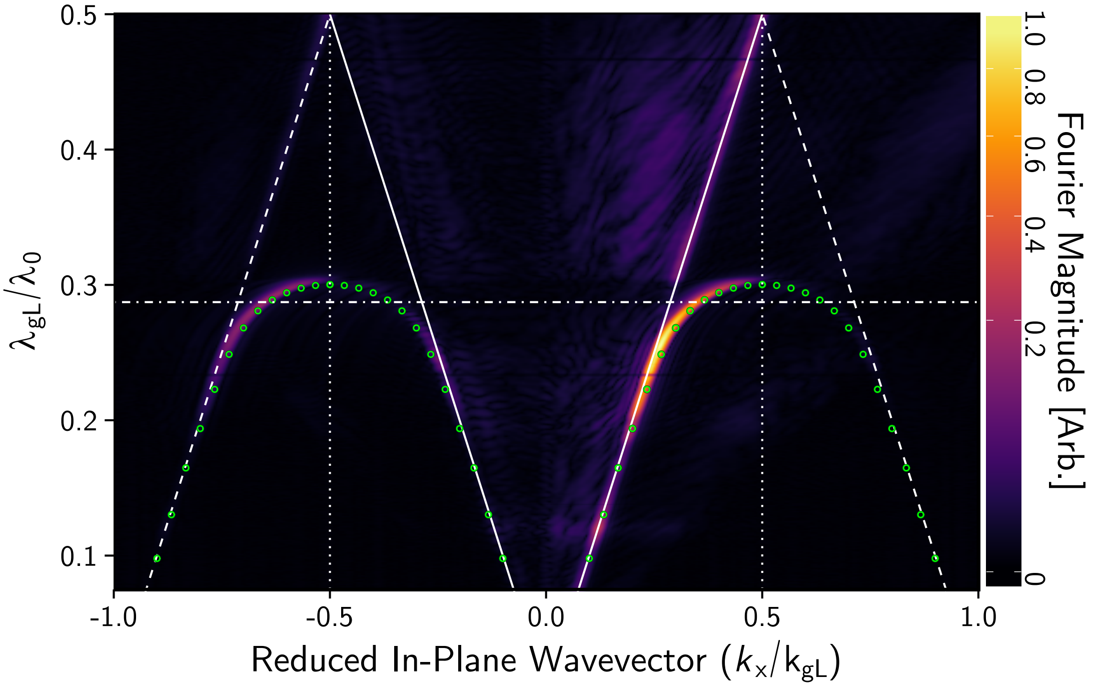

Figure 7.4: Dispersion for the line sample, obtained from the spatial Fourier transforms of the measured pressure fields on its surface such as in figure 7.3, the cross-section at $k_{\mathrm{y}} = 0$. The magnitude of the Fourier transform is plotted as a function of the normalized frequency (ratio of grating periodicity λ_{gL} to incident wavelength λ_0) vs the normalized in-plane wavevector, $\frac{k_{\mathrm{x}}}{k_{\mathrm{gL}}}$, along the array surface. A numerically-calculated dispersion is represented by the overlaid green circles. The positions of the sound-lines $\pm\, k_0$ are marked by the solid white lines, while diffracted sound lines from $\pm\,(k_0 + k_{\mathrm{gL}})$ (where $k_{\mathrm{gL}} = \frac{2\pi}{\lambda_{\mathrm{gL}}}$) are represented by dashed white lines. The edge of the first Brillouin zone is at $\frac{k_{\mathrm{x}}}{k_{\mathrm{gL}}} = 0.5$, and the value of $\frac{\lambda_{\mathrm{gL}}}{\lambda_0}$ corresponding to the pressure field plot in figure 7.2 is represented by the horizontal dotted line.

square-lattice arrangement). However, as would be expected, the Fourier amplitude changes with k_{y}, illustrating a change in coupling strength. The bright ALM feature (and its would-be associated diffractions) does not appear in the first Brillouin zone of the negative half of k-space, as the sample was only excited in one direction. There is an additional interference pattern arising from the finite width of the resonant cavities, which is visible as dark bands in the feature at $\frac{k_{\mathrm{y}}}{k_{\mathrm{gL}}} \approx \pm 1.3$. The effect that the width w_{L} of the sample has on the surface mode is too weak to be visible.

Stacking in frequency each of the two-dimensional arrays of data that represent the reciprocal space (such as that in figure 7.3) and taking an intersection through $k_{\mathrm{y}} = 0$ allows direct visualization of the $f - k_{\mathrm{x}}$ dispersion relation of the modes supported by such a structure (as explained in section 3.5.3). This procedure has been followed to create figure 7.4, the experimentally determined dispersion of the ALM supported by the line sample along the k_{x} direction. The surface mode is clear as a bright feature in the non-radiative regime ($k_{\mathrm{x}} > k_0$, k_0 being represented by the solid white line) and forms a standing wave at the first Brillouin zone boundary. See section 2.7.4 for a discussion of important dispersion relation features. Note, the amplitude of each wavevector component is normalized to the mean amplitude across all of k for each frequency, to compensate for the varying frequency response of the speaker and detector. Overlaid (green circles) are the eigenfrequencies of the structure (in air) calculated using a finite-element-method (FEM) model (see section 3.7), accounting for thermodynamic losses, and showing great agreement with the experimental data. As with the ASW on the square-array sample in chapter 6, the thermodynamic losses examined in chapter 4 act only to shift down in frequency and broaden the ALM in this configuration. Note there is also an indication of a much weaker ALM in the negative half of k-space, which arises from waves reflected from the far end of the sample. Also, note that data within the sound lines $|k_{\mathrm{x}}| > |k_0|$ in figure 7.4 arises from weak bulk air-borne sound reaching the detector directly from the source, and can be ignored.

7.5 Two-Dimensional Ring of Open-Ended Holes

The ALM (and indeed any similar acoustic surface wave) exists because of near-field coupling between adjacent resonant cavities (see section 2.7) and, provided that they are sufficiently well coupled (which is dependent on the geometry and spacing of the resonators), these ALMs will exist on any arrangement of the hole geometry, opening up the potential for bespoke control of acoustic energy on a surface. The second sample studied in this chapter, designed to test this, comprises a ring (radius R_{R}) of equally spaced holes (Figure 7.1B).

Figure 7.5A illustrates the experimentally measured instantaneous pressure field Δp (while figure 7.5B is the absolute pressure field $|\Delta p|$) at 14.625 kHz, corresponding to $\frac{\lambda_{\mathrm{gR}}}{\lambda_0} = 0.341$, for the ring sample when excited by an acoustic pulse, launched as for the line sample in one of the holes in the ring. Once again, it is clear that all of the cavities are excited, and are thus coupled, as the pressure field is concentrated above them (This is even more striking in the animation of the pulse in the time-domain data where the contrast in the group velocity of the mode compared to the speed of sound is directly visualised, although this cannot be easily shown here). The phase difference across each unit cell in figure 7.5A is approaching the standing wave condition, indicating that there must be a k_θ dependence of the ALM with a set of Brillouin zones spaced in equal amounts of $k_{\mathrm{g}\theta}$. It can also be seen that the cavities, while supporting a trapped mode in z, radiate more sound in the outward radial direction compared to the inward, a consequence of the mode having to radiate in this direction eventually due to the curvature of the geometry in which the holes are arranged[125]. Eigenmodes, quantised

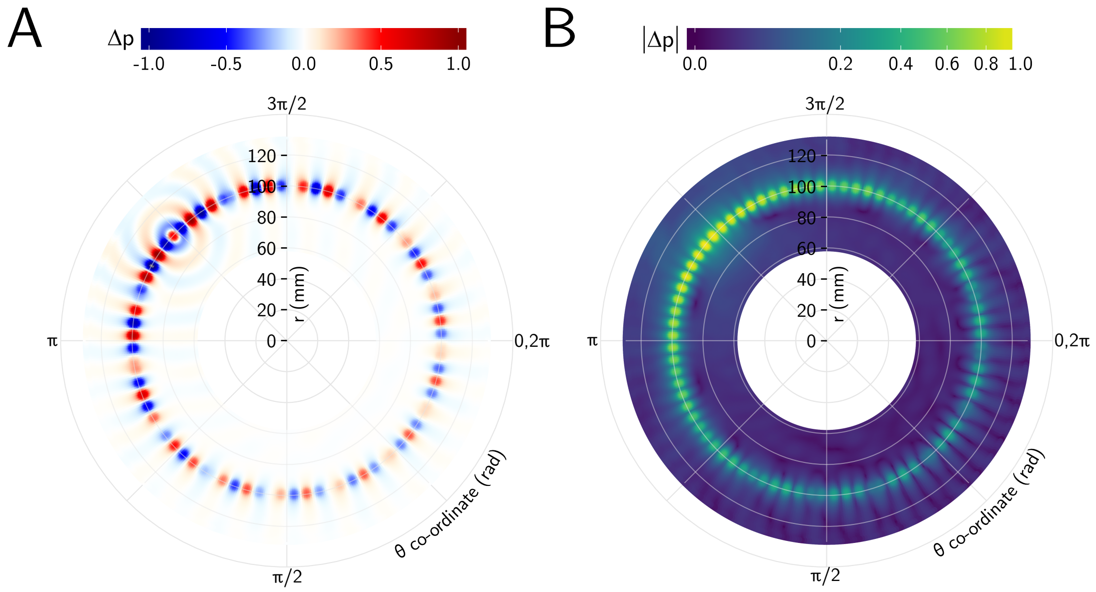

Figure 7.5: (A) Experimental data showing instantaneous pressure field Δp at frequency of 14.63 kHz ($\frac{\lambda_{\mathrm{gR}}}{\lambda_0} = 0.341$), measured as a function of r and θ coordinates along the ring sample's surface. The point-like source was located inside the hole at r$\sim$ 100 mm, θ = 2.3 rad. (B) The same as (A) except for the time averaged absolute pressure magnitude $|p|$ (with a square root applied to the colour scale for enhanced detail).

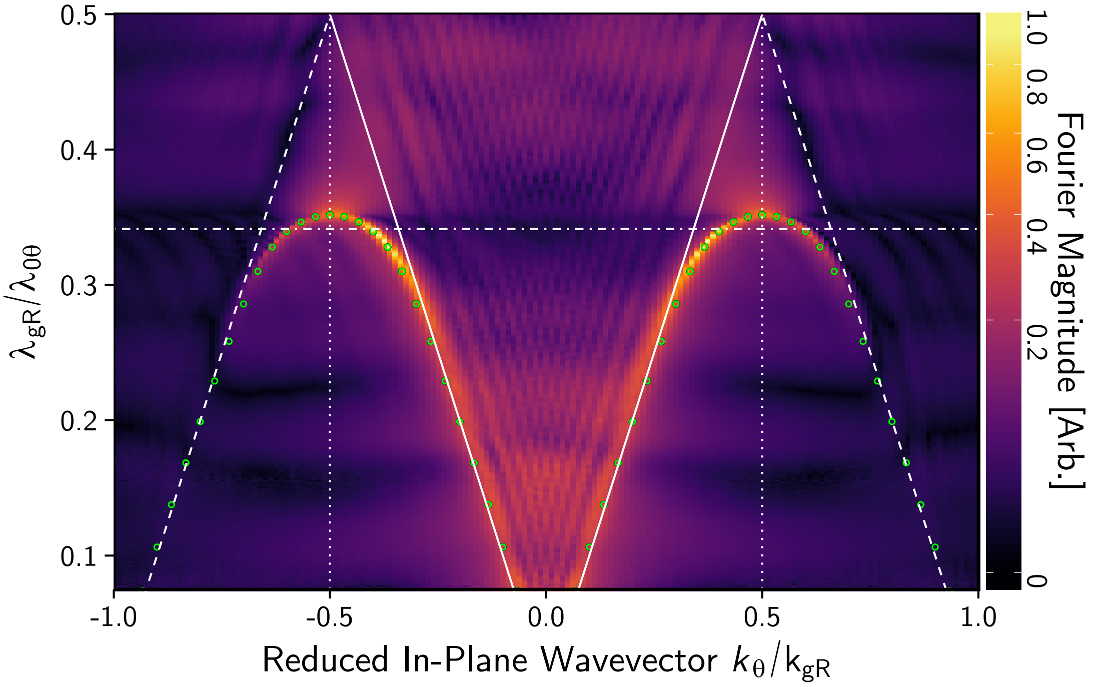

Figure 7.6: Experimental dispersion diagram for the ring sample, obtained from the spatial Fourier transforms (in polar coordinates) of the measured pressure fields on its surface around radius $r = R\mathrm{R}$. The magnitude of the Fourier transform is plotted as a function of the ratio of grating periodicity λ_{gR} to incident wavelength λ_0 vs normalized in-plane wavevector k_θ, along the array surface in the θ direction, along the holes. λ_{gR} is defined at the radius R_{R}, the centre of each hole. Solid white lines represent the 'sound-lines', the maximum wavevector $k_{0\theta} = \frac{2\pi}{\lambda_{0\theta}}$ that a grazing incidence sound wave can possess, here in the k_θ direction, while the dashed white lines are the diffracted sound lines $\pm\ (k_{0\theta} + k_{\mathrm{gR}})$, where $k_{0\theta}$ and k_{gR} have also been defined at the radius $r = R_{\mathrm{R}}$. A horizontal dot-dashed line marks the frequency to which figure 7.5 corresponds. The numerically calculated dispersion is represented by the overlaid green circles.

in circumference will exist, but are not easily identifiable because in this experiment, the acoustic power is mostly radiated away from the ring before strong circular standing waves can form.

The dispersion of the mode supported by the ring sample (figure 7.6) is obtained following a similar procedure used for the line, the key difference being that the spatial Fourier transforms are performed with an orthogonal grid of polar coordinates rather than Cartesian. This allows representation of the reciprocal lattice as a function of k_θ (which is proportional to the angular momentum[125]) and k_{r}. This change of geometry and co-ordinates also has important implications for the definition of a trapped surface wave. The angular wavelength λ_θ is given proportional to r ($\lambda_\theta = \theta \mathrm{r}$), hence the magnitude of the circumferential wavevector $k_\theta = \frac{2\pi}{\lambda_\theta}$ is not fixed. This means that for a given frequency, the phase speed of the radial wavefronts will depend on the radial

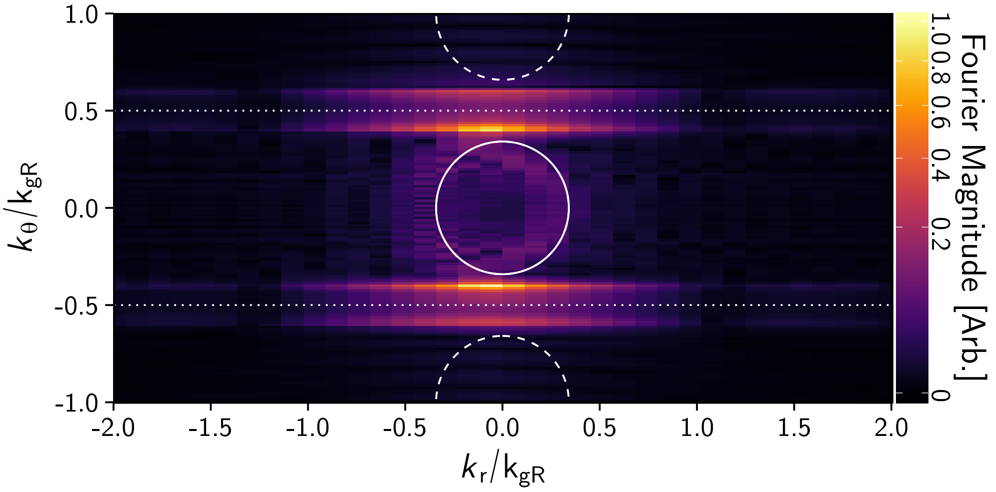

Figure 7.7: Two-dimensional reciprocal space plot corresponding to the spatial Fourier transform of the pressure field at 14.63 kHz shown in figure 7.5A, plotted as a function of reduced in-plane wavevectors $\frac{k_r}{k_{gR}}$ and $\frac{k_\theta}{k_{gR}}$. The colour scale represents the absolute magnitude of the complex Fourier transform. The solid white circle represents the sound-circles $k_{0\theta} = \frac{2\pi}{\lambda_{0\theta}} = \sqrt{k_r^2 + k_\theta^2}$, with the dashed white circles being the diffracted sound lines originating from the reciprocal lattice $\pm k_{gR}$. The dotted straight lines represent the first Brillouin zone boundaries $\pm\frac{k_\theta}{k_{gR}} = 0.5$. The r dependent values $k_{0\theta}$ and k_{gR} have been defined at the radius $r = R_R$, hence the sound lines are approximate.

coordinate r. At some radius, part of the wavefront will travel faster than the speed of sound c, and hence the wave will always have a radiative component[125]. In addition, to directly compare the dispersion of the ALM on the line sample and that on the ring sample requires that we choose a radius to define λ_θ, in order that $k_{0\theta}$ be defined. To provide this comparison, the Fourier transform was performed on a single arc of the pressure field at radius $r = R_R$, this radius corresponding to the centre of each hole cavity. Here, the periodicity in θ, (λ_{gR}) is approximately equivalent to the periodicity in x (λ_{gL}) of the line sample ($\sim$ 8 mm). The result is shown in figure 7.6, where the marked sound lines and Brillouin zones use k_{gR} and $k_{0\theta}$ defined accordingly, as well as the grating periodicity λ_{gR}. It is also possible to perform a Fourier transform with the use of all radial coordinates and produce a reciprocal space plot like the one for the line sample in figure 7.3, which is what has been done in figure 7.7, but the varying in magnitude of the k_θ coordinate (and the θ 'periodicity' k_{gR}) in units of m^{-1} makes this plot difficult to interpret. What is clear is that just as with k_y in the line sample, the k_r component affects only the mode amplitude, not significantly changing its dispersion.

With increasing k_θ, the mode forms a standing wave in θ at its equivalent Brillouin zone asymptote $\frac{k_\theta}{k_{gR}} = 0.5$, with its decay length along θ decreasing as this asymptote is approached. Eigenmode predictions from FEM modelling were obtained by applying cyclic symmetry periodic boundary conditions on a wedge-shaped unit-cell and then sweeping angular momentum number, which is equivalent to the use of Floquet periodic boundary conditions with a finite phase difference applied used in Cartesian based models as described in section 3.7. Agreement between the data and the eigenmode prediction (the overlaid green circles), is excellent.

Note, there is recent related theoretical work regarding Rayleigh-Bloch modes (a different type of ASW) formed by a two-dimensional ring of circular inclusions[126], which has some helpful mathematical insight. However, the geometry of that work is fundamentally different since the trapped surface mode there decays purely in the radial direction, unlike the ALM presented here, which also decays normal to the surface in the z-direction, with a limit frequency defined by the hole depths.

7.6 Conclusions

The experimental work presented in this chapter explored the existence of an acoustic surface wave supported by a simple line of holes, the Acoustic-Line-Mode. This line mode has been demonstrated for both a single line of open-ended cavity resonances and more significantly, for when such resonators are arranged into the shape of a circle. Using an acoustic imaging technique which involved a temporal Fourier transform to extract field amplitude and phase for a range of frequencies, followed by a two-dimensional spatial Fourier transform, the dispersion of the ALMs supported are obtained using both the Cartesian and Polar coordinate systems. This strongly localized acoustic line mode, whose behaviour is dominated by coupling between resonators along the line in which they are arranged, offers opportunity as a novel method for the control of sound.

Chapter 8

Acoustic Line Modes With Glide Symmetry

8.1 Introduction

In this final experimental chapter, the effect of ‘glide-symmetry’ on the dispersion of acoustic surface waves is investigated. Glide-symmetry is a type of symmetry possible in a two-dimensional periodic system. It is the result of a reflection along a line perpendicular to its periodicity, combined with a translation along that line in the direction of its periodicity, such as a ‘zig-zag’ pattern, or the footprints left by a person walking through snow. Three separate samples are compared, each formed of a pair of open-ended-hole line-arrays arranged side-by-side, two of them possessing glide-symmetry. All of the measurements performed are of the near-field acoustic imaging type, which, from the creation of detailed pressure field maps, allow direct characterisation of the dispersion relations of surface modes supported by the samples. First, the sample with the lines of holes arranged so that they are symmetric along the mid-plane between them is characterised. Insight gained from both chapters 5 and 7 is combined to explain the resulting pair of acoustic surface waves that are observed: acoustic line modes present on the two adjacent lines of holes strongly couple across the mid-plane between them, either in-phase or in anti-phase. Following this, one of the lines of holes is shifted along the direction of the periodicity exactly half of its grating pitch relative to the other, thus creating glide-symmetry. It is found that on this sample, the two surface modes that existed without glide-symmetry become indistinguishable from each other at the first Brillouin zone boundary. Importantly, this removes the conditions that usually result in the formation of standing-waves at this boundary, thus allowing a surface mode to evolve continuously with increasing frequency, and reach a far greater in-plane wavevector than without the glide-symmetry. It is observed that a standing-wave is eventually formed, but at an arbitrary wavevector determined non-trivially by the structure-factor of the geometry. Consequently, this shift in the position of the standing-wave appears to a create region of negative dispersion. A third sample is characterised, consisting of two lines of triangular holes inverted along the mid-plane between them, also arranged in glide-symmetry. This causes the near-fields of the two lines of holes to have a large overlap, significantly enhancing the coupling strength between them, and thus enhancing the glide-symmetry effect on the mode dispersion. This sample illustrates the degree of control possible over the surface mode dispersion, which could aid in the design of acoustic devices.

8.2 Background: Glide-Symmetry

So far throughout this thesis, every sample studied that supports a form of 'Acoustic-Surface-Wave' (ASW), the trapped surface waves that may exist when a periodic arrangement of resonant cavities couple together via diffraction (see section 2.7), have had one key aspect of their behaviour in common: at the edge of the first Brillouin Zone (BZ), the ASW group velocity falls to zero, and it splits to form a pair of standing-waves. Also, if the periodic unit-cell contained only one resonator, hence the acoustic near-field had only one degree-of-freedom available, only the low energy standing-wave formed at the Brillouin Zone Boundary (BZB) could be non-radiative (see section 2.7.6). This was the case for the square-lattice hole-array sample studied in chapter 6, the slit-array in chapter 4, and both types of line-array sample in chapter 7. The study of phase-resonances in chapter 5 showed how the addition of one or more cavities to the structure of the unit-cell (thereby creating a 'compound' grating) created additional degrees-of-freedom and allowed a second higher energy ASW to exist in the non-radiative regime, which also formed a standing wave at the first BZB. The difference in strength of the Fourier components of the fields of each of the available standing wave solutions, which had field amplitude concentrated in different regions of space, meant that there was still a significant frequency band-gap between them.

If a system could be designed such that the two standing waves formed by ASWs at the first BZB had exactly the same energy and thus became degenerate, no band-gap would form there, allowing the ASWs to exist continuously over a very broad frequency and wavevector range. This could be useful for the design of acoustic devices such as broadband acoustic absorbers. The 'glide-symmetry' configuration provides conditions necessary to achieve this[127,128].

If the periodicity λ_g of a system is along x, and this system also has some structure-factor component in y, glide-symmetry is defined as a system that is invariant under an inversion in the y dimension along its mid-plane, except for a shift of exactly half its periodicity $\lambda_\mathrm{g}/2$ along x. Many commonly found shapes have this property, such as a 'zig-zag', or the shape of monofrequency sine-wave. The glide operator G can be Stated mathematically as

$$G = \begin{cases} x \rightarrow x + \frac{\lambda_\mathrm{g}}{2} \\ y \rightarrow -y \\ z \rightarrow z \end{cases} \tag{8.1}$$

A generalised Floquet theory of electromagnetic systems with glide-symmetry has been developed in an extensive study by Hessel and Oliner[127], which, along with Mcweeny's treatise regarding symmetry and crystal band-structure[129], has since formed the basis for much research in this area (also discussed is 'screw-symmetry', a topic of interest to chapter 9). Hessel and Oliner's[127] work predicts that glide-symmetry can have a significant effect on the dispersion of surface modes. Summarised briefly, if a patterned electromagnetic waveguide containing periodic structure is re-arranged to become glide-symmetric, two surface modes that were originally separate with different energies, one having 'even' character (symmetric about the cavity mirror plane), and one 'odd' (anti-symmetric about the mirror plane), will form a single mode of mixed character. As separate even and odd modes, they interact with modes diffracted from $k_\mathrm{x} = k_\mathrm{g}$ to form standing waves at the first BZB, $k_\mathrm{x} = k_\mathrm{g}/2$, with a frequency band-gap between them. By displacing the position of the field anti-nodes by exactly half a unit-cell, the glide-symmetry results in the even and odd modes becoming degenerate at the first BZB, neither forming a standing-wave or band-gap. This mode instead forms a standing wave at some arbitrary point in k-space shifted from the BZB, but before crossing the second BZB at $k_\mathrm{x} = k_\mathrm{g}$, thus it is capable of reaching in-plane wavevectors beyond the first BZ with no discontinuities in its dispersion.

In the optical electromagnetic case, the interaction of surface-plasmons (a type of electromagnetic trapped surface wave) with diffraction gratings that have glide-symmetry has been studied before. Constant et al.[130] characterised the surface-plasmon dispersion on a 'zig-zag' grating, and confirmed that the dispersion of the surface-plasmon becomes gap-less at the first Brillouin zone boundary in such a system. Similarly, Quesada et al.[128] studied glide-symmetry in the microwave regime and found that the gap-less dispersion of surface plasmons within a waveguide possessing glide-symmetry enabled regions of subwavelength negative dispersion.

In this chapter, the effect that glide-symmetry has on acoustic surface waves is investigated, with conclusions drawn using analogies to the aforementioned electromagnetic research. To achieve this, the ease of manipulation of the Acoustic Line Mode (ALM) studied in chapter 7 is exploited with the creation of two easily-compared samples, one with and one without the glide-symmetry condition. Further, the relative insensitivity of the longitudinal acoustic pressure field to the shape of subwavelength resonant cavities is taken advantage of, resulting in the design of a glide-symmetric system where the separate lines of cavities support fields with significant overlap, thereby enhancing their coupling strength and thus the glide-symmetry effect. Via precise measurements of the acoustic near-field for each sample, high-resolution two-dimensional pressure maps are created, from which spatial fast-Fourier-transform algorithms can be applied to extract the dispersion relations of the trapped surface modes. It is found that, as well as removal of the band-gap at the first BZ and thus the possibility of very high-momentum ALMs, a region of negative dispersion within the second BZ also becomes apparent. Furthermore, it is shown that simple manipulation of the structure-factor allows for significant freedom in the design of the glide-symmetric ALM band-structure.

8.3 Sample Design and Experimental Method

Figure 8.1 is a schematic of the unit-cells that make up each of the periodic samples, whilst figure 8.2 depicts the samples in their entirety. In each case, important dimensions are labelled. All three samples were laser-cut into acrylic plates, and consist of 105 periodic unit-cells of grating pitch λ_g, thereby providing an adequate approximation to an infinitely periodic system. Sample A consists of two adjacent lines of circular holes, which are symmetric in the unit-cell's y mirror plane, providing a contrast to sample B, where one of the lines of holes is shifted along x by $\lambda_g/2$ and thus the unit-cell has glide-symmetry. Also, the y-separation of holes in sample B has been made as small as the manufacturing process allows, both to increase the diffractive coupling strength between fields of the two lines of holes, and make hole-centre-to-hole-centre displacement as close as possible to what it was in sample A. Sample C is markedly different. The triangular cavities are not only shifted along x but are also inverted in y (this is also true of sample B due to the radial symmetry of each cavity). The triangular shape thus allows the centre-to-centre separation between the two lines to be smaller than in sample B, significantly increasing coupling strength between them. For all samples, the acrylic thickness and thus hole-depth is $H = 9.7 \pm\ 0.2$ mm, placing the fundamental resonant wavelength $\lambda_{FP} \approx 2H = 19.6$ mm. This is more than twice the grating pitch $\lambda_g = 8$ mm, and thus they are short-pitch gratings. Also, this plate thickness places the cavities' resonant frequencies in the $10 - 15$ kHz range, making them possible to both excite and measure with widely available audio equipment.

To characterise the dispersion of each sample, the near-field measurement technique outlined in section 3.5 was utilised. Briefly, the samples' surface planes were aligned with a motorised XY stage that has a probe microphone attached, its aperture spaced $<$

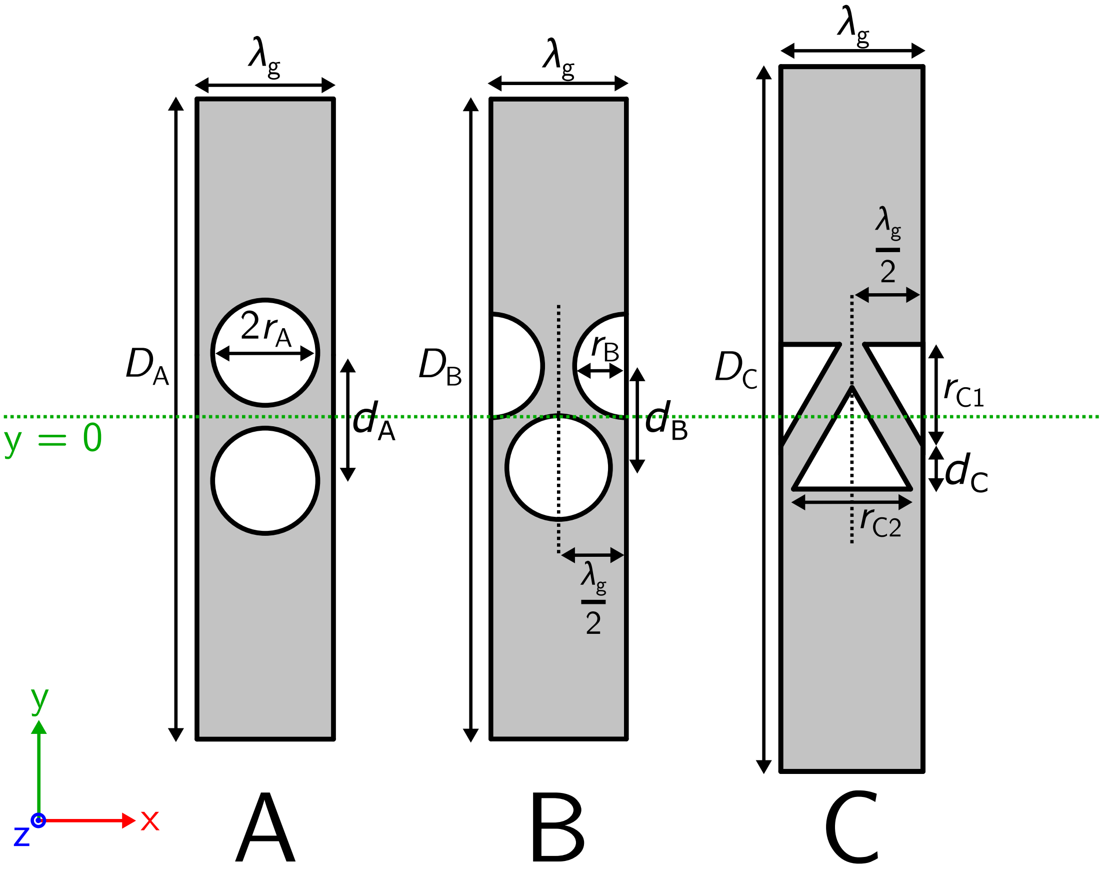

Figure 8.1: 2D schematic of the three different unit-cells that make up each of the full length samples A, B, and C depicted in figure 8.2, where grey represents the acrylic, and white-space the air. All three samples have constant periodicity $\lambda_g = 8 \pm 0.01$ mm along x. A is the sample consisting of two adjacent open-ended holes of radius $r_A = 3.20 \pm 0.05$ mm, with hole centres spaced $d_A = 7 \pm 0.01$ mm apart in y, the acrylic plate being $D_A = 36.30 \pm 0.05$ mm wide. Sample B has acrylic plate width $D_B = 35.55 \pm 0.05$ mm, and radius of holes $r_B = r_A$, but compared to sample A, the top line of holes are all shifted by $\lambda_g/2$ in x, and hole centres are separated by $d_B = 6 \pm 0.01$ mm in y (thus with total displacement between centres 7.21 ± 0.01 mm). Sample C consists of approximately equilateral-triangle cavities inverted along the mid plane in y, with triangle-hole centres separated by $d_C = 4 \pm 0.05$ mm in y (total displacement thus 5.65 ± 0.10 mm). Labelled triangle dimensions are $r_{C1} = 6.8 \pm 0.05$ mm and $r_{C2} = 5.9 \pm 0.05$ mm, while acrylic width $D_C = 44.40 \pm 0.05$ mm.

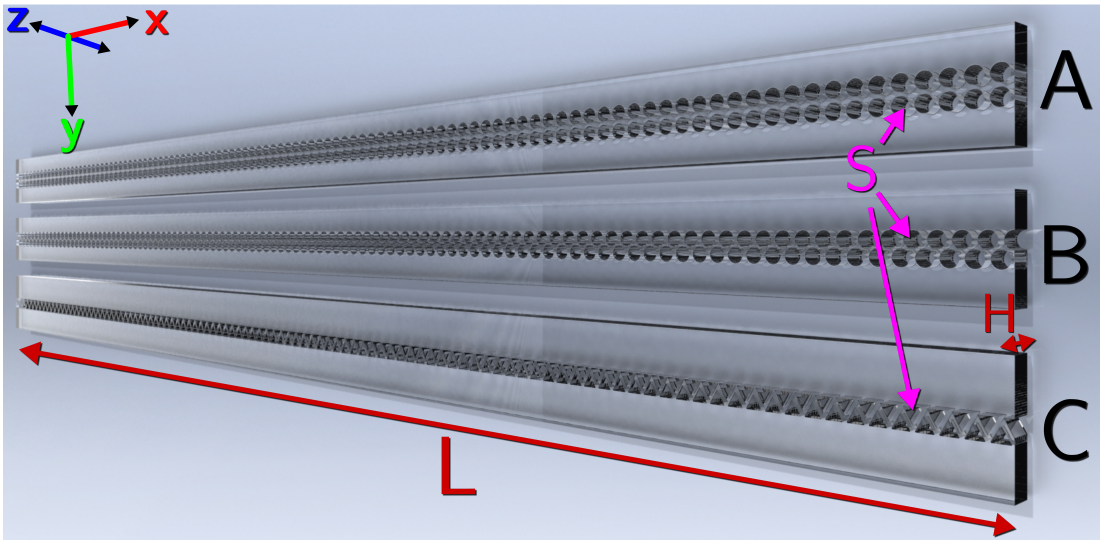

Figure 8.2: Schematic of the three types of acrylic samples, which have had 210 open-ended cavities laser-cut into them. The length of all 3 samples $L = 840$ mm, whilst the thickness $H = 9.7 \pm 0.2$ mm. The position of the source of excitation is marked on each sample by the purple arrow labelled 'S'.

1 mm from each sample surface. The motors are programmed to move the microphone in a precise grid of x and y coordinates. At each point, the microphone records the average value of a series of Gaussian pulses emitted by a point-like source placed inside one of the holes at a position near the sample edge in L, as marked in figure 8.2. The source was not placed directly within a hole on the sample edge, as reflections from the impedance mismatch presented by this edge could interfere with the recorded signal. Placing the source inside a hole further along in x significantly reduced the contribution of these weak reflections by both delaying them in time and reducing their amplitude. Also, the sample was longer in x than the XY stage's available scanning length, ensuring maximum possible spatial frequency resolution k_{x}. The resulting time-domain signals for each point are then combined to make detailed two-dimensional real-space pressure field maps, from which dispersions can be extracted via two-dimensional spatial Fourier transform algorithms. The resolution in (x,y) recorded for each sample is presented in their relevant captions, but in each case $(\Delta\mathrm{x}, \Delta\mathrm{y}) \ll \lambda_{\mathrm{g}}$, preventing the occurrence of aliasing in the regions of interest of the reciprocal space maps produced by the spatial Fourier transform analysis. For all samples, both zero-padding and Hanning-window functions are applied to the 2D real-space data matrices to reduce Fourier transform artefacts and enhance k-space resolution (the details of which can be found in both appendices A and B).

8.4 Double-Line-Array Without Glide-Symmetry (Sample A)

To understand how glide-symmetry changes the dispersion of an acoustic surface wave, first a system which does not possess it but that is otherwise identical to one which does, is characterised. Sample A provides this comparison. Figure 8.3 shows the experimentally-recorded instantaneous pressure field amplitude Δp and absolute pressure field magnitude $|\Delta p|$ of sample A at two frequencies 11.5 kHz and 13.1 kHz, which correspond to ratios of free-space wavelength to grating pitch of $\frac{\lambda_g}{\lambda_0} = 0.26$ and 0.30 respectively. The shape of the individually-excited cavities is very clear in all four images despite them having a radius much smaller than the excitation wavelength; the acoustic near-field is being measured (and this is true for all of the forthcoming sample measurements).

In chapter 7, it was shown that a single line of holes was all that was required to excite an acoustic surface wave, in the form of an acoustic line mode. Since a full two-dimensional hole array also supports an ASW, it follows that two adjacent lines of holes will support one, as it falls between the extremes of the line-array and the square-array. The lower frequency shown in figure 8.3 confirms this, being at a frequency where the fundamental ASW is excited strongly. This frequency is not-quite at the frequency where a standing-wave could form, but the phase shift between cavities in the x direction is clear. The other important detail is that each pair of holes are in-phase with each other, as marked by the black dashed line at $x = 57$ mm. Hence, across the y-dimension mirror plane, at this frequency the ASW is symmetric, i.e. it has ‘even’ character.

A key difference between this sample and both the square-array and line-array samples in chapters 7 and 6 is that the unit-cell here contains two resonant cavities, not just one. As seen in the ‘compound’ slit-array structures studied in chapter 5, this means that there should be an extra degree of freedom available to the near-field, allowing a ‘phase-resonance’ to become excitable. Indeed, this is the mode excited at the higher frequency in figure 8.3. Inspection of the fields show that not only is there a clear phase-shift between cavities along the x direction, but also that there is a π phase-shift between pairs of cavities in the y direction (also marked by a black dashed line at $x = 63$ mm); this mode is anti-symmetric in y, i.e. it has ‘odd’ character. This character is emphasized in the plot of the absolute pressure field $|\Delta p|$ at the same frequency: there is a sharp dip in pressure magnitude directly along the y mirror plane of the entire sample, compared to the same plot for the even mode, which has some pressure amplitude visible between holes in y as well as x. Another difference between the fields of the two frequencies is the decay length in the direction of ASW propagation

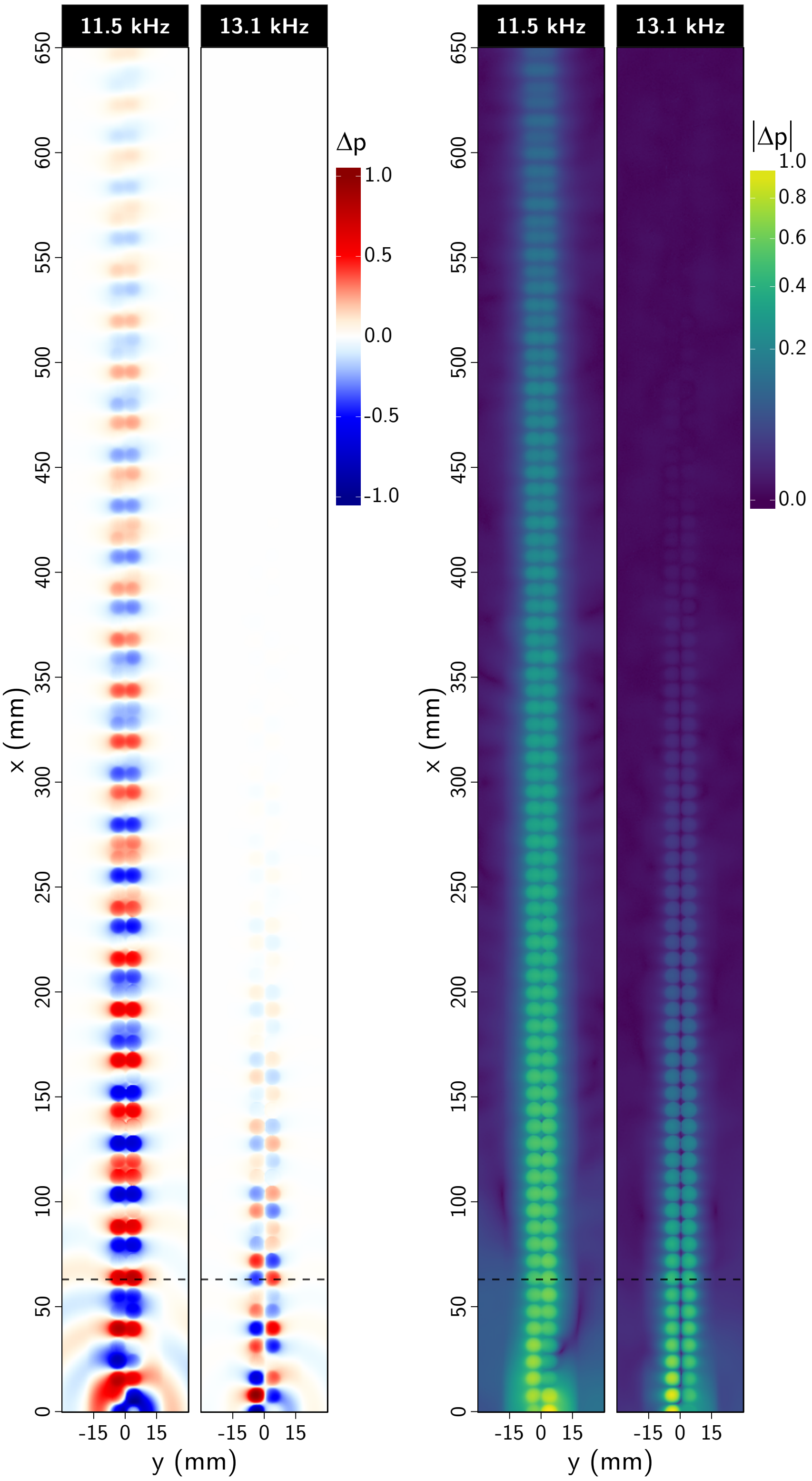

Figure 8.3: (Sample A) 2D real-space plots of the experimentally measured instantaneous pressure field amplitude Δp (left) and absolute pressure $|\Delta p|$ (right) at two separate frequencies (labelled), that have been normalised to their maximum amplitude for each individual frequency. The point-like source was located in the open-ended hole at $x = 0$ mm, $y = 4$ mm. Here, the spatial resolution is $\Delta x = 0.5$ mm and $\Delta y = 0.5$ mm. The dashed-lines represent the cross-section of the fields referenced in the main text.

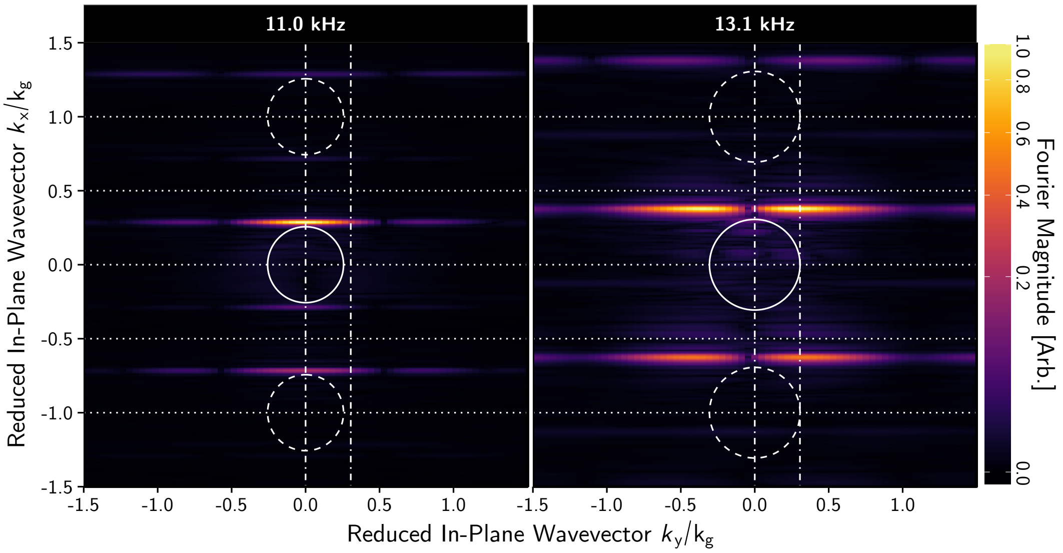

Figure 8.4: (Sample A) 2D k-space plots corresponding to the pressure field plots in figure 8.3 (oriented in the same way). Wavevectors k_x and k_y are scaled to grating wavevector k_g, with the colour scale representing the magnitude of Fourier components. The solid white circle represents the sound-circle $k_0 = \sqrt{k_\mathrm{x}^2 + k_\mathrm{y}^2} = \frac{2\pi}{c}$, the dashed circles $k_0 \pm nk_\mathrm{g}$. Dotted horizontal lines are Brillouin zone boundaries $\pm\frac{nk_\mathrm{g}}{2}$. Dot-dashed vertical lines are the cross-sections of k_y used to create dispersion plots in figure 8.5.

x, where the low frequency even mode has a much longer amplitude decay length than the high frequency odd one. This is because, as will be seen in the dispersions to be discussed forthwith, the odd mode must have a finite k_y component as well as k_x and k_z. The pressure field plots are not definitive however; the choice of frequency may place one of these modes closer to its standing-wave condition, where the group velocity necessarily decreases and so to the propagation distance. For both frequencies, the presence of the sample edge across dimension D_A is visible, as the change in surface impedance causes a reflection, but as with the line-sample in chapter 7, it is not expected that this will have a significant effect on the dispersion of the ALMs.

Inspection of the reciprocal-space maps of the surface modes excitable on sample A reveals much about their nature. Figure 8.4 are the reciprocal-space (or k-space) plots that resulted from spatial Fourier transforms of the experimentally recorded pressure fields in figure 8.3, truncated to show only the first three Brillouin zones (which are in this case one-dimensional), and with important features marked such as the sound-circle $k_0 = \sqrt{k_\mathrm{x}^2 + k_\mathrm{y}^2} = \frac{2\pi}{c}$ (see section 2.7.4 for a discussion of the basic features of k-space plots).

The low frequency k-space map is markedly similar to the equivalent plot seen for the simple line-array sample in chapter 7 (figure 7.3), in that there is a clear bright,

k_{y} independent feature that exists in the non-radiative regime of the first Brillouin zone ($k_{\mathrm{x}} > k_0$ and $k_{\mathrm{x}} < k_{\mathrm{g}}/2$). This even character acoustic line mode's strongest amplitude is at $\frac{k_{\mathrm{y}}}{k_{\mathrm{g}}} = 0$, and there is a sudden drop in amplitude visible at $\frac{k_{\mathrm{y}}}{k_{\mathrm{g}}} = 0.6$ that corresponds to the total width formed by the combined diameter and hole separation in y of each pair of holes. Features that result from the diffraction of the ALM are present just 'outside' the diffracted sound-circles at $\frac{k_{\mathrm{x}}}{k_{\mathrm{g}}} = \pm 1$, having identical character to the original. There is a also a weak feature within the first Brillouin zone in the negative half of k-space, which is the result of a reflection from the end of the sample exciting the ALM that propagates in the opposite direction.

The higher frequency k-space plot on the right of figure 8.4 has some new features of interest. First, the ALM visible that was visible in the low frequency k-space plot is no longer present (this is confirmed via inspection of the dispersions in 8.5, to be discussed). Second, the strong feature that *is* visible has a sudden drop in amplitude near $\frac{k_{\mathrm{y}}}{k_{\mathrm{g}}} = 0$, in contrast to the low frequency mode which had a maximum at that point. This feature thus corresponds to the ALM with odd (or anti-symmetric) character not excitable without some component of k_{y}, since it requires a π phase-change orthogonal to the x-axis. It still does not appear to disperse in the k_{y} direction as there is no y-periodicity, but the pattern of its amplitude is significantly different from the low frequency even mode. The other facet of the odd mode's behaviour to remark upon is its existence in the first BZ and not the second, unlike the anti-symmetric 'phase-resonant' ASWs on the compound grating structures in chapter 5. This is because, although there is an extra degree of freedom available to the acoustic near-field, it is along y and not x, thus does not enable the mode to reach a higher in-plane wavevector k_{x} than the simple line-array sample from chapter 7. A higher frequency mode can exist due to the extra k_{y} component of the grating's Fourier coefficients, but not at a higher wavevector k_{x}.

Also marked on figure 8.4 as vertical dot-dashed lines are the values of k_{y} used to create the two cross-sections of k-space in figure 8.5, necessary to show the dispersion of both the even and odd modes. Note, the sudden drop in the amplitude of the mode expected at $k_{\mathrm{y}}/k_{\mathrm{g}} = 0$ is slightly shifted toward negative k_{y} - this is the result of the sample not being perfectly aligned in either one or both of the xy and yz planes, and the resolution of k_{y} (Δk_{y}) not being high enough to prevent spectral leakage (see appendix B).

Following the method outlined in section 3.5.3, dispersion plots created from the experimental data are shown in figure 8.5, with important features marked. Results from a loss-inclusive FEM model are overlaid as coloured lines, to be discussed forthwith. Cross-sections of k-space at two values of k_{y} are included to further demonstrate the strong dependence on k_{y} of the high frequency odd mode, whilst the low frequency

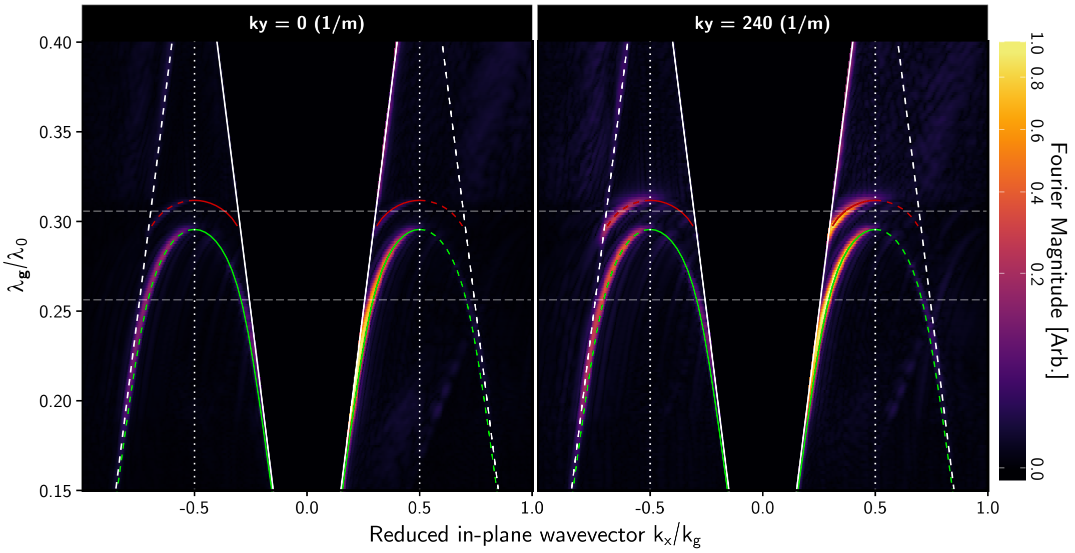

Figure 8.5: Dispersion diagrams calculated from the experimental data for sample A, at two different cross-sections of k-space wavevector k_y (labelled). The ratio of free-space wavelength to grating wavevector $\frac{\lambda_\mathrm{g}}{\lambda_0}$ is plotted as a function of reduced in-plane wavevector $\frac{k_\mathrm{x}}{k_\mathrm{g}}$. Solid-lines represent sound-line k_0, dashed lines their diffracted counterparts $\pm\ k_0\ \pm nk_\mathrm{g}$. Vertical dotted lines represent the first Brillouin zone boundaries $\pm\frac{nk_\mathrm{g}}{2}$, and horizontal dot dashed-lines the frequencies at which figures 8.3 and 8.4 are plotted. In both plots, eigenfrequency predictions of a loss-inclusive numerical model are overlaid as coloured lines. Green represents the even modes, Red the odd modes. A solid line is a mode that has not undergone diffraction from $\pm\ k_\mathrm{g}$, a dashed line is one that has.

even mode does not change significantly with k_y.

The dispersion of the low frequency mode originating at $k_\mathrm{x} = 0$ (represented by green solid lines calculated from the numerical model in both positive and negative k-space) follows the expected pattern (section 2.7). At low frequencies, this mode occurs very near the sound-line $k_0 = 2\pi/c$ and is thus indistinguishable from a grazing sound-wave. As the frequency increases, the ALM gradually increases its wavevector in x beyond k_0, becoming a fully trapped surface mode, until at the first BZB at $\frac{k_\mathrm{x}}{k_\mathrm{g}}$, its group velocity falls to zero.

In the dispersion plot taken from a cross-section of k-space at $k_\mathrm{y} = 0$, the high frequency odd mode is barely visible as a feature, since it requires a component of k_y to be excited (and as mentioned, it is only visible at all due to imperfections in sample alignment and lack of k_y resolution). When the cross-section is taken at the non-zero value of k_y marked in figure 8.4, the odd mode appears as a well defined feature at high-frequency (solid red lines, with its diffracted counterparts marked by dashed red lines). Since this mode originates in the first BZ due to not having the necessary degrees of freedom available along x, it disperses positively, with behaviour almost identical to that of the low frequency even mode. Also, instead of following the sound-line k_0 at low frequency, it appears to cease to exist in the non-radiative regime, instead crossing k_0 at some finite frequency: the pair of holes act like a waveguide along x with a cut-off frequency dictated by the hole separation in y. The model predicts that this odd mode would continue to exist in the radiative-regime that was not measured in this experiment (thus the model is also not shown here).

8.5 Double Line-Array With Glide-Symmetry (Sample B)

With the non-glide symmetric sample examined, the effect that glide-symmetry has on the mode dispersion can be isolated. Figure 8.6 shows the experimentally measured pressure fields for sample B at frequencies 11.5 and 13.1 kHz, the same as figure 8.3 for sample A. Many of the same features are visible, such as the strong localisation of the field above individual holes, and the reduction in intensity as x increases. However, there is a fundamental difference between the high and low frequencies compared to sample A.

In the previous case, there was a clear change in behaviour between the high and low frequency modes, where the low frequency one had even character (phase of the holes' pressure fields Δp symmetric in the y mirror plane) and the high frequency one odd character (a π phase-shift across the fields in the y mirror plane). For the glide-symmetric sample shown here, one cannot make this distinction. For both frequencies, at some cross-section of y, the excited ALM has both even and odd character. The low frequency mode generally has more even character, such as the point marked with a short-dashed line at $x = 56$ mm, whereas at a different cross-section such as marked by the long-dashed line at $x = 178$ mm, it appears to have odd character. Similarly, the high frequency mode has mostly odd character, such as at the cross-section marked by the long dashed line at $x = 48$ mm, with some areas of even character, again marked by the short-dashed line at $x = 32$ (one can also see the mixed behaviour in the absolute pressure field plots, where in the high frequency plot, there are intermittent pressure nodes along in the y mirror plane, inter-spaced with regions of even character). These frequencies represent the two extremes, the change in behaviour evolves as a continuum between them. Not included here (but an equivalent later shown for sample C), a frequency near the first BZ would show that the two types of character become very hard to distinguish. Other important changes in behaviour become clear in the corresponding k-space and dispersion diagrams.

Figure 8.7 shows the k-space plots of the fields in figure 8.6, with all of the marked features having the same meaning as they did in figure 8.4. Once again, there are some features similar to the non-glide symmetric sample A. First, for the low frequency,

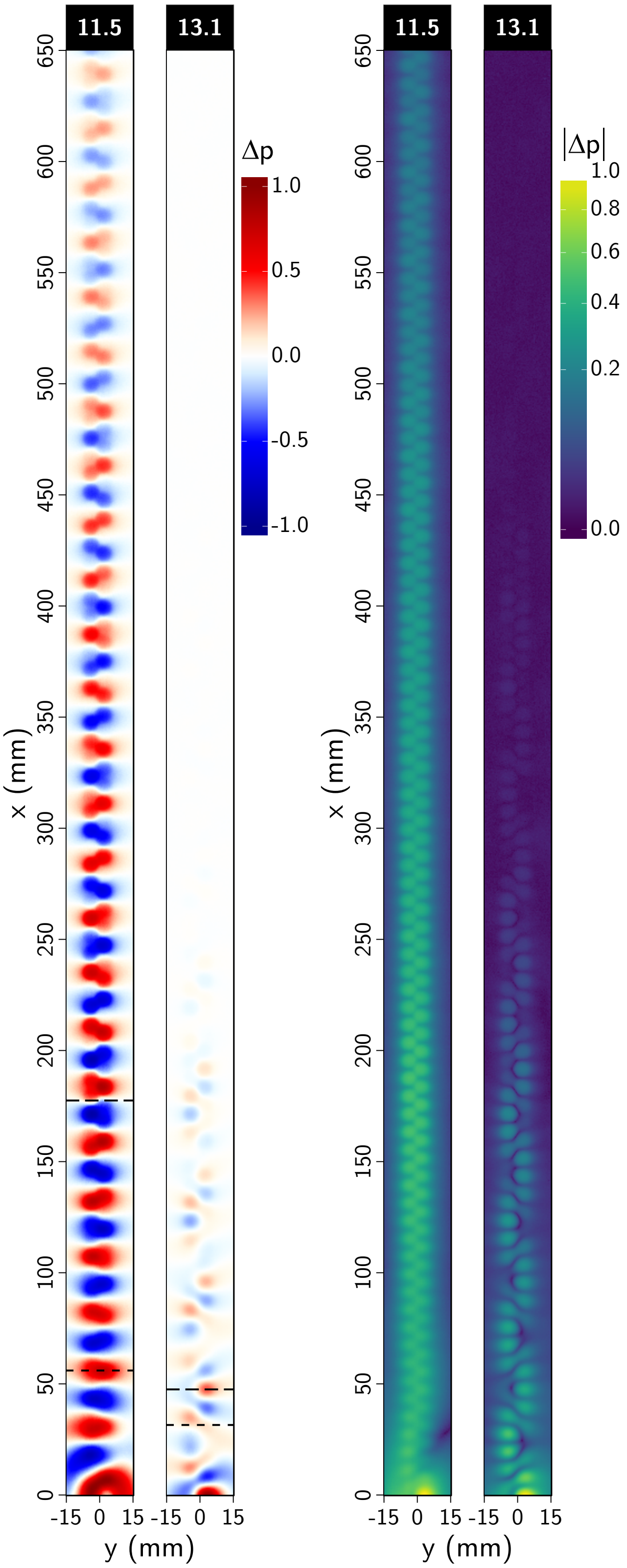

Figure 8.6: (Sample B) 2D real-space plots of the experimentally measured pressure field Δp (left) and absolute pressure $|\Delta p|$ (right) at two separate frequencies (labelled, in units of kHz), that have been normalised to their maximum amplitude for each frequency. The point-like source was located in the open-ended hole at $x = 0$ mm, $y = -3$ mm. $\Delta x = \Delta y = 0.5$ mm. Short-dashed and long-dashed lines mark cross-sections of x referenced in the main text.

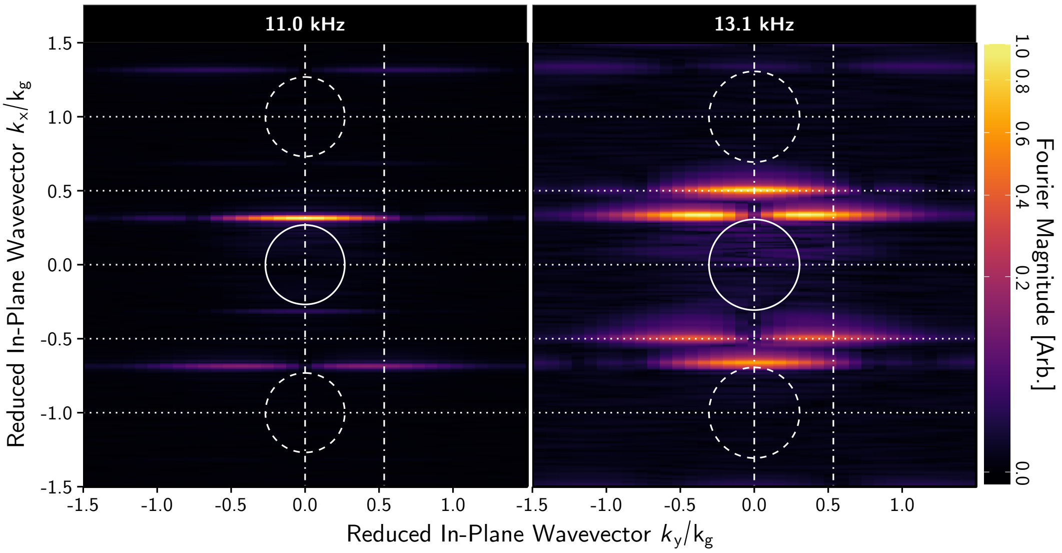

Figure 8.7: (Sample B) 2D k-space plots corresponding to the pressure field plots in figure 8.6 (oriented in the same way). Wavevectors k_x and k_y are scaled to grating wavevector k_g, with the colour scale representing the magnitude of Fourier components. The solid white circle represents the sound-circle $k_0 = \sqrt{k_x^2 + k_y^2} = \frac{2\pi}{c}$, the dashed circles $k_0 \pm nk_g$. Dotted horizontal lines are Brillouin zone boundaries $\pm\frac{nk_g}{2}$. Dot-dashed vertical lines are the cross-sections of k_y used to create dispersion plots in figure 8.8.

there is a bright, flat feature within the first BZ but outside of the sound-circle that corresponds to the trapped ALM. Its peak amplitude is at $\frac{k_y}{k_g} = 0$, and a sudden drop in intensity is visible at $\frac{k_y}{k_g} = 0.6$ that stems from the diameter of each hole. The two modes visible that correspond to the diffraction from $\pm$ k_g of the original, have a substantial change in their behaviour. These modes have a strong k_y dependence, implying that some finite component of k_y is required to excite the diffracted order, but not the original. This is the character that only the odd mode had in the dispersion of sample A, showing that the two modes have now mixed to create a new hybridised mode. This aspect of the mode dispersion implies that the glide-symmetry has removed first-order diffraction in the x plane alone, and as explained by Hessel and Oliner[127], this is due to a destructive phase cancellation resulting from the shift of the holes along x. This is the same reason that this mode does not now form a standing wave at the first BZB (visible in figure 8.8, to be discussed); the pressure anti-nodes that would form a standing wave along one of the pair of holes occur at a position directly in-line with the locations of the pressure nodes on the adjacent line of holes, and vice-versa, cancelling them out.

The k_y dependent diffraction is again clear in the high frequency k-space plot in figure 8.6. Here, there are now two modes visible in the positive half of the first BZ

$(0 < k_\mathrm{x} < k_\mathrm{g}/2)$ at one frequency, a result of the band-gap and standing wave pair not forming at the edge of this first Brillouin zone. There is a bright feature occuring at the first BZB $k_\mathrm{x} = k_\mathrm{g}/2$, and another feature just outside k_0 whose amplitude falls to zero with no k_y component. In the second BZ of the negative half of k-space $(-k_\mathrm{g} < k_\mathrm{x} < -k_\mathrm{g}/2)$, this behaviour is reversed; the feature at the first BZB has a null at $k_\mathrm{y} = 0$, and a feature with a maximum at $k_\mathrm{y} = 0$ is apparent just outside of the first diffracted sound-circle $-k_0$. This is a result of the hybrid ALM forming a standing wave at an arbitrary value of k_x between the two features, and the curvature of the mode thus changing its sign: part of it appears to disperse negatively. Hence, a feature appears in the negative half of k-space which corresponds to the region of apparent negative dispersion that is excitable on the mode originating at $k_\mathrm{x} = 0$ but propagating in the negative x direction. The equivalent segment of the mode travelling in the positive direction is in contrast not visible, as its negative-x group velocity prevents it from being excited when the source is only placed on one end of the sample. This behaviour is easier to understand with inspection of the corresponding dispersion relations.

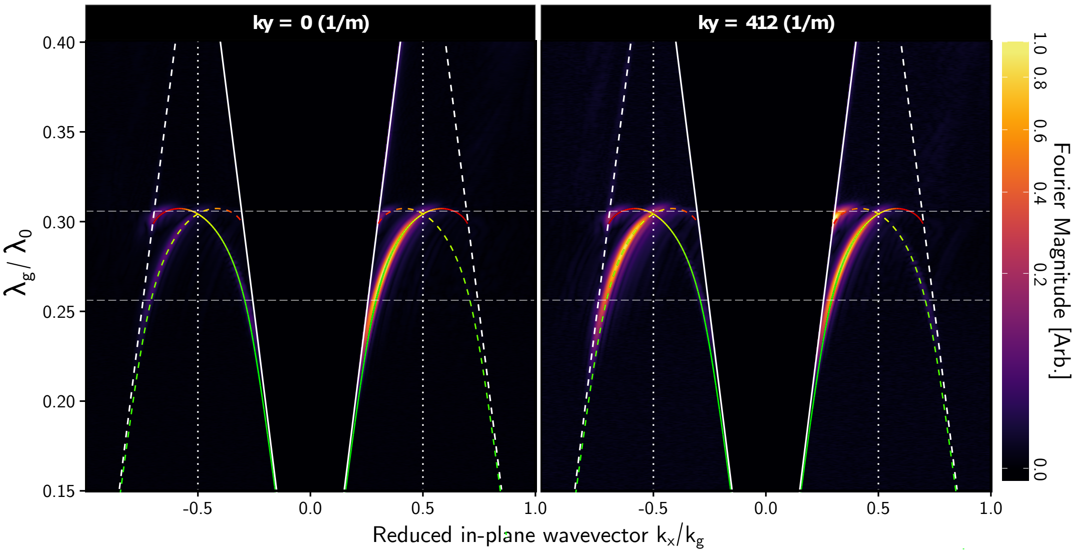

Figure 8.8: Dispersion diagrams calculated from the experimental data for sample B, at two different cross-sections of k-space wavevector k_y (labelled). The ratio of free-space wavelength to grating wavevector $\frac{\lambda_\mathrm{g}}{\lambda_0}$ is plotted as a function of reduced in-plane wavevector $\frac{k_\mathrm{x}}{k_\mathrm{g}}$. Solid-lines represent sound-line k_0, dashed lines their diffracted counterparts $\pm\ k_0\ \pm nk_\mathrm{g}$. Vertical dotted lines represent the first Brillouin zone boundaries $\pm\frac{nk_\mathrm{g}}{2}$, and horizontal dot dashed-lines the frequencies at which figures 8.3 and 8.4 are plotted. Eigenfrequency predictions of a loss-inclusive numerical model are overlaid as coloured lines, with the colour change explained in the main text. Solid lines are modes that are not diffracted, dashed lines are modes diffracted from $\pm\ k_\mathrm{g}$.

The plots in figure 8.8 are experimentally determined dispersions of sample B taken at cross-sections through k_{y} indicated by vertical dot-dashed lines in figure 8.7, with appropriate features labelled as before. Again, coloured lines represent the prediction of a loss-inclusive FEM model, the choice of colour and line-type dependant on the character of the mode they represent, to be discussed.

What is striking about this dispersion compared to that of sample A is that for both k_{y} cross-sections there are no longer two distinct modes with a clear separation in frequency. Instead, the low frequency non-diffracted (or non-band-folded) mode that previously formed a standing wave at $\frac{k_{\mathrm{x}}}{k_{\mathrm{g}}} = 0.5$ and $\frac{\lambda_{\mathrm{g}}}{\lambda_0} = 0.28$ (green lines in figure 8.5) continues to rise in frequency and k_{x} beyond the first BZB, until its group velocity eventually falls to zero at $\frac{k_{\mathrm{x}}}{k_{\mathrm{g}}} \approx 0.6$. The limit imposed by the lack of degrees of freedom in the x direction of the unit-cell in sample A is removed, as the shift of the second row of holes along x has created one. This feature is marked by a numerically calculated solid line whose colour changes from green to red, highlighting the changing character of the hybrid surface mode from mostly even at low frequency, to mostly odd at high frequency.

At $\frac{\lambda_{\mathrm{g}}}{\lambda_0} = 0.28$, a second feature has appeared at a lower wavevector than the non diffracted mode, whose origin is understood by comparing the two k_{y} cross-sections. For the cross-section at $\frac{k_{\mathrm{y}}}{k_{\mathrm{g}}} = 0$, this second feature appears only as a weak feature just outside the sound-line in the positive half of k-space, the same character that the high-frequency odd mode did for sample A (figure 8.5, red lines). However, the low frequency mode associated with diffraction from $-k_{\mathrm{g}}$ is simultaneously weakened (marked by the changing colour dashed line in the negative half of k_{x}), suggesting that the two features are somehow linked. Indeed, there is another feature above this diffracted mode visible just below the $k_0 - k_{\mathrm{g}}$ sound line, which has similar strength in both cross-sections of k-space, and which figure 8.7 showed did not have a minimum at $\frac{k_{\mathrm{y}}}{k_{\mathrm{g}}} = 0$: this feature is associated with the mode excitable at $-k_0$ existing in the negative half of k-space that has *not* been diffracted (again, marked by a changing colour solid line).

Beyond the k_{x} value which the non-diffracted ALM excited in the positive half of k-space (solid line in figure 8.8) has formed a standing wave at an arbitrary wave-vector, its sign changes, and it continues to evolve with a negative group velocity. Hence, as the source was placed at one end, this region of the mode's band structure ceases to be excitable. In the negative half of k_{x}, this same negative region of the other non-diffracted mode has become excitable, as relative to the source, it now has a positive group velocity. With the same argument, the equivalent feature in the positive half of k-space is associated with the negatively dispersing branch of the mode diffracted from $-k_{\mathrm{g}}$, requiring a component of k_{y} to be excited (thus represented by the dashed-line). Thus, on the glide-symmetry sample there is a frequency band where the ALM appears to be dispersing negatively, as was observed by Queseda et al.[128] in an electromagnetic waveguide. However, this region of the mode dispersion is not truly negative index, as the ASW fundamentally arises from diffraction. Note, as with the previous sample, weak coupling to the mode existing within the first Brillouin zone of negative k-space occurs because of reflections from the sample edge. Also, the cross-section through $\frac{k_{\mathrm{y}}}{k_{\mathrm{g}}} = 0$ is not quite at zero due to imperfections in sample alignment.

In summary then, the effect of the glide-symmetry is to remove the distinction between the even and odd character modes, creating one ALM with mixed character; at low frequencies, it appears more even-like, and at high frequencies, it appears more odd-like. Also, a new standing wave is formed at an arbitrary point in k_{x}, beyond the first Brillouin zone, where the ALM group velocity changes sign and thus appears to disperse negatively. This behaviour is analogous to that predicted by Hessel and Oliner[127] and observed by Queseda et al.[128], for an electromagnetic waveguide with glide-symmetry. The k_{x} value of the standing-wave that now forms is determined non-trivially via the Fourier coefficients of the unit-cell structure-factor, as it results from the balance between forward and back scattered ALMs that do not have to obey the symmetry conditions usually imposed at the first Brillouin zone boundary. The next sample studied illustrates this property further.

8.6 Triangular Cavities with Glide-Symmetry (Sample C)

The third sample studied in this chapter is designed to increase the coupling strength between the lines of holes that are arranged in glide-symmetry, and thus further perturb the dispersion of the excitable acoustic line modes. In sample B, the cylindrical cavities that formed the unit-cell were arranged so that they were as close together in the y dimension as possible, while remaining separated cylinders with the same radius as those in sample A. Sample C (figures 8.1 and 8.2) has different resonators altogether, consisting of open-ended cavities in the shape of equilateral triangular prisms. The two sets of prisms are inverted about the y mirror plane, and then shifted by $\lambda_{\mathrm{g}}/2$ to create the glide-symmetry condition. This allows them to have their central axes far more closely spaced without the cavities overlapping, thus reducing mean distance between resonator near-fields, and as a result increasing coupling strength between them. The distance in y measured in-between the centres of each triangular prism was as small as the manufacturing technique would allow (with the triangles remaining equilateral). Since the plate thickness H and thus resonator depth is the same as for samples A and B, it is expected that the resonant frequency f_{FP} would not change significantly, although the end-effect term can not now be approximated using a radiating circular piston model (such as described in section 2.6).

As with the previous two samples, figure 8.9 shows both the experimentally mea-

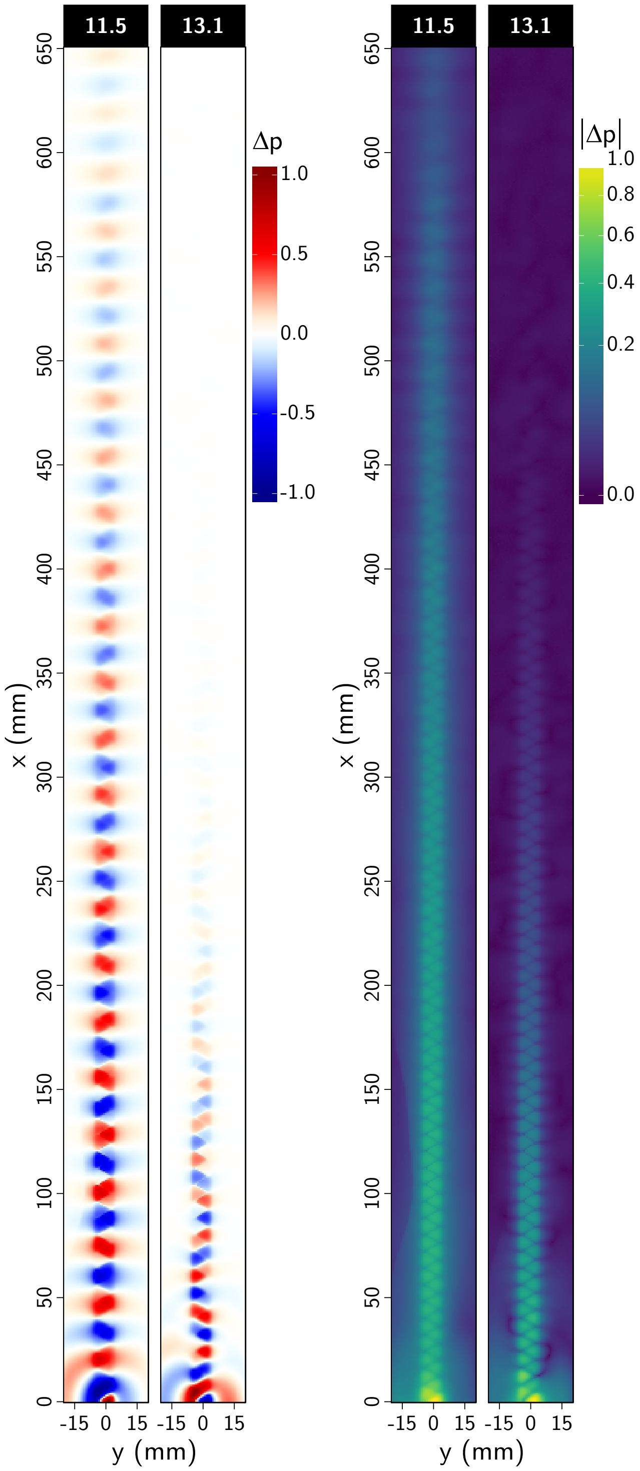

Figure 8.9: (Sample C) 2D real-space plots of the experimentally measured pressure field Δp (left) and absolute pressure $|\Delta p|$ (right) at two separate frequencies (labelled), that have been normalised to their maximum amplitude for each frequency. The point-like source was located in the open-ended triangular hole at $x = 0$ mm, $y = 3$ mm, and xy scan resolution was $\Delta x = \Delta y = 0.8$ mm.

sured instantaneous pressure field amplitude Δp and the absolute pressure magnitude $|\Delta p|$, at two frequencies 11.5 kHz and 13.1 kHz. Once again, the resonating cavities are clearly visible as the field amplitude is concentrated above the open-ended holes, though this time they form distinct triangular shapes. The difference between the two pressure fields is similar to that found with sample B; cross-sections across y show that the low-frequency field appears to have mostly even character, the high frequency more odd character. Also, the amplitude of the pressure field gradually reduces as x is increased, more so for the high frequency image. However, compared to the same high frequency image of sample B, the odd-like mode here decays over a longer distance in x, and also displays a greater percentage of regions of even character. This is because the stronger coupling of the two lines has pushed the point at which the standing-wave condition occurs to a larger in-plane wavevector and higher frequency, hence the field map pictured occurs at a relatively lower point on the dispersion of the mode compared to that of sample B. The reciprocal space plots in figure 8.10 and the resulting dispersions in figure 8.11 help to understand this.

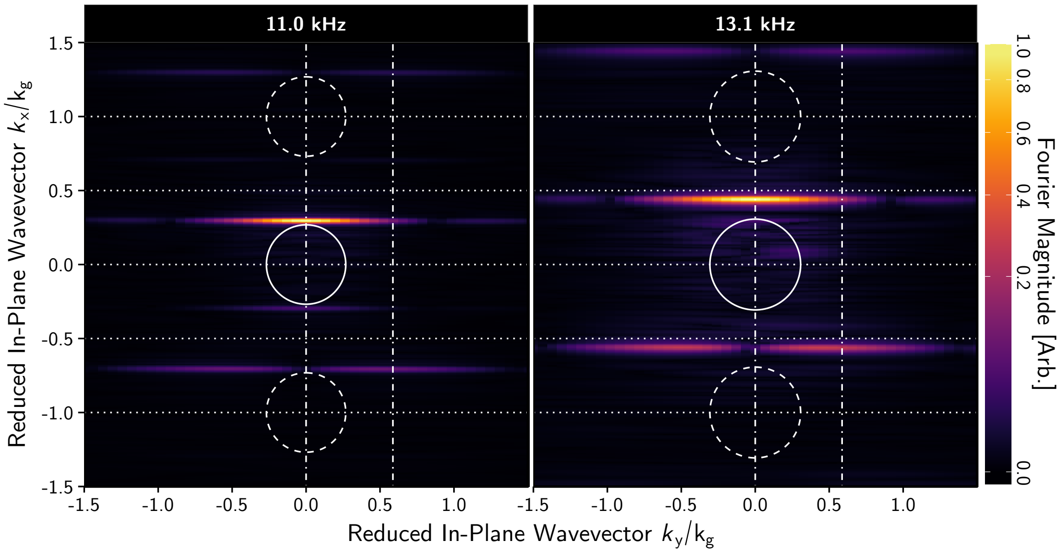

Figure 8.10: (Sample C) 2D k-space plots corresponding to the pressure field plots in figure 8.6 (oriented in the same way). Wavevectors k_x and k_y are scaled to grating wavevector k_g, with the colour scale representing the magnitude of Fourier components. The solid white circle represents the sound-circle $k_0 = \sqrt{k_\mathrm{x}^2 + k_\mathrm{y}^2} = \frac{2\pi}{c}$, the dashed circles $k_0 \pm nk_\mathrm{g}$. Dotted horizontal lines are Brillouin zone boundaries $\pm\frac{nk_\mathrm{g}}{2}$. Dot-dashed vertical lines are the cross-sections of k_y used to create dispersion plots in figure 8.8.

Following the same pattern as the previous two sections, figure 8.10 is the result of applying spatial Fourier transform algorithms to the two frequencies of pressure field plots for sample C in figure 8.9, with important features labelled in the same way as figures 8.4 and 8.7. Not all data is shown; the range of both k-axes is limited to the third Brillouin zone in either half of k-space, allowing greater detail to be visible in this region.

The low frequency plot is very similar to the same plot for sample B in figure 8.7. There is a bright feature in the non-radiative regime of the positive half of the first BZ that has its maximum amplitude at $\frac{k_\mathrm{y}}{k_\mathrm{g}} = 0$, corresponding to the acoustic line mode of mostly even character, with similar properties to that studied in 7. As before, there is a sudden drop in the amplitude of this mode at $\frac{k_\mathrm{y}}{k_\mathrm{g}} \approx 0.8$ associated with the size of the resonating cavities, though this time it is at a higher value of k_y because the combined width in y of two triangular cavities (including their y-separation) is smaller than that of the previous two samples. Also, the same behaviour of the flat feature arising from diffraction from $-k_\mathrm{g}$ is observed as in sample B, where this mode has a dip in intensity at $\frac{k_\mathrm{y}}{k_\mathrm{g}} = 0$ and a maximum value at some arbitrary point higher in k_y. Indeed, this dip in amplitude is broader than it was for sample B, suggesting that this diffracted mode is relying on yet stronger coupling across the y dimension (i.e. that the x-direction phase cancellation effect arising from the glide-symmetry is enhanced). The high frequency reciprocal space plot is markedly different from the equivalent plot in figure 8.7: only one mode is visible at this frequency, and it has not yet crossed the first Brillouin zone boundary. This implies that the dispersion of the ALM on this sample has changed quite significantly from that observed on sample B.

Figure 8.11 is the dispersion of sample C created from two cross-sections of k-space across the k_y coordinate at values indicated by the dot-dashed lines in figure 8.10, chosen to highlight the dependence of the dispersion of each mode on said k_y component. Once again, coloured lines represent the prediction of the loss-inclusive FEM model, with solid lines and dashed lines representing non-diffracted and diffracted modes respectively, and the change in colour from green to red representing the change in mode character from even to odd. The different features visible in each section of k-space are again very similar to those observed for sample B. For the cross-section at $k_\mathrm{y} = 0$, there is only one strong feature visible in the positive half of the first Brillouin zone, which crosses the first BZB without forming a standing wave. The horizontal dashed lines represent where the frequencies chosen for figures 8.9 and 8.10 lie on the dispersion curve of the mode, and it is clear that the higher frequency no longer intersects the ALM at the point where it crosses the first Brillouin zone boundary, unlike at the same frequency in figure 8.8. The ALM now reaches a significantly greater in-plane wavevector ($\frac{k_\mathrm{x}}{k_\mathrm{g}} \approx 0.7$, compared to $\frac{k_\mathrm{x}}{k_\mathrm{g}} \approx 0.6$ in figure 8.8) before forming a standing-wave, thereby possessing far greater in-plane momentum than possible on a simple grating structure. There is still a high frequency feature visible just below the $k_0 - k_\mathrm{g}$ sound-line that results from the change of sign of the group velocity of the non-diffracted ALM excitable in the

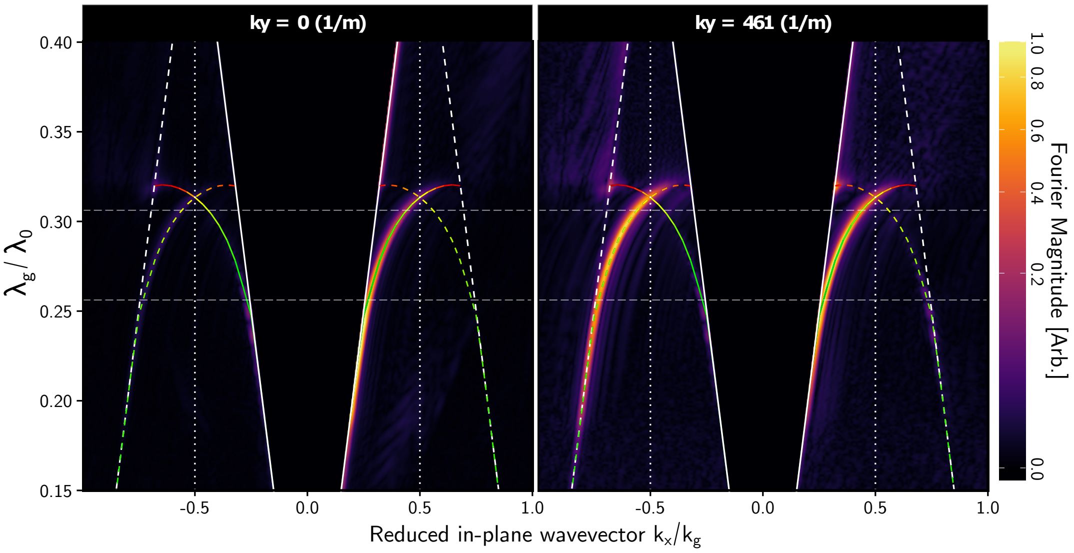

Figure 8.11: Dispersion diagrams calculated from the experimental data for sample A, at two different cross-sections of k-space wavevector k_{y} (labelled). The ratio of free-space wavelength to grating wavevector $\frac{\lambda_{\mathrm{g}}}{\lambda_0}$ is plotted as a function of reduced in-plane wavevector $\frac{k_{\mathrm{x}}}{k_{\mathrm{g}}}$. Solid-lines represent sound-line k_0, dashed lines their diffracted counterparts $\pm\ k_0\ \pm nk_{\mathrm{g}}$. Vertical dotted lines represent the first Brillouin zone boundaries $\pm\frac{nk_{\mathrm{g}}}{2}$, and horizontal dot dashed-lines the frequencies at which figures 8.3 and 8.4 are plotted. Eigenfrequency predictions of a loss-inclusive numerical model are overlaid as coloured lines, with the colour change explained in the main text. Solid lines are modes that are not diffracted, dashed lines are modes diffracted from $\pm\ k_{\mathrm{g}}$.

negative half of the first BZ, though this region of negative dispersion is significantly less broad than in sample B, as it occurs at a much larger wavevector.

Not shown here, FEM models predict that the position of the formation of the standing wave, hence the maximum positive wave vector that the ALM can reach, is controllable via the separation between the two separate lines of holes. When they are closer and thus more strongly coupled, the standing wave forms at a higher value of k_{x}, and vice versa. Note, it is possible to further perturb the structure via changing the aspect ratio of the triangular shapes, though this requires further study.

8.7 Conclusions

The last experimental chapter of this thesis investigated the effect of glide-symmetry on acoustic surface waves, in the form of acoustic line modes. Glide-symmetry refers to a kind of symmetry where a periodic system's unit-cell is inverted along its y axis mid-plane, and then one side translated by exactly half of the grating periodicity, such as in a 'zig-zag'. Three samples were characterised using a high resolution acoustic near-field measuring technique, whereby high quality two-dimensional pressure field maps can be created, then via spatial Fourier transforms, the dispersion of any present trapped surface modes extracted. The first sample consisted of two line-arrays arranged side-by-side, completely symmetric about a mirror plane in y, where two separate modes were found to exist; a low frequency mode whose fields had phase symmetry about y, i.e. having 'even' character, and a high frequency mode whose field's phase was anti-symmetric about y, i.e. having 'odd' character. Both modes had broadly the same characteristics of the acoustic surface waves investigated throughout the thesis, each forming a standing-wave at the first Brillouin zone boundary. The second sample was similar to the first, except one line of holes was translated along x by half of the width of a unit-cell, thereby creating glide-symmetry. As a result, it was observed that the previously distinct even and odd modes become mixed, and at the first Brillouin zone boundary, a standing wave was no longer formed. Instead, it formed at an arbitrary value of in-plane wavevector determined non-trivially by the Fourier components of the unit-cell structure-factor, as a generalised theory for the electromagnetic case constructed by Hessel and Oliner also predicted[127]. The resulting change in sign of the group velocity of the mode appeared to create a region of negative dispersion, as measured by Quesada et al.[128] in a similar electromagnetic system, though it is not really negative index as it arises from a diffraction effect. Finally, the third sample investigated was designed to increase the coupling strength between the two lines of holes by changing them from cylinders to triangular prisms, hence allowing their 'centres' to be separated by a shorter distance in y. It was observed that this configuration caused the standing-wave to form at a significantly larger in-plane wavevector, allowing an acoustic surface wave to exist with a gapless dispersion and a much greater mode index than usually possible in a simple acoustic impedance grating. As well as demonstrating one way in which the acoustic line modes that are the focus of chapter 7 can be easily manipulated, this chapter showed how the simple addition of glide-symmetry to a system can allow an improved degree of control over the dispersion of an acoustic surface wave, which could be useful for the design of e.g. a broadband acoustic absorber.

Chapter 9

Future Work

9.1 Introduction

In this chapter are suggestions for extensions of the experiments performed in the previous five chapters, to be completed in the future. Some of these ideas include preliminary experimental data, some are at the stage where prototype samples exist to be characterised, and others still are in the speculation stage. The majority of these suggestions expand on the work presented in chapter 7, utilising the existence of the 'Acoustic Line Mode' (ALM) in increasingly exotic geometries. There are other ideas relating to acoustic surface waves in general, and a brief discussion on how surface acoustic waves may be exploited closes the chapter.

9.2 Glide-Symmetry in a Hole-Patterned Slit-Cavity

In chapter 8, the effect of glide-symmetry on lines of holes placed side-by-side in the surface x-y plane was investigated, with the z-plane that was perpendicular to the sample not playing a role apart from being the direction of surface wave evanescent decay. The diameter of the open-cavities put a limit on how closely the lines of holes could be spaced, as they lay on the same surface plane and could thus not overlap. A different way to create glide-symmetry is to have two lines of holes on separate surfaces, this time separated in z and facing each other, thereby creating a patterned slit-cavity. This arrangement may offer a much greater degree of control as the slit-width w of this cavity can vary readily. Also, with this geometry the thermodynamic loss effects studied in chapter 4 may provide another method of changing ALM index, as narrowing the separation between the lines of holes changes the effective speed of sound within the patterned slit-cavity. This style of glide-symmetry was studied in the electromagnetic case by Quesada et al.[128], and more closely resembles the electromagnetic waveguide

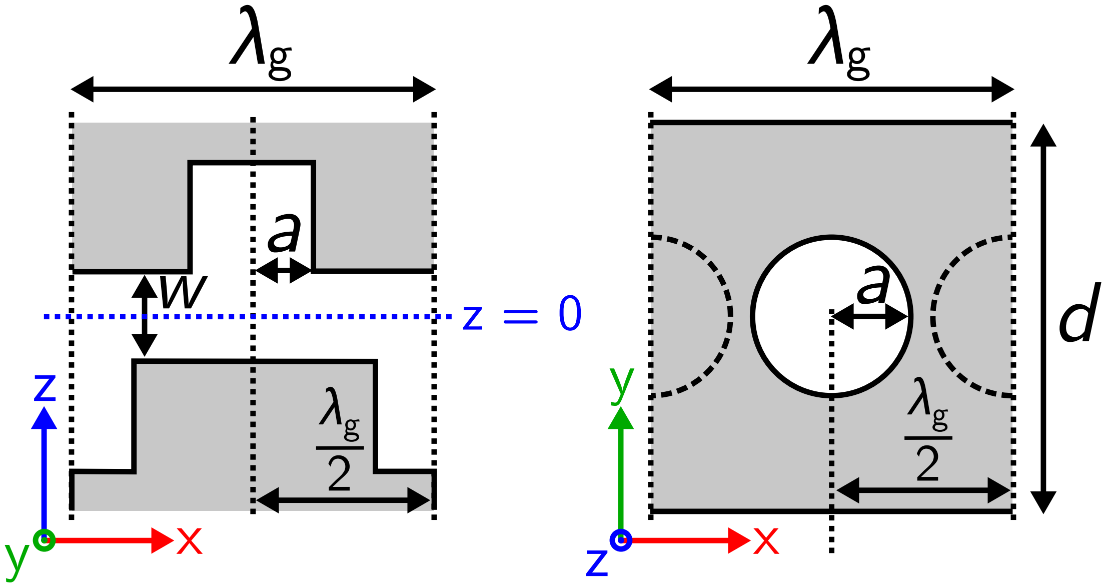

Figure 9.1: Schematic of the alternative glide-symmetry sample, from two perspectives. Grey represents aluminium. (Left) View through a cross-section across the centre of the hole cavities in the x-z plane. Each hole, of depth $h = 5$ mm and radius $a = 2$ mm, is part of a series of holes of periodicity $\lambda_g = 10$ mm. The two lines of holes are inverted along their z-axis mirror plane halfway between the two aluminium plates, which are separated by variable width w. One of the aluminium plates is shifted by $\lambda_g/2$ to create glide-symmetry between the holes. (Right) x-y plane cross-section of the sample. The aluminium plates are of width $d = 12$ mm.

that was presented by Hessel and Oliner[127].

A schematic of the periodic unit-cell which forms such a sample is depicted from two separate viewpoints in figure 9.1. This sample has been made from aluminium, and is pictured in figure 9.2. There are two aluminium blocks of length $L = 650$ mm and width $d = 10$ mm, which have been drilled with circular holes of radius $a = 2$ mm and depth $h = 5$ mm, spaced $\lambda_g = 10$ mm apart. The aluminium blocks are joined via vertical rods, which allow them to be arranged in two different ways. The first is so that the two lines of holes mirror each other in the z-plane, the second is so that one of the lines is shifted by $\lambda_g/2$ along x to create glide-symmetry. The separation between plates w can be varied, thereby changing both the coupling strength between the two lines of holes, and the contribution of thermodynamic loss within the cavity formed by the plates.

Preliminary FEM models of this system predict effects similar to that described in chapter 8, where it was observed that with glide-symmetry, it is possible to remove the standing wave at the first Brillouin zone boundary and thus create a mode of very high index. This resulted from the mixing of two modes that would exist at separate frequencies without the glide-symmetry. They were a low frequency ALM having ‘even’

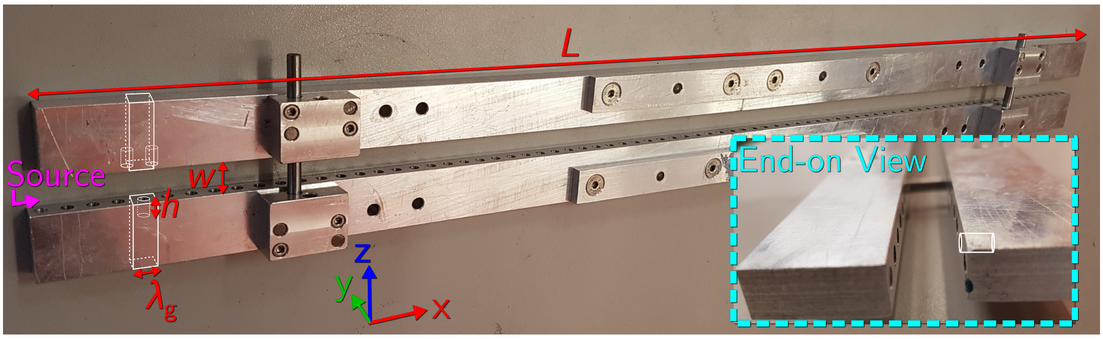

Figure 9.2: Labelled photo of aluminium sample. An alternative view is shown within the inset. Close-ended holes of depth $h = 5$ mm are drilled into a pair of aluminium plates of length $L = 400$ mm. The lines of holes are arranged in glide-symmetry along the z axis, and source placed on one end. The plate separation w can be varied with the use of acrylic spacers.

character, with the phase of its fields symmetric about the mirror plane, and a high frequency ALM having 'odd' character with its fields across the mirror plane in anti-phase. At $k_{\mathrm{x}} = k_{\mathrm{g}}/2$, these modes became indistinguishable and formed a degenerate pair. A notable difference between the samples in that chapter and the one presented here is the possible strength of the coupling between each line of holes. In chapter 8 the two lines coupled via diffraction in the surface plane y, perpendicular to the periodicity x, both evanescently decaying away from the surface in z. However, in this sample, the z-plane evanescent decay of each mode directly overlaps with the other, and the separation in z that determines this coupling strength can be controlled by the plate separation w. This appears to significantly increase the coupling strength between the holes, allowing for a hybrid ALM to posses wavevector far beyond the first Brillouin zone.

Figure 9.3 shows experimentally determined dispersion diagrams for this sample, using the near-field measurement technique outlined in chapter 3 and similarly used in chapters 6 through 8 (although, as this was actually the first use of the technique, it had not been optimised, and as such the measurements need to be repeated). The ALMs were excited with the point-like source placed at one end of the sample, the pointing along x (marked in figure 9.2). In figure 9.3, which has important features such as the sound-line $k_0 = \frac{2\pi}{c}$ marked, two measurements are shown. In the left panel, the measurement was performed with the sample arranged in glide-symmetry, and a separation between the two lines of $w = 1.6$ mm, and in the right, the same but with $w = 1.0$ mm.

For the $w = 1.6$ mm measurement, a very bright feature is visible in figure 9.3 above $k_{\mathrm{x}} = k_0$, which is the hybrid ALM that is a combination of modes supported on each separate line. This mode has character markedly different to that observed on

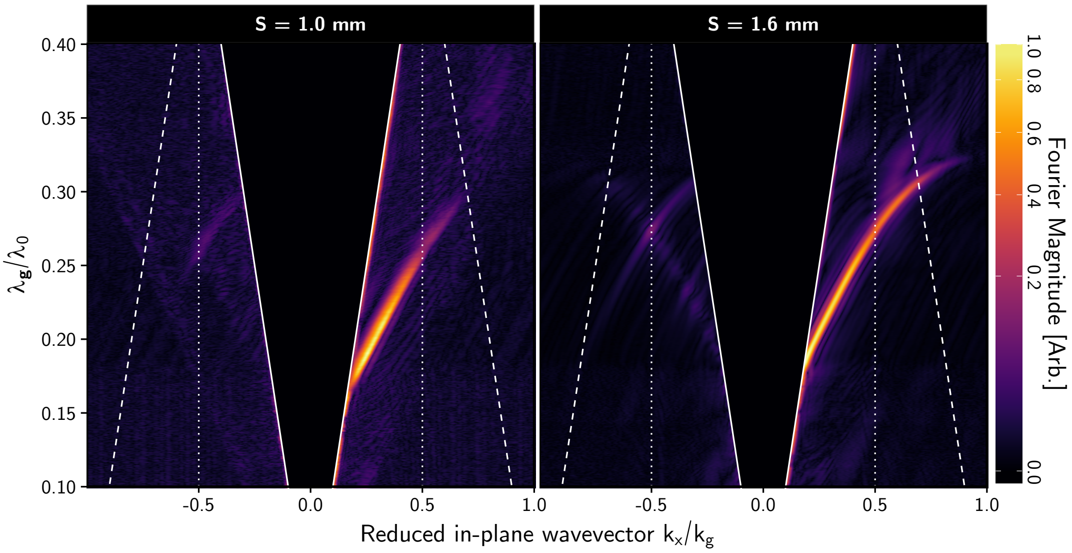

Figure 9.3: Dispersion diagrams calculated from near-field measurements of the sample pictured in figure 9.2, with two different values of plate separation $w = 1.6$ and $w = 1.0$ mm. The ratio of free-space wavelength to grating wavevector $\frac{\lambda_g}{\lambda_0}$ is plotted as a function of reduced in-plane wavevector $\frac{k_x}{k_g}$. Solid-lines represent sound-line k_0, dashed lines their diffracted counterparts $\pm\ k_0\ \ \pm n k_g$. Vertical dotted lines represent the first Brillouin zone boundaries $\pm\frac{n k_g}{2}$. The pressure fields were recorded along one line along x, hence with no information about wavevectors k_y or k_z measured directly.

either glide-symmetric samples B or C in chapter 8. The most notable contrast is how great an in-plane wavevector k_x the ALM can reach without forming a band-gap, as it now continues to exist as a bright feature close to the second Brillouin zone boundary at $k_x = k_g$, as opposed to just crossing $k_x = k_g/2$. A second difference is that this hybrid ALM has a near-constant phase and group velocity over a large subwavelength frequency range, rather than having a group velocity that tends to zero before reaching the first Brillouin zone boundary (such as did the various kinds of ASW measured throughout this thesis). This property in particular is useful for device design, as its mode index N is almost fixed over a broad frequency band. The third change in behaviour is visible at $\frac{\lambda_g}{\lambda_0} \approx 0.17$. Here, the ALM appears to approach the sound-line k_0 without gradually changing its group velocity to resemble a grazing surface wave, instead having a gradient discontinuity. This property appears to result from the arrangement of the two metal plates into a cavity, thus forming a waveguide. As the cavity length L is much greater than the wavelengths of the ALM and also $L \gg w$, one may expect the cavity formed to be below the waveguide cut-off and thus only allow planar wavefronts within it. However, the patterning of the slit walls with cylindrical cavities, as well as the finite width $d = 10$ mm of the aluminium blocks in y, both appear to change the waveguide behaviour in a complex way. More work needs to be done to investigate the effect each of these parameters have on the ALM, including measurement of the dispersion of the same two-plate system, but with no hole cavities present.

The $w = 1.0$ mm measurement also shown in figure 9.3 is not directly comparable to the $w = 1.6$ mm measurement, as both the probe microphone and high resolution digital oscilloscope were not available at the time of this experiment. Hence, a microphone with the larger diameter of 10 mm was used, with its detecting surface placed adjacent to slit-cavity in y, detecting the near-fields that were emitted either side of it. This set-up limited what near-fields the microphone could detect, as it was placed relatively far from each hole-cavity, and thus the measured fields not as highly confined. Still, some comparisons can be made. In contrast to the $w = 1.6$ mm measurement, the ALM here appears to have both a less-variable and larger mode index N within the first Brillouin zone, demonstrating how the mode index may easily be controlled via changing w. The ALM feature also appears to be broader, likely a result of the thermodynamic loss effects becoming significant, which from the conclusions drawn in chapter 4, implies that the effective speed of sound within the cavity is also reduced. The point at which the mode crosses the sound line k_0 is also at a lower frequency than before, suggesting that the plate separation w is having an important effect on this aspect of the mode's behaviour.

More work remains to be done with the sample, including new measurements with an optimised set-up, and a detailed study on how both the plate separation w and glide-symmetry condition effect the dispersion of the resulting ALM. In particular, a study of what effect thermodynamic boundary layers have on the propagation of the ALM itself (rather than just the cavity resonators which make their excitation possible) may prove insightful. As well as potentially allowing a great degree of control over mode index, this set-up provides many possibilities for further research. One may envision a system where each of the parameters unique to the set-up vary, such as a gradually decreasing plate separation w or deepening of hole resonators h as x is increased. Another idea is to create a system with 'double-glide-symmetry', by combining the samples in chapter 8 with the one discussed here, having a glide-symmetry plane in both the surface plane y and surface normal z. This would be one step closer to having a pair of full two dimensional square-arrays arranged in glide symmetry, being displaced by half of a unit-cell in both x and y, and separated by z. Such a sample has recently been explored in the electromagnetic regime[131], and an enhanced version of the 'beaming' effect such as that measured here in chapter 6 appeared to be possible. The idea is not constrained to the square array, as it could also be achieved with either a hexagonal, rectangular or rhombic Bravais lattice used as the basis. It may even be possible to use the patterned slit-cavity geometry outlined here as a basis for the creation a full periodic slit-array such as those studied in chapters 4 and 5, where the ALMs supported by each one of the slit-cavities may couple to those of its nearest neighbours.

9.3 Acoustic Orbital Angular Momentum from Screw-Symmetry in a Cylindrical Patterned Tube

In the detailed study by Hessel and Oliner of the effect that glide-symmetry has on electromagnetic waveguides is also included a second type of higher symmetry: 'screw-symmetry'[127]. In a system possessing screw-symmetry, the unit-cells periodic along z are arranged such that they are invariant under a translation S_p, which is a shift along z by some fraction of grating pitch λ_g/p, and then a rotation by some angle $2\pi/p$, where p is a positive integer. Stated mathematically in cylindrical polar coordinates,

$$S_\mathrm{p} = \begin{cases} r \rightarrow r \\ \theta \rightarrow \theta + \frac{2\pi}{p} \\ z \rightarrow z + \frac{\lambda_\mathrm{g}}{p} \end{cases} \tag{9.1}$$

A good example of system possessing such a symmetry is the slanted ridges which pattern a screw, hence the name, or alternatively the coil of a spring. The choice of p determines how many unit-cells overlap within any single one. In the 2D case of glide-symmetry, p is always two (and each unit-cell is overlapped by one other, so there are two in total). Hence, the two types of symmetry are related.

An example of how one may design an acoustic metamaterial with screw-symmetry is shown in figure 9.4. On the left is a cross-section across the z-plane of a hollow cylinder having some length in z, with outer radius $h_\mathrm{a} + h_\mathrm{b}$ and inner radius h_b. This cylinder is patterned with smaller open-holed cavities of radius a (and hole depth h_a), equally spaced around the ring by angle $\theta = 2\pi/3$, each shifted along z by $\lambda_\mathrm{g}/3$, though this is not visible. Thus the sample has screw-symmetry of order $p = 3$. A different way of representing this sample is depicted on the right of figure 9.4, which is what the surface of the cylinder would look like if one varied θ at constant radius $r = h_\mathrm{b}$. The shift of each line of holes relative to the others along the z axis is thus clear. Some preliminary FEM modelling of the above sample is presented in figure 9.5. Just as with the glide-symmetric systems, this sample appears to support an ALM that does not form a standing-wave at the first Brillouin zone boundary $k_\mathrm{z} = k_\mathrm{g}/2$. Further, it also does not form one at the second boundary, $k_\mathrm{z} = k_\mathrm{g}$, a result of the increase of integer p from 2 (glide-symmetry) to 3 (screw-symmetry). Indeed, FEM models of systems where $p > 3$ predict that the mode is able to continue beyond another Brillouin zone boundary each time p is increased (not shown), behaviour theorised by Hessel and

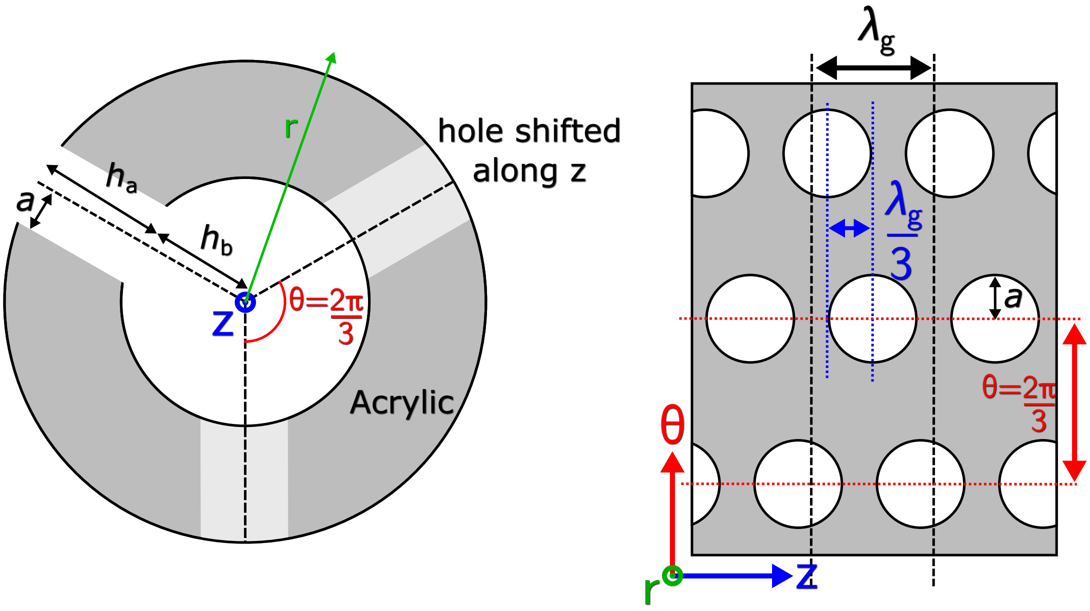

Figure 9.4: Schematics of example of a cylindrical sample, with holes arranged so at to create screw-symmetry. (Left) r-θ plane of the sample, with the periodicity in z not visible. There are three separate lines of holes of depth h_a and radius a, built into a hollow ring of acrylic with inner radius h_b. The holes are periodic in z having periodicity λ_g, and hole centres are equally distributed around the ring by $\theta = \frac{2\pi}{3}$, Each line is shifted by $\lambda_\mathrm{g}/3$ relative to the others to create screw symmetry. (Right) Example of z-θ plane, showing the surface of the cylinder as it would appear from a constant radius of $r = h_\mathrm{b}$. The periodicy along z of each of the 3 lines of holes is visible, including the $\lambda_\mathrm{g}/3$ shift that creates the screw symmetry.

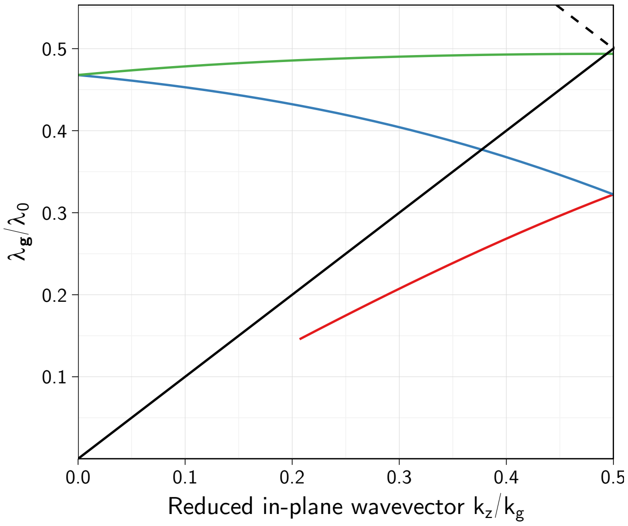

Figure 9.5: Dispersion diagram with numerically calculated eigenfrequencies of a screw-symmetric cylindrical waveguide with $p = 3$, as in figure9.4. In this reduced zone scheme, the red line represents the mode originating from $k_\mathrm{z} = 0$, the blue line the mode band folded from the second Brillouin zone, and the green line that from the third. Black solid and dashed lines represent k_0 and $-k_0 + k_\mathrm{g}$ respectively.

Oliner[127]. As well as this however, the models predict that it may be possible to create an acoustic line mode having pseudo 'orbital angular momentum', with a characteristic zero in field amplitude along the central axis z of the cylinder at $r = 0$. This was very recently shown to be possible by Jiang et al.[132] using a different mechanism. If such a sample was made, it could be characterised by measuring the near-fields emitted outside of the cylinder by each open-ended cavity, or by recording a cross section in z of the fields at the entrance and exit of the long cylinder.

9.3.1 A Note on Future Sample Fabrication

While it has not yet been experimentally characterised, a sample possessing screw-symmetry of the kind outlined above has been designed and created using a 3D rapid prototype machine, or '3D printer'. This machine can create samples from acrylic with a precision of between ~ 0.1 and 0.5 mm depending on printing orientation. A repeat of the measurements in chapter 7 with 3D-printed samples returned results indistinguishable from those obtained using the laser-cut or drilled samples, demonstrating that for acoustics, this fast and cheap method of sample creation is feasible. A picture of the screw-symmetry sample created this way is included in figure 9.6. The final version will require assembly of each segment into one long cylinder, a simple task if each piece is designed to fit together like a jigsaw puzzle. Acrylic dissolved in acetone can be applied to each join and acts as a strong glue, providing robust samples for measurement.

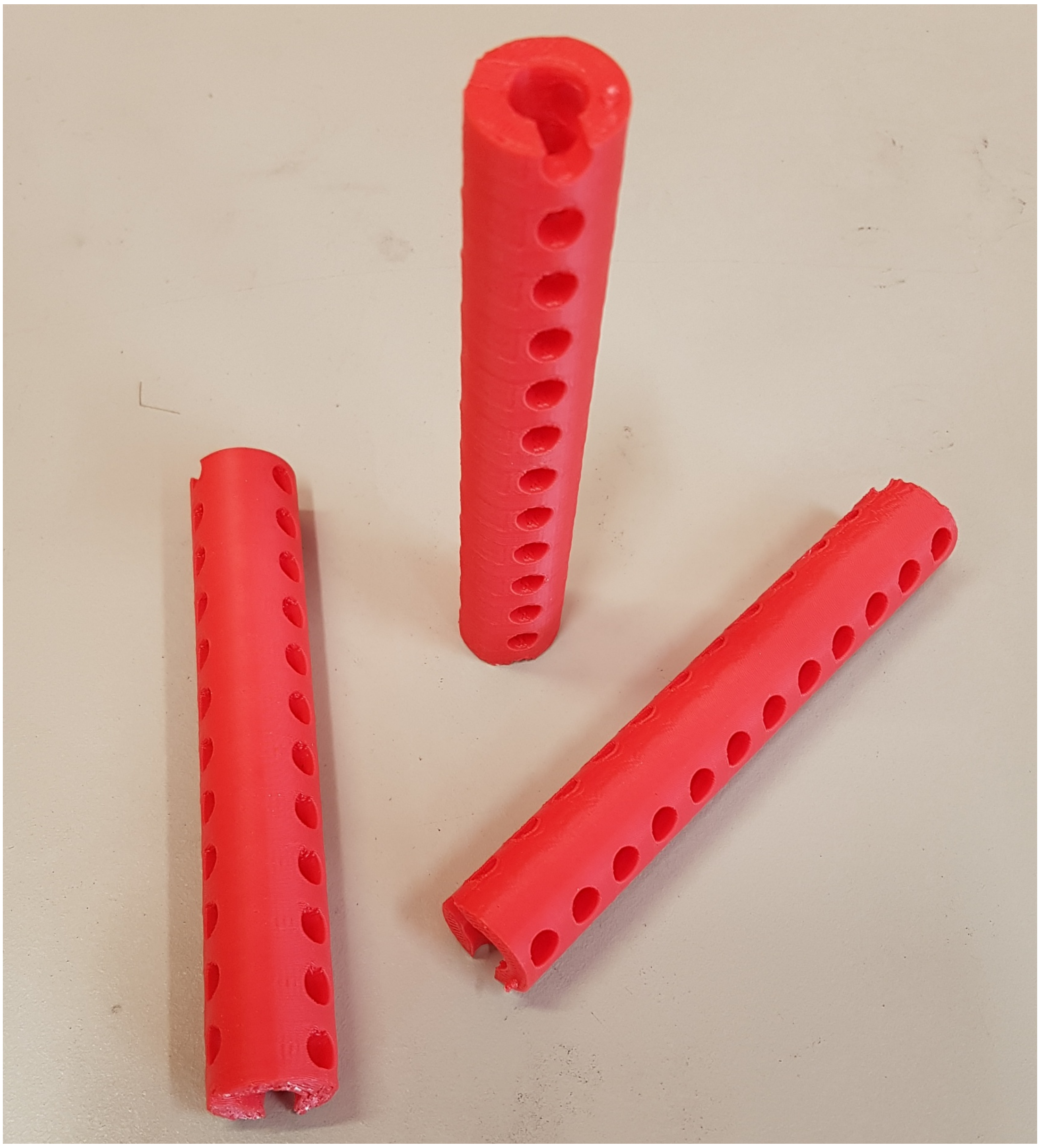

Figure 9.6: Picture of unassembled sample with screw-symmetry, printed by the 3D-prototype machine.

9.4 Acoustic Line Modes on Curved Geometry

The previous two samples were both ways of manipulating acoustic line modes using higher order symmetries. However, there remains much work to be done in characterising relatively simpler systems. In chapter 7, an ALM was shown to follow a line of holes when they were arranged into the shape of a ring. That system itself needs further investigation, such as a study on how the radius of the ring affects the mode, or for example whether a second circle of holes could be arranged in glide-symmetry along the θ axis relative to the first (either in z or r). However there is a different way to arrange the cylindrical holes altogether. Instead of having each cylindrical-cavity with its axis pointing along surface normal z, they could be arranged such that the axis points along surface normal r, via their placement on the inside of a larger solid cylinder. A 3D-printed sample created in this way is pictured in figure 9.7, with a labelled periodic unit-cell overlaid.

The major difference between this sample and the ring sample of chapter 7 is that instead of the surface mode being bound primarily in the z-plane, it is now bound in primarily in the radial r plane. This poses a few questions. Each cylinder is arranged periodically in θ, by a spacing of λ_{g_θ}. The faces of each open-ended hole are thus spaced more closely in Cartesian coordinates at radius $r = R$ than at radius $r = R+L$, L being plate thickness and thus hole-depth. However, a surface wave with the same frequency must exist on both surfaces as they are always connected[27], though the fields at each end must traverse separate distances and would thus have different periodicities if arranged in a straight line. This was also true of the radii of each hole in the ring sample of chapter 7, but to a lesser degree. As discussed there, this dilemma has important implications for the definition of a trapped mode. Berry[125] detailed similar geometries for surface-plasmons on curved surfaces, with the conclusion that on a convex surface, the surface mode must eventually radiate due to the speed of the radial wavefronts surpassing that of free-space radiation at some calculated radius. What Berry also concludes is that on a concave surface, the opposite is true, so that a real surface-wave is supported. Hence one might expect that the surface mode on the inside ring of the sample in figure 9.7 (or that in chapter 7) would be truly bound, but the one on the outside will radiate. Increasing the length L however gives a degree of control over the difference between the two radii, pushing this theory to its limits. Also, the fields would be strictly confined to each cavity before they emerge on the outer surface rather than being free to radiate, which may have an important effect. One could also cover the outer surface thus closing the outer end of the cylindrical cavities, and create a true surface mode that only existed on the inner radius. A long tube patterned with such rings of holes may prove useful as an acoustic baffle.

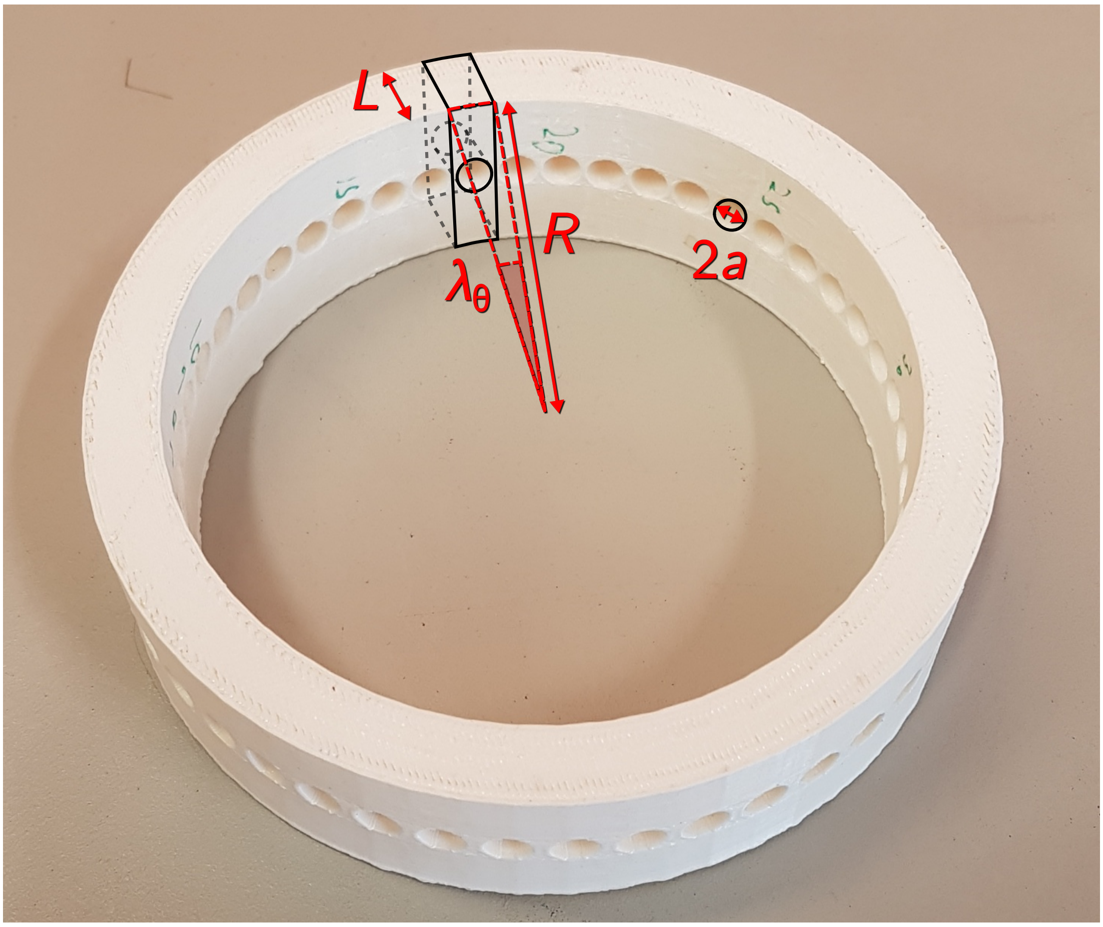

Figure 9.7: Picture of 3D-prototype printed sample, with schematic overlaid. A set of 46 open-ended cylindrical holes of depth $L = 8$ mm and radius $a = 3$ mm are periodically arranged into the shape of a ring, with periodicity $\lambda_{\mathrm{g}_\theta} = 2\pi/46$, and cylinder axis pointing along r.

9.5 Other Future Work

As well as the ideas and preliminary work outlined so far in this chapter, there are many other potential routes that the research throughout this thesis could be taken. In regard to ways of manipulating acoustic surface waves, the ever improving accuracy of modern 3D rapid-prototype machines is particularly exciting for acoustic metamaterials, as for airborne sound, almost any solid is rigid enough to be considered rigid and thus support the local resonances that are crucial to the acoustic impedance grating mechanism. Sample designs that may take a long time to assemble with more conventional methods can be created through simply sending a computer generated schematic to a 3D printer, which then proceeds to print it in as little time as a few hours. Not only is it faster and cheaper, but intricate structures can be replicated with precision in ways that may not be possible with traditional machine work, a highly important property for periodic metamaterials. A sample that demonstrates this capability is pictured in figure 9.8. This sample consists of a square-array of meta-atoms, each containing four-open ended cylinders. The cylinders do not go straight through the sample however (as they did in the sample studied in chapter 6), but instead their exit side is translated in either x or y such that it emerges in line with the position of one of the other four holes on the entrance side. This produces a ‘twist’ effect, where one might expect a rotation in phase of the pressure fields emitted on the exit side relative to the entrance side as the phase of the field cannot change within the resonant cavities (for the fundamental resonance), though modelling or experimental work that investigates this in detail is yet to be undertaken. What this sample does demonstrate is how readily such a complex structure may be created. The idea itself is based on recent research involving ‘Synthetic Gauge Flux’[133], a property of systems that may support topologically protected acoustic modes[134] that make possible the excitation of modes that can transverse obstacles with zero reflection. This topic is a complicated one that requires a very detailed discussion; the reader is referred to the references.

Finally, one area of research that has so far received little attention is the interaction between the air-bound acoustic surface waves that have been the focus of this thesis, and the solid-based surface acoustic waves (SAWs) outlined in section 2.7.9. While there exists much work regarding the interaction of SAWs with periodic solid-structures (phononic crystals)[88,83,22,89,90], how they interact with fluid bound acoustic surface waves has thus far only been explored in water, where the impedance mismatch between water and solid is not so great to forbid their interaction[92,135]. It may seem implausible that such modes could also play a role in air-based metamaterials due to the huge impedance mismatch, but with careful design of the sample, it could indeed be possible. For example, one could utilise a soft material such as rubber, or indeed, the class of

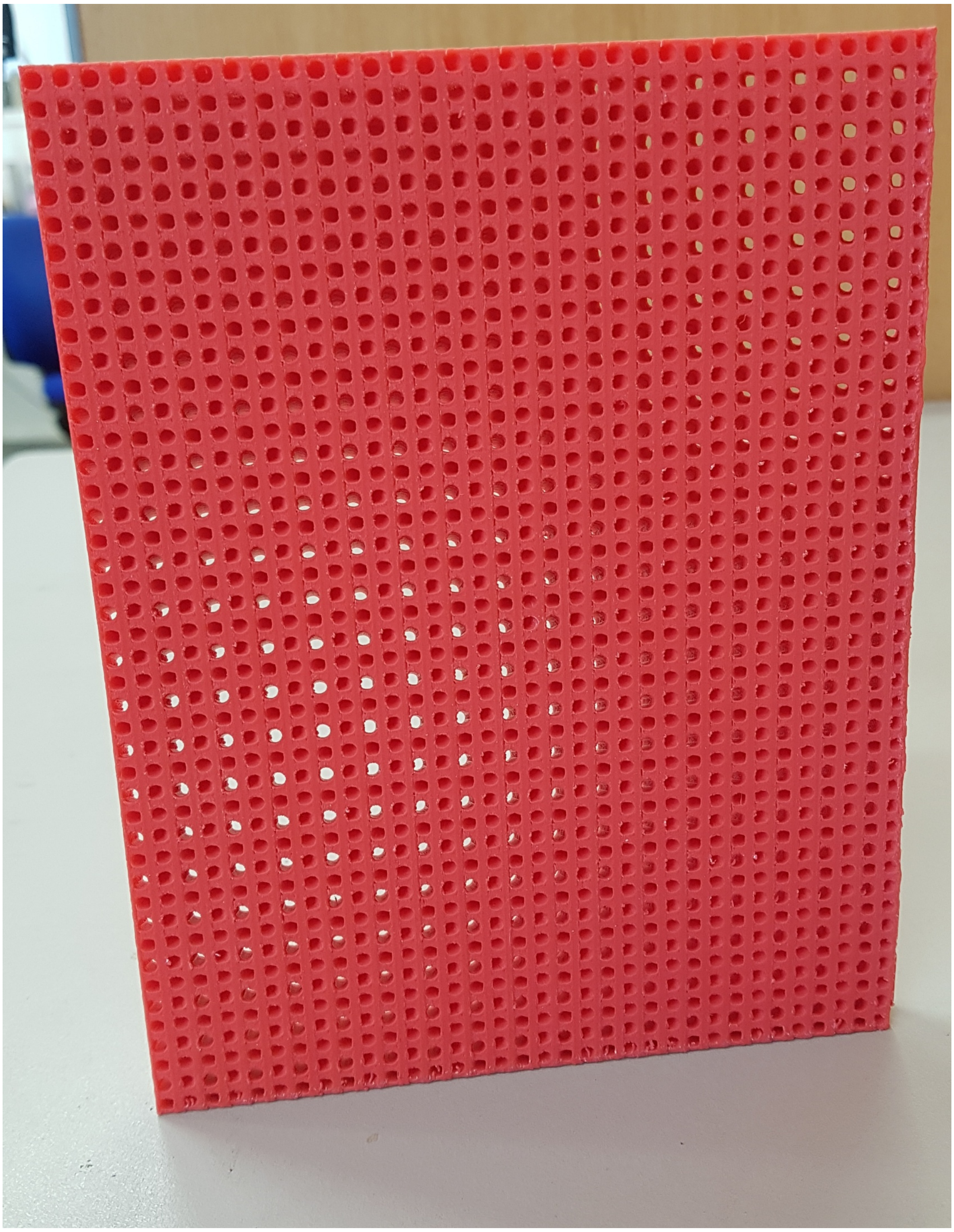

Figure 9.8: Picture of 3D-prototype printed sample, consisting of a square lattice of open-ended cylinders. Each unit cell contains 4 cylinders, and each cylinder is 'twisted' so that they emerge in a different location on the surface plane of the exit side than on the entrance side.

materials known as ‘aerogels’[136] (with speed of sound through these materials less than that of air). The lowest frequency Lamb mode[91] supported by a finite thickness plate crosses into the radiative regime of a dispersion diagram at the ‘coincidence frequency’ (determined by geometry and material properties), where the mode splits into a radiative and non-radiative pair[137]. A patterning of the surface could place an ASW at the same frequency of this non-radiative SAW, with the two potentially interacting in unforeseen ways. Further, the interaction between solid-based acoustics and thermoviscous-boundary layers appears to have been completely unexplored, as the rigid boundary approximation assumes that the wave in the fluid cannot penetrate the solid. This is only an approximation however, and a sufficient amplitude plate resonance placed at the correct frequency could lead to interesting behaviour, as the boundary layer effects studied in chapter 4 are very sensitive to slit-width or tube radius. Hence, a displacement of the plate induced by a SAW could change the response of the ASW supported by each resonant cavity, potentially producing a non-linear effect.

9.6 Conclusion

In this chapter, some ideas for extensions of the experimental work presented in chapters 4 through 8 are outlined. The majority of these ideas relate to extensions of the acoustic line mode research in chapter 7. The first extension is a different way to create a system with glide-symmetry than explored in chapter 8,which perhaps allows for a greater degree of control of the surface mode index . The second idea outlined how a different type of higher order symmetry, ‘screw-symmetry’, may be able to create a surface mode possessing acoustic orbital angular momentum. The third avenue for possible future research builds on the work presented in chapter 7, investigating a system where a ring of holes is arranged on a larger three-dimensional cylinder than a flat surface, which could have intriguing implications. Each of these ideas has a sample that has already been produced, and this was achieved with the use of a 3D rapid prototype machine. A brief discussion of the significant potential this device has for the design of acoustic metamaterials is included, its use further demonstrated with a picture of a complicated 3D structure. Finally, other ideas are touched upon, such as how well known solid-based surface acoustic waves may provide a new way to perturb airborne acoustic surface waves.

Chapter 10

Conclusions

The research contained within this thesis concerned the design and characterisation of acoustic metamaterials that all supported airborne acoustic surface waves, that were excitable via the diffractive coupling of periodically arranged resonant cavities. The experimental chapters of the thesis could be broken down into two sections, with regards to the type of measurement employed. The first two experimental chapters, 4 and 5, focused on measuring the far-field acoustic transmission spectra of sets-of or individual aluminium slit-cavities, arranged to create a variety of periodic structures, and thus indirectly detect the presence of acoustic surface waves. The latter three chapters, 6, 7 and 8, concerned the measurement of the near-field acoustic response of a variety of samples formed of open-ended hole cavities arranged into periodic lattices, thereby directly detecting the excitable acoustic surface waves.

Of all of the experimental chapters, the first in particular stands out from the rest, as it concerned fundamental physics that had ramifications for all of the chapters that followed it, and indeed all impedance-grating-style acoustic metamaterials. Chapter 4 explored in detail the effect of thermodynamic boundary layers on sound propagating through air confined to narrow slit-cavities. On the boundary of any perfectly-rigid material (such as most solids can be treated relative to air) exists a pair of thermodynamic boundary layers associated with the properties of the gas medium: the viscous boundary layer, and the thermal boundary layer. Their effect on sound propagating through long narrow tubes was studied in detail over a century ago by famous physicists such as Kirchhoff and Lord Rayleigh, with much work being done since. However, these boundary layers are typically very thin compared to the propagation wavelength of the sound, being two orders of magnitude or more smaller than the width of a resonant slit-cavity typically used in the design of acoustic metamaterials. A study by Lord Rayleigh at the turn of the 20^{th} century predicted that the work done regarding narrow tubes was also relevant to the slit-geometry, with a simple substitution of radius for slit-width, but this work has been largely ignored. As such, much modern acoustic metamaterial research has naively assumed boundary layers effects to be negligible when constructing their models, as they introduce much mathematical complexity. By careful measurement of the resonant frequency as a function of slit-width for both a slit-array and single slit, it was shown that on the contrary, boundary layer effects become important on a scale more than two orders of magnitude larger than their size. This was manifested as a reduction of the measured resonant frequency and significant attenuation of the resonance, the opposite behaviour to that predicted by loss-free models. The experimental data was compared to analytical theory, where it was found that a 5% reduction of the effective speed of sound through the slit is observed when the boundary layers formed only 5% of the cavity width for both samples, confirming Lord Rayleigh's predictions. Hence, not only was it shown that the loss-free treatment common in the wider acoustic metamaterial community is unrealistic, but also that it is possible to control the effective speed of sound through a slit-cavity just by changing its size, providing a new degree of control for future metamaterial design.

In chapter 5, four separate slit-array samples, each formed of aluminium slats, were utilised to demonstrate the existence of the acoustic 'phase-resonance'. This was achieved via both experimental and numerical measurement of the angular dependence of the transmission spectra of each of the gratings. It is well known that arranging a set of resonant cavities into a simple periodic periodic slit-array can lead to 'Enhanced Acoustic Transmission', whereby acoustic surface modes arising from diffraction can hybridise with the Fabry-Perot like resonant cavity modes, and lead to strong peaks in the grating's transmission spectrum. Altering the grating structure so that its basis was comprised of more that one slit-cavity, (i.e. it became a 'compound' grating structure) resulted in sharp dips in the transmission spectra, that may have had a strong angular dependence. These dips resulted from the excitation of phase-resonances, whereby the fields in adjacent cavities may be out-of-phase, made possible by extra degrees-of-freedom being available to the near-field. Mapping the angular dependence of the transmission spectra of these compound gratings illustrated the dispersion of the phase-resonances. Hence, it was shown that the phase-resonant features could be considered as acoustic-surface-waves band-folded into the radiative regime from larger wave-vectors than possible on a simple periodic grating, and could thus indirectly couple to the incident radiation to create dips in the transmission spectra. Also, one of the compound grating structures was optimised via numerical methods to account for the thermodynamic boundary-layer effects studied in chapter 4, thereby achieving deep, sharp transmission minimum in a broad transmission maximum, which may be useful for the design of acoustic filters.

Chapter 6 was the first chapter to utilise the high resolution near-field imaging technique that allowed direct measurement of acoustic surface waves. The ASWs excitable on a two-dimensional square-lattice of open-ended holes were characterised, via creation of high-resolution pressure field maps that visualised how sound interacted with the sample. It was found that over a range of frequencies, the acoustic power flow is channelled into specific, predictable directions, forming narrow beams with a well defined width. Two-dimensional spatial Fourier transforms of the real-space pressure field maps showed that this was a result of the dispersion of the acoustic surface waves being strongly dependent on the direction of propagation relative to the lattice. Over a controllable frequency band, an ASW could only form in one set of principle directions, thus creating the strong beaming effect.

In chapter 7 was demonstrated the existence of the 'Acoustic-Line-Mode', a type of acoustic surface wave that is excitable on a simple one-dimensional line of holes. High-resolution measurements of the acoustic near-field were again utilised to characterise the surface mode dispersion via spatial Fourier transforms. More significantly, it was demonstrated that the acoustic line mode may be readily manipulated. This was achieved via arrangement of the line of holes into a circular ring, and the measurement repeated using polar-coordinates, whereby an acoustic line mode was shown to propagate around the ring. This strongly localized acoustic line mode, whose behaviour was dominated by coupling between resonators along the line in which they are arranged, offers opportunity as a novel method for the control of sound.

The final experimental chapter, chapter 8, explored the effect that 'glide-symmetry' had on a pair of coupled acoustic line modes. Glide symmetry is achieved when a system periodic along x is inverted along its y-mirror plane, and then shifted by exactly half of a unit-cell, such as a 'zig-zag' shape. Three samples were characterised. The first was an arrangement of two lines of open-ended holes, symmetric about y and periodic along x. Two acoustic lines modes were found to exist, one with 'even' character (the phase of the adjacent cavities equal) and a higher frequency mode with 'odd' character (the fields of adjacent holes in anti-phase). The second sample was the glide-symmetric arrangement of the first, with one of the lines of holes appropriately shifted with respect to the other. It was then found that the two acoustic line modes excitable on the first sample become indistinguishable from each other at the first Brillouin zone boundary, where the glide-symmetry forbade the formation of a standing-wave. Hence, a mode with mixed 'even' and 'odd' character became excitable, with a larger in-plane wavevector and thus mode index than previously possible, as well as a region of apparent negative mode dispersion. The third sample is similar to the second, except that the cylindrical holes were replaced with triangular-prisms. These were able to be arranged in glide-symmetry in such a way that the fields within each cavity could couple strongly to its neighbours. This allowed a mode to form with a very large in-plane wavevector, demonstrating a degree of control possible over the band-structure of acoustic line modes with glide-symmetry, that may be useful for the design of devices such as acoustic-lenses.

In conclusion then, it has been successfully demonstrated that metamaterial design concepts can be applied to the classical field of acoustics. The experimental and numerical work throughout the thesis is in good agreement, and the ideas presented may well prove useful for future design of novel acoustic devices. As explored in chapter 9, many more ideas have since been spawned that when investigated could further contribute to the ever-growing field of acoustic metamaterial research.

Chapter 11

Publications and Conferences

11.1 Publications

- Ward, G. P., Lovelock, R. K., Murray, A. R. J., Hibbins, A. P., Sambles, J. R. and Smith, J. D., Boundary Layer Effects on Acoustic Transmission Through Narrow Slit Cavities, Physical Review Letters **115**, 044302 (2015)

- Ward, G. P., Hibbins, A. P., Sambles, J. R., and Smith, J. D., Acoustic transmission through compound subwavelength slit arrays, Phys. Rev. **B** 94, 024304 (2016)

- Ward, G. P., Hibbins, A. P., Sambles, J. R., and Smith, J. D., The Acoustic Line Mode, *In Submission*

- Ward, G. P., Hibbins, A. P., Sambles, J. R., and Smith, J. D., Acoustic Surface Wave Beaming, *In Preparation*

- Ward, G. P., Hibbins, A. P., Sambles, J. R., and Smith, J. D., Acoustic Line Modes with Glide Symmetry, *In Preparation*

11.2 Presentations and Conferences

11.2.1 Oral Presentations

- The Journal of The Acoustic Society of America Fall 2014 Meeting, Ward, G. P., Lovelock, R. K., Murray, A. R. J., Hibbins, A. P., Sambles, J. R. and Smith, J. D., Boundary Layer Effects on Acoustic Transmission Through Narrow Slit Cavities. Indianapolis, USA, November 2014

- Progress in Electromagnetic Research Symposium 2015, WARD, G. P., HIBBINS, A. P., SAMBLES, J. R., and SMITH, J. D., Acoustic transmission through compound subwavelength slit arrays. Prague, Czech Republic, June 2015
- Smart and Multifunctional Materials, Structures and Systems (CIMTECH) International Conference, WARD, G. P., LOVELOCK, R. K., MURRAY, A. R. J., HIBBINS, A. P., SAMBLES, J. R. and SMITH, J. D., Boundary Layer Effects on Acoustic Transmission Through Narrow Slit Cavities. Perugia, Italy, June 2016

Appendices

Appendix A

Time-Domain to Frequency-Domain (1D) Fast Fourier Transform

Throughout this thesis, the key technique underpinning all of the experimental methods - from recording transmission spectra to creating near-field pressure maps - is recording a signal in the time domain, and then extracting from it a frequency domain spectrum. This 'Fourier transform' is a very well known technique, but it is useful to outline the concepts behind it, and detail both the basic and more complex signal processing techniques that were used to produce all of the experimental data with which this thesis is concerned.

First, consider a simple time signal, whose frequency is already known. Figure A.1A is a computer generated 1D sine function in the time-domain, which goes through a full cycle from 0 to 2π in 1 second, thus having a frequency of 1 Hz. When recording this signal with digital equipment, it will be split into discrete points on the time axis, spaced ΔT apart. This value, multiplied by the total number of points N, will give the duration of the time-window over which data is recorded T (in figure A.1A, $\Delta T N = T = 1$ s, though as will be explained, this total time does not appear to correspond to the signal shown). The sample rate f_{s} is thus equal to $\frac{N}{T}$[138,139,140]. Figure A.1A shows two possible measurements of the sine wave signal, one with an odd number of points $N = 19$ (red), and one with an even number of points $N = 20$ (blue). In order to see what frequency components make up the time signal (which will allow characterisation of complex experimental data), one must convert from the time-domain to the frequency-domain[139]. Since the signal is divided into discrete points,it is necessary to use the discrete Fourier transform rather than the standard Fourier

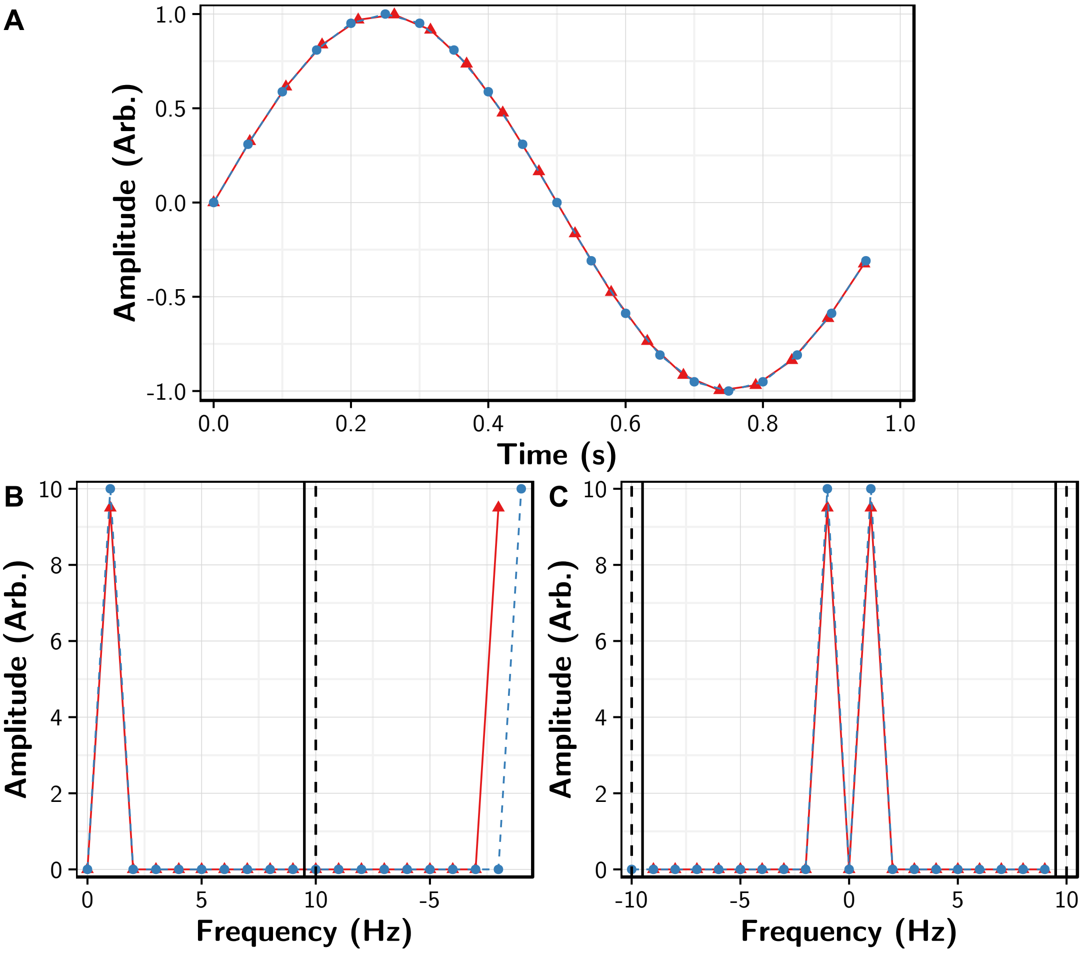

Figure A.1: Example of the properties of a time-to-frequency FFT. (A) One cycle of a 1 Hz sine wave oscillation, measured with number of samples $N = 19$ (red triangular points and red solid line) and $N = 20$ (blue circular points and blue dashed line). (B) Direct result of the FFTs on the two signals in plot A, with colours and points having corresponding meaning. The vertical dashed lines (coloured black and with line-type solid for odd, dashed for even) mark the Nyquist frequency, with higher valued points corresponding to negative frequencies. Zero represents the DC signal. (C) Result of applying the 'FFT-shift' function to B, placing DC in the centre, with positive and negative frequencies either side. Again, colours and line types are inherited from plot A. The extra point at the Nyquist frequency included in the $N = 20$ dataset has been placed on the negative side.

transform function[140] (Note, *not* a discrete-time Fourier transform - this produces a continuous result rather than a discrete one). One algorithm that makes this possible is the Fast-Fourier-Transform (FFT), commonly available in statistical analysis software such as R or MATLAB. This function can take any consistently sampled time signal and return a complex valued discrete frequency spectrum, containing amplitude and phase information. A detailed description of the computing processes behind such an algorithm is beyond the scope of this work, a reference is included[141]. Such a function is utilised in all subsequent signal analysis.

Note a potential point of confusion here - as it appears in figure A.1A, the time between first and last points is *not* 1 s. This is because the total time measured also has a period ΔT after the final point, as the FFT function treats the signal as though it repeated infinitely, and thus wraps around back to the start point (this property has important consequences to be discussed forthwith).

Figure A.1B shows the absolute value of the result of the FFT function applied to the two differently sampled time signals in figure A.1A. The properties of the resulting frequency spectrum are dependent on the parameters $\Delta T, T, N$ and f_s. The maximum frequency it is possible to extract from a given discrete time signal is known as the Nyquist-Limit or Nyquist frequency, given by $N_\mathrm{q} = f_\mathrm{s} = \frac{f_\mathrm{s}}{2} = \frac{1}{2\Delta T}$, and this is represented by the red dashed and blue dot-dashed vertical lines. This limit arises because any frequencies present in the signal greater than it, will fall victim to aliasing, where a lack of information means it is possible to reconstruct a lower frequency wave between the recorded points than the signal actually was. There is no way to know that this has not occurred without increasing the number of samples in the measured time window, thus the Nyquist limit. After the FFT is applied, the frequency resolution of the resulting frequency spectrum Δf, i.e the spacing between each unique frequency f (known as a ‘bin’) is given by $\Delta f = \frac{f_\mathrm{s}}{N} = \frac{1}{T}$, hence, the longer the time recorded, the better the frequency resolution becomes.

The direct result of the FFT (figure A.1B) appears counter-intuitive, with the Nyquist frequency appearing in the centre of the spectrum and not on the high end. This is because the FFT function returns both positive and negative frequencies, separated by the Nyquist limit. If the original sample included complex phase information, then these frequencies represent forward and backward travelling waves respectively. Both odd and even length samples will return a result with the bin at the origin $f = 0$ being the DC component, followed by the positive frequencies up to the Nyquist limit, and then the negative frequencies in descending order back down to the first non-zero bin. In figure A.1B both samples show a peak at $f = 1$ Hz and zero everywhere else since that was the original signal and no other frequencies were present.

A key distinction between the odd length and even length samples is that the

Nyquist frequency N_q always falls $\frac{\Delta_f}{2}$ outside of the maximum frequency bins of the odd sample, whereas it lies exactly on either the positive or negative maximum bin of the even one, as can be seen in figure A.1B. This is important when rearranging the spectrum as has been done in figure A.1C. Here, the 'FFT-shift' function is applied, which places the DC component in the centre of the signal and the positive and negative components either side, with the extra Nyquist point in the even length data set placed in the negative half (this choice is arbitrary, but is the pattern that the rest of this thesis follows). The frequency axis is thus given by:

$$f = \begin{cases} -f_\mathrm{max}, -f_\mathrm{max} + \Delta f,\ \ldots,\ 0,\ \ldots,\ (f_\mathrm{max} - \Delta f) & \text{if } N \text{ is even} \\ -(f_\mathrm{max} - \frac{\Delta f}{2}), -(f_\mathrm{max} - \frac{\Delta f}{2}) + \Delta f,\ \ldots,\ 0,\ \ldots,\ (f_\mathrm{max} - \frac{\Delta f}{2}) & \text{if } N \text{ is odd} \end{cases} \tag{A.1}$$

For the frequency spectrum analysis that used with the experimental measurements contained in this thesis, the negative half of frequency space is not needed, since phase information was not recorded in the time-domain data (the signals do not have an imaginary component, only the pressure amplitude at a given time was measured). This means that the two halves of frequency space are always mirror images of each other; mathematically it isn't possible to know what direction the waves were travelling in. Henceforth, the result of any experimental 1D FFT will only show the positive half of frequency space (and usually, only a small relevant section of that).

With the basics behind the fast-Fourier-transform outlined, it is clear that the ideal time domain measurement would have a very high sampling frequency f_s, measured over as long as possible a time T, in order to get the best frequency resolution Δf over the relevant frequency range $0 \rightarrow f_\mathrm{max}$. This is not always possible however, so the next step is to explain some of the difficulties encountered when performing real-world signal analysis, that may lead to false features in the measured frequency spectrum. One of the most problematic causes of these false features is 'spectral leakage'.

A.1 Spectral Leakage

As mentioned in the previous section, the FFT result figure A.1B of the 1 Hz sine wave in figure A.1A returned an answer where all of the Fourier amplitude was contained in the 1 Hz frequency bin. This is actually a rare scenario, which was possible to construct through suitable choice of $\frac{f_\mathrm{s}}{N}$ because the exact frequency of the original sine wave was already known. This is not possible in an experiment where one may wish to determine the frequency response of some sample: it is by definition unknown. A more realistic measurement scenario is presented in figure A.2, which shows the result of what

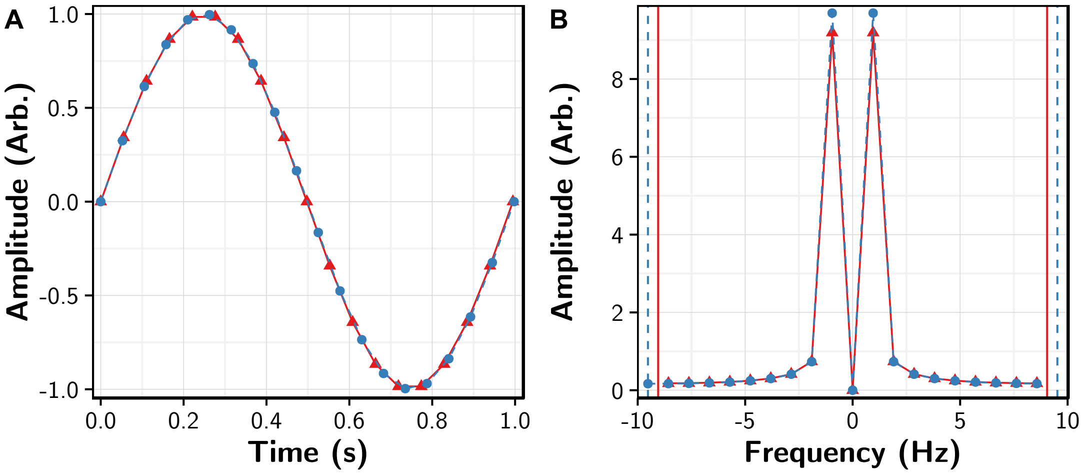

Figure A.2: (A) A 1 Hz sine wave signal sampled in the time-domain, measured with number of samples $N = 19$ (red triangular points and red solid line) and $N = 20$ (blue circular points and blue dashed line) (B) Result of the FFT function applied to the signals in A, with the FFT-shift function applied. Colours and line types correspond to those in A. The Nyquist frequency for each signal is represented by the vertical lines, styled accordingly.

happens if recorded sample points are not exactly commensurate with the underlying signal. In this sample, the number of points N in the odd and even time samples is the same as it was in figure A.1A, but the sample rate f_s has been increased slightly so that the first and last sampled points lie on the same point in the sine wave signal, and the resulting FFT does not have a frequency bin lying exactly at 1 Hz. Now, in the resulting FFT (figure A.2B) most of the amplitude is contained in the bin nearest to 1 Hz (in this case, $\Delta f = 0.952$, so at 0.952 Hz), however, the nearby bins are also non-zero. This is a phenomenon known as 'spectral leakage'[139,140], and is a result of the finite-width time segment, or 'window', that must be applied to analyse any time signal.

When the FFT function is performed, the segment of the signal that has been recorded is treated as though it repeated infinitely in both positive and negative time around the start point. This means that if the recording window was not exactly commensurate with the wavelength of the underlying signal, then there will appear a false feature where each end of the signal is 'stitched' together. In figure A.1A, we see that the first sample is exactly where the point following the last sample would be, perfectly reproducing the whole 1 Hz sine wave when treated as infinite. The same is not true of the signal A.2A, where the next point that would be in the sequence would not correspond to the first recorded sample - i.e. when this signal is 'stitched' together in an infinite chain, the first and last points have zero change in amplitude, producing a brief artificial flat feature. Sharp features in time lead to broad features in frequency, so this artefact 'leaks' into frequency bins surrounding the real signal, causing them to have a non-zero amplitude. Aside from giving us an incorrect measurement of the width of a peak in the spectrum, spectral leakage can be a particularly big problem when working with noisy signals, or when more than one frequency is present, and the signal one trying to measure is not as strong as a different signal present in the data. This is because the desired signal can be lost in the amplitude of the spectral leakage of the larger signal. Further, unless the bins are perfectly placed, the amplitude of the signal at its peak will be incorrect, as its true peak lies in between the available frequency bins - this is a problem known as scalloping loss, or the 'picket fence effect'[139,140].

Numerous methods have been developed to account for spectral leakage, some of which have been used throughout this thesis and are covered next.

A.2 Zero Padding

As will be explained in section 3.2, experimental samples will be excited with a broadband pulse, and resulting signals recorded while they 'ring-out' in order to determine the sample's frequency response. So, for the best frequency resolution Δ_f, one must record for as long as it is possible after the initial pulse is sent. However, there are realistic limits in place that prevent this, such as unwanted stray signals arriving at the detector that originate from e.g. a reflection from the wall of the room the experiment is contained in. These extra signals interfere with the signal emitted from the sample, and must be eliminated. The most effective way to do this is to 'time-gate' them out, i.e. stop the recording of the signal before any extra signals can interfere with it. However, this necessarily limits frequency resolution Δ_f, even if no reflections are recorded as a result. A method known as 'zero-padding' can reduce this problem, provided a few assumptions are made.

To access all of the possible frequency bins in the time-gated signal after it is determined that the most important part of the spectra have been allowed to ring-out (i.e., long enough that the sharpest signal one wished to measure will be within the frequency resolution), zero-padding can artificially increase the resolution of our frequency spectrum. This involves computationally adding time-points with no amplitude (zeroes) either end of the original time signal, still spaced ΔT apart, thus artificially increasing the total time measured T. This is the procedure followed to create the red signal in figure A.3A, where T and thus Δf has been tripled (the total number of points is now $N = 57$, up from 19, hence Δf is reduced by $\frac{1}{3}$). Figure A.3B compares the result of the original FFT with the zero-padded one, highlighting the resulting difference in frequency spectrum. Of course, since there is no new information contained in the extra zero points, it will not suddenly be possible to pick out two separate signals

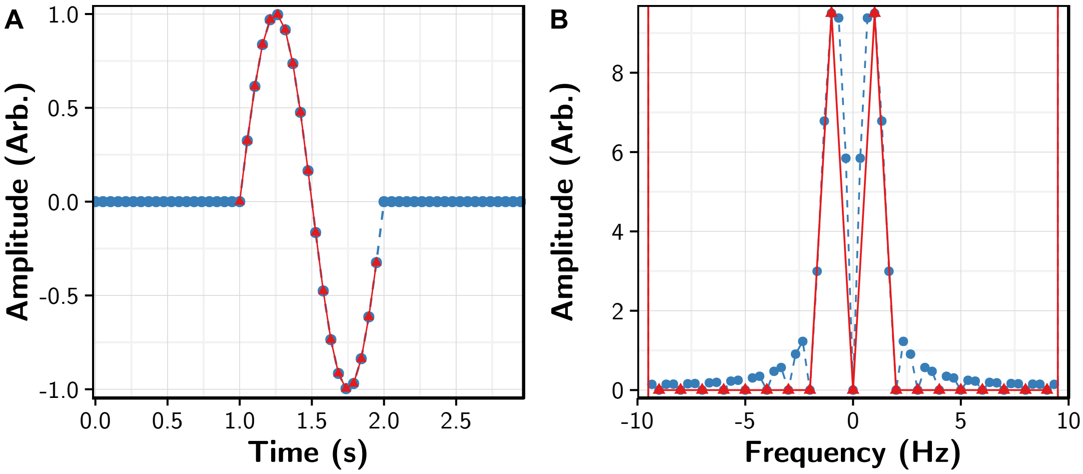

Figure A.3: (A) A single cycle of a 1 Hz sine wave signal, without (red triangles and solid line) and with (blue circles and dashed line) zero padding of the dataset. (B) Result of the FFT function applied to the signals in A, with the FFT-shift function applied. Colours and line types correspond to those in A. The Nyquist frequency is represented by the solid vertical line, and does not change between samples.

spaced less than Δf apart in the underlying signal, but what this does allow for is to see extra frequency bins and thus know which bin contains the strongest amplitude, giving a more accurate centre frequency (and reducing the scalloping loss). There is an obvious consequence; the perfect continuity of the signal at each end is destroyed, thereby introducing large amounts of spectral leakage, as is visible in the multiple new non-zero peaks in the zero-padded signal (figure A.3B). These extra peaks are known as ‘side lobes’; an explanation of ‘window’ functions allows a better understanding why this occurs, and hence how to reduce the issue, discussed in the forthcoming section.

Note, there is another reason one might want to use zero-padding. There exists a subset of FFT algorithms that are far more efficient than others, but they can only be used if the number of sampled points N is a power of two, which can be achieved by selectively adding zeroes[139,140]. The small size of the recorded time signals (less than 20,000 points) meant computer processing speed was generally not an issue here, so this feature was ignored.

A.3 Window Functions

When one records a finite length time segment from a continuous signal, what has effectively occurred is that the signal has been multiplied by a rectangular window function[139,140]. This is a function which has a value of one for some defined width (T), while being zero elsewhere. This rectangular function has its own frequency response, which is a sinc function, and this sinc function is convolved in frequency space with

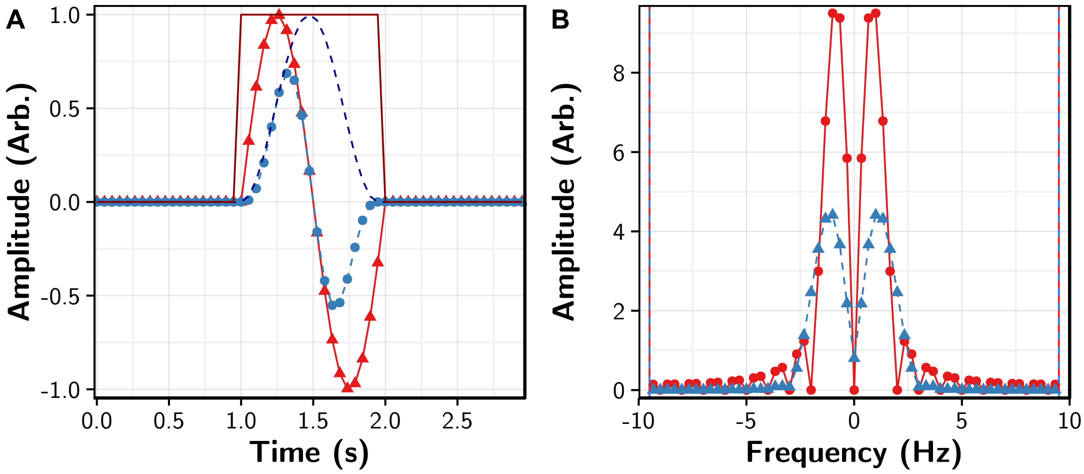

Figure A.4: (A) A zero padded single cycle of a 1 Hz sine wave signal, with the red solid line multiplied by a rectangular window function (dark red solid line) and with the blue dashed line multiplied by a Hanning window function (dark blue dashed line). (B) Result of the FFT functions applied to the signals in A, with the FFT-shift function applied. Colours and line types correspond to those in A. The Nyquist frequency is represented by the solid vertical line, and is unchanging between samples.

the frequency response of the signal that is being analysed[142]. When the finite width signal is zero-padded (section A.2) or spectral leakage occurs (section A.1), all that is actually happening is that more of the response of this rectangular window function is uncovered, manifesting as the 'side-lobes' that appear either side of the fundamental peak. When the signal is sampled such that the bins of the FFT overlap perfectly with the frequency of the signal (as in figure A.1), the bins coincide perfectly with the nulls of the rectangular window's sinc function, so it appears not to exist. This is clearly illustrated in figure A.3B, where the extra resolution gained from the zero-padding uncovers the sinc function between the nulls of the original signal's frequency response.

So, since this sinc function appears in the frequency spectrum due to the response of the imposed rectangular window (alternatively, because the signal is forced suddenly to zero at each end), it follows that one could reduce this problem by changing the fundamental window function. Numerous such window functions have been developed, each having its own set of strengths and weaknesses[143,142,139,140]. Window functions are characterised by the strength of its FFT's side-lobes, as well as a few other properties such as the window's effect on the accuracy of the amplitude or the sharpness of the main peak. Throughout the measurements in this thesis, it is the shape of the frequency response that is sought, with specific and accurate values for amplitude and width made less important with the use of a reference signal. Hence, the window function that has been chosen is the 'Hanning' window that is in particular useful for reducing spectral leakage[143,144], since it smoothly tailors the recorded signal to zero at each end of the finite time window.

The effect of the Hanning window in the time-domain is shown by the red signal in figure A.4A, compared with the plain rectangular window function (blue signal). In both cases the signal is zero padded (after application of their respective window functions). The differences in the resulting FFT spectra (figure A.4B) are stark. As before, the original signal shows a strong peak at 1 Hz, with the rectangular window's sinc function spread out through the rest of the bins. The signal that was multiplied by the Hanning window is much lower in amplitude, also being broadened, but the side lobes have been significantly weakened. With this spectrum we can be much more confident that the true signal is contained within the main peak, and that any sharp features that could be either side of it in a more complex time signal will not be 'drowned out' by the side lobes of the imposed rectangular window function. It is also far easier to fit a Lorentzian peak to this signal, allowing a more accurate extraction of the centre frequency of the resonance - this is particularly true if the real signal is significantly damped, unlike the perfect sine wave example used here.

These are the fundamental techniques that have been applied to analyse experimentally recorded time signals throughout this thesis. Section 3 contains details on how these times signals are generated and recorded in the first instance, with a few examples of FFTs that have been performed on real measurements.

Appendix B

Real-Space-Domain to Reciprocal-Space-Domain (2D) Fast-Fourier-Transforms

The two dimensional fast Fourier transform that converts from real-space to reciprocal-space is fundamentally the same as the one dimensional version that allowed transition from the time-domain to the frequency-domain covered in appendix A (also, it is not necessarily two-dimensional, though only 2D datasets are used within this thesis). This means that all of the implications of e.g. spectral leakage, apply here as well, only with an extra degree of freedom[145]. The only differences are the factor of 2π introduced, and that the 2D FFT is performed on a two-dimensional matrix of complex values (since phase information is now known) rather than a one-dimensional real valued vector. It is possible to apply window functions or to zero pad each dimension separately, which may be useful depending on the sample. The methodology behind zero-padding and window functions is as described in section A, but it is still useful to examine a basic 2D FFT and examine the differences between having an odd and even number of samples. There is an important difference to remark upon between the results of the experimental 2D spatial FFTs when compared to the 1D time-to-frequency FFTs. Since the 2D pressure fields contain complex phase information, the positive and negative halves of k-space will no longer necessarily mirror each other as they did with the 1D frequency axis. The extra information allows discrimination between waves propagating in different directions along the surface vectors.

Figure B.1 shows the result of the FFT applied to a simple 2D image, and the effect of the 'FFT-shift' function as applied in two dimensions. The top row (labelled A and B) are plots of the Hanning window function over a square grid of x and y

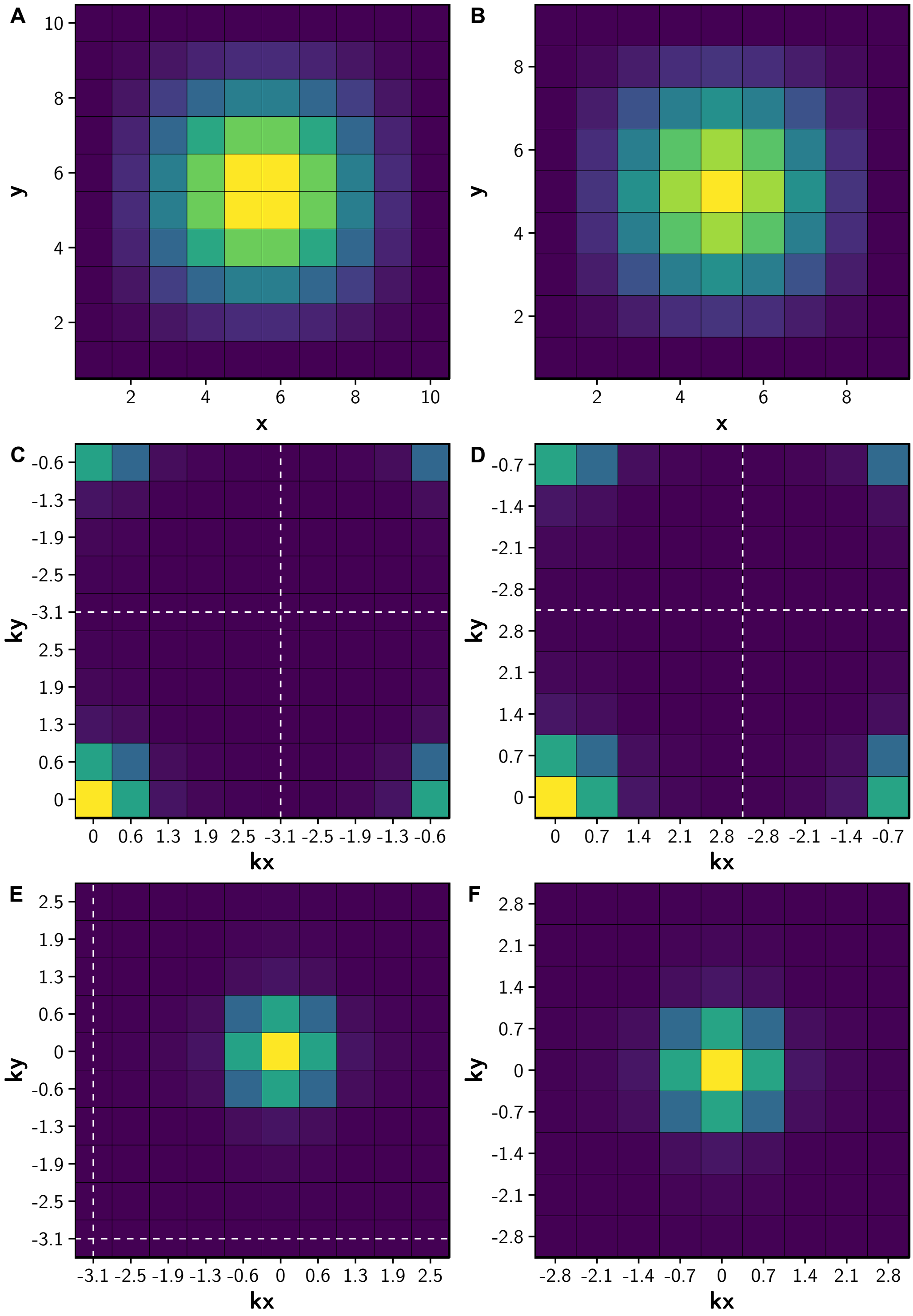

Figure B.1: Example of two basic spatial (2D) FFTs, with colour scale representing an arbitrary magnitude. (A) 2D signal generated from the Hanning window function, with number of points in each dimension $N_{\mathrm{x}} = N_{\mathrm{y}} = 10$ (i.e. an even dataset). (B) Same as A, except with an odd number of points $N_{\mathrm{x}} = N_{\mathrm{y}} = 9$. (C-D) Reciprocal space plot showing the absolute value of the direct result of the FFT of the signals in A and B respectively. The white-dashed line represents the 2D Nyquist limit. (E-F) The FFTs from C and D after the FFT-shift function is applied across both dimensions, highlighting the difference between even and odd length signals, with the white-dashed Nyquist limit appearing outside of the odd sample F.

coordinates, with the colour scales indicating relative (arbitrary) values, where bright (yellow) corresponds to a high value. There is no imaginary component to keep the example simple. The left column (A) has an even length grid of $N_\mathrm{x} = N_\mathrm{y} = 10$, while the right column (B) shows the same function applied over an odd length grid of size $N_\mathrm{x} = N_\mathrm{y} = 9$. For clarity, individual 'pixels' have a border drawn around them. The second row (labelled C and D) shows the direct result of the 2D FFT as applied to the values in A and B. Just as with the 1D FFT, the direct results are counter intuitive, with the maximum values of wave vectors k_x and k_y placed in the centre of the plot, and the small values in each corner. The white dashed line represents the 2D version of the Nyquist limit, i.e. the maximum wave vector accessible $k_{\mathrm{x}\max} = \frac{\pi}{\Delta x}$, similarly $k_{\mathrm{y}_{\max}} = \frac{\pi}{\Delta y}$. The Nyquist limit in 2D represents the boundary between quadrants, where the bottom left quadrant represents the positive values of k, while the top right represents the double negative quadrant of k-space. As with the 1D case, an even length number of samples has an extra pixel on this boundary, while the boundary lies between the pixels of an odd length sample. The k-space resolution Δk_x is determined from $\frac{2\pi}{L_\mathrm{x}}$, where L_x is the total number of steps in the real space direction N_x multiplied by the step size Δx (it is *not* simply the length of the sample as it appears, for the same reasons as explained in appendix A). So, rearranging the data using the 2D version of the FFT-shift function (which simply applies the 1D FFT-shift over each row and column individually), results in the plots labelled E and F, where the high k components are placed on the edge and the low k components in the centre, in the order:

$$k_\mathrm{x} = \begin{cases} -k_{\mathrm{x}\max}, -k_{\mathrm{x}\max} + \Delta k_\mathrm{x},\ \ldots,\ 0,\ \ldots,\ (k_{\mathrm{x}\max} - \Delta k_\mathrm{x}) & \text{if } N_\mathrm{x} \text{ is even} \\ -(k_{\mathrm{x}\max} - \frac{\Delta k_\mathrm{x}}{2}), -(k_{\mathrm{x}\max} - \frac{\Delta k_\mathrm{x}}{2}) + \Delta k_\mathrm{x},\ \ldots,\ 0,\ \ldots,\ (k_{\mathrm{x}\max} - \frac{\Delta k_\mathrm{x}}{2}) & \text{if } N_\mathrm{x} \text{ is odd} \end{cases} \tag{B.1}$$

This is how all reciprocal space plots throughout the thesis are presented, as it allows clear definition of different regions of reciprocal space such as the radiative regime $|k| < |k_0|$, where $k_0 = \frac{2\pi}{\lambda} = \sqrt{k_\mathrm{x}^2 + k_\mathrm{y}^2}$ and Brillouin zone boundaries, as explained in sections 2.7 and 6. An example of one of these spatial FFTs as applied to the sample in chapter 6 is shown in figure 3.11.

B. Real-Space-Domain to Reciprocal-Space-Domain (2D) Fast-Fourier-Transforms

References

[1] Rayleigh, L. *The Theory of Sound - Volume 1.* Macmillan, London, second edition (1896). 1, 10, 15

[2] Rayleigh, L. *The Theory of Sound - Volume 2.* Macmillan, London, second edition (1896). 1, 10, 21, 22, 27, 76, 78, 79, 89

[3] Young, T. Outlines of experiments and inquiries respecting sound and light. *Philosophical Transactions of the Royal Society of London*, pages 106–150 (1800). 1

[4] Kirchhoff, G. Ueber den Einflufs der Warmeleitung in einem Gase auf die Schallbewegung. *Annalen Der Physik Und Chemie*, **134**, 177 (1868). 1, 22, 75, 78, 88

[5] Laplace, P.S. *Pierre-Simon Laplace Philosophical Essay on Probabilities: Translated from the fifth French edition of 1825 With Notes by the Translator*, volume 13. Springer Science & Business Media (2012). 1

[6] Newton, I., Bernoulli, D., MacLaurin, C., and Euler, L. *Philosophiae naturalis principia mathematica*, volume 1. excudit G. Brookman; impensis TT et J. Tegg, Londini (1833). 1

[7] Lighthill, M.J. On sound generated aerodynamically. ii. turbulence as a source of sound. volume 222, pages 1–32. The Royal Society (1954). 1

[8] Lighthill, M.J. and Lighthill, J. *Waves in fluids.* Cambridge university press (2001). 1, 19, 77

[9] Long, M. *Architectural acoustics.* Elsevier (2005). 1, 24

[10] Cutler, C.C. Genesis of the corrugated electromagnetic surface. volume 3, pages 1456–1459. IEEE (1994). 1

[11] Craster, R.V. and Guenneau, S. *Acoustic metamaterials: Negative refraction, imaging, lensing and cloaking*, volume 166. Springer Science & Business Media (2012). 2, 3

[12] Pendry, J.B., Holden, A., Stewart, W., and Youngs, I. Extremely low frequency plasmons in metallic mesostructures. *Physical review letters*, **76**, 4773 (1996). 2

[13] Jikov, V.V., Kozlov, S.M., and Oleinik, O.A. *Homogenization of differential operators and integral functionals*. Springer Science & Business Media (2012). 2

[14] Veselago, V.G. The electrodynamics of substances with simultaneously negative values of and μ. *Soviet physics uspekhi*, **10**, 509 (1968). 2

[15] Pendry, J.B. Negative refraction makes a perfect lens. *Physical review letters*, **85**, 3966 (2000). 2

[16] Pendry, J.B., Schurig, D., and Smith, D.R. Controlling electromagnetic fields. *science*, **312**, 1780 (2006). 2

[17] Ramakrishna, S.A. Physics of negative refractive index materials. *Reports on progress in physics*, **68**, 449 (2005). 2

[18] Pendry, J.B. Negative refraction. *Contemporary Physics*, **45**, 191 (2004). 2

[19] Ebbesen, T.W., Lezec, H.J., Ghaemi, H., Thio, T., and Wolff, P. Extraordinary optical transmission through sub-wavelength hole arrays. *Nature*, **391**, 667 (1998). 2, 4, 31, 96

[20] Glybovski, S.B., Tretyakov, S.A., Belov, P.A., Kivshar, Y.S., and Simovski, C.R. Metasurfaces: From microwaves to visible. *Physics Reports*, **634**, 1 (2016). 3

[21] Ma, G. and Sheng, P. Acoustic metamaterials: From local resonances to broad horizons. *Science advances*, **2**, e1501595 (2016). 3, 4, 9

[22] Liu, Z., Zhang, X., Mao, Y., Zhu, Y., Yang, Z., Chan, C., and Sheng, P. Locally resonant sonic materials. *Science*, **289**, 1734 (2000). 3, 33, 48, 172

[23] Li, J. and Chan, C. Double-negative acoustic metamaterial. *Physical Review E*, **70**, 055602 (2004). 3

[24] Fang, N., Xi, D., Xu, J., Ambati, M., Srituravanich, W., Sun, C., and Zhang, X. Ultrasonic metamaterials with negative modulus. *Nature materials*, **5**, 452 (2006). 3, 31, 75

[25] Pierre, A.C. and Pajonk, G.M. Chemistry of aerogels and their applications. *Chemical Reviews*, **102**, 4243 (2002). 3

[26] Pendry, J., Martin-Moreno, L., and Garcia-Vidal, F. Mimicking surface plasmons with structured surfaces. *Science*, **305**, 847 (2004). 4, 31

[27] Christensen, J., Martin-Moreno, L., and Garcia-Vidal, F.J. Theory of resonant acoustic transmission through subwavelength apertures. *Physical Review Letters*, **101**, 014301 (2008). 4, 33, 35, 36, 42, 43, 46, 77, 84, 94, 96, 100, 106, 116, 127, 170

[28] Wang, X. Theory of resonant sound transmission through small apertures on periodically perforated slabs. *Journal of Applied Physics*, **108**, 064903 (2010). 4, 28, 32, 33, 35, 36, 77, 96, 100, 104, 116

[29] Ivanov-Shits, K. and Rozhin, F. investigation of surface waves in air. *Sov. Phys. Acoust*, **5**, 510 (1959). 4, 31

[30] Wenzel, A.R. Propagation of waves along an impedance boundary. *The Journal of the Acoustical Society of America*, **55**, 956 (1974). 4, 30, 31

[31] Donato, R. Propagation of a spherical wave near a plane boundary with a complex impedance. *The Journal of the Acoustical Society of America*, **60**, 34 (1976). 4, 31

[32] Stinson, M.R. and Daigle, G.A. Surface wave formation at an impedance discontinuity. *The Journal of the Acoustical Society of America*, **102**, 3269 (1997). 4, 30, 31, 32

[33] van Der Heijden, L. and Martens, M. Traffic noise reduction by means of surface wave exclusion above parallel grooves in the roadside. *Applied Acoustics*, **15**, 329 (1982). 4, 29, 31

[34] Cummer, S.A., Christensen, J., and Alù, A. Controlling sound with acoustic metamaterials. *Nature Reviews Materials*, **1**, 16001 (2016). 4

[35] Hou, B., Mei, J., Ke, M., Wen, W., Liu, Z., Shi, J., and Sheng, P. Tuning Fabry-Perot resonances via diffraction evanescent waves. *Physical Review B - Condensed Matter and Materials Physics*, **76**, 054303 (2007). 4, 35, 42, 43, 77, 96, 100, 104, 106, 115, 116, 125, 127

[36] Christensen, J., Fernandez-Dominguez, A., de Leon-Perez, F., Martin-Moreno, L., and Garcia-Vidal, F. Collimation of sound assisted by acoustic surface waves. *Nature Physics*, **3**, 851 (2007). 4

[37] Ye, Y., Ke, M., Li, Y., Wang, T., and Liu, Z. Focusing of spoof surface-acoustic-waves by a gradient-index structure. *Journal of Applied Physics*, **114**, 154504 (2013). 4, 116, 127

[38] Jia, H., Lu, M., Wang, Q., Bao, M., and Li, X. Subwavelength imaging through spoof surface acoustic waves on a two-dimensional structured rigid surface. *Applied Physics Letters*, **103**, 103505 (2013). 4, 116, 122, 127

[39] Zhu, J., Christensen, J., Jung, J., Martin-Moreno, L., Yin, X., Fok, L., Zhang, X., and Garcia-Vidal, F. A holey-structured metamaterial for acoustic deep-subwavelength imaging. *Nature physics*, **7**, 52 (2011). 4, 75, 115, 116, 127

[40] Kaina, N., Lemoult, F., Fink, M., and Lerosey, G. Negative refractive index and acoustic superlens from multiple scattering in single negative metamaterials. *Nature*, **525**, 77 (2015). 4, 127

[41] Cummer, S.A. and Schurig, D. One path to acoustic cloaking. *New Journal of Physics*, **9**, 45 (2007). 4

[42] Sanchis, L., García-Chocano, V., Llopis-Pontiveros, R., Climente, A., Martínez-Pastor, J., Cervera, F., and Sánchez-Dehesa, J. Three-dimensional axisymmetric cloak based on the cancellation of acoustic scattering from a sphere. *Physical review letters*, **110**, 124301 (2013). 4

[43] Zigoneanu, L., Popa, B.I., and Cummer, S.A. Three-dimensional broadband omnidirectional acoustic ground cloak. *Nature materials*, **13**, 352 (2014). 4

[44] Kinsler, L.E., Frey, A.R., Coppens, A.B., and Sanders, J.V. Fundamentals of acoustics (1999). 10, 12, 17, 19, 21, 24, 25, 27, 28, 41, 52, 76, 77, 78, 100

[45] Raichel, D.R. *The Science and Applications of Acoustics*. Springer, New York, second edition (2006). 10, 12, 14, 15, 17, 24, 25, 27

[46] Pierce, A.D. et al. *Acoustics: an introduction to its physical principles and applications*, volume 20. McGraw-Hill New York (1981). 10

[47] Lemmon, E.W., Jacobsen, R.T., Penoncello, S.G., and Friend, D.G. Thermodynamic properties of air and mixtures of nitrogen, argon, and oxygen from 60 to 2000 k at pressures to 2000 mpa. *Journal of physical and chemical reference data*, **29**, 331 (2000). 12, 15, 23

[48] Morse, P.M. and Ingard, K.U. *Theoretical acoustics*. Princeton university press (1968). 14, 18

[49] Rienstra, S.S. and Hirschberg, A.A. An introduction to acoustics (2004). 14, 29, 54

[50] Cramer, O. The variation of the specific heat ratio and the speed of sound in air with temperature, pressure, humidity, and CO2 concentration. *The Journal of the Acoustical Society of America*, **93**, 2510 (1992). 16, 82, 100, 130

[51] Lautrup, B. *Physics of continuous matter: exotic and everyday phenomena in the macroscopic world*. CRC press (2011). 18

[52] Evans, L., Bass, H., and Sutherland, L. Atmospheric absorption of sound: theoretical predictions. *The Journal of the Acoustical Society of America*, **51**, 1565 (1972). 19

[53] Bass, H., Sutherland, L., Zuckerwar, A., Blackstock, D., and Hester, D. Atmospheric absorption of sound: Further developments. *The Journal of the Acoustical Society of America*, **97**, 680 (1995). 19

[54] Weston, D.E. The Theory of the Propagation of Plane Sound Waves in Tubes. *Proceedings of the Physical Society. Section B*, **66**, 695 (2002). xi, 21, 22, 75, 76, 78, 86, 88, 89, 91, 94

[55] Tijdeman, H. On the propagation of sound waves in cylindrical tubes. *J. Sound Vib.*, **39**, 1 (1975). 21, 22, 75, 76, 78, 91, 92, 94

[56] Rayleigh, L. On a Problem Relating to the Propagation of Sound Between Paralell Walls. *Philosophical Magazine*, **1**, 301 (1901). v, 22, 27, 28, 75, 77, 79, 86

[57] Stinson, M.R. The propagation of plane sound waves in narrow and wide circular tubes, and generalization to uniform tubes of arbitrary crosssectional shape. *The Journal of the Acoustical Society of America*, **89**, 550 (1991). xi, 22, 75, 76, 79, 86, 87, 88, 89, 94

[58] Yazaki, T., Tashiro, Y., and Biwa, T. Measurements of sound propagation in narrow tubes. *Proceedings of the Royal Society A: Mathematical, Physical and Engineering Sciences*, **463**, 2855 (2007). xii, 22, 77, 78, 88, 91, 92

[59] Haynes, W.M. *CRC handbook of chemistry and physics*. CRC press (2014). 24

[60] Hernandez, G. *Fabry-perot interferometers*. 3. Cambridge University Press (1988). 28

[61] Donato, R. Model experiments on surface waves. *The Journal of the Acoustical Society of America*, **63**, 700 (1978). 30, 31

[62] Dong, H. and Hovem, J.M. *Chapter 6 - Interface Waves*, pages 31 – 39. InTech, Rijeka (2011). 30, 48

[63] Gulyaev, Y.V. and Plesskiĭ, V. Propagation of acoustic surface waves in periodic structures. *Physics-Uspekhi*, **32**, 51 (1989). 30, 31, 48

[64] Feng, S. and Johnson, D.L. High-frequency acoustic properties of a fluid/porous solid interface. i. new surface mode. *The Journal of the Acoustical Society of America*, **74**, 906 (1983). 31

[65] Attenborough, K. and Richards, T.L. Solid particle motion induced by a point source above a poroelastic half-space. *The Journal of the Acoustical Society of America*, **86**, 1085 (1989). 31

[66] Kelders, L., Lauriks, W., and Allard, J.F. Surface waves above thin porous layers saturated by air at ultrasonic frequencies. *The Journal of the Acoustical Society of America*, **104**, 882 (1998). 31

[67] Lauriks, W., Kelders, L., and Allard, J. Poles and zeros of the reflection coefficient of a porous layer having a motionless frame in contact with air. *Wave Motion*, **28**, 59 (1998). 31

[68] Embleton, T.F., Piercy, J.E., and Olson, N. Outdoor sound propagation over ground of finite impedance. *The Journal of the Acoustical Society of America*, **59**, 267 (1976). 31

[69] Albert, D.G. Observations of acoustic surface waves in outdoor sound propagation. *The Journal of the Acoustical Society of America*, **113**, 2495 (2003). 31

[70] Zhu, W., Stinson, M.R., and Daigle, G.A. Scattering from impedance gratings and surface wave formation. *The Journal of the Acoustical Society of America*, **111**, 1996 (2002). 31

[71] Kelders, L., Allard, J.F., and Lauriks, W. Ultrasonic surface waves above rectangular-groove gratings. *The Journal of the Acoustical Society of America*, **103**, 2730 (1998). 31, 32, 33, 100, 116

[72] Daigle, G.A., Stinson, M.R., and Havelock, D.I. Experiments on surface waves over a model impedance plane using acoustical pulses. *The Journal of the Acoustical Society of America*, **99**, 1993 (1996). 31

[73] Tizianel, J., Allard, J.F., and Brouard, B. Surface waves above honeycombs. *The Journal of the Acoustical Society of America*, **104**, 2525 (1998). 31

[74] Zhang, X. Acoustic resonant transmission through acoustic gratings with very narrow slits: Multiple-scattering numerical simulations. *Physical Review B - Condensed Matter and Materials Physics*, **71**, 241102 (2005). 31, 77, 96

[75] Mechel, F.P. and Munjal, M.L. *Formulas of Acoustics*. Springer, Berlin (2008). 32, 76, 87, 100

[76] Wang, X. Acoustical mechanism for the extraordinary sound transmission through subwavelength apertures. *Applied Physics Letters*, **96**, 134104 (2010). 32, 33, 43, 100, 116, 125

[77] Barnes, W.L., Dereux, A., and Ebbesen, T.W. Surface plasmon subwavelength optics. *Nature*, **424**, 824 (2003). 33

[78] Li, Y., Qi, S., and Assouar, M.B. Theory of metascreen-based acoustic passive phased array. *New Journal of Physics*, **18**, 043024 (2016). 33

[79] Hou, B., Mei, J., Ke, M., Liu, Z., Shi, J., and Wen, W. Experimental determination for resonance-induced transmission of acoustic waves through subwavelength hole arrays. *Journal of Applied Physics*, **104**, 014909 (2008). 33, 75, 77, 116

[80] Neittaanmäki, P., Rossi, T., Majava, K., Pironneau, O., Périaux, J., and Krizek, M. A finite element method for the modeling of thermo-viscous effects in acoustics (2004). 33

[81] Yablonovitch, E. and Gmitter, T. Photonic band structure: The face-centered-cubic case. *Physical Review Letters*, **63**, 1950 (1989). 33

[82] Kittel, C. and Holcomb, D.F. Introduction to solid state physics. *American Journal of Physics*, **35**, 547 (1967). ix, xvi, 33, 36, 37, 47, 68, 120, 121, 124

[83] Zhang, X. and Liu, Z. Negative refraction of acoustic waves in two-dimensional phononic crystals. *Applied Physics Letters*, **85**, 341 (2004). 33, 48, 172

[84] Hooper, I.R. and Sambles, J.R. Dispersion of surface plasmon polaritons on short-pitch metal gratings. *Physical Review B*, **65**, 165432 (2002). 35, 41

[85] Zhou, Y., Lu, M.H., Feng, L., Ni, X., Chen, Y.F., Zhu, Y.Y., Zhu, S.N., and Ming, N.B. Acoustic surface evanescent wave and its dominant contribution to extraordinary acoustic transmission and collimation of sound. *Physical review letters*, **104**, 164301 (2010). 35

[86] Ashcroft, N.W. and Mermin, N.D. Solid state physics (1976). 37, 38, 43

[87] Lu, M.H., Liu, X.K., Feng, L., Li, J., Huang, C.P., Chen, Y.F., Zhu, Y.Y., Zhu, S.N., and Ming, N.B. Extraordinary acoustic transmission through a 1D grating with very narrow apertures. *Physical Review Letters*, **99**, 174301 (2007). 42, 75, 77, 96, 100, 116

[88] Kushwaha, M.S., Halevi, P., Dobrzynski, L., and Djafari-Rouhani, B. Acoustic band structure of periodic elastic composites. *Physical review letters*, **71**, 2022 (1993). 48, 172

[89] Badreddine Assouar, M. and Oudich, M. Enlargement of a locally resonant sonic band gap by using double-sides stubbed phononic plates. *Applied Physics Letters*, **100**, 123506 (2012). 48, 172

[90] Badreddine Assouar, M. and Oudich, M. Dispersion curves of surface acoustic waves in a two-dimensional phononic crystal. *Applied Physics Letters*, **99**, 123505 (2011). 48, 172

[91] Lamb, H. On waves in an elastic plate. volume 93, pages 114–128. The Royal Society (1917). 49, 174

[92] Estrada, H., Candelas, P., Belmar, F., Uris, A., de Abajo, F.J.G., and Meseguer, F. Engineering surface waves in flat phononic plates. *Physical Review B*, **85**, 174301 (2012). 49, 172

[93] Attenborough, K. Acoustical characteristics of porous materials. *Physics reports*, **82**, 179 (1982). 52

[94] Tóth, P. and Schram, C. Simultaneous calibration of multiple microphones for both phase and amplitude in an impedance tube. *Archives of Acoustics*, **39**, 277 (2014). 52

[95] PicoScope Technologies PicoScope 2000 series a api programmers guide (2017). 60

[96] Profunser, D.M., Muramoto, E., Matsuda, O., Wright, O.B., and Lang, U. Dynamic visualization of surface acoustic waves on a two-dimensional phononic crystal. *Physical Review B*, **80**, 014301 (2009). 66

[97] Dockrey, J., Horsley, S., Hooper, I.R., Sambles, J., and Hibbins, A.P. Direct observation of negative-index microwave surface waves. *Scientific reports*, **6** (2016). 66, 122

[98] Otsuka, P.H., Nanri, K., Matsuda, O., Tomoda, M., Profunser, D., Veres, I., Danworaphong, S., Khelif, A., Benchabane, S., Laude, V. et al. Broadband evolution of phononic-crystal-waveguide eigenstates in real- and k-spaces. *Scientific reports*, **3**, 3351 (2013). 66

[99] CRAN Viridis colour scale package repository (2017). 67

[100] Akin, J.E. *Finite Elements for Analysis and Design*. Academic Press, San Diego, first edition (1994). 70

[101] Comsol multiphysics. `http://www.comsol.com/products/multiphysics/` (2017). Accessed: 31-01-2017. 70

[102] COMSOL Multiphysics Acoustics Module. `http://hpc.mtech.edu/comsol/pdf/Acoustics_Module/AcousticsModuleUsersGuide.pdf` (2017). Accessed: 02-02-2017. 71, 72

[103] Bathe, K.J. *Finite element method*. Wiley Online Library (2008). 72

[104] Dhatt, G., Lefrançois, E., and Touzot, G. *Finite element method*. John Wiley & Sons (2012). 72

[105] Christensen, J., Martín-Moreno, L., and García-Vidal, F.J. Enhanced acoustical transmission and beaming effect through a single aperture. *Physical Review B - Condensed Matter and Materials Physics*, **81**, 174104 (2010). 77

[106] Estrada, H., Candelas, P., Uris, A., Belmar, F., Meseguer, F., and García de Abajo, F.J. Sound transmission through perforated plates with subwavelength hole arrays: A rigid-solid model. *Wave Motion*, **48**, 235 (2011). 77, 96

[107] Badreddine Assouar, M., Senesi, M., Oudich, M., Ruzzene, M., and Hou, Z. Broadband plate-type acoustic metamaterial for low-frequency sound attenuation. *Applied Physics Letters*, **101**, 173505 (2012). 77

[108] Homentcovschi, D., Miles, R.N., and Tan, L. Influence of viscosity on the diffraction of sound by a periodic array of screens. *J. Acoust. Soc. Am.*, **117**, 2761 (2005). 79, 88

[109] Homentcovschi, D. and Miles, R.N. Influence of viscosity on the reflection and transmission of an acoustic wave by a periodic array of screens: The general 3-D problem. *Wave Motion*, **45**, 191 (2008). 79

[110] Fantino, A.N., Grosz, S.I., and Skigin, D.C. Resonant effects in periodic gratings comprising a finite number of grooves in each period. *Physical Review E*, **64**, 016605 (2001). 95, 96

[111] Skigin, D.C. and Depine, R.A. Transmission resonances of metallic compound gratings with subwavelength slits. *Physical review letters*, **95**, 217402 (2005). 95, 96, 101, 104

[112] Skigin, D.C. and Depine, R.A. Narrow gaps for transmission through metallic structured gratings with subwavelength slits. *Physical Review E*, **74**, 046606 (2006). 95, 96

[113] Hibbins, A.P., Hooper, I.R., Lockyear, M.J., and Sambles, J.R. Microwave transmission of a compound metal grating. *Physical review letters*, **96**, 257402 (2006). 95, 96, 101, 104

[114] Skigin, D.C., Loui, H., Popovic, Z., and Kuester, E.F. Bandwidth control of forbidden transmission gaps in compound structures with subwavelength slits. *Physical Review E*, **76**, 016604 (2007). 95, 96

[115] Rance, H.J., Hamilton, O.K., Sambles, J.R., and Hibbins, A.P. Phase resonances on metal gratings of identical, equally spaced alternately tapered slits. *Applied Physics Letters*, **95**, 041905 (2009). 95, 96

[116] Zhou, L. and Kriegsmann, G.A. Complete transmission through a periodically perforated rigid slab. *The Journal of the Acoustical Society of America*, **121**, 3288 (2007). 96

[117] Martin-Moreno, L., Garcia-Vidal, F., Lezec, H., Pellerin, K., Thio, T., Pendry, J., and Ebbesen, T. Theory of extraordinary optical transmission through subwavelength hole arrays. *Physical review letters*, **86**, 1114 (2001). 96

[118] Liu, Z. and Jin, G. Resonant acoustic transmission through compound subwavelength hole arrays: the role of phase resonances. *Journal of Physics: Condensed Matter*, **21**, 445401 (2009). 96

[119] Zhang, H., Fan, L., Qu, J., and Zhang, S. Sound transmission properties assisted by the phase resonances of composite acoustic gratings. *Journal of Applied Physics*, **119**, 084902 (2016). 96

[120] Ulrich, R. and Tacke, M. Submillimeter waveguiding on periodic metal structure. *Applied Physics Letters*, **22**, 251 (1973). 122

[121] Camacho, M., Boix, R.R., and Medina, F. Computationally efficient analysis of extraordinary optical transmission through infinite and truncated subwavelength hole arrays. *Physical Review E*, **93**, 063312 (2016). 124

[122] Murray, A.R., Summers, I., Sambles, J.R., and Hibbins, A.P. An acoustic double fishnet using helmholtz resonators. *The Journal of the Acoustical Society of America*, **136**, 980 (2014). 127

[123] Christensen, J., Martín-Moreno, L., and Garcia-Vidal, F. All-angle blockage of sound by an acoustic double-fishnet metamaterial. *Applied Physics Letters*, **97**, 134106 (2010). 127

[124] Torrent, D. and Sánchez-Dehesa, J. Acoustic analogue of graphene: observation of dirac cones in acoustic surface waves. *Physical review letters*, **108**, 174301 (2012). 127

[125] Berry, M. Attenuation and focusing of electromagnetic surface waves rounding gentle bends. *Journal of Physics A: Mathematical and General*, **8**, 1952 (1975). 128, 134, 136, 137, 170

[126] Maling, B. and Craster, R. Whispering bloch modes. volume 472, page 20160103. The Royal Society (2016). 138

[127] Hessel, A., Chen, M.H., Li, R.C., and Oliner, A.A. Propagation in periodically loaded waveguides with higher symmetries. *Proceedings of the IEEE*, **61**, 183 (1973). 140, 141, 152, 155, 160, 162, 166, 168

[128] Quesada, R., Martín-Cano, D., García-Vidal, F., and Bravo-Abad, J. Deep-subwavelength negative-index waveguiding enabled by coupled conformal surface plasmons. *Optics letters*, **39**, 2990 (2014). 140, 141, 154, 155, 160, 161

[129] McWeeny, R. *Symmetry: An introduction to group theory and its applications.* Courier Corporation (2002). 141

[130] Constant, T.J., Taphouse, T.S., Rance, H.J., Kitson, S.C., Hibbins, A.P., and Sambles, J.R. Surface plasmons on zig-zag gratings. *Optics express*, **20**, 23921 (2012). 141

[131] Mitchell-Thomas, R., Hooper, I., Sambles, J., Hibbins, A., and Quevedo-Teruel, O. Broadband metasurface for surface wave lenses. pages 605–606. IEEE (2016). 165

[132] Jiang, X., Li, Y., Liang, B., Cheng, J.c., and Zhang, L. Convert acoustic resonances to orbital angular momentum. *Physical Review Letters*, **117**, 034301 (2016). 168

[133] Xiao, M., Chen, W.J., He, W.Y., and Chan, C.T. Synthetic gauge flux and weyl points in acoustic systems. *Nature Physics*, **11**, 920 (2015). 172

[134] He, C., Ni, X., Ge, H., Sun, X.C., Chen, Y.B., Lu, M.H., Liu, X.P., and Chen, Y.F. Acoustic topological insulator and robust one-way sound transport. *Nature Physics* (2016). 172

[135] Moiseyenko, R.P., Declercq, N.F., and Laude, V. Guided wave propagation along the surface of a one-dimensional solid–fluid phononic crystal. *Journal of Physics D: Applied Physics*, **46**, 365305 (2013). 172

[136] Gross, J., Fricke, J., and Hrubesh, L. Sound propagation in sio2 aerogels. *The Journal of the Acoustical Society of America*, **91**, 2004 (1992). 174

[137] Junger, M.C. and Feit, D. *Sound, structures, and their interaction*, volume 225. MIT press Cambridge, MA (1986). 174

[138] Rabiner, L.R. and Gold, B. Theory and application of digital signal processing. *Englewood Cliffs, NJ, Prentice-Hall, Inc., 1975. 777 p.*, **1** (1975). 183

[139] Parker, M. *Digital Signal Processing 101: Everything you need to know to get started*. Newnes (2010). 183, 187, 188, 189, 190

[140] Antoniou, A. *Digital signal processing*. McGraw-Hill Toronto, Canada: (2006). 183, 185, 187, 188, 189, 190

[141] Van Loan, C. *Computational frameworks for the fast Fourier transform*. SIAM (1992). 185

[142] Harris, F.J. On the use of windows for harmonic analysis with the discrete fourier transform. *Proceedings of the IEEE*, **66**, 51 (1978). 190

[143] Heinzel, G., Rüdiger, A., and Schilling, R. Spectrum and spectral density estimation by the discrete fourier transform (dft), including a comprehensive list of window functions and some new at-top windows (2002). 190

[144] Testa, A., Gallo, D., and Langella, R. On the processing of harmonics and interharmonics: Using hanning window in standard framework. *IEEE Transactions on Power Delivery*, **19**, 28 (2004). 190

[145] Anuta, P.E. Spatial registration of multispectral and multitemporal digital imagery using fast fourier transform techniques. *IEEE transactions on Geoscience Electronics*, **8**, 353 (1970). 193